Determination of Soil Grain Size Distribution by Soil Sedimentation and Image Processing

by
Yongsub Jung

A dissertation submitted in partial fulfillment
of the requirements for the degree of
Doctor of Philosophy
(Civil Engineering)
in The University of Michigan
2010

Doctoral Committee:

Professor Roman D. Hryciw, Chair
Professor Steven J. Wright
Associate Professor Elizaveta Levina
Assistant Professor Adda Athanasopoulos-Zekkos
Assistant Professor Dimitrios Zekkos

This dissertation is dedicated

to my father, Sukchool Jung,
to my mother, Sinyoung Han,
to my sister, Imsung Jung,
to my little daughter, Irene Y. Jung, and
to my lovely wife, Yumi Lee who has supported me tremendously
throughout my graduate career.

ACKNOWLEDGEMENTS

First and foremost, I heartily wish to express my deepest gratitude to Professor Roman D. Hryciw, chairman of the doctoral committee, for his unselfish guidance, patience, support, during the study at the University of Michigan. He always took the time to teach me and to help me develop my skills as an engineer and as a person. I would like to thank him again for his profound and valuable efforts in reviewing on the material in my dissertation work. Without him, it would be impossible to complete this work. I am and will always be proud of being a student of him.

I would also like to thank to the other members of the doctoral committee, Professor Adda Athanasopoulos-Zekkos, Professor Elizaveta Levina, Professor Steven J. Wright, and Professor Dimitrios Zekkos, for their invaluable time and efforts in reviewing the material of this work, thankful suggestions, and guidance regarding this dissertation work.

I would also like to acknowledge the help and assistance of my fellow colleagues and friends during the study at the University of Michigan. Special thanks to Mr. Bob Fischer and Mr. Harold W. Eberhart for their valuable help and opinions in designing and building Sedimaging test devices. Their help and suggestions have made a difference.

I also extend my gratitude to my fellow colleagues, Dr. Jongwon Lee, Dr. Youngjae Kang, Dr. Seungchoel Shin, Mr. David A. Safter, and Mr. Hyonsohk Uhm, for being friends and for the support they have lent me during my stay in Ann Arbor, MI.

My very special thanks to my parents whom I owe everything I am today, my father and my mother, Sukchul Jung and Sinyoung Han. Their unwavering faith and confidence in my abilities and in me is what has shaped me to be the person I am today.

I greatly appreciate my lovely and beautiful wife, Yumi Lee for her understanding and love during the past few years. Her support and encouragement was in the end what made this dissertation possible.

Last, but not least, I thank my little daughter, Irene Yunseo Jung for her bright smiles.

TABLE OF CONTENTS

LIST OF FIGURES

LIST OF TABLES

ABSTRACT

Determination of Soil Grain Size Distribution by
Soil Sedimentation and Image Processing

by

Yongsub Jung

Chair: Roman D. Hryciw

Over the last decades, advances in digital imaging have moved many industries to adopt digital image processing (DIP) to determine the grain size distribution of their products. However, despite of the fact that image-based soil grain size assessment methods have advantages over traditional sieve testing, they have lagged behind due to the inability of single camera-lens systems to capture the wide range of soil grain sizes.

Since no DIP technique exists for determination of grain size distribution of 3-dimensional soil assemblies of non-uniform sized particles, an eight foot long glass sedimentation column was constructed to rapidly segregate particles by size prior to imaging. Following sedimentation through the water-filled column a camera is used to collect digital images of the segregated soil sediment. Image sections with a height of 256 pixels, which contain relatively uniform sized particles, are image-processed for soil grain size to obtain a volume-based soil grain size distribution. With this approach,

the need for determining soil grain sizes from images of non-uniform sized grains is eliminated. The method is termed ‘Sedimaging’.

To determine soil grain size at each image section, statistical DIP methods based on wavelet decomposition, pattern spectrum, and edge pixel density were developed. They utilize a ‘wavelet index’ (*CA*), the ‘edge pixel density’ (*EPD*), and a ‘structuring element size at peak of pattern spectrum’ (*SP*) calibrated against the soil grain size in units of pixels per diameter.

The effects of effective stress and soil grain size on void ratio in a sedimented soil column were studied to address the influence of void ratio variations on soil grain size distribution by Sedimaging. Void ratio variations developed in the soil sediment were found to be so small that no correction to the image-based grain size distribution is necessary.

Soil grain size distribution by Sedimaging fairly well mimics the sieve-based grain size distribution. In particular, the wavelet decomposition and pattern spectrum methods demonstrated their suitability to Sedimaging. However, the edge pixel density method’s implementation into Sedimaging was not as successful as the other two methods mainly due to the sensitivity of *EPD* to grain size uniformity.

CHAPTER I

Introduction

Soil is a material which human beings have lived with and which is prevalent everywhere on the surface of the Earth. In ancient times, its familiarity and easy accessibility allowed human beings to use the material for the purpose of self protection from external threats, such as weather, natural disasters, and predatory creatures. Now days, the purpose of using soil is not much different from that in ancient times. However, much larger and more stable soil structures are built with a better understanding of soil engineering properties and mechanical behavior. One of the most fundamental and important soil properties is its grain size distribution.

Soil grain size distribution is used for soil classification and thus serves as the first estimator of almost every mechanical and hydrologic soil behavior including compressibility, shear strength, hydraulic conductivity, and water-soil interaction. The most widely used methods for soil grain size distribution determination are sieve and hydrometer tests. In spite of the fact that these standard test methods are physically cumbersome, noisy, dusty, and somewhat inaccurate, geotechnical engineers and soil scientists have remained inextricably tied to them due to the large range of soil particle

sizes found in nature and the large number of grains typically required for a specimen to be statistically representative.

With advances in high speed computers and high resolution digital cameras, geotechnical engineers and soil scientists have been attracted to the potential of digital imaging technologies for determining soil grain size. The use of digital imaging technologies for soil grain size analysis involves obtaining digital soil images, which are basically two dimensional signals, and digitally processing them. Successful application of digital imaging technologies to soil grain size analysis would make numerous positive impacts. Compared to sieve and hydrometer tests, image based grain size distributions are much more reliable as they eliminate human errors. They are consistent and independent of operators' skills and experiences. Digital image based tests are faster and simpler so that a greater number of tests could be performed per unit of time. This also ensures a cost saving per test. Since more soil samples can be collected and analyzed, better and more statistically valid results would be achieved.

Many researchers have attempted grain size analysis of various sizes of soil particles from gravel to clay using digital imaging technologies. An early approach evaluated the sizes of only non-contacting and non-overlapping soil grains in two dimensions (Rao et al., 2001; Brzezicki and Kapserkiewicz, 1999; Park et al., 2008; Raschke and Hryciw, 1997; Ghalib and Hryciw, 1999). Since individual grains were not touching, simple image processing techniques such as thresholding were used to digitally delineate soil gains from the image background. The sizes of the non-contacting soil grains could be determined by counting the number of pixels that lay within the grain boundaries.

For preparing samples of non-contacting and non-overlapping soil grains, the particles are laid out on a flat plate and vibrated or chemically treated (when soil grains are very small) to disperse them. However, it takes a great deal of time, space, and effort to prepare and take statistically representative images. Also, as soil grain size gets down to fine sand, physical separation becomes very difficult.

The limitations in the soil grain size analysis with non-contacting and non-overlapping soil led researchers to move toward seeking size distributions of three dimensional soil grain assemblies, or contacting soil grains without physical separation (Dahl and Esbensen, 2007; Graham et al., 2005; Maragos et al., 2004; Ghalib and Hryciw, 1999). The advantage of this approach is that much less effort is needed to prepare soil specimens than that required for non-contacting soil grain analysis. Now, instead of simple image thresholding methods and pixel counting, advanced image processing techniques are needed for digital separation of contacting grains and completion of missing edges. However, the performance of such techniques is greatly influenced by operator skills and thus would not produce consistent reliable results.

Aside from the difficulties of developing image processing techniques for the analysis of images of three dimensional soil assemblies, it is important for images to contain all sizes of grains that are present in the soil while maintaining statistical validity. However, small soil grains fall through the pore spaces between larger grains and thus, are often hidden or occluded by the larger grains. This is one of the biggest downsides found in the mining industry when images are taken of soil aggregate on a conveyor belt for quality control (Maerz and Zhou, 1998; Yen, Lin, and Miller, 1998).

In spite of the great potentials of imaging technologies as a powerful tool for soil grain size analysis and the efforts by many researchers, soil grain size analysis by imaging technologies is still in its infant stage while other disciplines and industries including pharmaceuticals, medical research and diagnosis, manufacturing and food processing have successfully applied imaging technologies to the evaluation of their respective products or features of study. The difficulty in soil grain size analysis using image technologies comes from the fact that a large range of soil grain sizes are found in nature and a large number of grains are required for statistical validity of specimens.

Due to the difficulty mentioned above, efforts were taken to determine size of assemblies of uniform soil grains using texture analyses (Ghalib et al., 1998; Shin and Hryciw, 2004). Since image texture of assemblies of uniform grains is largely dictated by soil grain size, size assessment of uniform grains based on image texture became feasible by developing a textural index and establishing its calibration model for various soil grain sizes. If soil grains could be quickly segregated by size so that the grains could be sorted into areas of somewhat uniform sized soil grains, digital image processing could be applied to image sections containing uniform sized soil assemblies. This would eliminate the need for digitally separating soil grain assemblies into individual grains.

In this study, due to the fact that no ideal method has yet been developed for determination of grain size distribution from images of three dimensional soil assemblies of non-uniform grain size, efforts were focused on finding a technique to physically segregate grains by size prior to imaging. The solution was to use a long glass sedimentation column filled with water. A soil specimen is released into the top of the column and allowed to settle to the bottom. Digital images of the segregated soil

sediment are taken and followed by image processing to determine soil grain size incrementally but continuously with height in the column. With this "*Sedimaging*", approach for determining soil grain sizes from images of non-uniform sized grains is eliminated. The computer vision system and experiment setup for Sedimaging and test procedure are presented in Chapter III.

Since a soil sediment in the sedimentation column contains voids as well as soil solids and Sedimaging produces a volume based soil grain size distribution contrary to other image based soil grain size analyses, which seek a soil grain surface area based grain size distribution, the influence of void ratio variations in soil sediments on soil grain size distribution should be studied. To address void ratio variation in the soil sediment, the effect of effective stress, soil grain size, and elapsed time after deposition on void ratio is studied in Chapter IV.

In this study, three different techniques are used to determine soil grain size from three dimensional soil assemblies of uniform grain size. The first technique, developed by Shin and Hryciw (2004), utilizes the Haar (1910) wavelet transform and the amount of energy contained at each wavelet decomposition level. The energy at each wavelet decomposition level depends on the soil grain size in the images. The energy distribution among the decomposition levels is used to compute *wavelet index*, *CA* which correlates well with the diameter measured in units of image pixels. Initially, *CA* was calculated from images of dry uniform grained solids of various sizes to establish the relationship between *CA* and soil grain diameter. Then, the effect of water on *CA* was studied to allow its implementation to Sedimaging. This method is presented in Chapter V. The second image processing method uses Canny edge detection (Canny 1986) followed by the

removal of internal false edges to detect only soil grain boundaries. By observation, the number and length of edges of soil grains in a Canny edge map decreases with increasing soil grain size. So, the ratio of edge pixels to the total number of pixels in an image is termed the *Edge Pixel Density* (*EPD*). Chapter VI presents this method. The last image processing technique for Sedimaging uses mathematical morphology operation (Matheron. 1975; Serra, 1982), called *Opening* which is *Dilation* followed by *Erosion*, to construct a *pattern spectrum*. In a binary image where objects are not touching each others, opening removes objects smaller than a certain size defined by a *structuring element* while preserving objects larger than the structuring element. By repeating the opening operation and using sequentially larger structuring elements a pattern spectrum is developed. The resulting pattern spectrum from the binary image represents a histogram of object size in an image. However, the pattern spectra of a gray scale image of three dimensional assemblies of soil grains are not an exact size histogram but do reflect the distribution of grain sizes somewhat. Pattern spectrum as an approach for determining average soil grain size from three dimensional assemblies of relatively uniform sized grains is presented in Chapter VII.

In Chapter 8, Sedimaging tests with sand sized soils are performed and the resulting soil grain size distribution curves obtained using the three different image processing techniques are presented and compared to the results by sieve analysis. Also, *Three Point Imaging* (*TPI*) is presented for AASHTO soil classification.

CHAPTER II

State of Art, Literature Reviews, and Shortcoming of Existing Soil Grain Size Analysis

2.1 Introduction

This chapter reviews existing soil grain size analysis methods. Standard test methods for grain size distribution, sieve test and hydrometer test, and other test methods not related to imaging technologies are presented with a discussion of their major shortcomings. Imaging systems and image processing techniques developed for the quantification of soil grain properties, especially focusing on soil grain size distribution, are then reviewed.

2.2 Traditional Test Methods for Soil Grain Size Analysis

The standard test method used for determining size distribution of coarse grained soil fraction (soil grains larger than 0.075 mm) is the mechanical sieve test in accordance with ASTM D-422 and ASTM E-11. Sieving uses a stack of sieves placed in order of decreasing screen opening size from top to bottom. A soil specimen is poured into the top

sieve and the stack is shaken in vertical and horizontal directions to facilitate soil grain passage through the stack. In sieving, soil grain shape influences sieving results since soil grain sizes are determined by their shortest length. The sizing mechanism leads to inaccurate measurement when soil grain shape is elliptical rather than spherical.

Furthermore, sieving can produce erroneous soil grain size distributions because: 1. When a soil is poorly graded, a large amount of material is retained on one or two sieves, thus, the sieve openings tend to become clogged thereby preventing finer grains from easily passing through the openings. Even a soil whose size is relatively well distributed clogs the sieve openings. Also, overloading a sieve can distort the sieve openings. 2. Sieve test results depend on the duration and method of shaking. 3. More mechanical energy is required to make smaller soil gains pass through small sieve openings because of the surface attraction between the soil grains and between the soil grains and sieve openings. This can underestimate percentage of smaller particles. 4. Sieving results could depend on which and how many sieves are used.

For size distribution of fine grained soil (soil grains smaller than 0.075 mm), a hydrometer test (ASTM D-422 and ASTM E-100) is most widely used. The two principles on which the hydrometer test is based are : 1. Different soil grain sizes fall with different settling velocities in water. With a knowledge of the distance and time of fall, the settling velocity is determined. Then, the size of the soil grain is computed using Stokes' law, which relates the settling velocity of a sphere to its diameter. 2. The hydrometer is used to determine the density of the soil suspension, which enables the percent finer than a certain soil grain size to be calculated. The hydrometer test suffers from inherent difficulties. One problem arises from the use of Stokes' law which is based

on settlement of spherical objects. So, calculating soil grain size based on Stokes' law involves uncertainties since soil grains, especially fine grained particles are not spherical. Even if all of the soil grains were ideal spheres the insertion and removal of the hydrometer from the soil-water mixture disturbs the path of the falling soil grains and changes their settling velocities. Also, the concentration of soil grains is high so that they are not settling independently of each other, which results in questionable soil grain size computation by Stokes' law.

There are other methods that are based on settling velocity of soil grains in calculating soil grain size, such as the pipette method (Krumbein, 1932), the "diver" method (Berg, 1940), the closed manometer method (Heywood, 1938), the photometric method (Atherton, 1952), and the photoextinction method (Simmons ,1959). All these methods are subject to the same problems as the hydrometer test in terms of calculation of soil grain size because they all determine soil gain size based on Stokes' law.

Laser diffraction method has been used in other disciplines but is relatively new to geotechnical engineering applications (Buurman et al., 1997; Isbell, 1996; Liozeau et al., 1994). Laser diffraction method is by shooting laser light into a suspension of soil grains and measuring the scattered light angle and intensity. The laser diffraction method uses the fact that grains with different sizes scatter laser light at different ranges of angle and intensity. With the known intrinsic range of the light scattering angles and intensities of various particle sizes, Mie light scattering theory (Mie, 1908; Stratton, 1941) allows determination of scattered light intensity distribution from a known grain size distribution. The total scattered light intensity distribution with regard to scattered angles is deconvoluted to identify the contribution of each grain size to the intensity distribution.

Then, the contribution of each grain size is converted into a grain size distribution. This test method works well for perfect spheres like glass beads (Stuut 2001, Xu and Di 2003) and for non-spherical but uniform object shape by introduction of appropriate correction factors. However, for grain size analysis of soil which has various shapes and surface angularities, the laser diffraction method is not reliable and repeatable since the Mie light scattering theory assumes that the objects in suspension are perfect spheres. Many studies have shown the weaknesses and inaccuracies of the laser diffraction method for determination of soil grain size distribution. Campbell (2003) reported overestimation of the coarse-grained soil fractions while Loizeau et al. (1994), Buurman et al. (1997), Konert and Vandenberghe (1997), and Beuselinck et al. (1998) showed that laser diffraction method consistently underestimates the fine-grained soil fractions.

2.3 Digital Image Processing for Soil Grain Size Analysis

A digital image is an expression of a physical scene in two dimensional electronic form by discretization of the physical image into small regions called *pixels*, which are the smallest units of a digital image, each being assigned a numerical value as shown in Figure 2.1. For monochrome image, gray scale values represent the brightness of the area represented by a pixel. The gray scale value ranges from 0 (black) to 255 (white) for an 8 bit image. With the capture of physical scenes to digital images, it becames possible to digitally change, alter, and rearrange a physical image to extract information of interest.

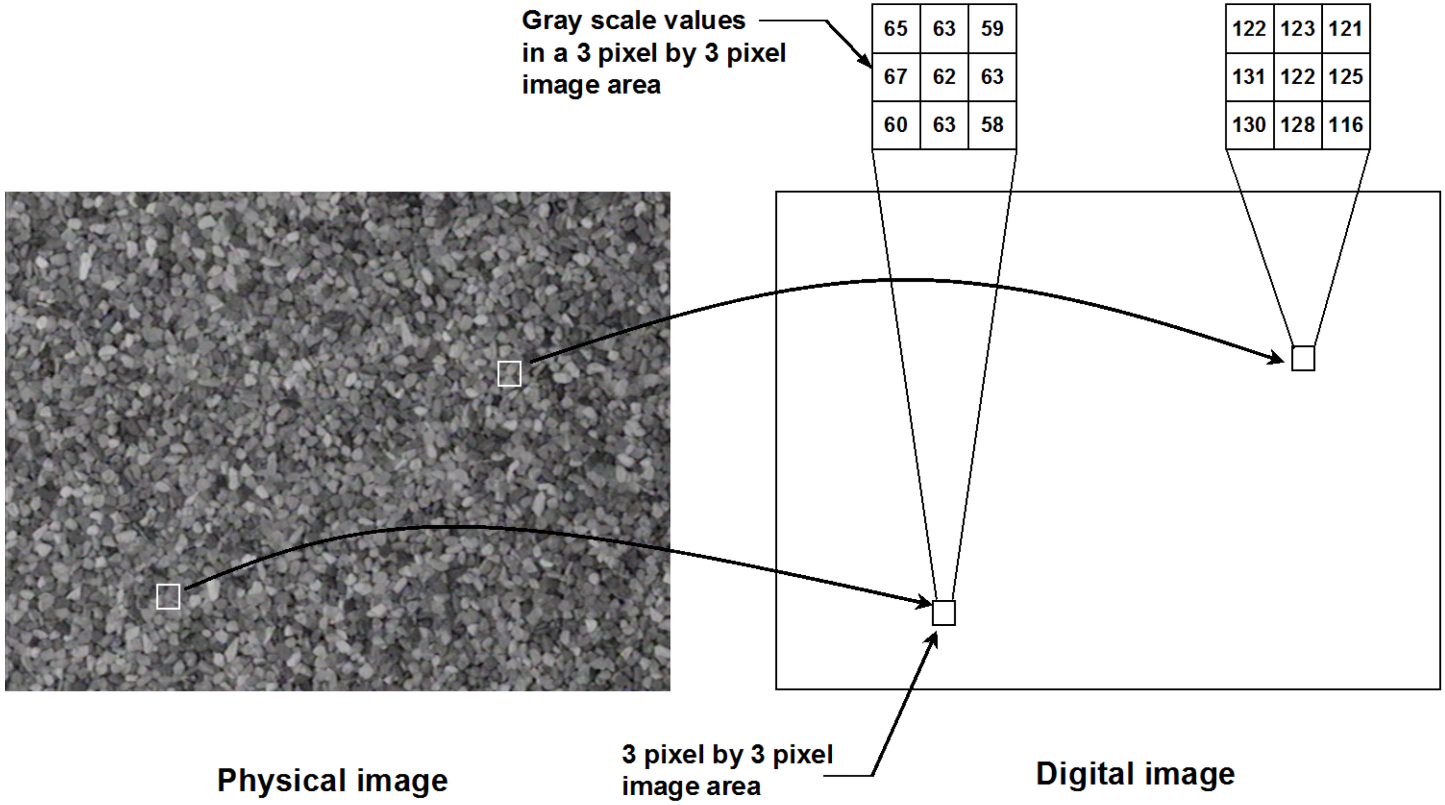

Figure 2.1 Physical image and its digitalization.

Image processing is the digital (computer-based) analysis and modification of digital images to extract desired information. Many techniques of digital image processing were developed in the 1960s for application to satellite imagery and medical imaging. However, due to the high cost of digital image processing, it was not widely applied to other disciplines and industries until the 1990s when inexpensive personal computers and digital cameras became available. Since then, digital image processing techniques have been adapted to many civil and geotechnical engineering applications to quantitatively analyze soil properties. One of the earliest applications of digital image processing to geotechnical engineering discipline was in evaluation of the shape of individual soil grains. It is important to see how soil grain shape analysis by digital image processing has been developed because many soil grain size analysis methods are an extension of soil grain shape analysis.

2.3.1 Soil Grain Shape Analysis

The standard shape evaluation method (ASTM D4791, 1995) consists of manual measurement of the longest dimensions of particles in three orthogonal directions and determination of two indices, the ratio of length to width (elongation index) and the ratio of width to height (flakiness index). The method provides very rough characterization, regular or irregular, based on the indices. Furthermore, roundness of soil grains (or conversely, the angularity) is determined qualitatively by visual observation. Since the manual method is labor intensive, tedious, and costly, often times, an insufficient number of tests are performed to produce statistically valid shape indices. With digital image processing, the disadvantages of the manual measurement and visual observation could

be overcome and quantitative results are obtainable (Yudhbir and Abedinzadeh, 1991; Li et al., 1993; Warner, 1995; Kuo et al., 1996; Brezezicki and Kasperkiewicz, 1999; Hubner et al., 2001; Darboux and Huang, 2003; Maerz, 2004; Al-Rousan et al., 2007).

Many image acquisition systems for soil grain shape analysis require that each individual soil grain be physically placed where it can be photographed. Brzezicki and Kasperkiewicz (1999) developed an imaging system, called 'fragment of cylindrical surface with a system of parallel indentations', which uses one camera and two light sources to get the projections of individual soil grains. Maerz and Lusher (2000) used two orthogonally mounted cameras to picture side and overhead views of soil grains moving on a conveyor belt. Rao et al. (2001) used three cameras to capture views in three orthogonal directions. Also, three dimensional imaging systems such as X-ray tomography (Wang et al., 2002; Garboczi, 2002; Garboczi and Bullard, 2004; Matsushima, 2009) and laser triangulation (Tolppanen et al., 1999; Lanaro and Tolppanen, 2002; Lee et al., 2007), were developed to obtain a three dimensional view of soil grains.

The majority of image processing techniques used for soil grain shape analysis rely on pixel counting methods. The method directly measures length, perimeter, and area of individual soil grains by counting the number of image pixels that lie within or on projected grain boundaries to quantify the relatively simple shape indices, such as elongation and flakiness (Yudhbir and Abedinzadeh, 1991; Li et al., 1993; Kuo et al., 1996; Brzezicki and Kasperkiewicz, 1999; Maerz and Zhou, 1999; Kuo and Freeman, 2000; Wang and Lai, 1998). Before counting the number of image pixels, soil images are binarized to discriminate soil grains from their background. Provided the background is

sufficiently darker or lighter than the particle, the image binarization can be performed by simply applying a "threshold" to the image. By image binarization, the background and soil grains can be expressed by black and white pixels, respectively. When the local curvature (angularity) is pursued, other image processing techniques rather than the pixel counting method were used. Image processing techniques for this category include the Hough transform (Wilson and Klotz, 1996), wavelet transform (Kim et al., 2002), fast Fourier transform (Penumadu and wettimuny, 2004), Fourier morphological analysis (Wang et al., 2005), and mathematical morphology (Lee et al., 2007).

2.3.2 Soil Grain Size Analysis

Soil grain size analysis of non-contacting particles

An approach taken from the early stage of soil grain size analysis by digital image processing is that soil grains are mechanically dispersed by vibration to separate particles (Raschke and Hryciw, 1997a; Mora et al., 1998; Ghalib and Hryciw, 1999; Raco et al., 2001), Some studies utilized chemical treatment to ensure soil grain separation (Park et al., 2008). Also, soil thin section where individual soil grains are separated by artificial binder materials has been used to obtain images of non-contacting soil grains (Pareschi et al., 1990; van den Berg et al., 2002; Marinoni et al., 2005; Mertens and Elsen, 2006). Many researchers used a single camera magnification level and utilized similar approach to mosaic imaging (Ghalib and Hryciw, 1999), wherein numerous images acquired at a single high magnification level are digitally stitched to obtain a large composite image that contains a large number of grains for statistical validity. Alternatively, rather than using a single magnification, a multiple magnification level procedure was used by

Raschke and Hryciw (1997). In the approach, the grain size distribution of well-graded soils can be pieced together using successive magnification levels. Statistical corrections are made for particles found on image boundaries. At each level, only grains within a specified size range are counted.

Image processing techniques used for analyzing non-contacting soil grains are relatively simple and similar to those for soil grain shape analysis. The procedure consists of two main steps: 1. Digital soil grain separation from the background using a threshold value. 2. Counting number of pixels that lie within soil grain boundaries. It should be noted that the selection of optimal threshold value is easy since soil grains are easily distinguished from a uniform background color.

The approach for non-contacting soil grains is straightforward and produces reliable results for fairly uniform soil grains. However, this approach has little practical benefit for very well graded soils since it requires a huge sample size and consequently a great number of images before a statistically representative sample is achieved. It is very tedious and time consuming to prepare non-contacting soil grains when the grain sizes are very small.

Contacting soil grain size analysis

For soils containing a wide range of grain sizes, contact between grains is unavoidable. Therefore, a search began for advanced digital image processing techniques that digitally separate the contacting grains and complete missing edges at grain contacts. Such techniques utilize edge detection and image segmentation methods such as active contouring (Kass et al., 1987; Hryciw et al., 1998), region growing (Pavlidis and Liow,

1990; Zhou et al., 2004), and watershed analysis (Beucher and Meyer, 1990; Ghalib and Hryciw, 1999; van den Berg et al., 2002; Graham et al., 2005; Sofou et al, 2005). These techniques were promising for relatively uniform soil samples whose grains are laid out on a flat surface, that is, for two dimensional soil grain assemblies. The procedure for size distribution of two dimensional soil grain assemblies consists of four steps; 1. Digital soil grain separation from the background, 2. Digital separation of grains from each other, 3. Missing edge completion, and 4. Counting the number of pixels that lie within each soil grain boundary. However, when a soil sample contains various shapes and colors of grains the techniques do not produce consistent, repeatable and reliable results. That is because edge detection and image segmentation methods involve image thresholding which is used to maintain the desired feature (soil grain boundaries) while removing the undesired features (internal textures within soil grain boundaries). The selection of a proper image threshold value is difficult when soil grains are contacting each other. Practically, there is no one unique optimal image threshold value applicable to all soil grains in an image due to the large variation of gray scale pixel values caused by different particles, colors, and internal textures. For example, when a specific image thresholding value is used for edge detection or segmentation of contacting soil grains, digital breakdown of a large grain into smaller grains and fusion of small grains can not be completely avoided. So, soil grain size analyses that use edge detection and image segmentation are inevitably dependent on the skills of the operators.

It is much more difficult to analyze images of real three dimensional soil assemblies. In real three dimensional soil assemblies, some grains are hidden behind others. Thus, the percentage of missing edges is much larger and edge detection and

image segmentation methods fail to provide adequate edge completion. Furthermore, some smaller soil grains fall into pore spaces and are hidden by larger grains. This will cause the larger soil grains to be more exposed to the camera's line of sight, which results in an apparent grain size distribution coarser than its actual size distribution. In the end, while successful in a limited number of idealized cases, the computational demands, the limitation to two dimensional assemblies, and the soil segregation problem make such deterministic methods nearly impossible for determining grain size distribution of multi-sized three dimensional assemblies of soil grains.

Statistical soil grain size analysis

Recognizing that deterministic pixel counting methods for sizing individual grains in images of three dimensional soil assemblies are too difficult, statistical methods based on "soil image texture" were investigated. Image texture implies spatial variation of gray scale pixel values in an image. It is known that variations in gray scale pixel values generate edges in the edge map of an image. Therefore, with the knowledge that edges in the edge map of soil image correspond mostly to soil grain boundaries, image texture can be used to determine soil grain size. Unlike deterministic soil grain size determination methods, statistical methods based on image texture do not directly measure soil grain size. Rather, they compute textural indices of various images containing different soil grain sizes and establish a unique relationship (calibration) between the indices and soil grain size. Then, using the pre-established relationships, the soil grain size in other images may be determined from their textural indices.

Image scale (magnification) is a controlling factor for soil grain size analysis with image texture indices. Depending on the image scale and soil grain sizes, the image texture drastically change. For example, boulders photographed from an airplane may appear similar and produce identical textures as would silt observed under a microscope. Thus, computed image texture indices cannot be correlated directly to physical grain size. So, Ghalib et al. (1998) proposed using *Pixels Per Diameter* (*PPD*) as illustrated in Figure 2.2 to represent the perceived soil grain size in images rather than the actual grain size for correlation to the image texture indices.

Haralick et al. (1973) defined 14 textural indices for images. With the development of the pixel per diameter (*PPD*) concept, Ghalib et al. (1998) developed the relationships between Haralick's textural indices (Angular second moment, Contrast, Correlation, and Variance) and *PPD* for uniform sized three dimensional soil assemblies and also established a neural network model to determine average soil grain size on the basis of several of Haralick's textural indices. Unfortunately, Shin and Hryciw (2004) found that a single calibration between the textural indices and *PPD* does not exist because the indices are also dependent on the degree of illumination on the soil specimen and on the soil grain color. Given the failure to develop a universal calibration for uniform soils, no attempts were made to extend the research to non-uniform sized particles.

The problem of illumination intensity and grain color was overcome by Shin and Hryciw (2004) using *wavelet transform analysis*. The result of an image decomposition using a Harr (1910) wavelet transform can be used to plot a *Normalized Energy* vs. *Decomposition Level* for images of uniform grained soils of various *PPD*. Hryciw et al.

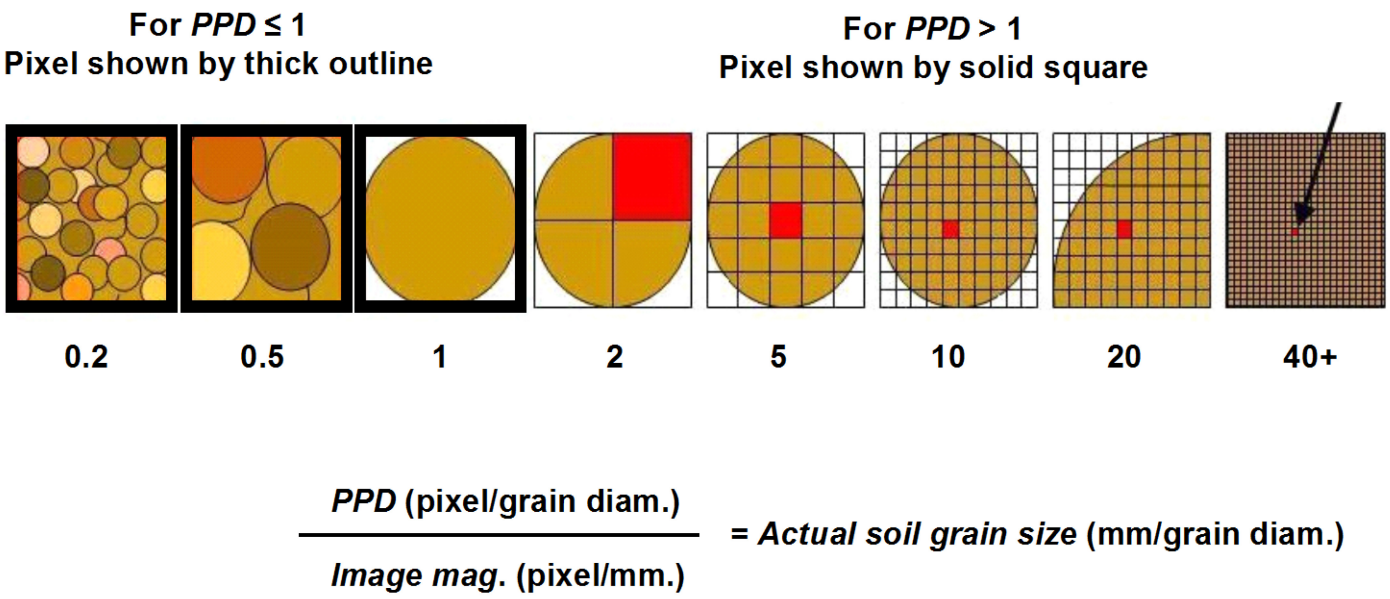

Figure 2.2 Pixels Per Diameter (PPD) and calculation of actual soil grain size (Hryciw et al., 2006).

(2006) showed that the *Center of the Area* (*CA*) beneath the normalized energy plots is related to *PPD*. This relationship is universal for all uniform grained soils while being unaffected by soil color, soil color uniformity, soil translucence and illumination intensity. Having established the relationship between *CA* and *PPD* for assemblies of uniform grains, normalized energy plots were developed for mixtures of two grain sizes. The results were disappointing; the *CA* of mixtures always reflected the *CA* of the more abundant grain size. Thus, while the dominant grain size was revealed, the percentages of the particles by size were not.

Barnard et al. (2007) used an autocorrelation algorithm for statistically determining grain size of uniform sized soil. Autocorrelation is a measurement of spatial similarity between a given image and a spatially lagged version of itself over successive pixel intervals. The idea of using autocorrelation algorithm for soil grain size analysis came from the observation that the plot of *autocorrelation value* versus *pixel intervals* for a fixed *PPD* is unique and different from those of other *PPD*. When a pixel interval is zero (when the two same images are stacked on each other without any offset) the autocorrelation value is 'one'. As a pixel interval increases and approaches the soil grain diameter, the autocorrelation value drops sharply toward 'zero'. After the pixel interval exceeds the soil grain diameter the autocorrelation becomes stable at around 'zero'. This method showed promising test results for uniform sized soil. However, it had the same problem in analyzing non-uniform sized soil as wavelet transform analysis did.

2.3.3 Significance of Volume Based Soil Grain Size Analysis by Image Processing

Most imaging methods for determining soil grain size distribution use only the surface area information of soil grains without evaluating the third dimension of soil solids. Since many natural soil grains are elliptical rather than spherical, the true soil grain size distribution based on volume can not be correctly estimated by using soil grain surface area information. Nevertheless, exclusion of the volume of soil grains in the methods was inevitable due to the difficulty of having 3-dimensional images of numerous soil grains.

Rao et al. (2001) developed the "University of Illinois Aggregate Image Analyzer" (UI-AIA) to analyze soil grains in three dimensions. Three cameras located in three orthogonal directions are used to stereoscopically delineate individual soil grains which are carried by a conveyor belt. As discussed previously, the downside of this method is that it is time consuming to prepare and image a statistically representative soil specimen. Fernlund et al. (2007) took a different approach. Instead of getting the actual volume of soil grains, they introduced a conversion factor to convert the surface area based soil grain size distribution by an image processing technique to a volume based one. The conversion factor was determined based on the minimum-bounding square around the minimum projected area of soil grains. Cunningham (1996) tried to convert surface based size to volume based size of soil grains with an assumption for grain shape. The conversion from surface area to volume based soil grain size distribution by either the conversion factor or assumption of soil grain shape, however, may not apply to situations other than those from which they were derived.

CHAPTER III

Sedimaging

3.1 Introduction

In the previous chapter it was indicated that grain size determination by deterministic analysis (pixel counting) on images of three dimensional soil assemblies containing non-uniform grains may be infeasible. That is not only because no image processing technique has been developed or found for digital separation of individual contacting soil grains, but also because of the highly irregular soil grain shapes, colors, and textures in a typical soil. Moreover, finer soil grains hide behind larger ones making the deterministic approach impractical for grain size evaluation from images of three dimensional soil assemblies. Size analysis of non-contacting soil grains is not even considered here because of the impracticality as explained in the previous chapter. On the other hand, statistical soil grain size was shown by Shin and Hryciw (2004) to produce reliable size information of three dimensional soil assemblies of uniform grains even if it is inapplicable to three dimensional soil assemblies of non-uniform grains.

Having said that, if a technique could be found to rapidly segregate soil grains by size prior to capturing sequential images, statistical soil grain size analysis could be

performed sequentially on images (or area in an image) containing reasonably uniform sized particles. The results could then be used to assemble the grain size distribution curve piece-wise. The solution to the rapid segregation is a long square-sided glass sedimentation column. Following soil sedimentation through the water-filled column, a camera is used to collect digital images of the segregated soil deposit in which the largest soil grains are deposited at the bottom of the column and soil grain size gradually decreases toward the top of the deposit. Since the soil grains at any elevation in the segregated soil deposit are fairly uniform in size, statistical soil grain size analysis can determine the soil grain size at every elevation. The segregation method combined with statistical soil grain size analysis is termed "*Sedimaging*".

Sedimaging uses the projected surface area of soil grains to determine their size. Nevertheless, Sedimaging is practically a volume based method for the following two reasons: 1. The size of soil grains at each elevation is uniform and thus, the size of the soil grains seen through the flat-sided glass sedimentation column at an elevation is presumably the same as that of soil grains hidden behind other grains at the same elevation. 2. The percent of the total soil specimen volume contained in a layer of the deposit is equal to the ratio of the layer thickness to the total height of the deposit. It should be noted that the second statement holds only if the void ratio is constant along the entire soil deposit. Otherwise, void ratio variation in the deposit should be evaluated for correct percent volume. The effect of void ratio variation in the soil deposit on the percent volume in a layer will be presented in Chapter IV.

This chapter presents the computer vision system, a detailed description of the soil sedimentation apparatus, and the Sedimaging test procedure.

3.2 Soil Sedimentation System

At the beginning of the study, a prototype of the soil sedimentation apparatus as shown in Figure 3.1 was constructed to demonstrate the concept and to perform pilot tests. The column was a 2 inch by 2 inch by 48 inch glass tube with 1/8 inch thick walls. Near the bottom of the column, a square porous stone rests on an internal pedestal contained in an enlarged base. The porous stone is used for water drainage and is separable from the column to easily clean the column. Silicon rubber is applied to the sides of the square porous. The silicon rubber ensures that soil grains do not to fall through the gap between the column and the porous stone. The silicon rubber also helps the porous stone to be removed from the column without scratching the glass column surface. The square tube transitions into a circular section below the porous stone. The circular section is clamped through a rubber O-ring seal to a circular base. A valve in the base permits water drainage from the system. A support tower was built to hold the glass column safely and maintain its verticality.

It was expected that two design features would ensure uniform and adequate exposure of soil for imaging. In the pilot tests, uneven introduction of soil specimen into the column initially produced irregular horizontal surfaces. To resolve this, a soil release box containing 16 ½ inch by ½ inch by 5 inch vertical chutes with hinged trap doors for instantaneous soil release was constructed as shown in Figure 3.2. The box is placed over the top of the glass column and the trap doors are opened to instantaneously release the soil grains. Secondly, a 14 inch tall and 1 inch wide prismatic separator was installed at the bottom of the column as shown in Figure 3.1. This separator channels the falling

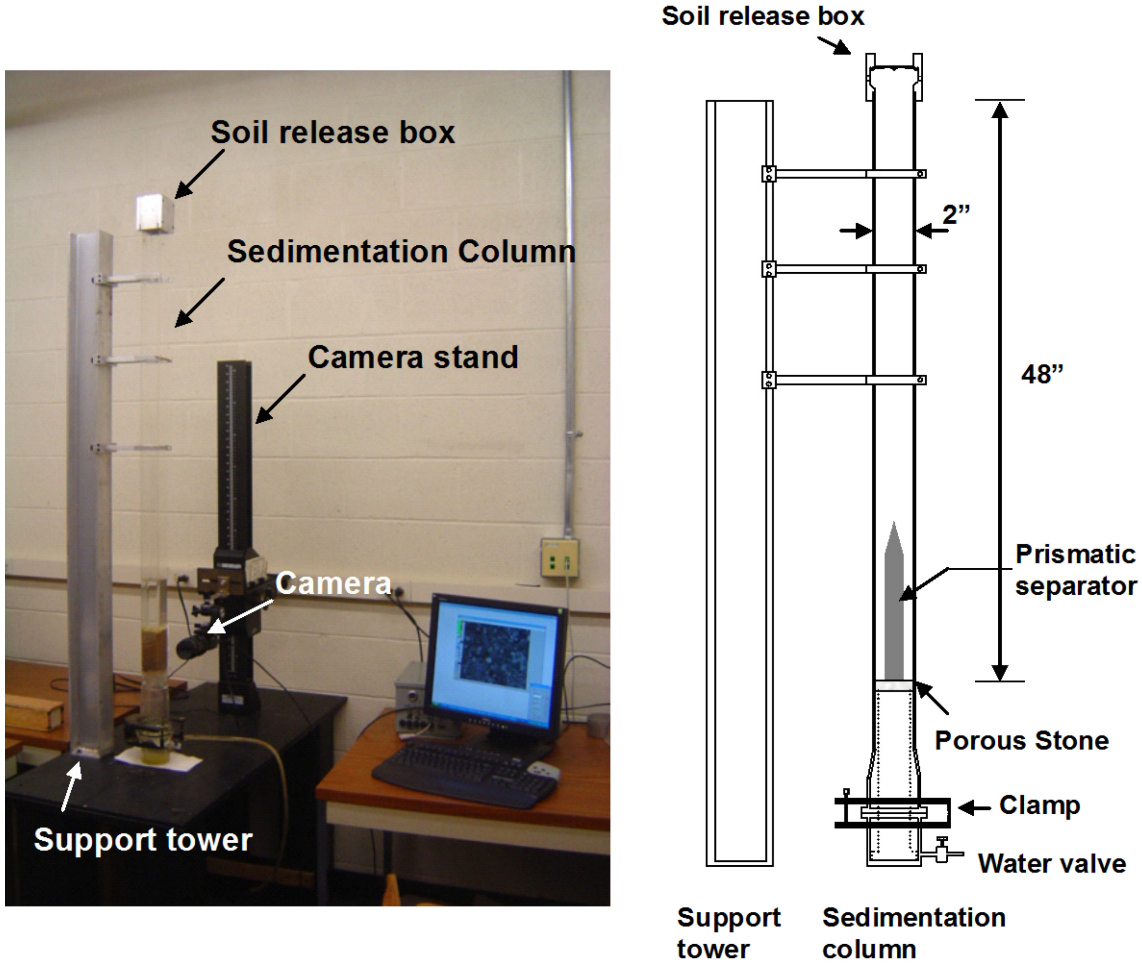

Figure 3.1 Preliminary soil sedimentation column with vision system.

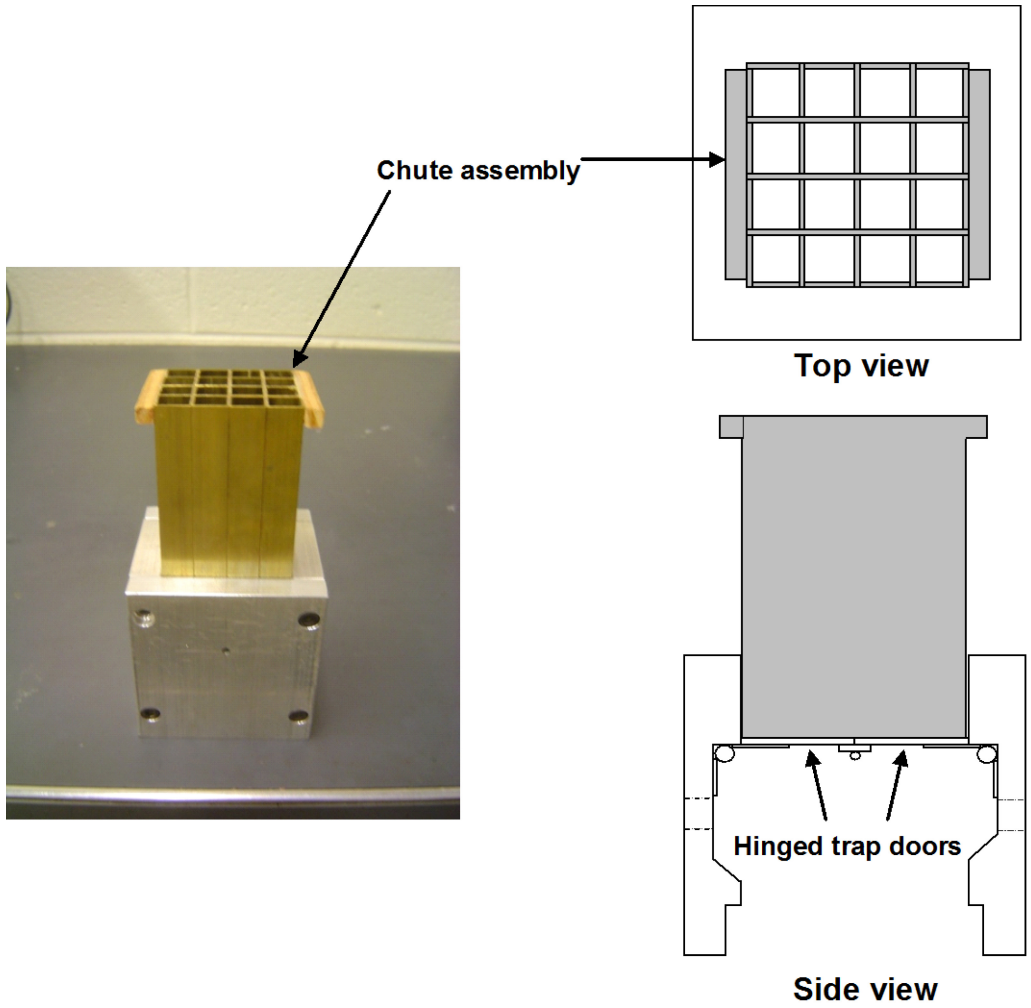

Figure 3.2 Soil release box.

grains into two opposite facing 2 inch by ½ inch column. The separator decreases the volume of soil needed for grain size analysis by 50 percent. Unfortunately, the length of the column was not long enough to facilitate segregation of soil grains by size during sedimentation through water.

To improve segregation, two changes were made to the prototype. First, a longer, 96 inch sedimentation column with the same cross sectional area was employed as shown in Figure 3.3. The falling mass of soil initially enters the water as a plug with a high concentration of solids. This creates a turbulent boiling condition by the water being displaced upward by the falling soil mass. The upward flow enhances particle segregation by fluidizing the finest particle most. As the largest particles escape from the plug the upward seepage diminishes slightly allowing the next grain size to overcome the upward seepage. The battle between upward seepage and gravitational deposition is "settled" one particle size at a time. In the end, the finest particles will have travelled up, down, and around over a distance many times the length of the column. This phenomenon eliminates the need for an excessively long column and greatly enhances the segregation of particles by size at the bottom of the column.

The second change made to the sedimentation system is that the prismatic separator was removed from the original design. It was shown that the separator disturbs the flow of the falling grains by increasing the falling distance of the soil grains because they bounce off the separator. The small change in the falling distance has an insignificant effect on segregation of small soil grains but has a significant effect on

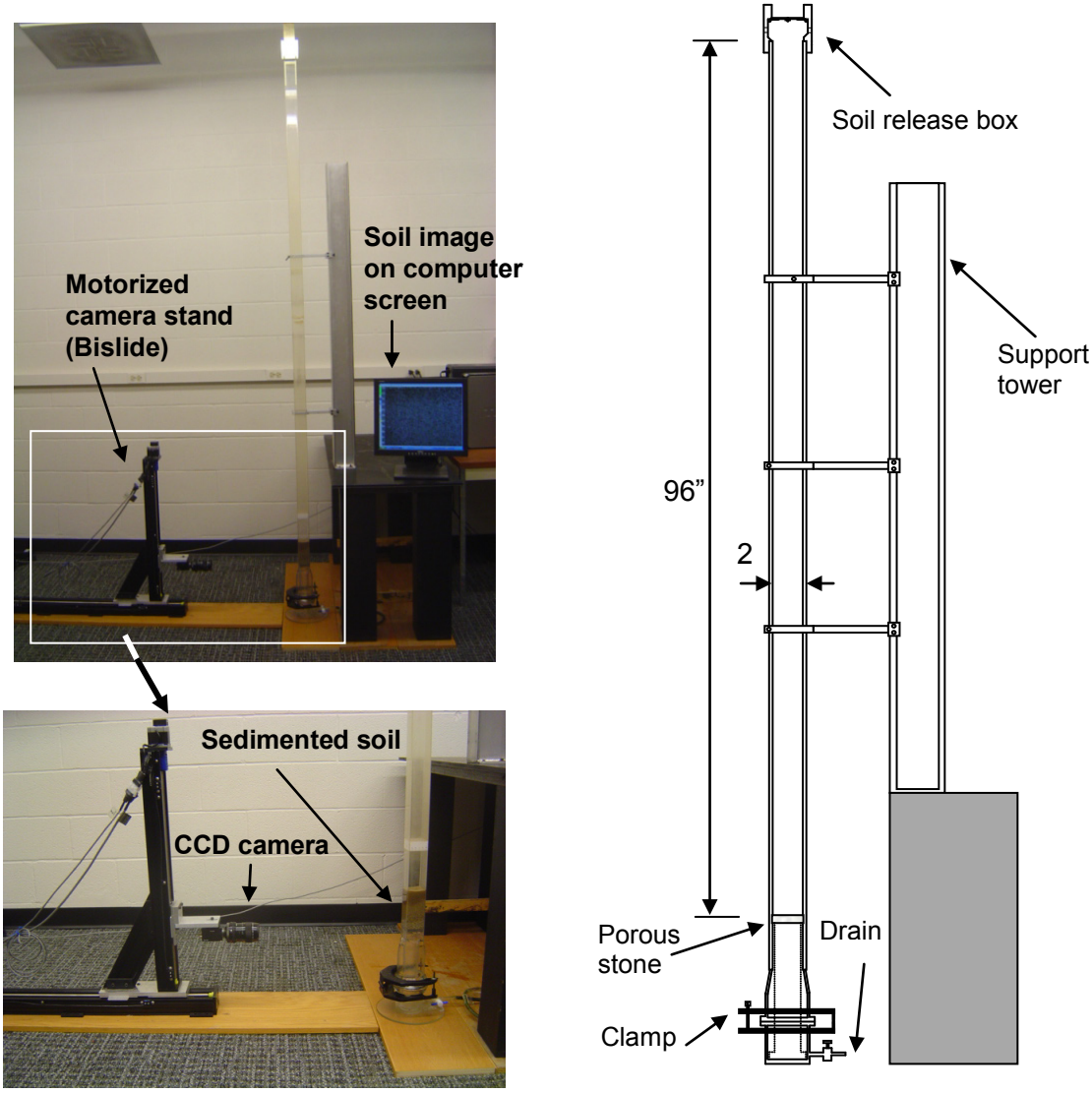

Figure 3.3 92 inch long soil sedimentation column with a motorized X-Z positioning camera stand.

larger grains. This is because the travel time difference between similar sizes of soil grains is fairly small and thus soil grain segregation can be greatly affected by any obstacle in the pathway of falling grains.

3.3 Computer Vision System

For capturing images of the soil sediment, a high quality industrial monochrome CCD camera (Pulnix model TM-7CN) with a ½ inch interline transfer imager is used. The CCD camera provides 480 pixel by 752 pixel resolution with 8 bits, 256 gray scale values from 0 to 255. The pixel aspect ratio is 1.18 to 1. Since the range of soil grain size is large, a macro lens (Canon FD 50mm/f 3.5) is used to achieve wide range of magnification levels with a maximum magnification level of about 60 pixels/mm. The camera produces standard RS-170 analog video signals. The analog video signals are digitized and then, the digitized video signals' frames are grabbed to obtain digital images for image processing using a high performance image digitizing board (PIXCI model SV5). Another camera, a commercial digital camera (Nikon D300) with a macro lens (AF-S Micro NIKKOR 60mm 1:2.8 G) was also used for calibrating the image soil grain size index versus *PPD*. The Nikon camera has a square pixel aspect ratio (1 to 1). For easy access to the digital camera and remote control from a personal computer, software NKRemote 1.2 by Breeze System was used.

The CCD camera does not have high enough pixel resolution to capture the entire sedimented column which is typically 110 mm tall. So, a camera stand, which allows the CCD camera to move vertically to capture images of the soil sediment incrementally with

height, is used as seen in Figure 3.1. This system is manually operated. Later, for remote positioning of the camera from a personal computer, an X-Z positioning system (Velmex, Inc model Bislide) shown in Figure 3.3 replaced the manually operated positioning system. The camera can move up and down, back and forth to collect soil sediment images at all elevations continuously. Finally, widely used commercial software (Adobe Photoshop) was used to stitch the soil images taken at different elevations to produce one single image of the entire sedimented soil column.

3.4 Sedimaging Test Procedure

The procedure for determination of the soil grain size distribution by Sedimaging is illustrated in Figure 3.4. The testing begins with filling the soil release box (Figure 3.2) with approximately the same amount of soil in each of the 16 ½" by ½" chutes. The soil is instantaneously released into the water-filled sedimentation column by opening two hinged trap doors at the bottom of the box. As previously discussed, the soil grains segregate by size en route to the bottom of the glass column. Starting from the bottom, the deposited soil is then scanned continuously by the CCD camera to produce a complete soil column image. Statistical soil grain size analysis (to be presented in Chapter V, VI, and VII) is applied to vertical 256 pixel increments in the image to compute various soil grain size indices. Next, the soil grain size indices are converted into *PPD* using a pre-established relationship between *PPD* and the soil grain size indices. The actual soil grain size (mm/diameter) in each increment is then determined by dividing *PPD* (pixel/diameter) by the camera magnification (pixel/mm). Finally, with the

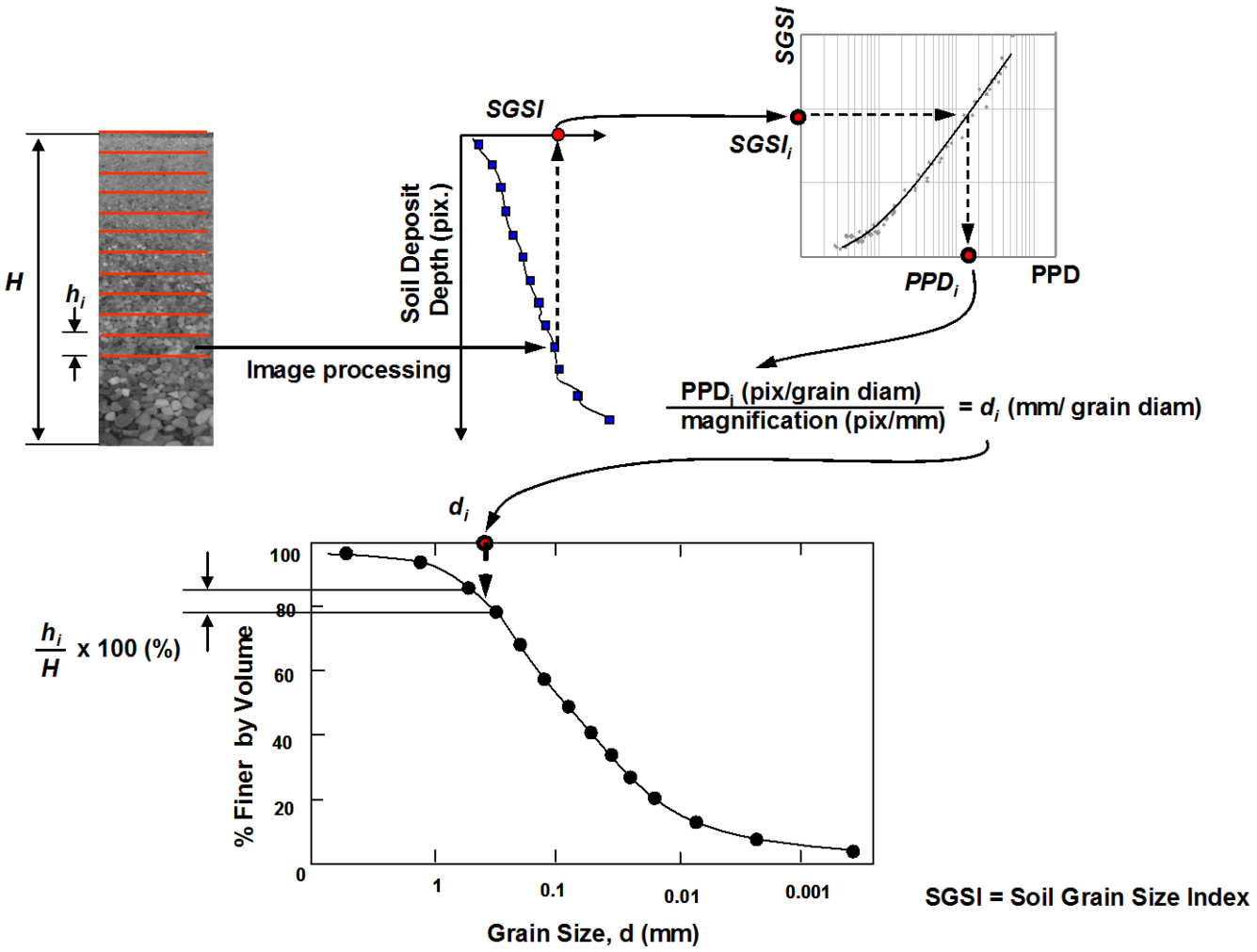

Figure 3.4 Sedimaging procedure.

known volume of soil solids in each 256 pixel increment of the soil column image, a complete soil grain size distribution curve is constructed.

CHAPTER IV

Void Ratio Variations in Soil Sediment

4.1 Introduction

The determination of soil grain size distribution by Sedimaging consists of three tasks:

1. Physical equipment must be developed to rapidly and thoroughly segregate a specimen's soil grains by size, obviously without sieving; (discussed in Chapter III)
2. An accounting has to be made for possible variations in soil void ratio in the sedimented soil column;
3. Appropriate soil image processing algorithms must be adopted for obtaining grain size from images of the segregated specimen.

The second task is addressed in this chapter.

Sedimaging pursues the determination of soil gain size distribution by volume of soil solids. Non-uniform void ratios (e) develop in the segregated soil column for two reasons. First, soil particles will obviously (and fortuitously for segregation) settle through water with different terminal velocities. According to Stokes' law, a 1 mm

particle will fall at 800 mm/s while a 0.1 mm grain will sediment at only 8 mm/sec in water. Accordingly, the velocities at impact will be significantly larger for soils arriving at the bottom of the column earlier than those arriving later. Thus, larger particles should exhibit lower void ratios in the segregated soil column.

Secondly, vertical effective stress increases with depth. While the vertical effective stresses, σ_v' are very small in a short 5 to 8 inch laboratory soil column, the changes from top to bottom are large on a percent basis. The soil column experiences self-weight consolidation with time after deposition due to the soil's relatively low density. It is important to note how the void ratio is distributed with depth due to the increasing effective stress with depth. It is also important to see if the void ratio distribution may change with time after deposition.

The significance of a variable void ratio distribution with depth is illustrated in Figure 4.1. Assuming a linearly increasing particle diameter, but a constant void ratio with depth as shown on the right side of Figure 4.1, will produce the correct linear grain size distribution shown by the dashed line in the center of the figure. By contrast, if the void ratio decreases as shown on the left, the actual grain diameters shown by the data points at each elevation will be slightly smaller than they would be in the case of a constant e. If the average void ratio ($\bar{e}$) in both cases is the same, the maximum difference between the grain size distributions would occur at the depth where $e = \bar{e}$.

Given that a decreasing e is more likely than a constant e, a quantitative assessment of this effect on the resulting grain size distribution curve must be made. If the effects are significant, corrections would have to be applied to the image based soil grain size distributions.

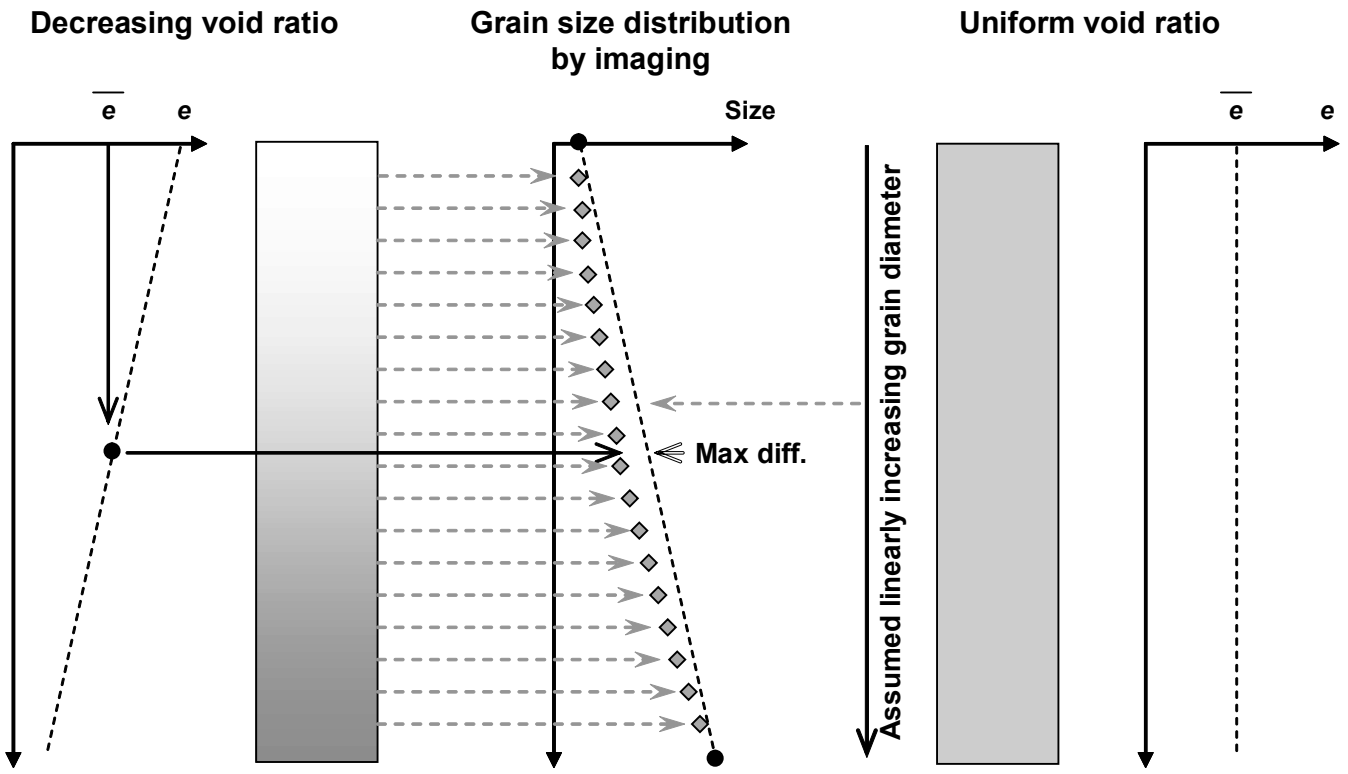

Figure 4.1 Effect of variable void ratio on perception of grain size distribution.

4.2 Effect of Effective Stress on Void Ratio of Soil Sediment

4.2.1 Relationship between Void Ratio and Effective Stress in Soil Sediment

Referring to Figure 4.2, with a known weight of soil solids (W_s) and the height of soil sediment (H), the average void ratio, $\bar{e}$, of the soil sediment column can be obtained by:

$$\bar{e} = \frac{HA\gamma_w G_s}{W_s} - 1 \tag{4.1}$$

where A is the cross sectional area of the column, γ_w is the unit weight of water and G_s is specific gravity of soil solids. With known average void ratio, the height of solids is:

$$H_s = \frac{H}{1+\bar{e}} \tag{4.2}$$

If 256 rows of pixels in an image correspond to an actual height increment of h_i as shown in Figure 4.2, the height of solids in the i^{th} increment is:

$$h_{si} = \frac{h_i}{1+e_i} \tag{4.3}$$

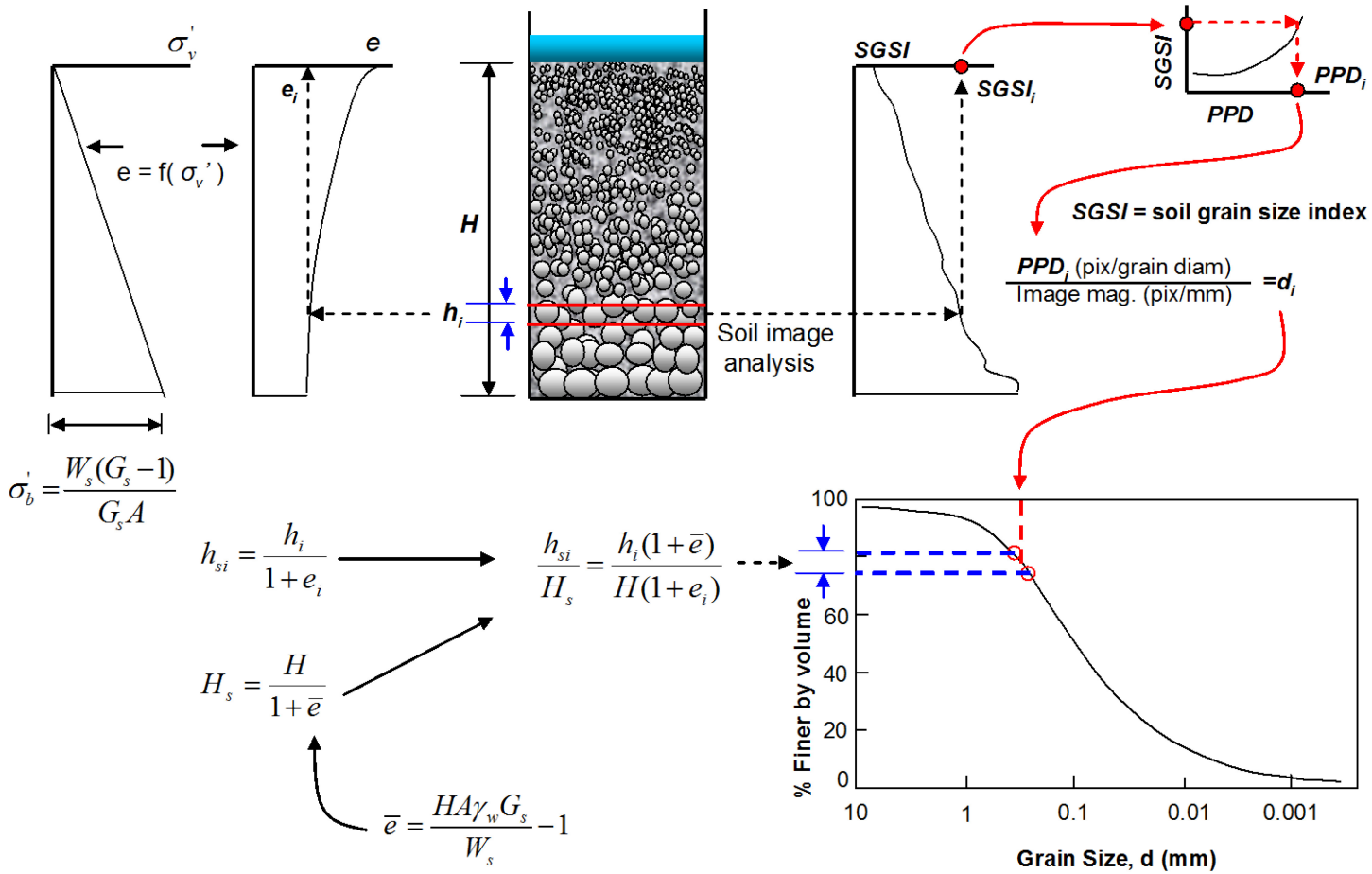

Figure 4.2 Consideration of void ratio variations to Sedimaging procedure.

where e_i is the i^{th} increment's void ratio. Dividing Equation 4.3 by Equation 4.2 yields an expression for the fraction of the total soil sample solids that are contained in the i^{th} increment:

$$\frac{h_{si}}{H_s} = \frac{h_i(1+\bar{e})}{H(1+e_i)} \tag{4.4}$$

As shown in Figure 4.2, Equation 4.4 provides the distance along the ordinate, incremented from the previous (i-1) ordinate at which the grain size d_i for i^{th} increment is plotted.

The data reduction procedure hinges on the knowledge of the void ratio distribution with depth. The development of void ratio calibration models would not be necessary, if e were constant with height. That is,

$$\frac{h_{si}}{H_s} = \frac{h_i}{H} \quad \text{when} \quad e_i = \bar{e} \tag{4.5}$$

Unfortunately, it is believed that this is unlikely to be the case. Actually, e will decrease with depth due to the increase in σ' under the weight of the finer overlying grains. Models for void ratio distribution in recently deposited sediments have generally been of the form:

$$e = a\sigma'^{-b} \tag{4.6}$$

where σ' is the vertical effective stress while a and b are empirical constants (Somogyi, 1979). Carrier et al. (1983) presented e - log σ' data for various dredged soils. The data reveals a ranging from 2.2 to 34.0 and b correspondingly ranging from 0.16 to 0.23 (for σ' expressed in psf). A best fit through many sets of data for dredged soils finds a = 7.0 and b = 0.18. However, these values are typical of fine-grained silts, clays and silt/clay mixtures and may not be applicable to coarser sediments. They may also be inappropriate for very near-surface deposits. Nevertheless, the form of the e - σ' relationship appears to be correct for any soil grain size and the corresponding effective stress profile would be as shown in Figure 4.2.

Since W_s is known, the effective stress at the base of the sediment column, σ_b' can be computed as follows:

$$\sigma_b' = \frac{W_s(G_s - 1)}{G_s A} \tag{4.7}$$

With σ_b' known, Equation 4.6 can be written in a normalized form:

$$e(\zeta) = A\zeta^{-B} \tag{4.8}$$

where $\zeta = \sigma' / \sigma_b'$, while A and B are new empirical constants. The average void ratio in the sedimentation column would then be as follows:

$$\overline{e} = \int_0^1 e(\zeta)d\zeta = \int_0^1 A\zeta^{-B}d\zeta = \frac{A}{1-B} \tag{4.9}$$

where

$$A = \bar{e}(1 - B) \tag{4.10}$$

Inserting Equation 4.10 into Equation 4.8 yields:

$$e = \bar{e}(1 - B)\zeta^{-B} \tag{4.11}$$

where the average void ratio, $\bar{e}$, is known from Equation 4.1. Thus, the relationship between e and σ', despite being non-linear requires only one empirical constant (B) to be experimentally determined. With B determined for a given soil sample, e_i values for Equation 4.4 can be computed and the grain size distribution can be determined.

4.2.2 Void Ratio Model Calibration

To calibrate the e versus σ' model, that is, to determine the constant B for Equation 4.11, void ratio distribution with depth in the sedimentation column was determined experimentally using "incremental deposition" as follows. Referring to Figure 4.3, equal weights of soil were deposited in stages A, B, C, D, etc. Each new lift will initially be under the same effective stress condition and therefore, initially have the same depositional height as the preceding lift originally had. Meanwhile, earlier lifts compress under the increasing overburden pressure. With each new soil placement, the overall height of the soil column is measured, providing heights, H_A, H_B, H_C, H_D, etc as

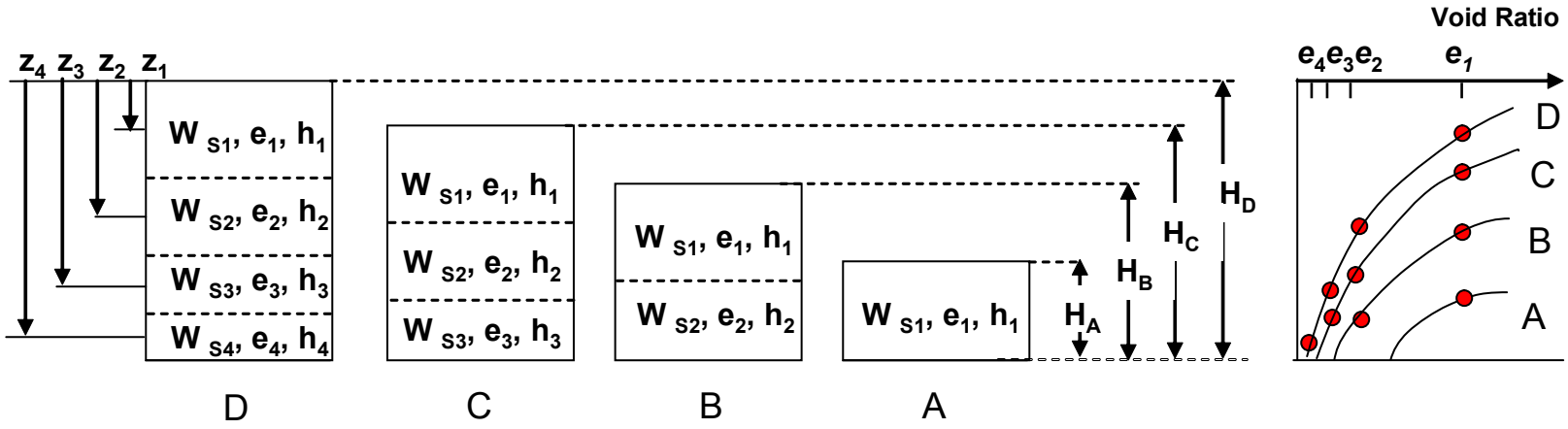

Figure 4.3 Staged deposition to determine effects of overburden on void ratio.

shown in Figure 4.3. It can be shown that the void ratios of the lifts beginning from the top will be:

$$e_1 = h_1 K - 1 = H_A K - 1 \tag{4.12a}$$

$$e_2 = h_2 K - 1 = (H_B - H_A) K - 1 \tag{4.12b}$$

$$e_3 = h_3 K - 1 = (H_C - H_B) K - 1 \tag{4.12c}$$

$$e_4 = h_4 K - 1 = (H_D - H_C) K - 1 \tag{4.12d}$$

where

$$K = \frac{A G_s \gamma_w}{W_s} \tag{4.13}$$

The corresponding depths to the mid-heights of the lifts are:

$$z_1 = 0.5(H_A) \tag{4.14a}$$

$$z_2 = 0.5(H_A + H_B) \tag{4.14b}$$

$$z_3 = 0.5(H_B + H_C) \tag{4.14c}$$

$$z_4 = 0.5(H_C + H_D) \tag{4.14d}$$

From the e_i values computed by Equations 4.12 and with known G_s, the corresponding effective stresses at depths z_1, z_2 etc. can be determined and the (σ_i', e_i) pairs can be used to best-fit Equation 4.11 for B.

4.2.3 Results

Two 500g sample of fairly uniformly sized soil which is from a glacial deposit in Ann Arbor, MI were used for the experiment. Each soil was retained between No. 70 and No. 80 and between No. 170 and No. 200, respectively. Ten 50g depositions from each soil were prepared. Water was filled up to 93 inches from the bottom of the sedimentation column and then, each 50 g of soil is introduced into the sedimentation column. Immediately after complete deposition of the first 50 g of soil, void ratio of the first incremental soil deposit was measured. Then, after the i^{th} incremental soil deposition, void ratio of i^{th} deposit and the void ratio change in the previous soil incremental deposits were measured.

For the evaluation of void ratio and the change in void ratio with effective stress, images of soil incremental deposits are taken before and after new addition of 50g of soil using the CCD camera fixed to the camera stand and the camera magnification level of 21 pixel/mm. Then, incremental deposit height is measured by counting the number of pixels in the incremental deposit height with one pixel representing 0.048 mm (one pixel divided by 21 pixel/mm). Also, the vertical movements of many individual soil grains are

traced by comparing the images taken before and after new soil incremental deposition to accurately deal with the small change in void ratio. The camera magnification level chosen for measuring the change in the incremental deposit height is considered good enough in that, in the soil sedimentation column, void ratio associated with 50 g of the soil (Gs = 2.71) due to the error in reading soil deposit height by one pixel (0.048 mm) changes by only 0.007.

The largest void ratio change in the first incremental soil deposit was expected due to the largest effective stress. However, the results of these tests were unanticipated. Using 500 g of uniform 70/80 and 170/200 sand with 10 lifts of 50 g each showed no perceptible compression of the underlying previously deposited sand. No motions of individual soil grains in vertical direction were observed by the CCD camera. Therefore, *B* in Equation 4.11 is set to 0, which leads back to Equation 4.5.

A supporting test to the result of the void ratio calibration model was performed. The tests were performed by preparing separate specimens being retained between No. 70 and 80 sieves and having dry weights of 50g, 100g, 200g, 300g and 400g. The heights of the sedimented soil columns were almost perfectly and linearly correlated to the respective dry weights as shown in Figure 4.4, which implies the influence of effective stress on void ratio distribution is insignificant in producing variations in void ratio with depth in the 2 in. x 2 in. glass column. It is believed that sidewall friction may be limiting the effective stress increase with depth. The friction is also providing some resistance to settlement of soil grains at the glass wall.

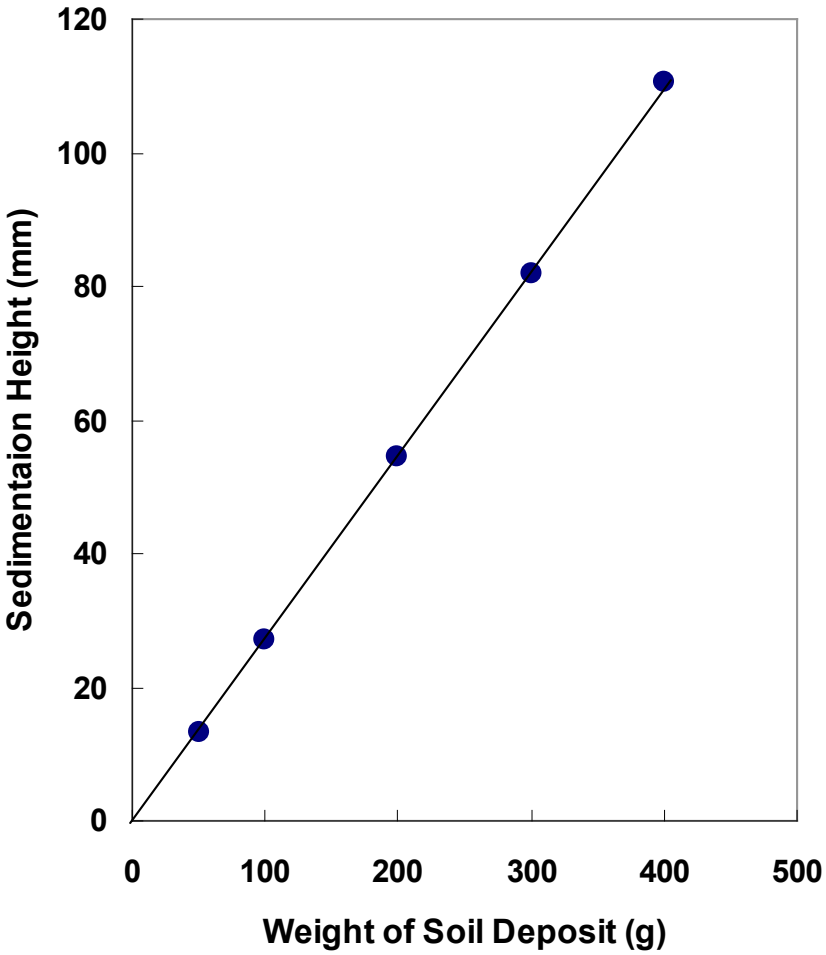

Figure 4.4 Sediment height vs. weight of solids.

4.3 Effect of Soil Grain Size on Void Ratio in the Sedimented Soil Column

According to Stoke' law, the terminal velocity of a solid spherical object falling through a liquid is proportional to the square of its diameter. In addition, as discussed in Section 3.2, finer grains are much more susceptible than larger grains to the upward seepage as water is displaced by falling soil grains. Therefore, effective settling velocity of the coarsest grains could be several orders of magnitude higher than that of the finest

grains. Thus, the impact of the coarsest grains when they hit the bottom of the sedimentation column is considerably larger than that of the finest grains which leads to the hypothesis that void ratios in the soil column will vary with grain size.

The effect of grain size on void ratio distribution was studied by sedimenting nine 400g soil specimens of different but uniform size ranging from 1.00 mm (No. 18 US Standard sieve) to 0.075 mm (No. 200 US Standard sieve). All of the specimens were collected by sieving glacial till found on the College of Engineering Campus of the University of Michigan in Ann Arbor, MI.

The actual original grain size distribution of the soil is irrelevant but its shape can be described as subrounded and its specific gravity is virtually constant at 2.71 for all size ranges.The size ranges of the nine specimens, their computed terminal velocities based on the central grain size in each increment, the sedimented specimen heights and the computed void ratios are provided in Table 4.1.

Table 4.1: Soil data for studying effect of grain size on sedimented void ratio.

US Sieve No.	Max. diam (mm)	Mid-size diam. (mm)	Min. diam. (mm)	Velocity (mm/s)	Soil mass (g)	Specific gravity	Height of deposit (mm)	Void ratio
18/20	1.000	0.925	0.850	672	400	2.71	109.0	0.878
20/30	0.850	0.725	0.600	413	400	2.71	109.0	0.878
30/40	0.600	0.513	0.425	206	400	2.71	108.0	0.861
40/50	0.425	0.363	0.300	103	400	2.71	109.0	0.878
50/60	0.300	0.275	0.250	59	400	2.71	111.0	0.912
70/80	0.212	0.196	0.180	30	400	2.71	110.5	0.904
80/100	0.180	0.165	0.150	21	400	2.71	112.0	0.903
100/140	0.150	0.128	0.106	13	400	2.72	114.0	0.964
170/200	0.090	0.083	0.075	5	400	2.71	116.5	1.007

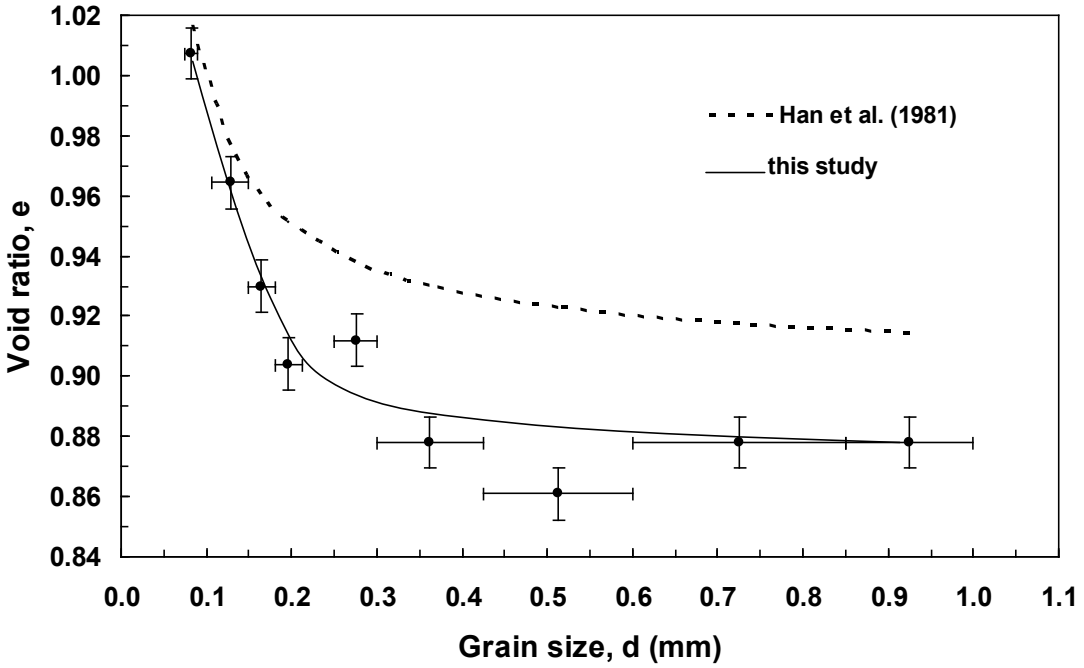

Figure 4.5 Observed depositional void ratios for various grain sizes.

In Figure 4.5, the observed void ratios are plotted vs. grain diameter. The vertical error bars correspond to the above described uncertainty in the measured height of specimen while the horizontal error bars represent the range between two sieve openings that were used to prepare the specimens. As expected, the finer particles exhibited a higher void ratio than coarser particles with the void ratio decreasing significantly as the size increased from 0.083 mm to about 0.35. Somewhat more surprising is that grains larger than about 0.35 mm settled at a common void ratio of about 0.88. This may be attributed at least partially to a smaller variation (as a percentage) in the depositional velocities in the coarser particle range. In the finer range (0.083 mm to 0.35 mm) the velocity changes by a factor of about 20. In the coarser range (0.35 mm to 1.0 mm) it changes only by a factor of about 7.

The sedimentology and hydrodynamics research communities have studied the relationships between sediment porosity, grain size and settling velocity (Wu and Wang, 2006). However, the reported data is generally for non-uniform soils yet uses only a single grain size parameter, d_{50}. Not surprisingly, these studies predict significantly lower void ratios than observed in this study. The only porosity data found for uniform sediment was by Han et al. (1981) as reported by Wu and Wang (2006). Their curve, shown Figure 4.5, agrees well with the data from the present study for fine sand but diverges by a void ratio difference of about 0.035 for coarser material. Any number of reasons could explain this small divergence including particle shape, roughness, mineralogy, uniformity, and the sedimentation apparatus.

4.4 Effect of Elapsed Time after Deposition on Void Ratio

Since there is a delay between the time when a soil specimen settles at the bottom of the sedimentation column and the time when digital images of the soil sediment are taken, the void ratio of the soil sediment as a function of time should be known for the determination of correct soil grain size distribution by Sedimaging. If the vertical strains, are not constant at all depths with time, void ratio variations will develop that should be taken into consideration in the analysis. Conversely, if the vertical strain at all elevations is zero or constant with time, then no consideration for varying void ratio is needed.

The change in void ratio with depth at various elapsed times after soil deposition was studied by depositing 521 g of fairly uniform soil, which was retained between the No. 70 and 80 sieves, into the sedimentation column. The water surface level in the

column was kept the same as in the experiments for the effect of effective stress and soil grain size. The initial height of the sediment was 142 mm at zero time. “Zero” time is designed as the moment at which all of the soil grains have come to rest in the sedimentation column. The vertical movements of a number of individual soil grains at various depths were traced and recorded with time as shown in Figure 4.6 using the CCD camera. Total 1.05 mm of vertical settlement at the top of the deposition occurred after 84 hours, which corresponds to a void ratio decrease of only 0.014. From Figure 4.6, it can be observed that the vertical settlement is nearly linear relationship with depth at all measurement times. This indicates that the vertical strain is nearly constant with depth and thus, so is the change in void ratio with depth.

It should be noted that no movement was even observed before at least 10 minutes of elapsed time. The complete set of soil images for soil grain size analysis can be easily acquired within this time frame.

Two additional tests, using soil grain sizes (retained between No. 40 and 50 sieves and between No. 80 and 100 sieves) conducted for shorter periods of time, produced similar results. Therefore, it was concluded that there is no significant effect of elapsed time on void ratio variations in the sedimented soil column, even though the void ratio itself changes slightly.

4.5 Evaluation of the Significance of Void Ratio Variations

Having found that the effect of effective stress on void ratio in the soil sediment is very minor and having established the relationship between void ratio and grain diameter

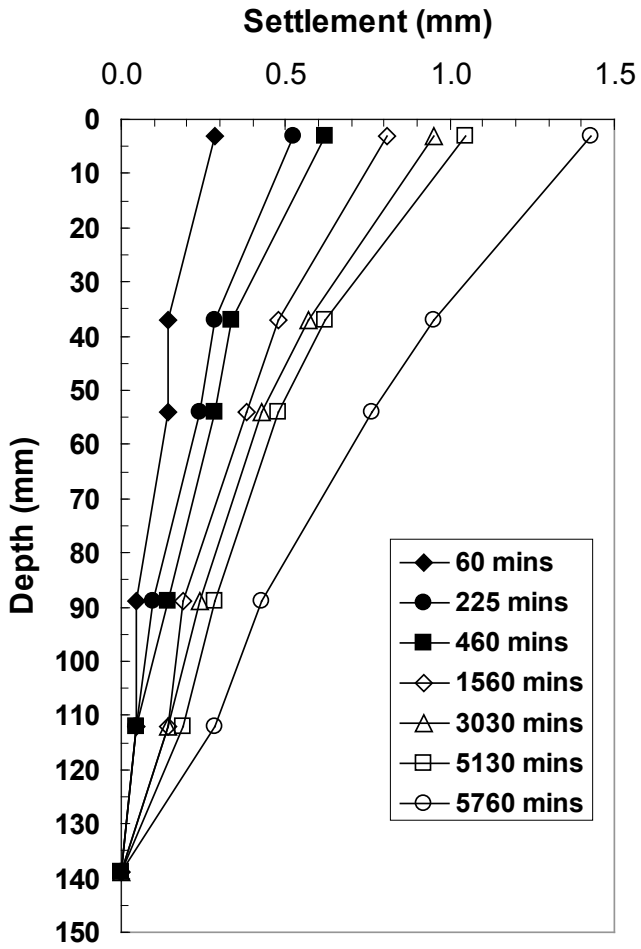

Figure 4.6 Vertical displacement of soil column at various elevations with time.

in sedimented soil as shown in Figure 4.5, a grain size distribution obtained by imaging could be corrected to account for the decreasing void ratio with increasing grain size. In order to gauge the magnitude and significance of this correction, a soil with a known grain size distribution was hypothetically "sedimented" through water. It was assumed that the soil would find itself at void ratios ranging linearly from 0.80 at the bottom to 1.05 from at the top of the column. In order to evaluate a worst case scenario, this assumed range is significantly larger than is actually observed in Figure 4.5.

The resulting grain size distribution curve is shown in Figure 4.7 where it is compared to the actual known grain size distribution. While the differences are discernable, they are very small and for practical consideration, can be considered negligible. Thus, in most cases, the variations in void ratio that would develop in the sedimented soil specimen due to the combined effects of increasing effective vertical stress and increasing grain size with depth can be ignored.

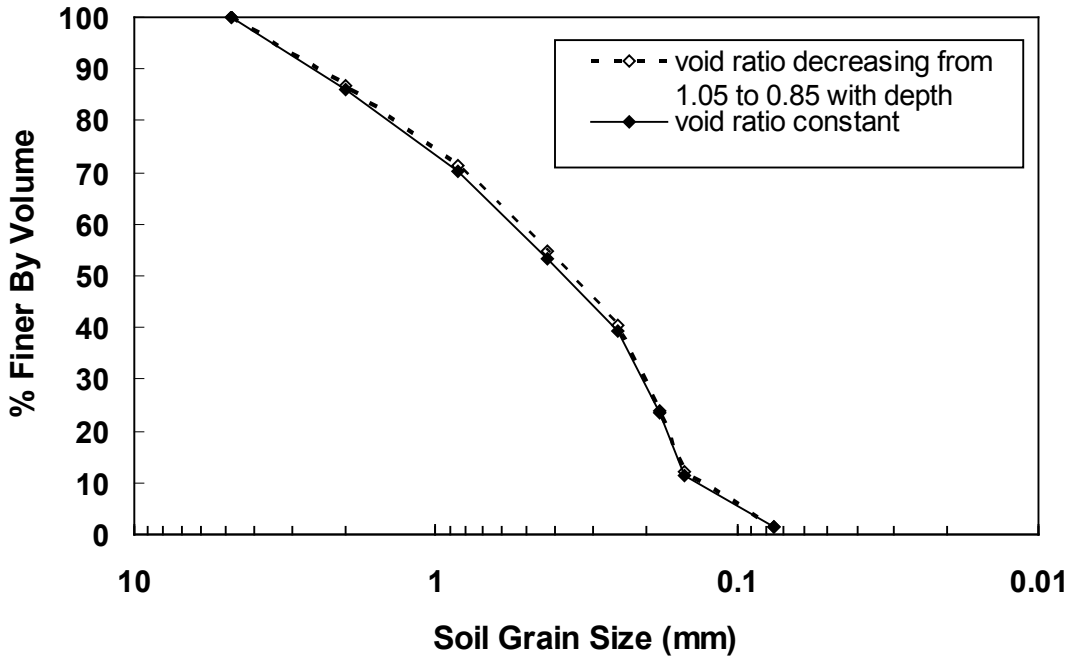

Figure 4.7 Grain size distributions compared for constant void ratio and void ratio decreasing with depth.

4.6 Conclusions

The grain size distribution of soil specimens can be obtained by image processing if the particles can be segregated by size such that each successive image contains only

relatively uniform particle sizes. A long sedimentation column achieves this segregation quickly and effectively. A possible problem arises due to a decreasing void ratio with depth in the column. The decrease was hypothesized to occur due to increasing overburden pressure with depth and the fact that larger grains settle at higher velocities and thus impact the already sedimented particles column with more energy and momentum. Laboratory tests showed that uniform soils do not exhibit significant variation with depth in a 2 in. x 2 in. (50.8 mm x 50.8 mm) sedimentation column. However, the void ratios were observed to decrease somewhat with increase in grain size. While corrections can easily be applied to the image-based grain size distributions to obtain better agreement with the actual grain size distribution, the corrections are small and can be neglected for practical purposes.

CHAPTER V

Soil Grain Size by Wavelet Analysis

5.1 Introduction

For images of three dimensional soil assemblies of uniform grains as shown in Figure 5.1, the frequency content of the gray scale pattern is the key to determination of the soil grain size. More concretely, the dominant frequency in such soil images is related to the size of the soil grains. This is because the soil grain boundaries are the most consistently repeating feature in the image pattern. By contrast, internal textures within a soil grain appear quite randomly. Qualitatively, it can be said that when the soil grain size is large, the dominant frequency in the image is relatively low and vice versa. However, such qualitative frequency information is not useful in determining soil grain size.

Mathematical transformations which process digital images to extract the dominant frequency information could statistically determine soil grain size quantitatively. Among a number of mathematical transformations, Fourier transformation is most often used in many disciplines to obtain the frequency information. Equation 5.1 shows the mathematical expression for the two dimensional Fast Fourier Transform (FFT).

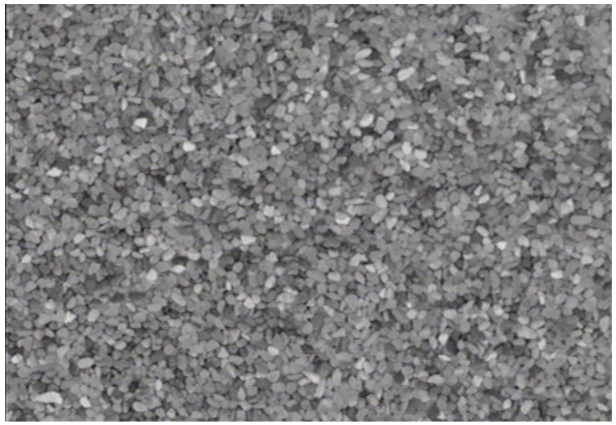

(a) magnification = 10 pixel/mm, *PPD* = 9.3

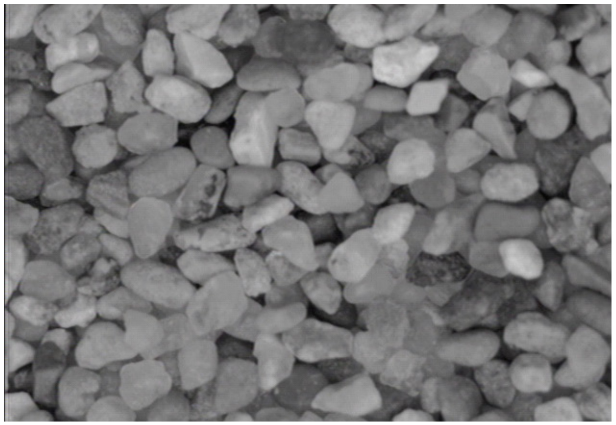

(b) magnification = 44.25 pixel/mm, *PPD* = 40.9

Figure 5.1 480 pixel by 752 pixel image of three dimensional soil assemblies of uniform grains retained between No. 18 and 20 sieves (average sieve opening = 0.925mm).

$$F(u,v) = \frac{1}{MN} \sum_{x=0}^{M} \sum_{y=0}^{N} f(x,y)\, e^{-i2\pi\left(\frac{ux}{M}+\frac{vy}{N}\right)} \tag{5.1}$$

where $f(x,y)$ is the image gray scale matrix, $u = 0, 1, 2, \ldots, M-1$, $v = 0, 1, 2, \ldots, N-1$, and M and N are the number of pixels in the horizontal and vertical directions. The FFT provides a frequency spectrum, $F(u,v)$ that indicates dominant frequencies in the image by their respective amplitudes in the spectrum.

In images of three dimensional soil assemblies of uniform grains, soil grain boundaries are the only features that exhibit a consistent pattern throughout the image. Therefore, the soil grain boundaries produce the dominant frequency in the spectrum. Theoretically, this dominant frequency should be the lowest frequency in the spectrum since there are no other larger and more distinct features in the soil image. However, this is unfortunately not the case because the FFT is also very sensitive to low frequencies caused by uneven illumination and gray scale distributions over regions of the image. The amplitudes of such low frequencies in the Fourier frequency spectrum could be very large and could obscure the frequency response of the soil grain boundaries. Consequently, extraction of the range of frequency components corresponding to the soil grain boundaries from the frequency spectrum is practically unachievable.

In the real world, many time varying signals have high frequency components for short durations and low frequency components over long durations. The same thing happens in images of three dimensional soil assemblies of uniform grains. Internal textures within the soil grains have relatively high frequency components over small areas while the soil grain boundaries have relatively low frequency components over the

entire image area. The internal texture is the most undesirable feature in the soil grain images for purposes of size analysis. They yield false grain size information by generating internal boundaries within a soil grain that has similar characteristics to real soil grain boundaries. As a result, the actual soil grain size will be underestimated.

There is an effective method called Multi Resolution Analysis (MRA) for analyzing images which have high and low frequencies for short and long durations, respectively. Unlike the FFT that resolves all frequencies in the frequency spectrum with similar resolution, MRA analyzes images at different frequencies with different resolutions. Specifically, the MRA gives poor resolution at high frequencies and good resolution at low frequencies. In other words, lower frequency components are better resolved than higher frequency components, which implies that lower frequency components are detected with better accuracy. This feature is particularly well suited to soil grain size analysis since soil grains have the lowest frequency components in an image of uniform soil grain size while undesirable noise and textures have the highest frequency components. A mathematical transformation that follows the MRA approach is discrete wavelet transformation.

In this chapter, a statistical soil grain size analysis utilizing discrete wavelet transformation is presented. Initially, Shin and Hryciw (2004) developed a wavelet soil grain size index for dry soil. For the purpose of using this soil grain size index for Sedimaging, the effect of water on the index is studied and a new wavelet soil grain size calibration chart for saturated soil is presented. Also, the effect of pixel aspect ratio on the index is studied.

5.2 Continuous Wavelet Transforms

Wavelet transformation is defined as the representation (decomposition) of a signal or image by basis functions. Before the Discrete Wavelet Transform (DWT) is introduced, the Continuous Wavelet Transforms (CWT) is presented and its meaning is discussed to provide a better understanding of the wavelet transformation concept.

The one dimensional CWT of a signal, *f(x)*, is mathematically defined as:

$$W_f(s,t) = \int_{-\infty}^{\infty} f(x)\psi_{s,t}(x)dx \tag{5.2}$$

where $W_f(s,t)$ is the CWT coefficient of $f(x)$ while $\psi_{s,t}(x)$ is the basis function, referred to as a *wavelet*, which is generated by scaling a mother wavelet, $\psi(x)$, by s and translating it by t. As shown by Equation 5.2, the transformed signal (CWT coefficient) is obtained by taking the inner product of $f(x)$ with the wavelet. Just as with Fourier transforms amplitude (coefficient), the CWT coefficient is a value that indicates the degree of similarity of a signal to the chosen wavelet. If a signal is similar to the wavelet, the CWT coefficient is higher than that of a signal which is not similar to the wavelet. Unlike Fourier transformation basis functions that have infinite-length and consist of sines and cosines, wavelet transformation basis functions (wavelets), $\psi_{s,t}(x)$, are finite in length and are generated by scaling and shifting a mother wavelet, $\psi(x)$, which is a real number function obeying the zero mean condition:

$$\int_{-\infty}^{\infty} \psi(x)dx = 0 \tag{5.3}$$

and the admissibility condition:

$$\int_{-\infty}^{\infty} \frac{|\Psi(\omega)|}{|\omega|} d\omega < \infty \tag{5.4}$$

where $\Psi(\omega)$ is the Fourier transforms of $\psi(x)$. From the two conditions, a mother wavelet forms a function that has a finite-length and a fast-decaying oscillating waveform. The basis function of the wavelet transformation is defined as:

$$\psi_{s,t}(x) = \frac{1}{\sqrt{s}} \psi\left(\frac{x-t}{s}\right) \tag{5.5}$$

where $s > 0$ and t is a real number. t, is a translational factor that allows a mother wavelet to move onto a specific location in a signal. As seen in Equation 5.5, the basis functions do not include a frequency parameter. Instead, there is a scaling factor, s. The scaling factor in wavelet transformation is related to the frequency of the wavelet by:

$$s = \frac{1}{f} \tag{5.6}$$

where f is frequency. Since the scaling factor is the inverse of frequency it serves as a parameter which changes the wavelegnth of wavelets. The implication of a scaling factor in a mother wavelet is that wavelet transformation has the ability to analyze a signal's

different frequencies at different resolutions. This is one of the most important advantages of wavelet transformation over Fourier transformation in terms of the determination of soil grain size of relatively uniform sized particles.

It should be noted that the basis functions of wavelet transformation are localized not only in the frequency domain but also in the spatial domain, which means that the spatial information (location) of a frequency component is known, while those of Fourier transforms are sinusoidal and therefore, are located only in the frequency domain. Having said this, the spatial information is not of particular interest in this research since only the soil grain size of a uniformly sized soil mass is being pursued.

5.3 Discrete Wavelet Transforms

The basis functions (wavelets) of CWT are generated by continuously scaling and translating a mother wavelet and thus, there can be an infinite number of basis functions. This leads to a huge amount of redundant wavelet transformation coefficients and requires substantial computation. On the other hand, the basis functions of Discrete Wavelet Transformation (DWT) for analyzing digital signals are generated in a dyadic grid. In other words, the basis functions are generated by binary scaling and dyadic translation of a mother wavelet as shown in Figure 5.2. “Binary scaling” means scaling of a signal by a factor of 2 and “dyadic translation” is the shifting of a signal by the signal’s scale, that is, its width. By using the DWT, the number of basis functions and wavelet transformation coefficients is significantly reduced. This also removes the redundancy of the CWT. In Figure 5.2, it should be noted that the frequency resolution gets poorer and

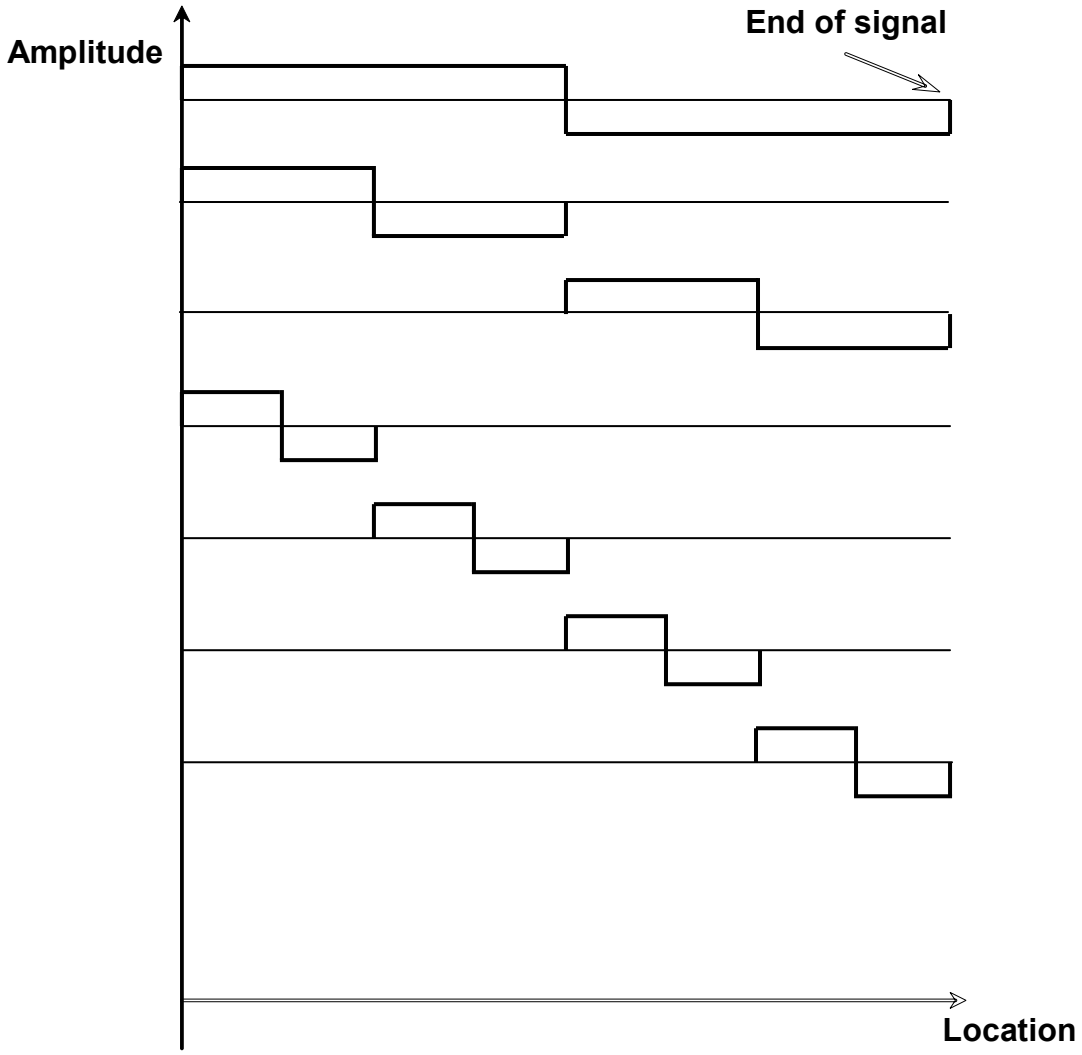

Figure 5.2 Binary scaling and dyadic translating of a mother wavelet.

the spatial resolution gets better as frequency increases and that the coverage of each basis function (the product of space and frequency resolution) in the frequency-space plane is constant. This implies that DWT obeys Heisenberg's uncertainty principle (Heisenberg, 1927). The Heisenberg's uncertainty principle says that it is impossible to have a function that is perfectly located in both the frequency and spatial domains at the same time.

The DWT is essentially same as the CWT. They are only different in how they are implemented. DWT with dyadic grid sampling is considered as half band sub-band coding, which is designed to decompose a signal into a narrow frequency band, using a filter bank which consists of a half band low-pass filter and high-pass filter. The low-pass filter is a filter that retains lower frequencies than a cut-off frequency and attenuates higher frequencies. The cut-off frequency used in the half band low-pass filter is half the highest frequency that exists in a signal. A high-pass filter does exactly the opposite. Half band low-pass filters and high-pass filters are the *scaling functions* and *wavelets*, respectively.

At the first level of the DWT decomposition, an original signal is filtered with both a half band low-pass filter and high-pass filter. Filtering is the same as mathematical convolution and is expressed as:

$$x(n) * h(n) = \sum_k x(n)h(n-k) \tag{5.7}$$

$$x(n) * g(n) = \sum_k x(n)g(n-k) \tag{5.8}$$

where $x(n)$ is a signal and $h(n)$ and $g(n)$ are half band low-pass filter and high-pass filter, respectively. In Equation 5.7 and 5.8, the symbol, *, represents mathematical convolution. The filtering produces two signals with halved bandwidths, the lower half band signal and the upper half band signal. After filtering, half of pixels (samples) in the two signals are redundant. So, half of pixels from both the lower half band signal and the upper half band signal are down-sampled by a factor of 2, which can be performed by simply eliminating every other sample. The lower half band signal is called an *approximation*

signal or average signal and the upper half band signal as the *wavelet transformation coefficient* of the first decomposition level. Filtering followed by down-sampling by a factor of 2 is expressed as:

$$y_h(n) = \sum_k x(2n-k)h(k) \tag{5.9}$$

$$y_g(n) = \sum_k x(2n-k)g(k) \tag{5.10}$$

This completes the first level of DWT decomposition. It should be noted that after the first level of decomposition the frequency resolution is doubled and the number of pixels is halved. For the second level of decomposition, the approximation signal generated in the first decomposition level is once again subjected to half band sub-band coding. The approximation signal is filtered with the same half band low-pass filter and high-pass filter and down-sampled by a factor of 2. The second half band sub-band coding generates an approximation signal and wavelet transformation coefficient of the second level decomposition whose size is a quarter of the original signal. Half band sub-band coding continues with decomposing approximation signals at each decomposition level while retaining wavelet transformation coefficients until only one pixel remains in an approximation signal. The complete half band sub-band coding of a signal can be expressed as:

$$X_j(n) = \sum_k x_{j-1}(2^{j-1}n-k)h(k) \tag{5.11}$$

$$Coeff_j(n) = \sum_k x_{j-1}(2^{j-1}n-k)g(k) \tag{5.12}$$

where X_j and $Coeff_j$ are approximation signals and wavelet transformation coefficient at the j-th DWT decomposition level. The maximum possible number of decomposition levels depends on the number of pixels in a signal. In binary scaling, up to j levels of DWT decomposition can be performed when the number of pixels in a signal is 2^j. Figure 5.3 illustrates complete half band sub-band coding.

It is instructive to see what serves as the mother wavelet and the basis functions (wavelets) in DWT with half band sub-band coding. The half band high-pass filter is the mother wavelet. Convolution and half band low-pass filtering with downscaling, which are considered as translating and scaling the mother wavelet, respectively, generate the basis functions. Strictly speaking, half band low-pass filtering with downscaling does not actually scale the mother wavelet. Instead, it offers the effect of scaling the mother wavelet by filtering and downscaling an original signal or approximation signal. This is an efficient move in terms of computation time rather than actually generating large scale basis functions.

5.3.1 One Dimensional Haar Wavelet Transforms

DWT basis functions can be of any form as long as they satisfy Equations 5.3 and 5.4. In this study, the Haar basis functions (Haar, 1910) are used. The Haar half band low-pass and high-pass filters are shown in Figure 5.4. Unlike other basis functions that attenuate smoothly, Haar basis functions have discontinuities. Generally speaking, discontinuities in basis functions may not be a desired feature in other signal or image processing applications. However, for soil images where gray scale pixel values change sharply at soil grain boundaries while being relatively constant within a grain, the Haar

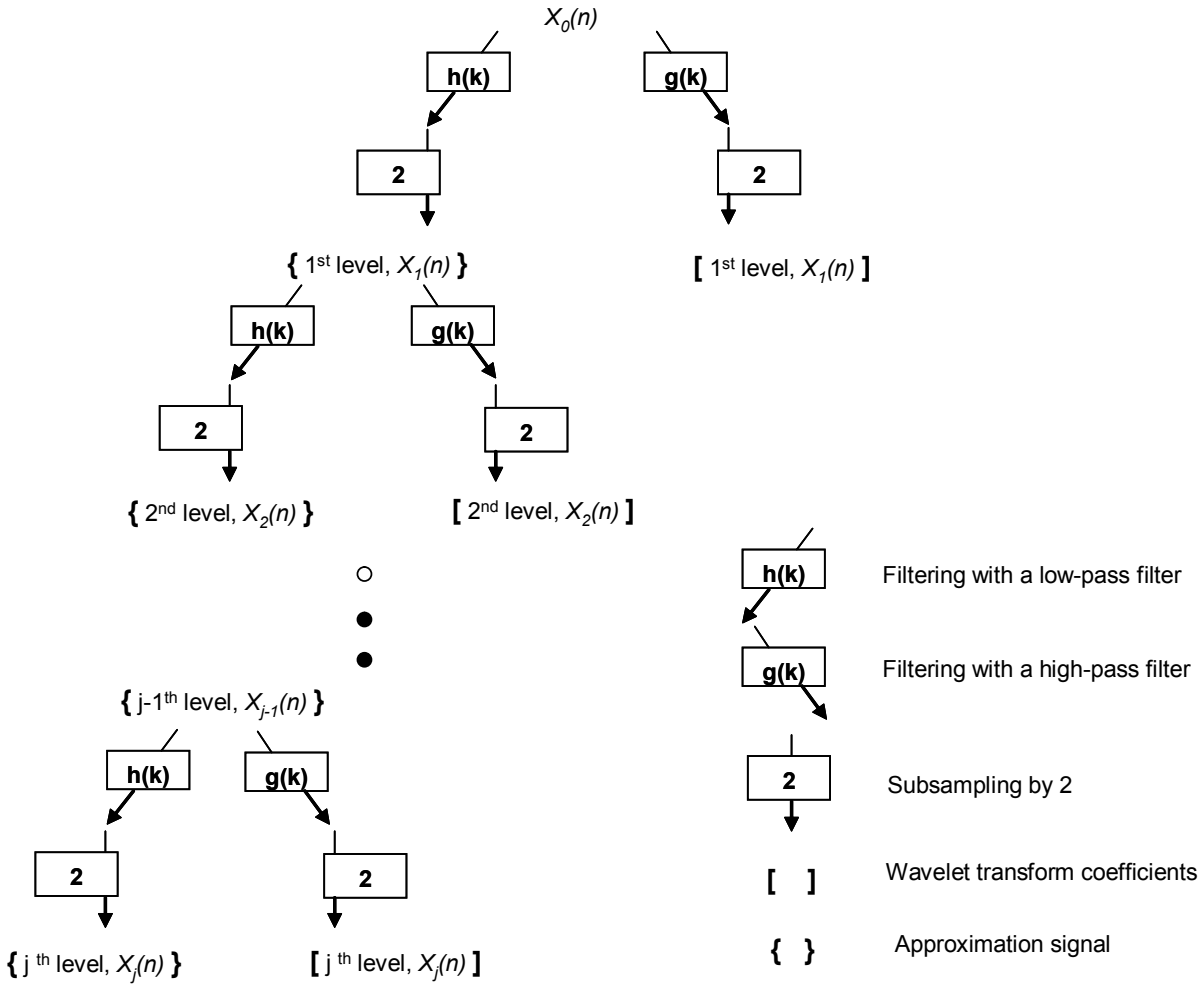

Figure 5.3 The scheme of half band subband coding for one dimensional signal using Haar wavelets.

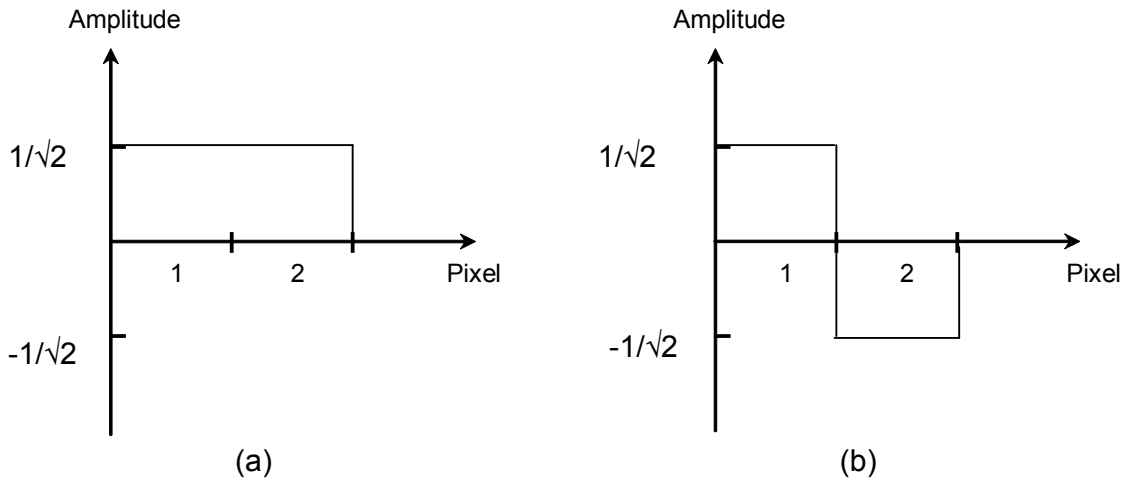

Figure 5.4 Haar basis functions: a) Haar half band low-pass filter and b) Haar half band high pass-filter.

basis function is an excellent choice since its discontinuities resonate with the soil grain boundaries.

To illustrate the computation of one dimensional Haar wavelet transformation through sub-band coding, Figure 5.5 is provided. The signal (one dimensional image) used in Figure 5.5 has a total of 8 (= 2^3) pixels. So, up to three levels of wavelet decomposition can be performed. First, the original signal is filtered (convolved) with the low-pass, $h(k)$, and high-pass filter, $g(k)$. It generates the two signals, the upper and lower half band signals. Since the two filtered signal now have only half the original signal's frequency information while they have same number of pixels as the original signal, half the pixels are redundant. To remove the redundancy, the upper and lower half band signals are "sub-sampled by 2" by eliminating every other pixel. Such sub-sampling does not result in any loss of information. After sub-sampling, one approximation signal and one set of four wavelet transformation coefficients of the 1^{st} decomposition level are obtained. The ultimate result of the DWT is shown in the bottom of Figure 5.5. Haar

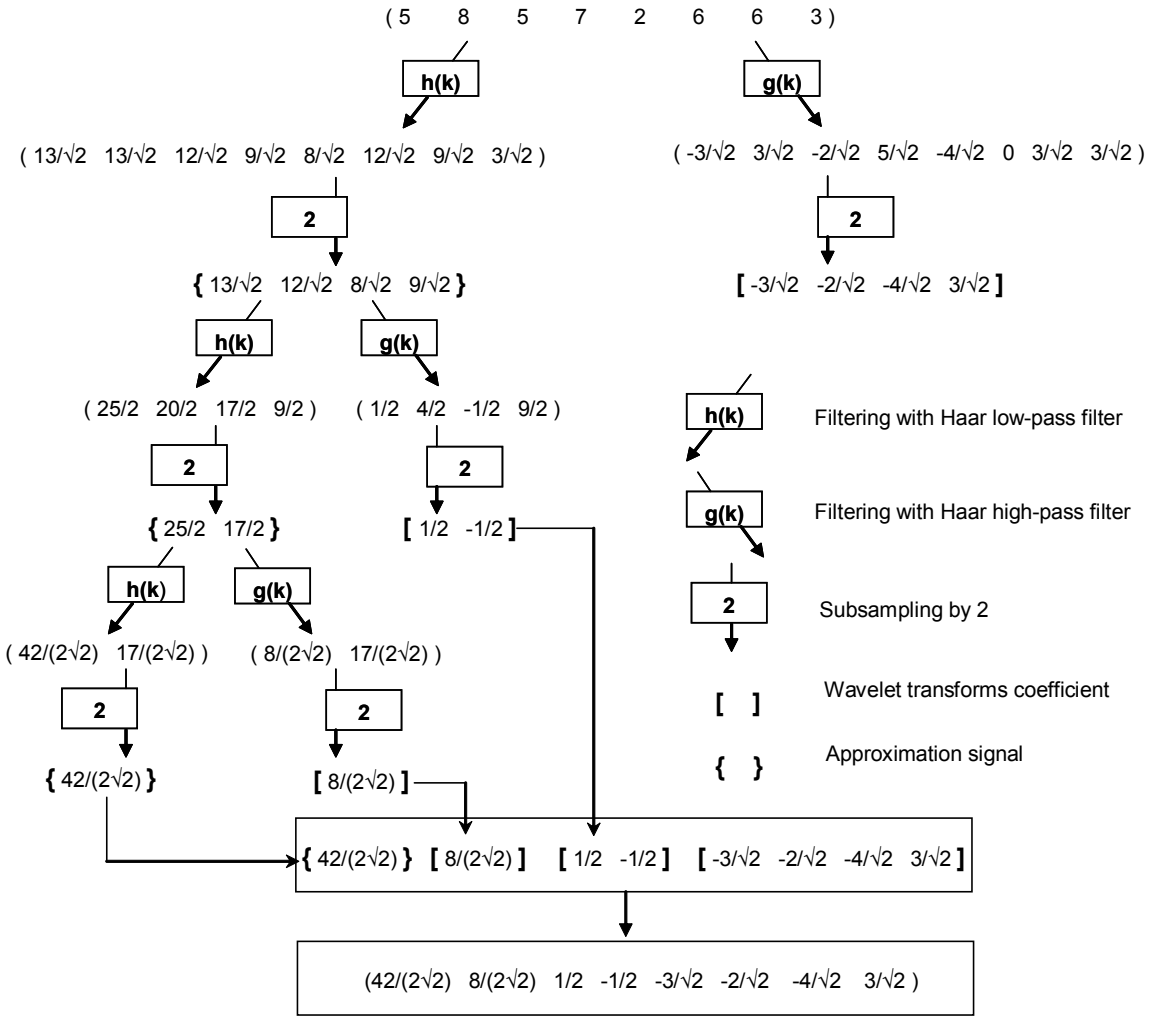

Figure 5.5 One dimensional Haar wavelet transforms.

wavelet transformation can be simplified by eliminating sub-sampling steps and filtering every two samples as shown in Figure 5.6.

5.3.2 Two Dimensional Haar Wavelet Transforms

The one dimensional Haar wavelet transformation algorithm can be easily extended to two dimensions in which the basis functions are applied to each row and column of pixels separately. After the first level of decomposition of an N by N image, one N/2 by N/2 approximation signal (c_{approx}) and three N/2 by N/2 wavelet transformation coefficients in three directions, horizontal (*cH*), vertical (*cV*), and diagonal(*cD*) are generated. Then, after the second level, the size of the approximation signal and three wavelet transforms reduces to N/4 by N/4. Figure 5.7 shows how the size of c_{approx}, *cH*, *cV*, and *cD* changes with each decomposition level as an image is decomposed by DWT. Figure 5.8 illustrates the scheme for two dimensional Haar wavelet transformation using the simplified method without showing the sub-sampling step. Using a 4 pixel by 4 pixel image, an example implementation of the two dimensional Haar wavelet transformation is shown in Figure 5.9.

5.4 Energy in Wavelet Decomposition Levels and Wavelet Soil Grain size index

In Haar wavelet transformation, the values of *cH1*, *cV1*, and *cD1*, which are the responses of basis functions to an original image (or c_{approx}), represent the gray scale

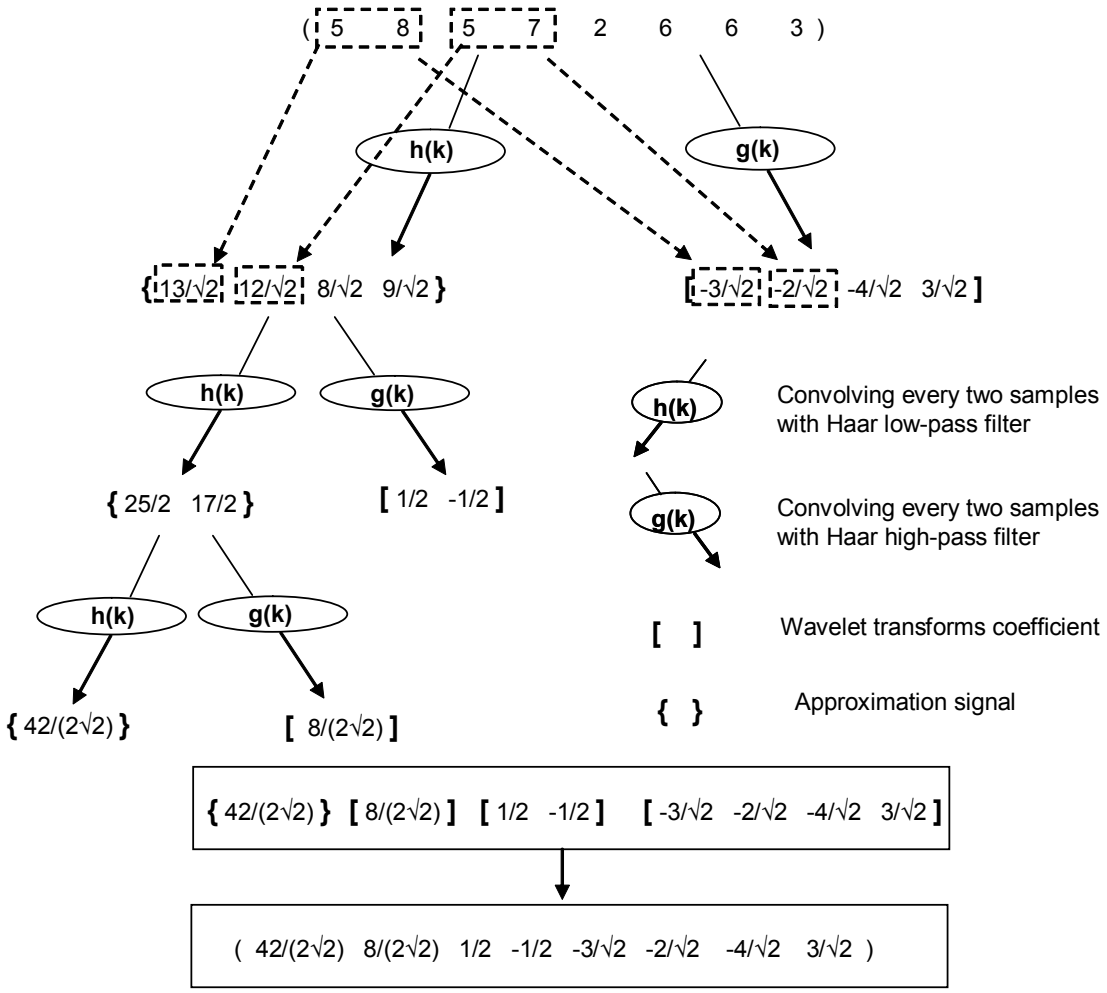

Figure 5.6 Simplified one dimensional Haar wavelet transforms.

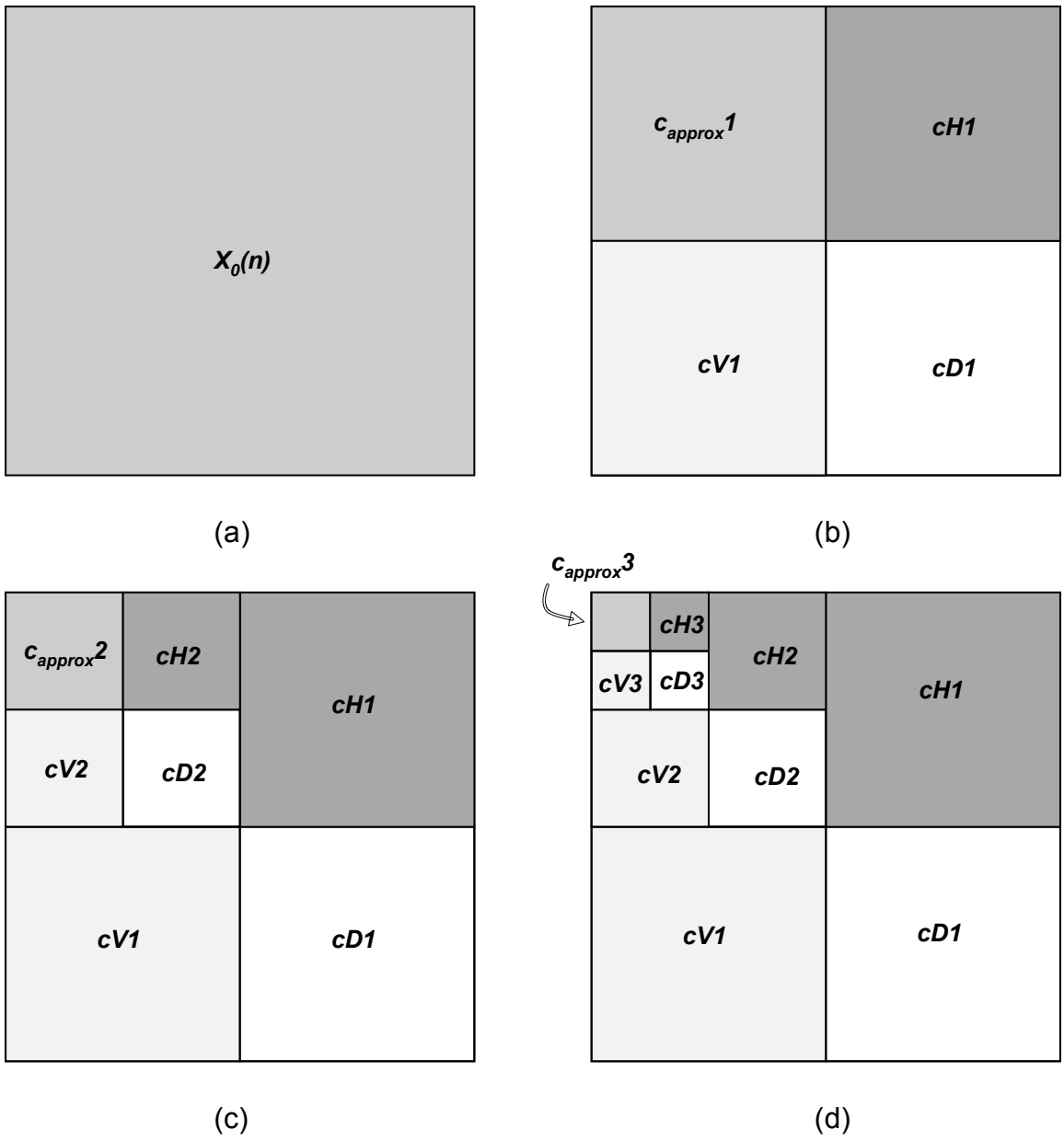

Figure 5.7 Approximation signal and three wavelet transforms coefficients (*cH*, *cV*, and *cD*) of two dimensional wavelet transforms. a) original image, b) first wavelet decomposition, c) second wavelet decomposition, d) third wavelet decomposition.

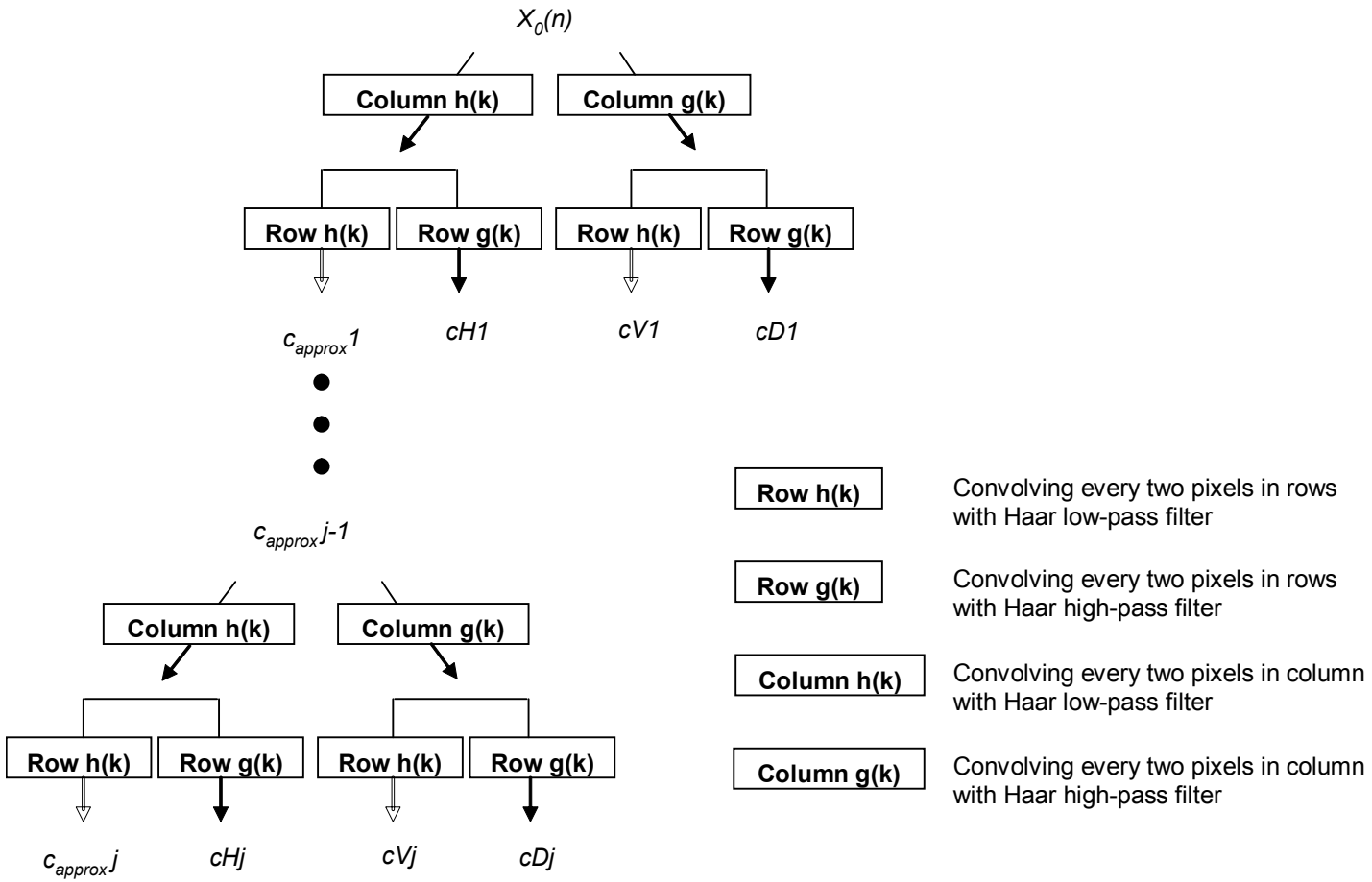

Figure 5.8 The scheme of half band subband coding for two dimensional Haar wavelet transforms.

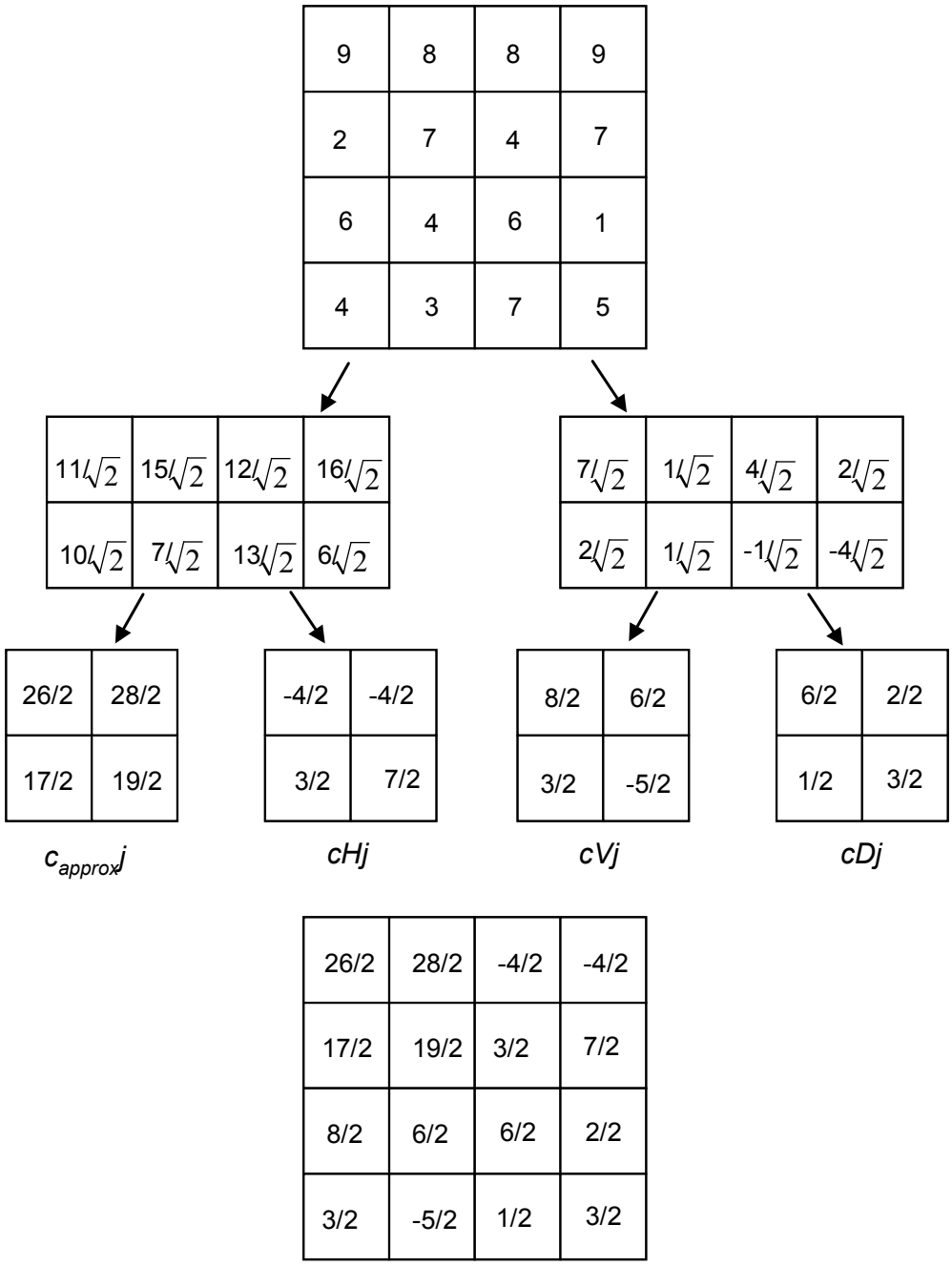

Figure 5.9 Two dimensional Haar wavelet transforms using a 4 pixel by 4 pixel image.

differences between two adjacent pixels of an original image in the horizontal, vertical, and diagonal directions respectively. Similarly, the values of *cH2*, *cV2*, and *cD2* are gray scale differences between two adjacent pixels of $c_{approx}1$ in the three directions. The magnitudes of the responses depend on the location of two adjacent pixels in the image (or c_{approx}). If the two adjacent pixels are located within a soil grain, the response will be low or close to zero since gray scale pixel values are relatively constant within a grain. The opposite happens at soil grain boundaries because such boundaries are characterized by sudden change in gray scales. Therefore, the responses in *cH1*, *cV1*, and cD1 contain soil grain boundary information (or size information) of the original image in the three directions. Figure 5.10 shows Haar wavelet transformation performed on a soil image up to the second level of decomposition. The responses in *cH*, *cV*, and *cD* are scaled to the range from 0 to 255. Zero is expressed as black and 255 as white. It is clearly seen from Figure 5.10 that responses are low within a soil grain and high at the boundaries.

In an image of uniform small sized soil grains, more responses at low levels of wavelet decomposition are observed than in an image of uniform large sized soil grains because the soil grain boundaries are more prevalent. Figure 5.11 shows the first wavelet decomposition level of two soil images having different *PPD*. The image on the left is of soil grains retained between the No. 50 and No. 60 sieves taken with a magnification of 22 pixel/mm. The corresponding *PPD* is 6.6. Soil grains retained between the No. 18 and No. 20 sieves are shown on the right image at a magnification of 33 pixel/mm, corresponding to *PPD* = 30.5 The size of both images is 256 pixel by 256 pixel. It can be reasonably predicted that the image on the right will exhibit greater response at higher levels of decomposition since soil grain boundaries in low *PPD* image become less

distinctive or disappear at higher levels' c_{approx} while those in high *PPD* image remain well defined.

Figure 5.12 is provided to better show how the response of different decomposition level changes depending on *PPD*. Objects in the upper three images have the same shape of black and white squares but differ in size. The left image consists of 1 by 1 pixel squares representing *PPD* = 1. The central and left images contain 2 pixel by 2 pixel and 4 pixel by 4 pixel squares, respectively, representing *PPD* = 2 and *PPD* = 4. Each image was decomposed up to the third decomposition level. The lower three images show the results. The left, central, and right images have response only at the first, second, and third decomposition levels, respectively. This clearly shows that as *PPD* increases the response shifts to higher decomposition levels. It should be noted that if an object shape is not an ideal square all decomposition levels will carry some response but generally, one particular decomposition level will contain the largest response depending on *PPD*. This of course assumes that the objects are nearly uniform in size.

Having said the above, the distribution of response by wavelet decomposition level contains the key information for determining soil grain size. Thus, a simple image index that would characterize the response distribution was sought. Shin and Hryciw (2004) used *Energy* (E) to quantify the magnitude of the response at each decomposition level. This energy at each wavelet decomposition level can be calculated by:

$$E_i = \sum_{x,y} \left(cH_i(x,y)^2 + cV_i(x,y)^2 + cD_i(x,y)^2 \right) \tag{5.13}$$

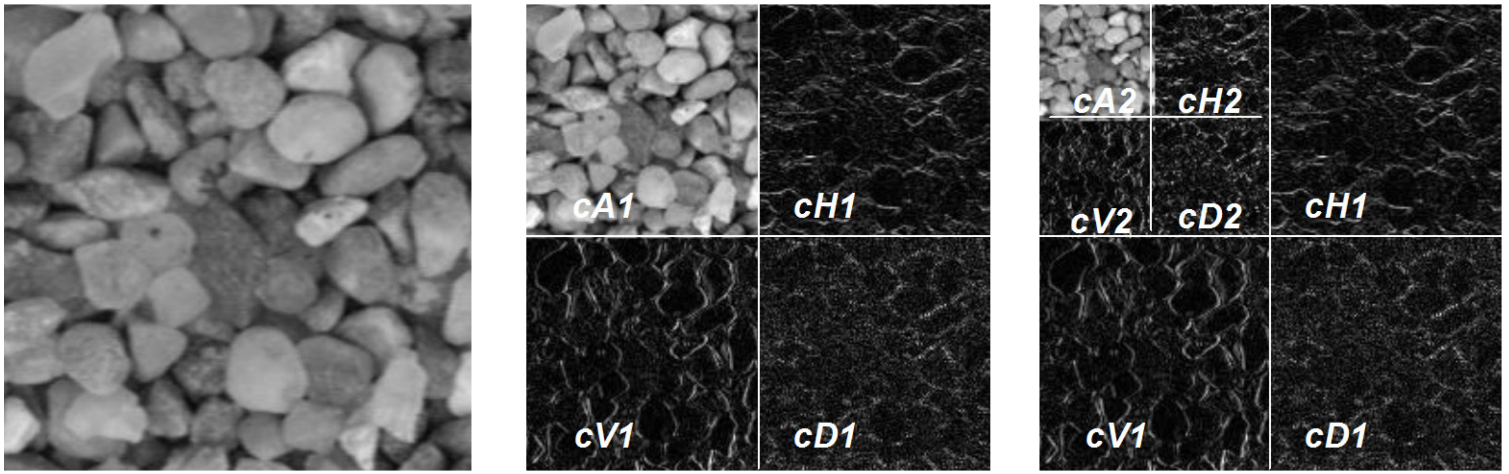

(a) Original image

(b) First wavelet decomposition level

(c) Second wavelet decomposition level

Figure 5.10 Two dimensional Haar wavelet transforms of a 256 pixel by 256 pixel soil image. *cH1*, *cV1*, and *cD1* contain soil grain size information in horizontal, vertical diagonal direction respectively.

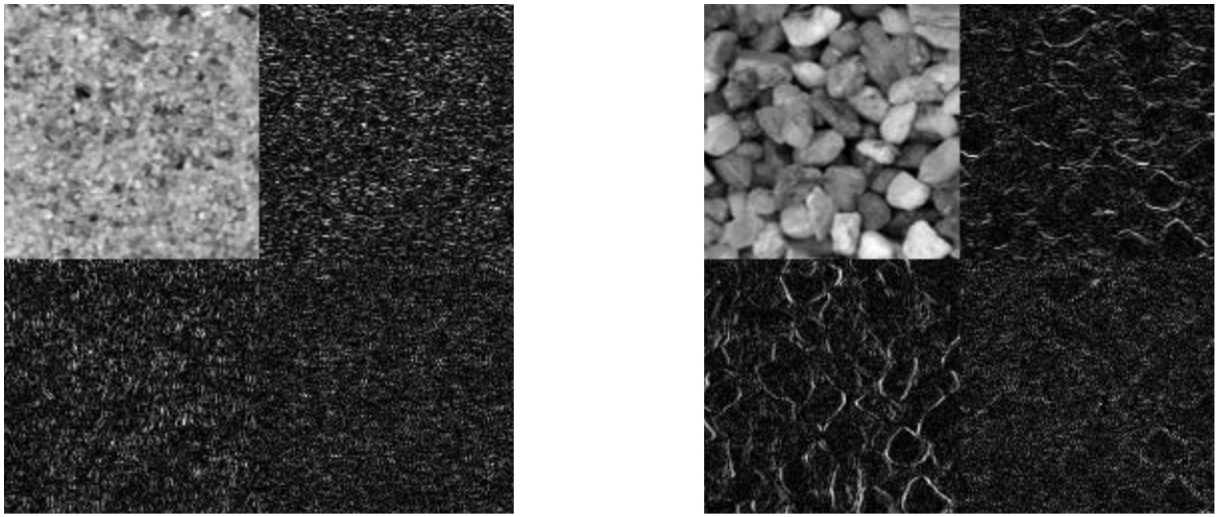

Figure 5.11 First wavelet decomposition levels for two different *PPD*, a) *PPD* = 6.6 and b) *PPD* = 30.5.

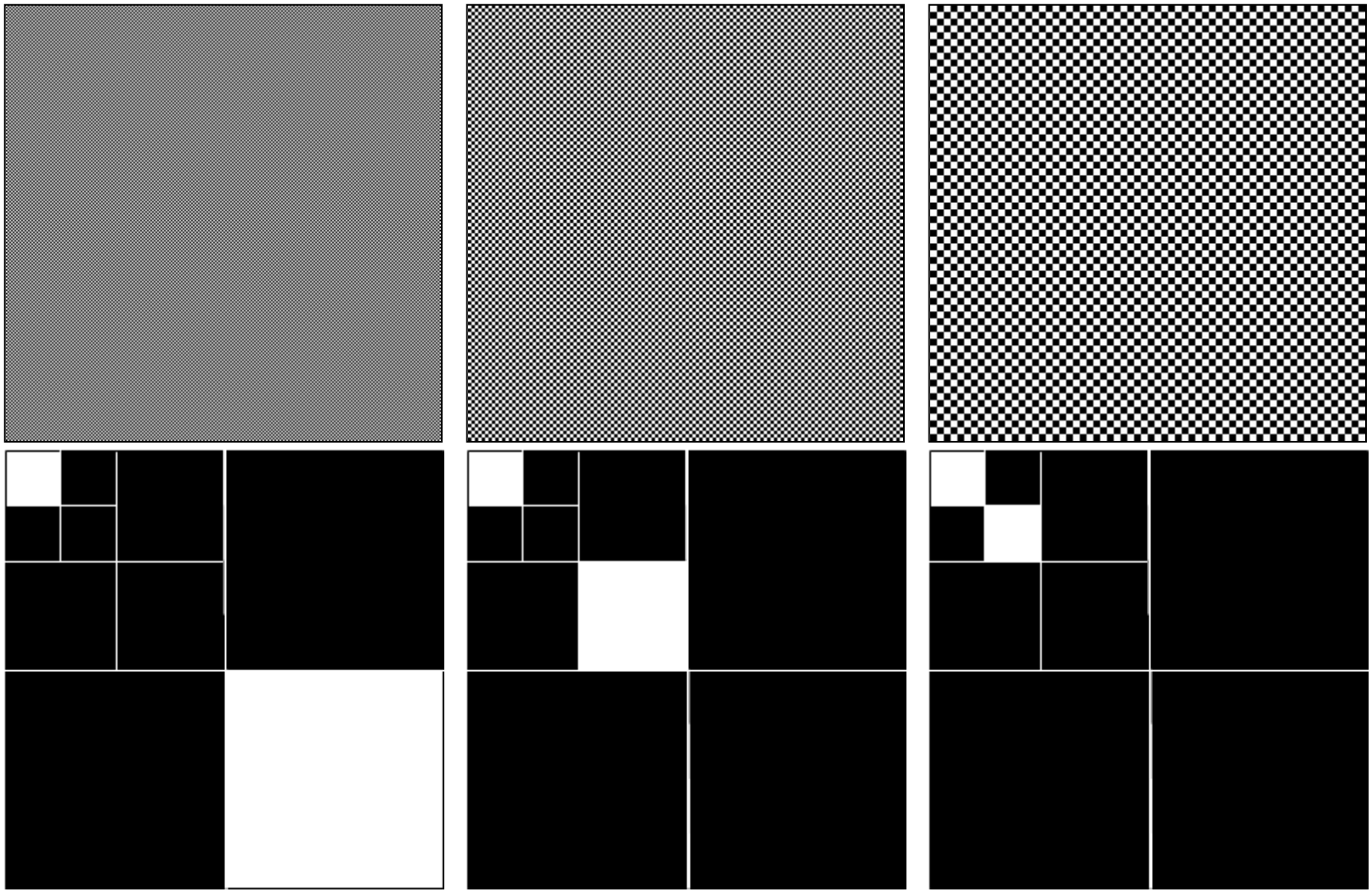

Figure 5.12 Three images containing ideal black and white square objects with different sizes and two dimensional wavelet transforms of them. The size of the objects in a), b), and c) is 1 by 1, 2 by 2, and 4 by 4 pixel respectively.

where the subscript *i* represents the decomposition level. The energy distribution obtained by Equation 5.13 has a shortcoming as universal soil grain size index. When two identical soils are photographed under different illumination conditions the energy distribution of the two images is not the same because the total energy of an image is influenced by illumination intensity. The total energy is the sum of the energies at all decomposition levels. So, Shin and Hryciw (2004) further introduced the *Normalized Energy* ($E_{normailzed}$) to eliminate the undesirable effect of the illumination intensity. $E_{normailzed}$ is computed by dividing E of each decomposition level by total energy.

$$E_{normailzed} = \frac{(E_1, E_2, E_3, ...E_7)}{\sum_{i=1}^{7} E_i} \times 100\% \tag{5.14}$$

Figure 5.13 shows the normalized energy distribution versus wavelet decomposition level for soil images of various *PPD*, from 1 to 125. The size of the soil images used to get the normalized energy distribution for various *PPD* is 256 pixel by 256 pixel. As *PPD* increases, the normalized energy profile is observed to shift to higher decomposition levels as previously discussed. This behavior of the normalized energy is logical in that as *PPD* increases, the soil grain boundaries in an image become sparser, which leads to low frequency of soil grain boundary in the image, and high decomposition levels carry low frequency signal information. A 256 pixel by 256 pixel image can be decomposed up to eighth decomposition level but only first seven decomposition levels are used. That is because the basis function of the eighth decomposition level has too low frequency width, 256 pixels, which covers the entire 256 pixel by 256 pixel soil image, so that the eighth level includes undesirable information,

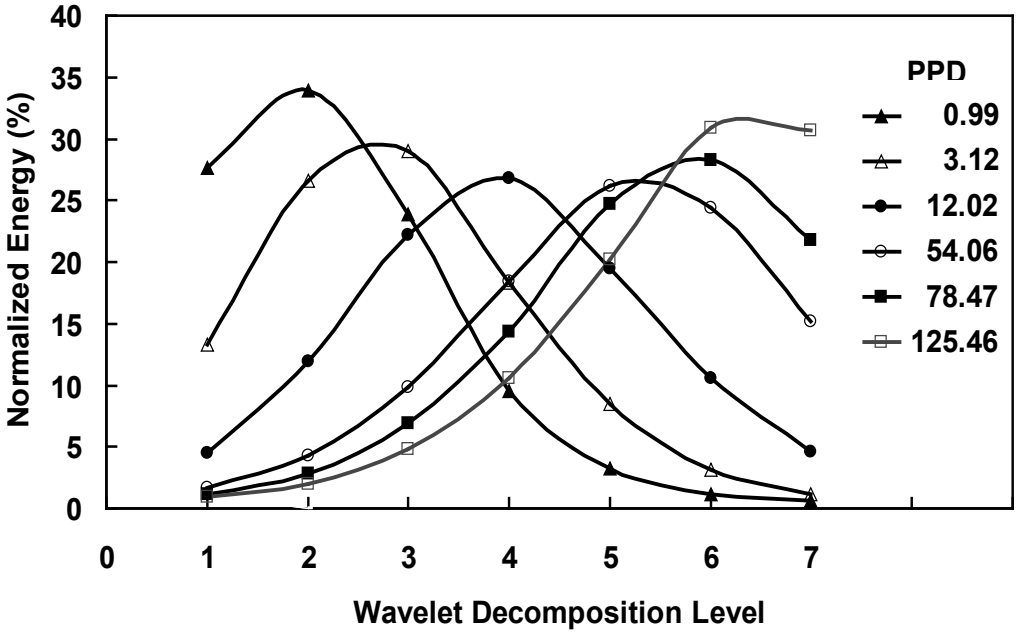

Figure 5.13 Normalized energy versus decomposition level for select soil images of various *PPD*.

such as uneven illumination distribution (if such exists) and color distribution rather soil grain size information.

Shin and Hryciw (2004) brought the behavior of the normalized energy governed by *PPD* to one single index, Center of area (*CA*) beneath the normalized energy profiles (first moment with regard to the ordinate). Initially, 256 pixel by 256 pixel images of two different dry soils placed on a flat surface (multi-colored soil retained between No. 40 and No. 50, and uniform colored soil between No. 40 and No. 60) were collected using a CCD camera (Pulnix model TM-7CN) with various magnifications to calculate the *CA* at a wide range of *PPD* from 2 to 50. Figure 5.14 shows the calibration chart of *CA* versus *PPD*. The vertical bars indicate 1 standard deviation in the data spread. Later, laboratory tests by Hryciw et al. (2006) extended the range in both directions to values as low as

PPD = 0.26 and as high as *PPD* = 110 as shown in Figure 5.14. Each data point in Figure 5.14 represents the average of at least 20 images of the same soil at the same magnification (i.e. same *PPD*). However, different soils were also used ranging in grain size from silt (0.038 mm) to almost coarse sand (1.19 mm) and the magnifications were varied by more than a factor of 5. Both single color and multi-colored grains were investigated.

It was shown that wavelet transformation produces low resolution in the high frequency range (low decomposition levels) and high resolution in the low frequency range (high decomposition levels). This results in larger deviations in *CA* at small *PPD* than at large *PPD*. However, as seen in Figure 5.14, the *CA* at small *PPD* shows less scatter than that at large *PPD*. This is mainly because of three reasons:

1. As *PPD* increases the number of soil grains in an image becomes small relative to the 256 pixel by 256 pixel image and thus more statistical deviation is observed in a normalized energy profile.
2. For calibration, the *PPD* was pre-determined from the known magnification and the average soil grain size.The average grain size was determined by taking the average of two successive sieve opening sizes. So, the *PPD* in the calibration chart reflect or represent a range at each *PPD* as shown in Figure 5.15. It should be noted that the possible *PPD* range at large *PPD* is much larger than at small *PPD* on an absolute basis, but not a percentage basis.
3. At small *PPD*, internal textures within a grain would not be distinguishable since they are averaged into a few pixels. So, variations in gray scale within a grain are not discernible when the *PPD* is small. On the other hand, at large

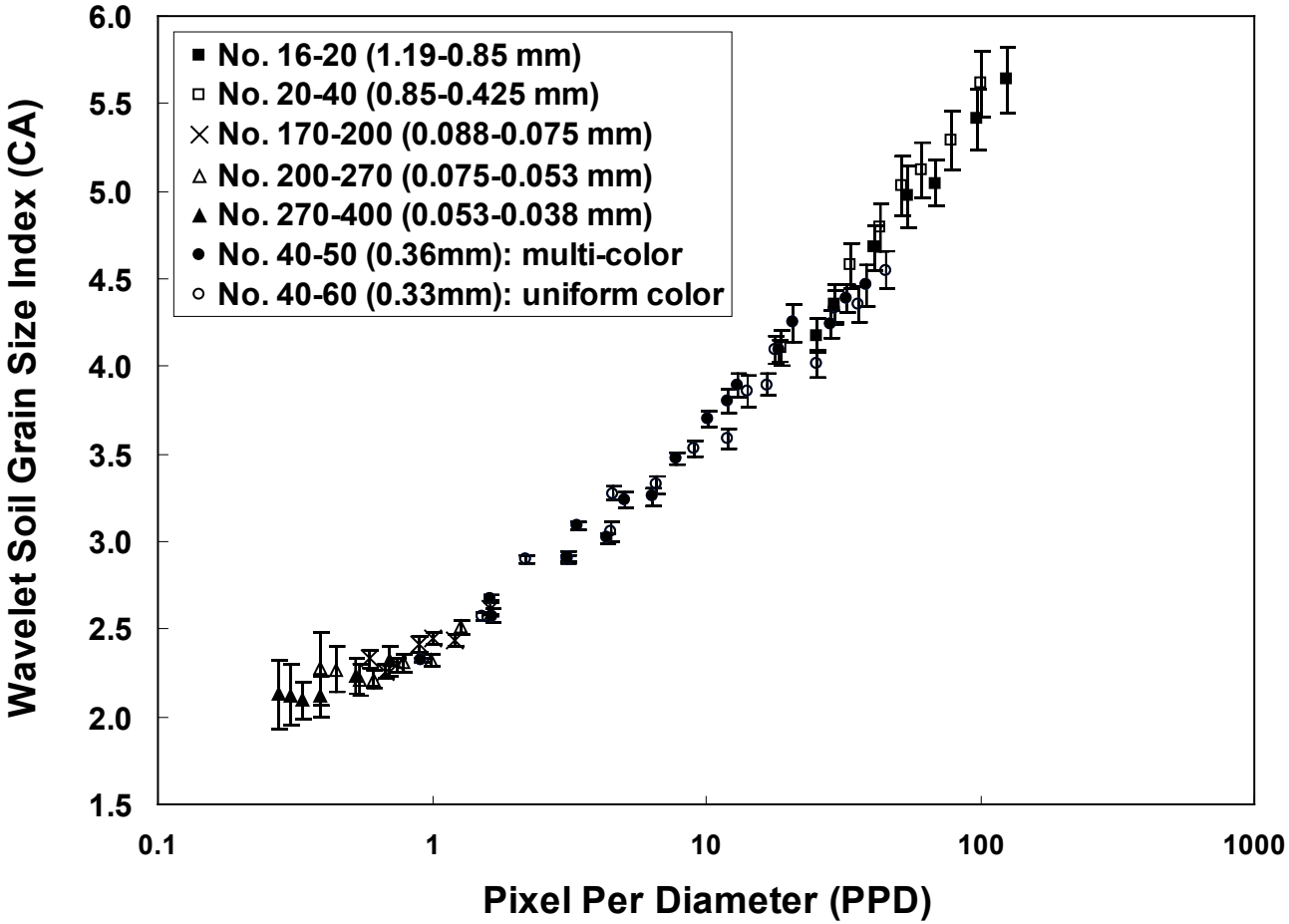

Figure 5.14 Center of area (*CA*) versus pixel per diameter (*PPD*) for *PPD* ranging from 0.27 to 110.

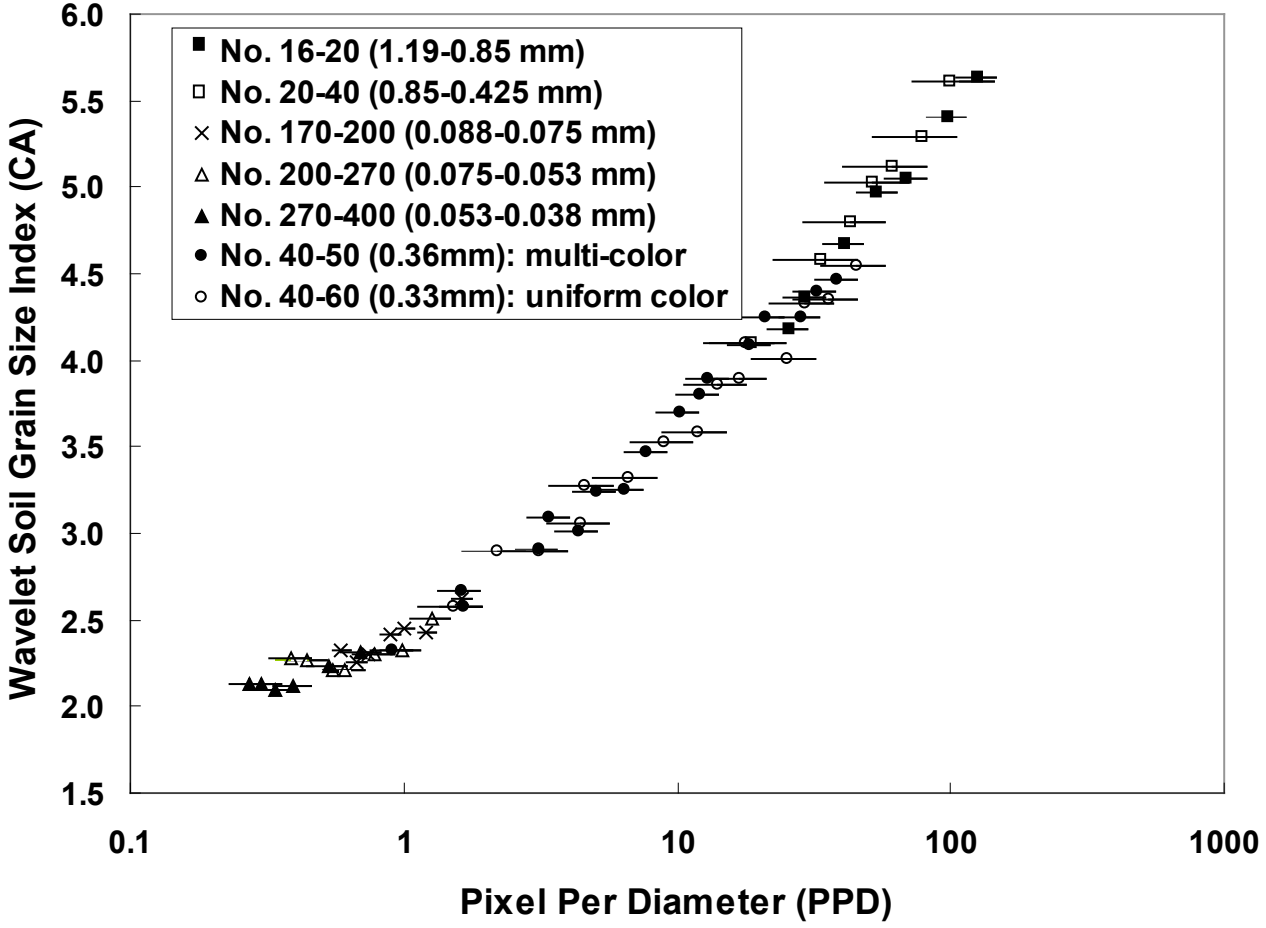

Figure 5.15 Center of area (*CA*) versus pixel per diameter (*PPD*) with a possible *PPD* range.

PPD, internal textures are well seen. So, they can be recognized as false small soil gains and generate undesirable energy at low frequencies.

It can be observed that the scatter in *CA* for *PPD* less than 1 increases drastically as *PPD* decreases. Also, *CA* for *PPD* less than 1 tends to approach 2.2 asymptotically. These phenomena are explainable with digital merging effect of soil grains. When *PPD* is smaller than 1, say 0.5 *PPD*, there should be approximately 4 soil grains whose gray scales are averaged into one pixel. Then, the majority of soil grain boundaries are lost, and the merged four grains appear as one single grain. Rather than soil grain boundaries, color variation and distribution of individual soil grains controls the normalized energy profile.

5.5 Wavelet Soil Grain Size Index of Saturated Soils

Since soil in a sedimentation column is fully saturated, the relationship between *CA* and *PPD* described in the previous section and shown in Figure 5.14 must be verified for saturated soil conditions.

To simulate saturated soil conditions and see the effect of water on *CA*, the Vision Cone Penetrometer (VisCPT), which was originally developed by Raschke and Hryciw (1997a) to capture continuous soil images with depth for in-situ soil grain size analysis and delineation of site stratigraphy (Ghalib et al., 2000), is used as shown in Figure 5.16. VisCPT can largely be divided into two parts, vision part and cone penetrometer (CPT) part. The latter is the regular CPT used to measure tip resistance, friction ratio, and pore

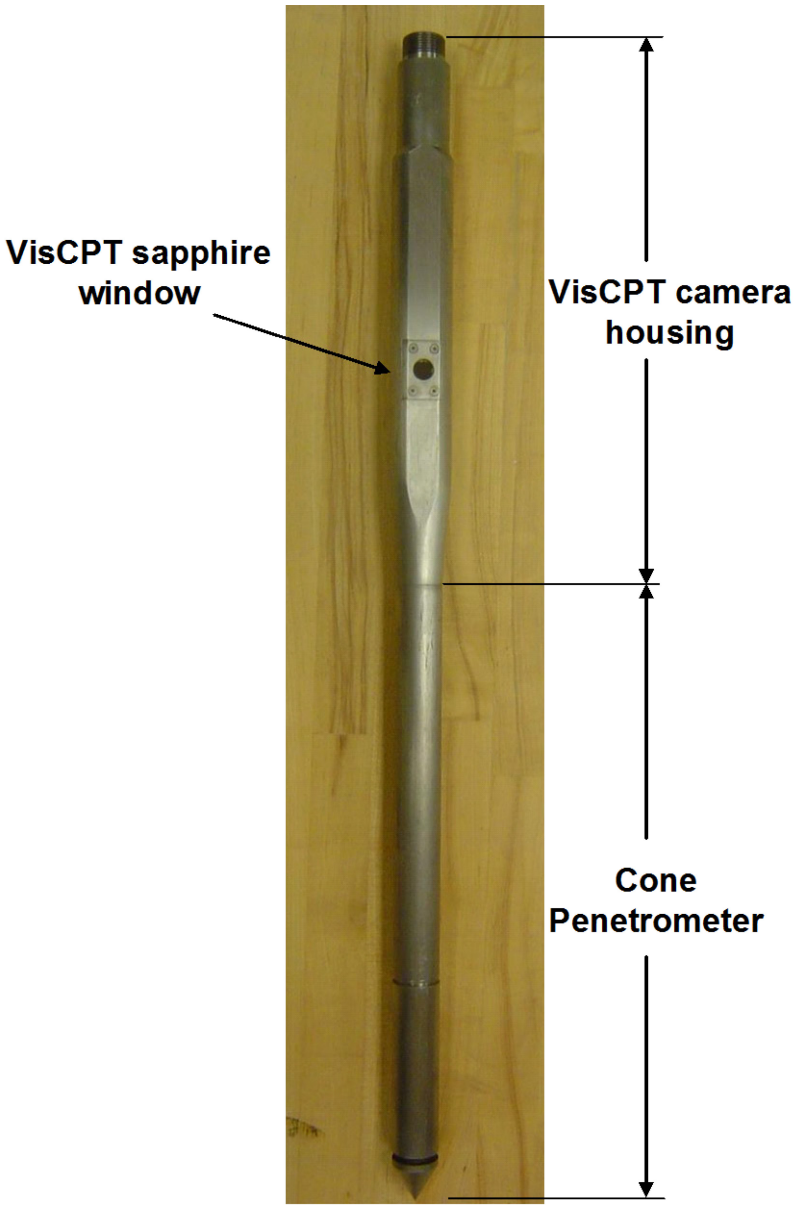

Figure 5.16 Vision Cone Penetrometer (VisCPT).

water pressure. The former consists of a camera housing, sapphire window, and camera behind sapphire window. The camera in the VisCPT housing is a CCD camera (ELMO MN-30) with a ¼ inch imager that has the same pixel resolution (480 pixel by 752 pixel) and pixel aspect ratio (1 to 1.17) as the laboratory CCD camera with a ½ inch imager

(Pulnix model TM-7CN). A double ring soil saturator (DRSS) was designed and constructed as shown schematically in Figure 5.17 a). The device is placed over the VisCPT sapphire window as shown in Figure 5.17 b). A thin bed of vacuum grease is applied to the perimeter of the DRSS/VisCPT contact to immobilize the DRSS and to ensure a tight water seal. The central area of the double ring saturator is filled with dry soil and a VisCPT image is taken. Water is then introduced into the annular area between the inner and outer rings of the DRSS. It flows into the soil through 3 pinholes at the base of the inner ring thereby saturating the soil specimen from below. Full saturation is guaranteed by introducing the water very slowly to ensure a vertically rising horizontal wetting front. Slow saturation also ensures that the soil skeleton remains undisturbed, even without application of a vertical surcharge on the specimen. The saturation process is monitored by the VisCPT camera output to a computer monitor where the image is greatly magnified.

Images of the same highly uniform (0.71 mm – 0.80 mm) sand under dry and saturated conditions are shown in Figure 5.18. Since all other conditions including lighting, magnification, soil skeleton, etc. are identical; the only difference between the specimens is the presence of water in the pore space. Thus, measured differences in the wavelet index, *CA* are entirely due to water effects.

Using 256 pixel by 256 pixel images, Figure 5.19 shows the relationship between *CA* and *PPD* for dry and saturated soil. Twelve different uniform grain sizes, obtained by sieving, were used to produce the various *PPD* at a fixed VisCPT magnification of 50 pixels/mm. Each data point in the chart represents the average of 10 *CA* values at a given *PPD*. The vertical bars at each data point show the 1 standard deviation in the *CA* values.

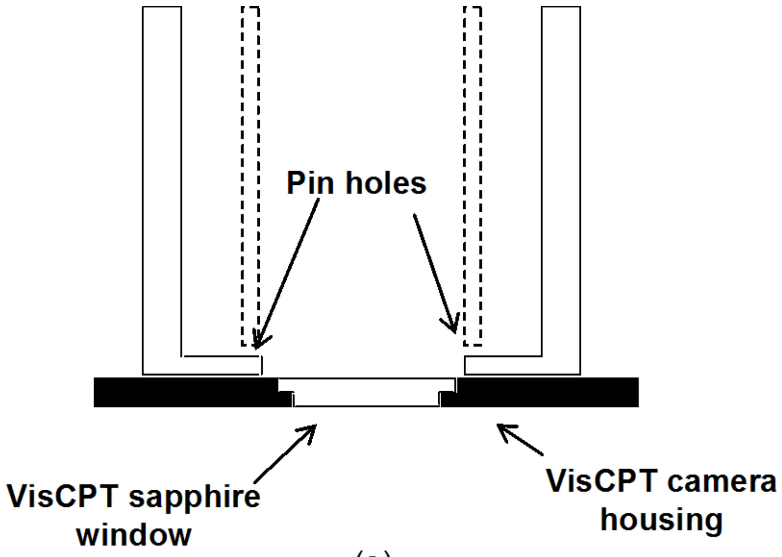

(a)

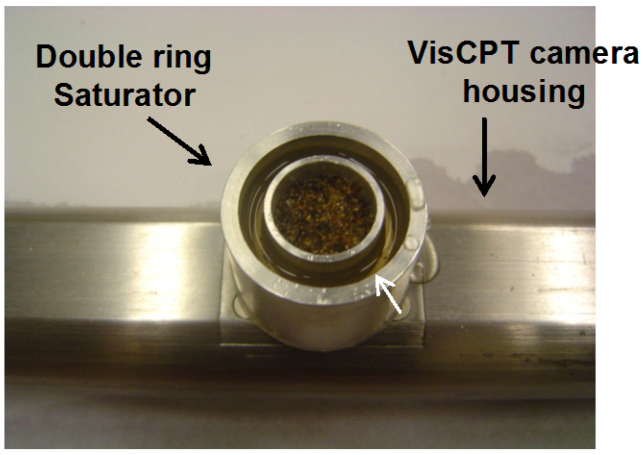

(b)

Figure 5.17 a) Double ring soil saturator schematic. b) Double ring soil saturator placed over sapphire window.

(a)

(b)

Figure 5.18 Image of the same soil (a) dry and (b) saturated.

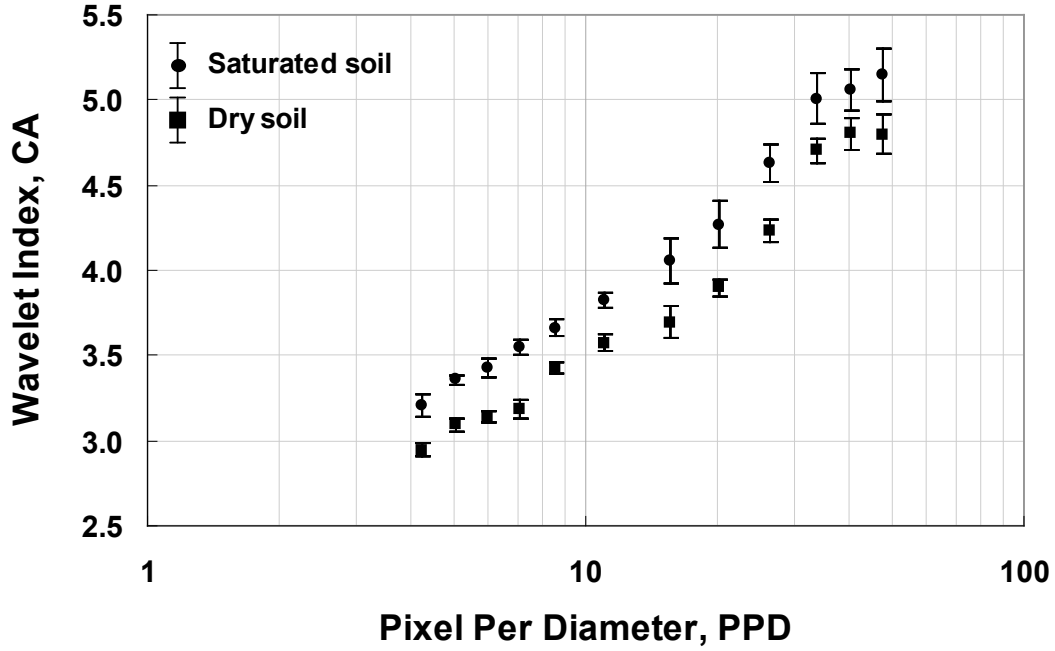

Figure 5.19 Comparison of *CA* for dry and saturated soils at various *PPD* (with standard deviation bars).

The difference in *CA* between saturated soil and dry soil is clear; saturated soil images produce consistently higher *CA* at all *PPD*.

The reason for the increase in *CA* in saturated soil conditions is the magnifying effect of water. Water appears to make the sand grains look larger in the images. Another reason for the increase in *CA* can be explained by the apparent blurring of internal textures within individual soil grains. So, the internal textures become muted and even disappear as can be seen in Figure 5.18. The disappearances of the internal textures reduce the energy at low decomposition levels, which leads to the increase in CA. The fundamental reason for the variations in image appearance and the resulting differences in *CA* can probably be explained by variations in the refraction indices of the pore fluid and the viewing window.

In Figure 5.20, the relationship between *CA* and *PPD* using saturated soil images collected by the VisCPT is compared with that using saturated soil images by the laboratory CCD camera (Pulnix model TM-7CN). In the latter case, the soil was deposited through water in the sedimentation glass column that has the approximately same thickness as the sapphire VisCPT window. The excellent agreement indicates that the effect of water on the *CA* versus *PPD* calibration developed with the CCD camera and the soil sedimentation column is the same as the effect of water on the *CA* versus *PPD* calibration by VisCPT. Also, it should be noted from Figure 5.20 that *CA* is independent of lighting since the lighting sources for the two sets of data in Figure 5.20 were different. While no special lighting system was used with the laboratory CCD camera (Pulnix model TM-7CN) the VisCPT camera has twelve built-in white LED lights.

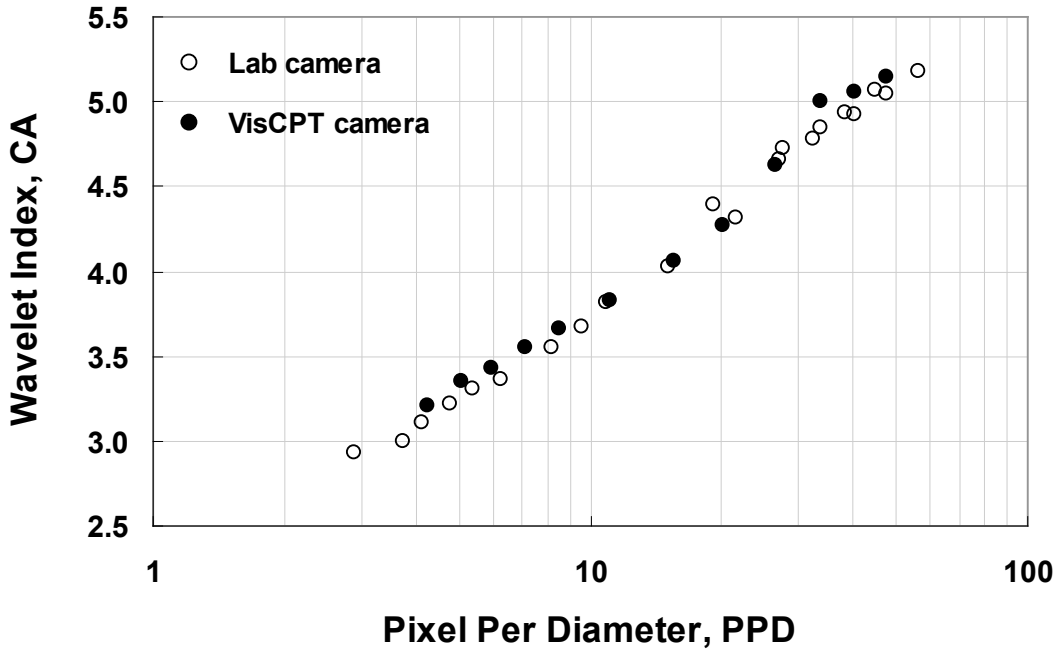

Figure 5.20 Comparison of *CA* from lab camera images with *CA* from VisCPT camera images.

Figure 5.21 compares two different *CA* versus *PPD* calibration charts obtained by various soils. The two calibration charts are developed using the laboratory CCD camera under two different conditions, saturated soil condition behind sedimentation glass column (Figure 5.20) and exposed dry soil condition (Figure 5.14). Finally, for the easy calculation of soil grain size from the wavelet index, *CA*, a best-fit model to the *CA* versus *PPD* calibrations was developed:

$$\log PPD = A \log\left(\frac{CA}{CA_1}\right) \tag{5.15}$$

where CA_1 is the *CA* corresponding to *PPD* = 1.0 and *A* is an empirical constant equal to 5.5 +/- 0.4. The lower limit of $A \approx 5.1$ was observed when soil was saturated and behind the glass.

It should be noted that the *CA* values were computed using only the red image layer of the RGB image. It should also be noted that the differences between *CA* values computed from the three image layers were negligible.

5.6 Pixel Aspect Ratio with Wavelet Index

The pixel aspect ratio is the ratio of the width of a pixel to its height. If an object is photographed by an imaging system which has the aspect ratio of 1 to 1, the object appearing in the image will preserve its shape when shown on a computer monitor having

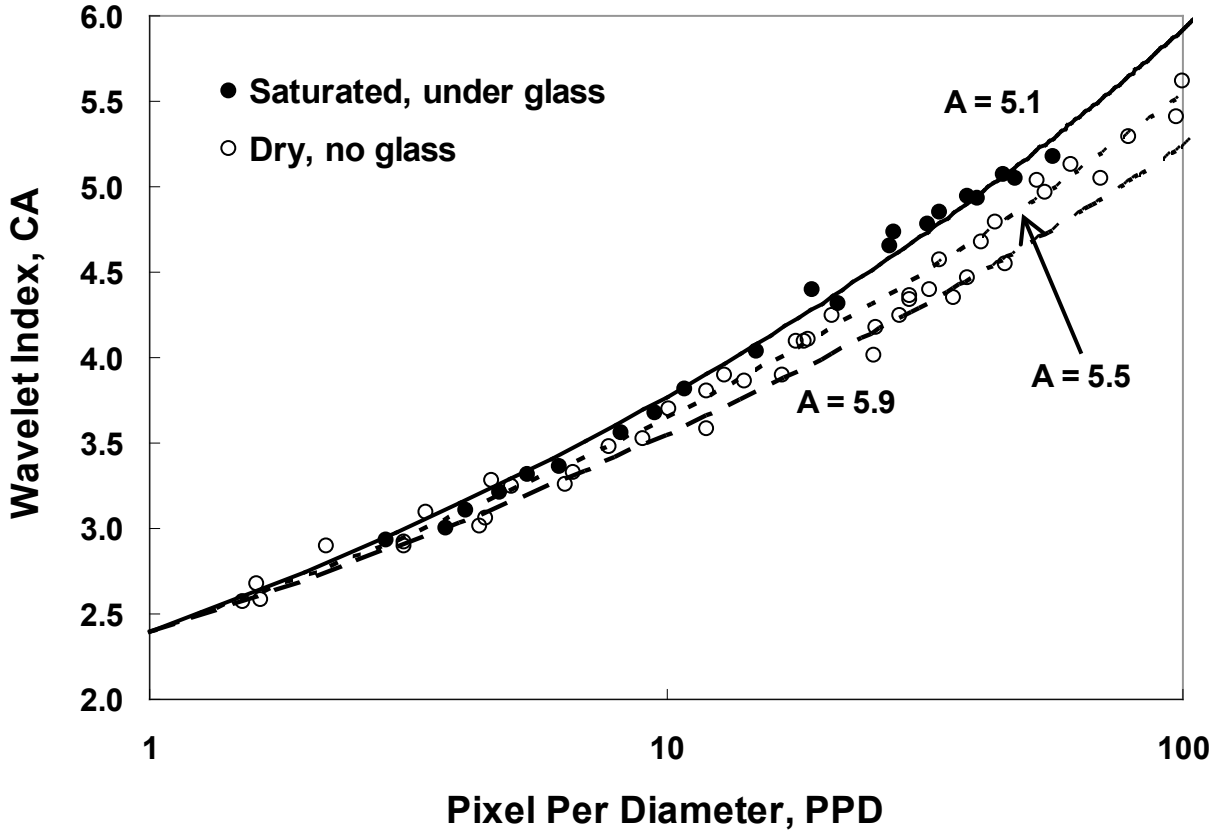

Figure 5.21 *CA* versus *PPD* soil grain size calibration charts for saturated and dry soil.

square pixel aspect ratio (1 to 1). Contrarily, if the pixel aspect ratio is not 1 to 1 the object on the computer monitor is rather distorted or enlarged in horizontal or vertical direction. Therefore, it is important to identify pixel aspect ratio of an image in using image processing techniques to determine size of an object appearing in digital images.

Many video imagers, such as CCD and CMOS, have non-square pixel aspect ratios. That is because when video engineers in 1990s' standardized 480i and 576i digital electrical standards they decided to use non-square pixel due to the technical difficulty in sampling analog signals to get square pixels. The cameras (ELMO MN-30 and Pulnix TM-7CN) used for establishing the relationship between *CA* and *PPD* have pixel aspect ratios of 1 to 1.17. So, when shown on a computer monitor having square pixel aspect ratio, soil grains appearing in the image taken with the cameras is 17 percent larger in horizontal direction than those in the image taken with a camera with square pixel aspect ratio.

In soil grain size analysis with statistical approaches based on soil images textures, there is nothing wrong to develop soil grain size calibration charts using a camera with non-square pixel as long as the image textural indices are obtained from images taken by a camera that has the same non-square pixel aspect ratio. However, as high resolution digital cameras with square pixel become widely available, establishing a *CA* versus *PPD* calibration chart with a camera having square pixel aspect ratio is essential. Also, it is important to see how pixel aspect ratio influences *CA*.

Figure 5.22 shows two normalized energy profiles of a soil image taken with the laboratory CCD camera having 1 to 1.17 pixel aspect ratio. *PPD* of the soil image is 9.5 in the vertical direction. Each normalized energy profile with solid and dot line was

obtained by using only horizontal and vertical wavelet transforms coefficients (*cH* and *cV*) respectively. As clearly seen in Figure 5.22, the normalized energy profile obtained from *cH* has more energy in higher decomposition levels than that obtained from *cV*. This is because *cH* contains only horizontal soil grain size information and soil grains in the image are stretched in the horizontal direction. The soil image used for Figure 5.22 was digitally compressed in the horizontal direction by 17 percent so that the soil grains in the compressed image appear to be same as those in the image taken from a camera having square pixel aspect ratio. Figure 5.23 shows the resulting normalized energy profiles obtained from *cH* and *cV*. They are very similar to each other and have almost the same center of area beneath them (*CA*).

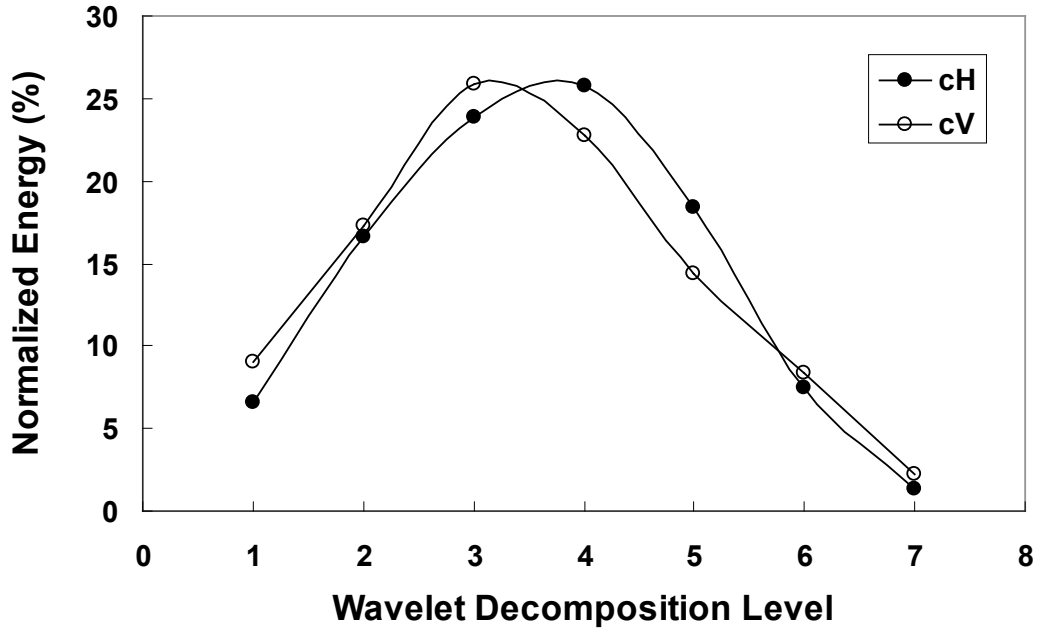

Figure 5.22 Normalized energy profiles of *cH* and *cV* using 1 to 1.17 pixel aspect ratio.

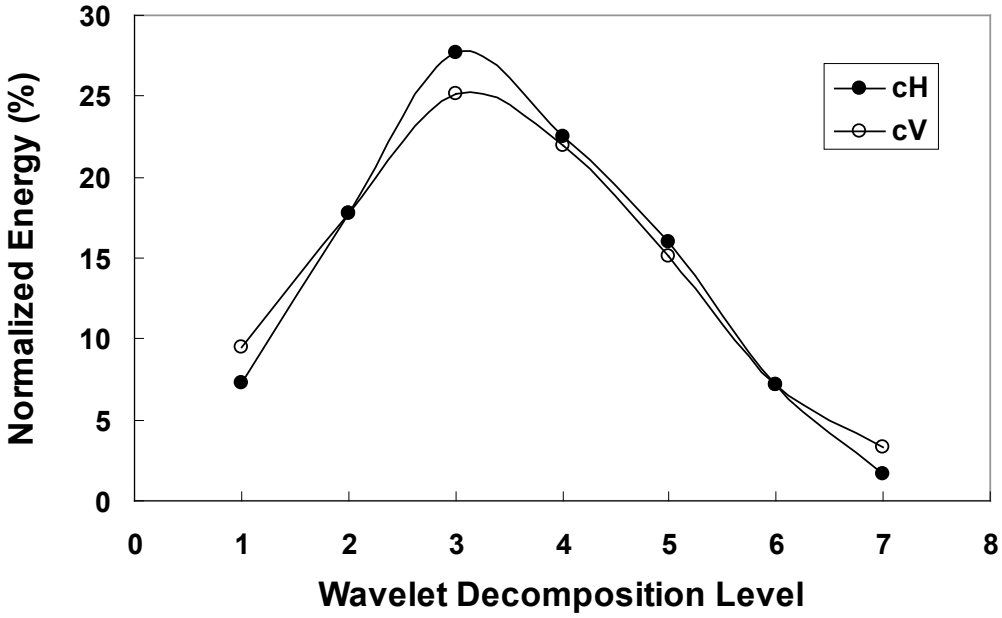

Figure 5.23 Normalized energy profiles of *cH* and *cV* using 1 to 1 pixel aspect ratio.

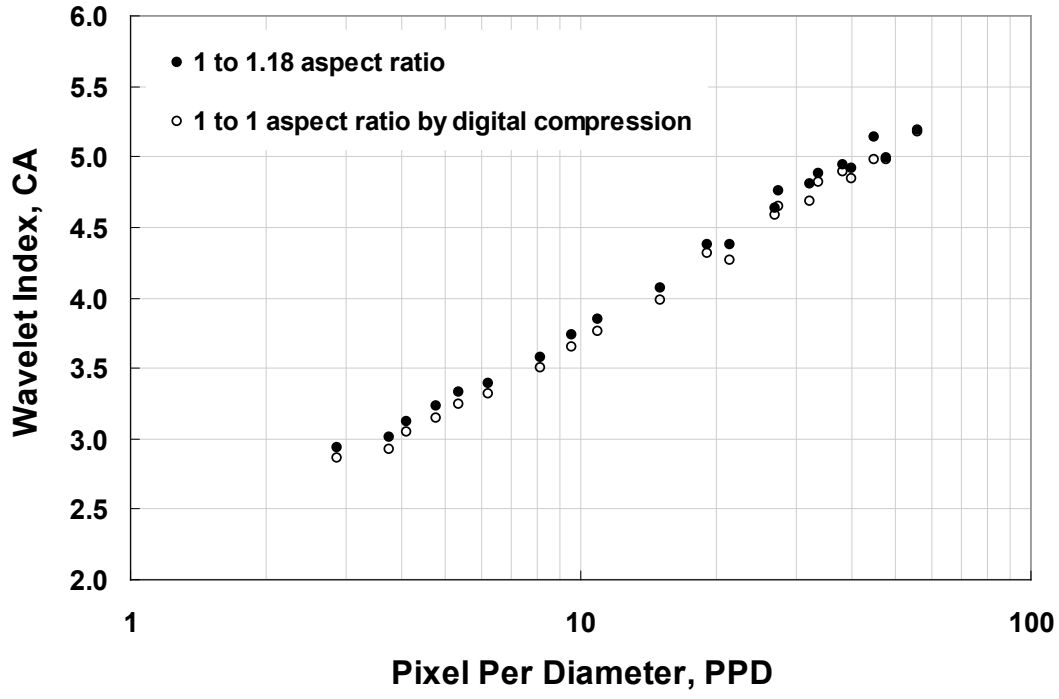

Figure 5.24 Effect of different pixel aspect ratio on *CA* values.

From the observation, it can be expected that all *CA* values in Figure 5.21 will decrease a bit when the soil images used for Figure 5.21 are digitally compressed in the horizontal direction by 17 percent. Figure 5.24 validates the expectation by comparing *CA* versus *PPD* calibration chart from the digitally compressed images with the calibration chart in Figure 5.21.

Using a commercial digital camera (Nikon D300) that has square pixel aspect ratio, *CA* versus *PPD* calibration was developed and shown in Figure 5.25. It shows excellent agreement with the *CA* versus *PPD* calibration of the digitally compressed soil images shown in Figure 5.24. The result indicates that *CA* value is independent of camera

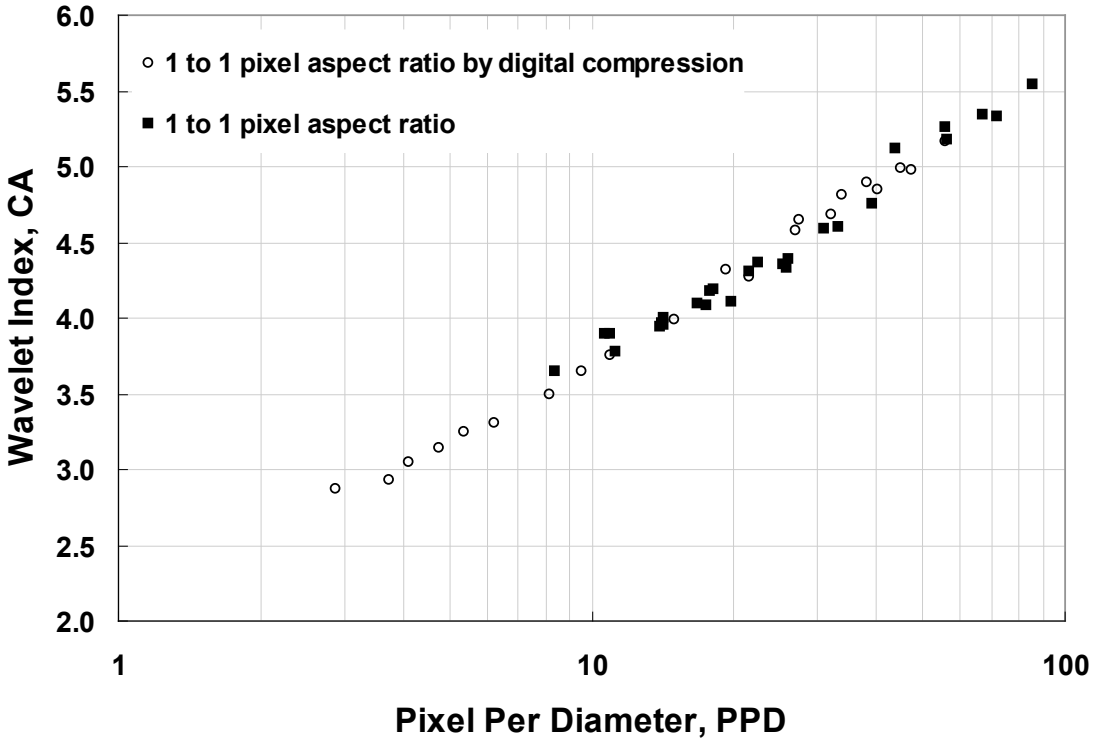

Figure 5.25 The relationship between *CA* and *PPD* obtained from 1 to 1 pixel aspect ratio images. Two different camera systems with 1 to 1 and 1 to 1.17 pixel aspect ratio were used. The images from the camera with 1 to 1.17 pixel aspect ratio were digitally compressed to have 1 to 1 aspect ratio.

manufacturers and thus, can be used by any laboratory image capturing systems as long as the pixel aspect ratio is kept consistent by either digitally compressing digital images or by using camera systems that produce same pixel aspect ratio.

5.7 Conclusions

Wavelet decomposition provides a consistent and reliable method for determination of the average soil grain size. A wavelet soil grain size index, *CA*, correlates very well with soil grain size as defined by the average number of pixels per grain diameter (*PPD*). Also, by normalizing the *Energy* at each wavelet decomposition level by the total energy, the undesirable illumination effect was eliminated.

The *CA* versus *PPD* calibration for dry soil condition was developed by Shin and Hryciw (2004) under laboratory conditions using a variable magnification camera. Initially, the calibration was available for a *PPD* range of 2 to 50. In this study, the calibration is extended to the range from 0.2 to 110 *PPD*. It was shown that *CA* for *PPD* less than 1 does not carry any useful soil grain size information not only because of wide statistical spread but also because of the merging effect of soil grains into one pixel.

To adopt the wavelet soil grain size index to Sedimaging, the effect of water on the index was studied using the Vision Cone Penetrometer (VisCPT) and the double ring soil saturator (DRSS). It was shown that water blurs the internal textures within individual soil grains and thus decreases *CA*. A new *CA* versus *PPD* calibration for saturated soil condition was therefore developed.

The *CA* versus *PPD* calibrations for dry and saturated soil condition were developed by using soil images taken by a CCD camera having pixel aspect ratio of 1.17 to 1. As digital cameras with square pixel aspect ratio become widely available and replace CCD cameras for image analysis, establishing a *CA* versus *PPD* calibration chart with a camera having square pixel aspect ratio is essential. After digitally shrinking the images taken by the CCD camera by 17 percent in the horizontal direction, the *CA* versus *PPD* calibration had very good agreement with the calibration obtained by images taken by a digital camera having square aspect ratio.

CHAPTER VI

Mathematical Morphology for Soil Grain Size Analysis

6.1 Introduction

Determination of particle size from images of three dimensional soil assemblies of uniform grains by wavelet decomposition method has one weakness for use in *Sedimaging*. The weakness comes from having to use 256 pixels in the vertical direction and the same number of pixels in the horizontal direction. Considering that the number of pixels in the horizontal direction of a soil column image used for Sedimaging is at least twice as large as 256 pixels, the wavelet decomposition method for statistical soil grain size analysis uses only half of the available soil grain size information. This could result in wide statistical spreading in wavelet soil grain size index (*CA*) since the less soil grain size information is used for the statistical analysis, the poorer its statistical validity is. In fact, this weakness can be overcome by more vertical pixel lines. For example, 512 pixel by 512 pixel image area can be used to compute *CA* to utilize most of available information and increase statistical validity. However, in such a case, resolution of soil grain size distribution curve by Sedimaging will be poor, which is not desired. Furthermore, the 512 pixel by 512 pixel image area is likely to include several different

soil grain sizes, which wavelet decomposition method can not deal with. So, using *mathematical morphology*, a more robust and flexible statistical soil grain size analysis method which does not restrict the size of images is presented in this chapter.

The most common applications of mathematical morphology are in removal of unwanted objects or noise from digital images or for enhancement of important details such as the outlines of objects. The use of mathematical morphology for *granulometry* (object size and object size distribution determination) was suggested and investigated by Matheron in the 1960's after the introduction of two basic morphological operators, *erosion* and *dilation*. Subsequent work such as by Matheron (1975) and Serra (1982) was limited mainly to binary images of non-contacting objects. Attempts were made to determine pore size in rocks from binary images of thin sections (Serra, 1982). However, this can only be effective if the pores are disconnected and have a gray scale distinct from the rock minerals.

Since then, mathematical morphology has been used to determine the size and shape of a variety of simple non-contacting and non-geologic materials including steel marbles and ground pea kernels (Devaux et al., 1997), cellular structure of bread crumbs (Lassoued et al., 2007) pore size and structure of sodium chloride tablets (Wu et al., 2007); and synapses in cultured cells (Prodanov et al., 2006).

Recently, mathematical morphology for characterization of geologic materials has begun to attract new attention. Horgan (1998) presented the application of mathematical morphology to study pore size distribution of soil structures and the lengths and geometric patterns of cracks in drying soil. Masad and Button (2000) used it to quantify the texture and angularity of soil aggregates. Balagurunathan and Dougherty (2002)

suggested using mathematical morphology as a tool to measure soil surface roughness. For the determination of soil grain size distribution, Maragos et al. (2004) and Lira et al. (2009) applied mathematical morphology but their works were limited to non-contacting soil grains or digitally segmented individual soil grains. However, mathematical morphology is not known to have been used for soil grain size analysis of three dimensional soil assemblies.

In this chapter, mathematical morphology is studied for determining size of three dimensional soil assemblies of uniform grains by taking a statistical rather than a deterministic approach. The latter has been used by many researchers to extract geometric properties of their products. To this end, a *pattern spectrum* of soil images is used for statistical soil grain size analysis which does not require digital segmentation of the soil grains.

6.2 Basic Morphological Operations and Structuring Elements

Mathematical morphology for image processing uses a filter called a *structuring element*. The structuring element is typically a regular geometric shape such as a square or diamond of any size but much smaller than the image. For example, a square structuring element may be 3 pixels by 3 pixels, 15 pixels by 15 pixels, or n pixels by n pixels where n is commonly an odd number in order to have a "central pixel" and thus, to maintain operational symmetry. There are two basic morphological operators: *dilation* and *erosion*. To dilate or erode an image, the structuring element "moves" across the image stopping with its center over each pixel to perform a specific operation. Operation

of the two basic mathematical morphological operators on binary images will be covered in detail first. The extension of the operation to gray scale images will be presented next.

6.2.1 Dilation and Erosion of Binary Image

The *dilation* of objects (or foreground) in a binary image, A, by the *structuring element*, B, is defined as:

$$A + B = \left\{ x \mid \left(B^{s} \right)_{x} \cap A \neq \phi \right\} \tag{6.1}$$

where $(B)_x$ is translation of B by x (B^s) is the reflection (or symmetric) of B about its origin. If a structuring element is symmetric about its center in the horizontal, vertical, and diagonal directions and its origin is set as the center of the structuring element (this is the only case considered in this study) Equation 6.1 becomes:

$$A \oplus B = \left\{ x \mid \left(B \right)_{x} \cap A \neq \phi \right\} \qquad \text{(Dilation)} \tag{6.2}$$

Equation 6.2 simply means that the structuring element, B, is translated by x over the binary image and then, all x such that the intersection of B translated by x with A forms the resulting dilation. Thus, dilation of A by B expands the boundary of A.

More explicitly speaking, dilation of a binary image is the process by which objects (foreground) in the image are expanded by first, placing the center (origin) of a

structuring element on object pixels (foreground pixels) and then, turning all of the image pixels beneath the structuring element into object pixels. Of course, the image pixel beneath the center of the structuring element must be an original foreground pixel and not have become foreground as a result of dilation. Figure 6.1 shows step by step how dilation works on one-dimensional binary image. Object pixels (foreground pixels) and non-object pixels (background pixels) are presented as 1 and 0 respectively in the binary image. It should be noticed from Figure 6.1, that the dilation will completely remove any runs of zeros smaller than the length of the structuring element. Figure 6.2 shows an example of dilation of objects in an image using a 3 pixel by 3 pixel square structuring element. In Figure 6.2, the foreground and background consists of black and white pixels, respectively.

Erosion is the opposite of dilation. The erosion of objects (foreground) in a binary image, A, by the *structuring element*, B, can be expressed as:

$$A \Theta B = \left\{ x \mid (B)_x \subseteq A \right\} \qquad \text{(Erosion)} \tag{6.3}$$

which means that erosion of A by B is all x such that translated B by x is included inside of A. So, erosion is the process by which objects in an image are shrunk by placing the center (origin) of a structuring element on foreground pixels and keeping only those pixels that allow the structuring element to fit fully inside the objects. Figure 6.3 shows

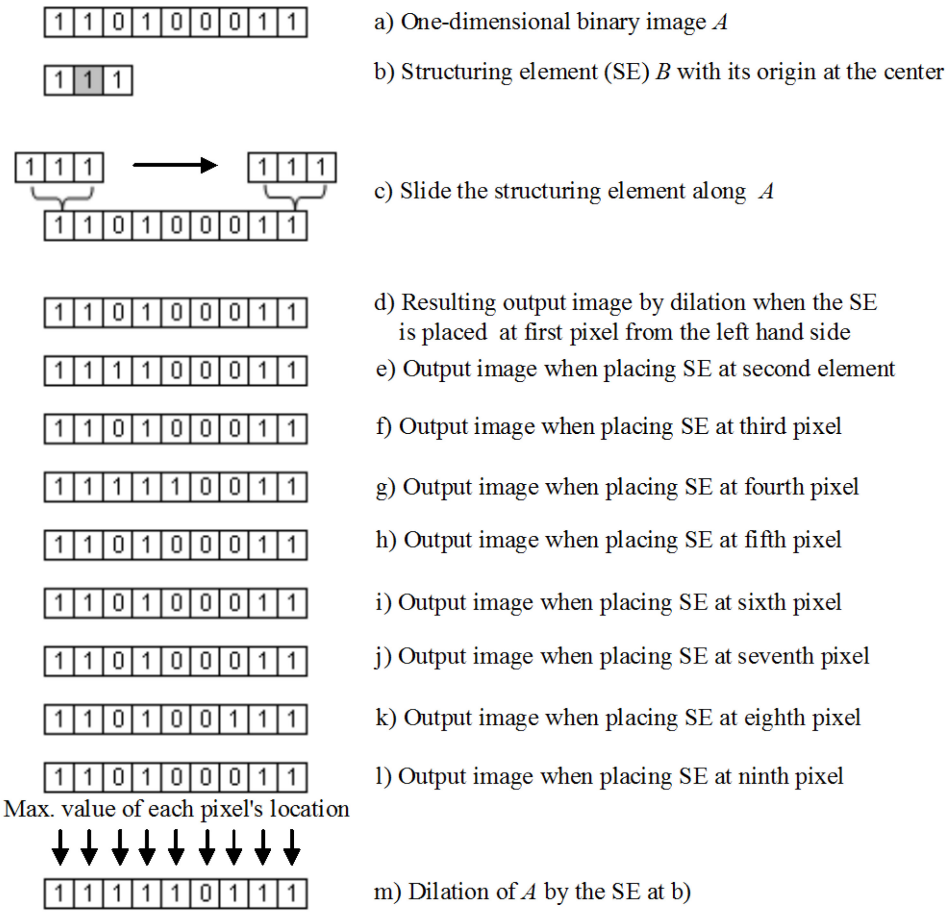

Figure 6.1 Morphological dilation on one dimensional binary image.

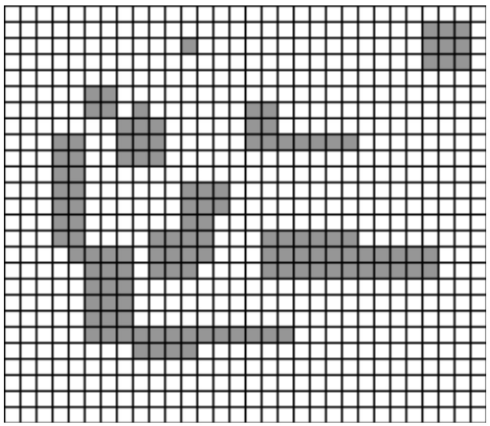

(a) A binary image and a 3 square pixels by 3 pixels structuring element at upper right corner.

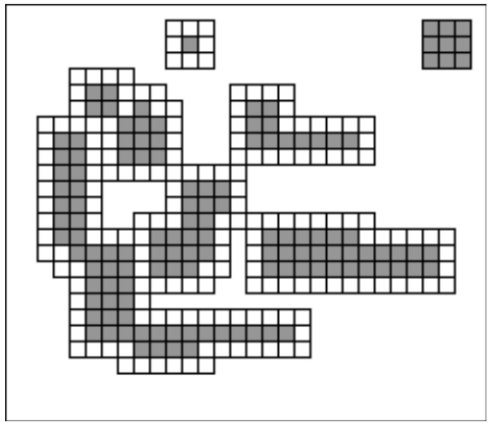

(b) The image about to be dilated. All outlined White pixels will be turn into foreground pixels.

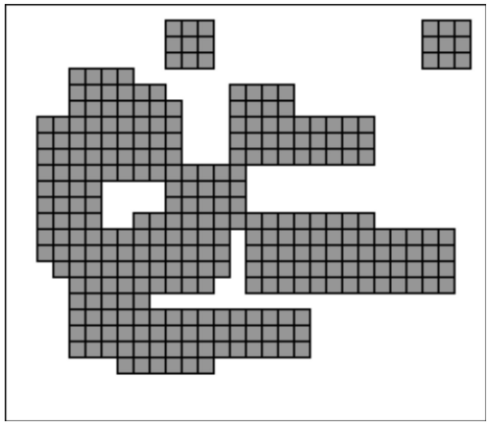

(c) The dilated image.

Figure 6.2 Graphical illustration of morphological dilation on a binary image by 3 by 3 square structuring element.

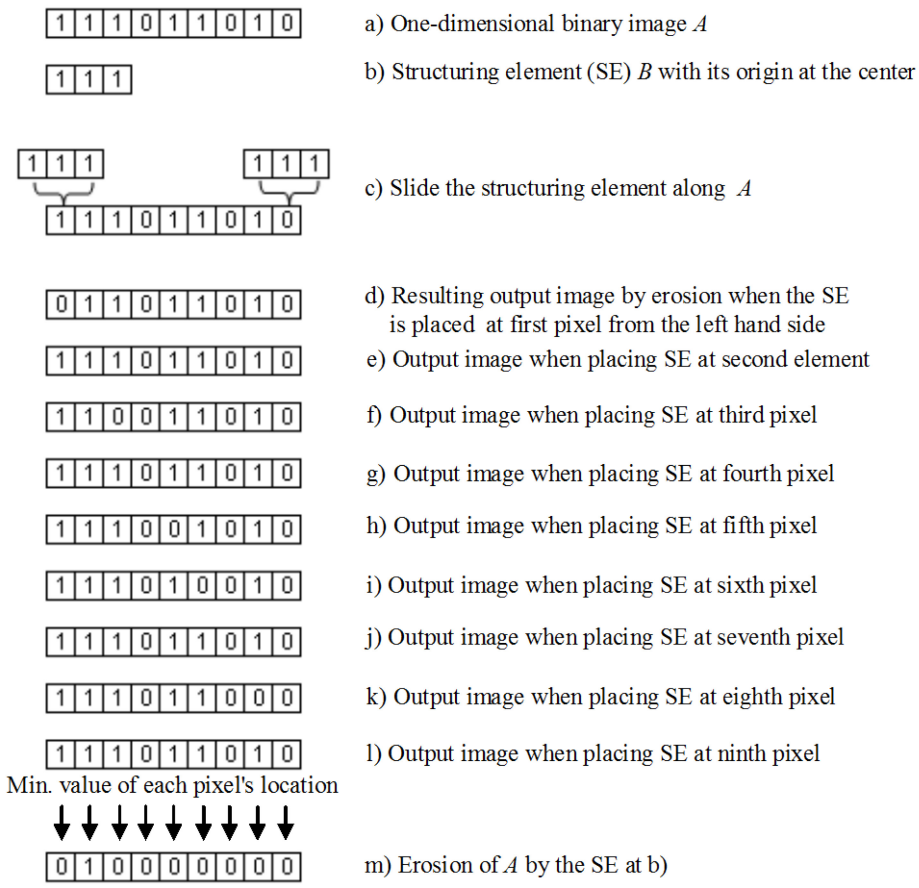

Figure 6.3 Morphological erosion on one dimensional binary image.

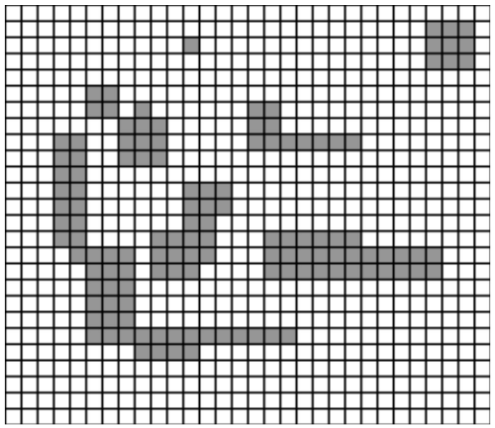

(a) A binary image and a 3 square pixels by 3 pixels structuring element at upper right corner.

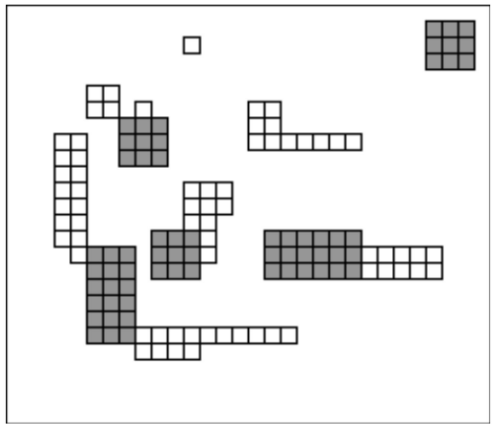

(b) The image about to be eroded. All outlined White pixels will be turn into foreground pixels.

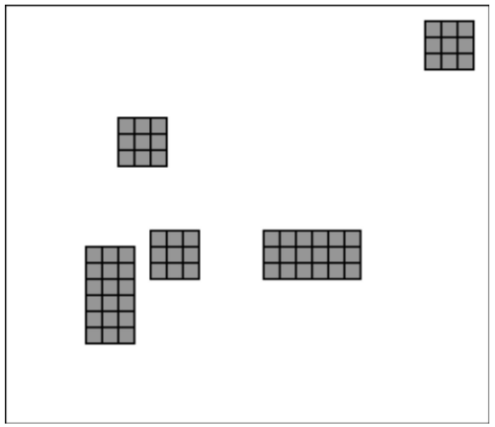

(c) The eroded image.

Figure 6.4 Graphical illustration of morphological erosion on a binary image by 3 by 3 square structuring element.

how erosion works on a one dimensional binary image. It removes any runs of '1's less than the length of the structuring element. The erosion of the binary image in Figure 6.2 is shown in Figure 6.4. As shown, the foreground is shrunk by the diameter of the structuring element and any objects smaller than or the same as the structuring element is removed by the erosion operator. So, when objects smaller than a certain size require elimination from an image, erosion can be used. While *erosion* is easier to visualize as "erasing", it should be noted that eroding the black foreground pixels is equivalent to dilating the white background pixels.

6.2.2 Dilation and Erosion of Gray Scale Image

While dilation and erosion are easier to explain and understand for binary images, the operations are essentially the same for gray scale images. *Dilation* and *erosion* of gray scale image, A, by a structuring element with gray scale value, B, is defined as:

$$A \oplus B(x,y) = \max_{(i,j)\in B}\{A(x-i,y-j)+B(i,j)\} \qquad \text{(Dilation of gray scale image)} \qquad (6.4)$$

$$A \Theta B(x,y) = \min_{(i,j)\in B}\{A(x-i,y-j)-B(i,j)\} \qquad \text{(Erosion of gray scale image)} \qquad (6.5)$$

A flat structuring element is one in which all of the element's pixels have the same gray scale value. That is, $B(i, j)$ is constant for all i and j. When a flat structuring element with $B(i,j) = 0$ is chosen, Equation 6.4 and 6.5 can be simplified to:

$$A \oplus B(x,y) = \max_{(i,j)\in B}\{A(x-i, y-j)\} = \max_{B}(A) \qquad \text{(Dilation by flat S.E.)} \qquad (6.6)$$

$$A \Theta B(x,y) = \min_{(i,j)\in B}\{A(x-i, y-j)\} = \min_{B}(A) \qquad \text{(Erosion by flat S.E.)} \qquad (6.7)$$

This means that, for dilation of gray scale images by a flat structuring element, the center of the structuring element is sequentially placed over each image pixel and each pixel is replaced by the *maximum* original gray scale value of all pixels covered by the structuring element. Conversely, for *erosion* of gray scale images, the pixel beneath the center of the structuring element takes the *minimum* original gray scale value of all the pixels covered by the structuring element. Figure 6.5 numerically illustrates the dilation and erosion operations on the same gray scale image.

It is important to note the implications of dilation and erosion of a gray scale image of a three dimensional soil particle assembly. Pixels on soil grain boundaries have low gray scale values due to lower exposure to ambient illumination and thus, can be considered as background pixels. So, erosion of a three dimensional soil image by a flat structuring element has the effect of widening soil grain boundaries while dilation makes them thinner or even make them disappear.

6.3 Morphological Opening and Closing

Dilation and *erosion* are often used sequentially on an image. If dilation is followed by erosion the operation is called *closing*. Conversely, if erosion is followed by

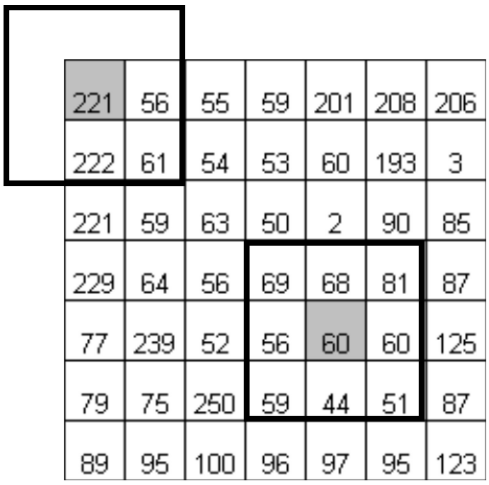

221	56	55	59	201	208	206
222	61	54	53	60	193	3
221	59	63	50	2	90	85
229	64	56	69	68	81	87
77	239	52	56	60	60	125
79	75	250	59	44	51	87
89	95	100	96	97	95	123

(a) Original image gray scale values with 3 x 3 structuring elements shown at two locations.

222	222	61	201	208	208	208
222	222	63	201	208	208	208
229	229	69	69	193	193	193
239	239	239	69	90	125	125
239	250	250	250	81	125	125
239	250	250	250	97	125	125
95	250	250	250	97	123	123

(b) Dilated image.

56	54	53	53	53	3	3
56	54	50	2	2	2	3
59	54	50	2	2	2	3
59	52	50	2	2	2	60
64	52	52	44	44	44	51
75	52	52	44	44	44	51
75	75	59	44	44	44	51

(c) Eroded image.

Figure 6.5 Numerical illustration of dilation and erosion on gray sale image at two locations by 3 by 3 flat square structuring element. (Note: 0 = black, 255 = white)

dilation the operation is termed *opening*. Equation 6.8 and Equation 6.9 represent closing and opening in terms of the two basic morphological operators.

$$A \bullet B = (A \oplus B) \Theta B \tag{6.8}$$

$$A \circ B = (A \Theta B) \oplus B \tag{6.9}$$

where A is an image and B is a structuring element. It is the opening morphological operation that will be employed in this study while *closing* needs no further discussion.

Erosion used alone removes objects and undesirable anomalies (noise) smaller than a structuring element. It also reduces the size of all objects in an image. *Opening* removes any object smaller than a structuring element like erosion does but still preserves the size of the larger remaining objects. Figure 6.6 illustrates the effect of opening on a binary image. Figure 6.6 a) shows various sizes of white roundish objects foreground and Figure 6.6 b) and c) show the morphologically *eroded* and *opened* images by the structuring element shown in a square box at the upper right.

Through the morphological opening, the number (or percentage) of objects smaller than the structuring element can be counted. By repeating the opening operation using sequentially larger structuring elements, the distribution of sizes can be developed.

Most significantly to this study, opening removes small objects from images even when they are in contact with larger ones. In Figure 6.6, several large grains are shown originally in contact with smaller grains. They appear as single "bumpy" objects. After opening, the smaller contacting grains disappear. This is because morphological opening treats the smaller round objects contacting the larger ones as distinctive objects. Thus, determination of grain size distributions from images of contacting grain assemblies becomes feasible.

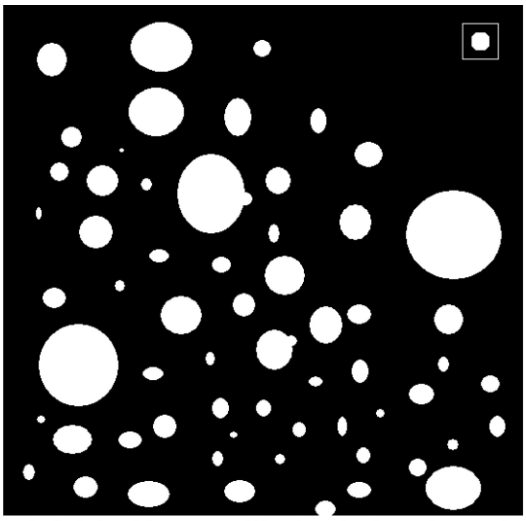

a) Original image with structuring element in upper right.

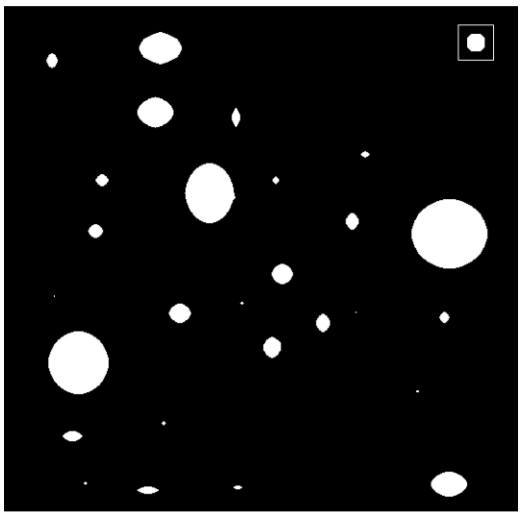

b) Eroded image.

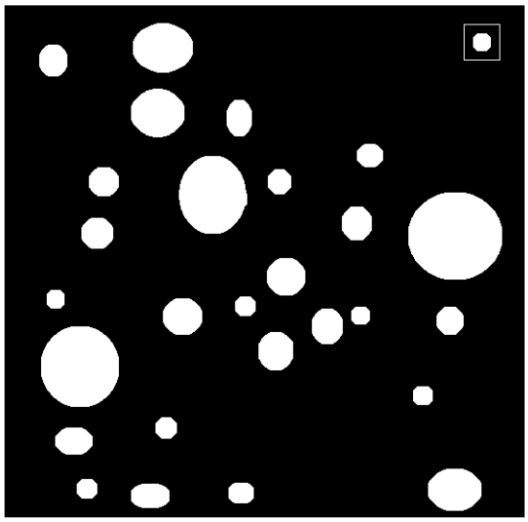

c) Opened image.

Figure 6.6 Morphological opening on a binary image.

In binary images, it should be noted that irregularly shaped particles and rough surfaced soil grains are truly "bumpy" objects. Removal of such "bumps" is not desirable as it implies that the soil is finer- grained than it really is. In gray scale images of three dimensional soil assemblies, morphological opening does not actually remove soil grains smaller than a structuring element. Instead, high gray scale valued pixels (lighter color),

which lie just inside soil grain boundaries, are replaced by the lower gray scale valued pixels (darker color) of the boundaries. This blurs the distinction between actual boundary pixels and interior pixels. The degree of this blurring depends on the size of structuring element. It results in soil grains smaller than a structuring element being faded out.

6.4 Pattern Spectrum

For simple binary images of non-contacting grains spread out on a flat surface, opening is not even needed and a histogram showing the number of grains removed versus the *structuring element size* (*SES*) used for *erosion* is effectively the grain size distribution. For gray scale images of three dimensional assemblies of soil grains, the procedure results in histograms that will require considerably greater interpretation. If individual soil grains could be identified from a three dimensional soil assembly, soil grain size distribution can easily be determined. However, as mentioned in the previous chapters, it is very difficult to develop a segmentation algorithm universally applicable to overlapping and contacting soil grains.

Matheron (1975) proposed the use of a *pattern spectrum* in which *spectral values* are plotted versus *structuring element size*. The pattern spectrum can be defined as response distribution of an image to morphological *opening* with sequentially increasing structuring element size. In this study, the *structuring element size* (*SES*) is defined as the number of pixels along the diagonal (pixel row) of a diamond structuring element. Figure

6.7 shows various sizes of diamond structuring elements used in this study. The *pattern spectral value* shown versus a structuring element of size *SES* is the summation of all pixel values in an image obtained by *opening* the original image using a structuring element of size *SES minus* the summation of all pixels in an image obtained by *opening* the original image using a structuring element of size *SES+2*. Mathematically, the *pattern spectral value* (*PSV*) at *SES* can be expressed as:

$$PSV_{SES} = \sum_{y \in whole\ image} \{(A \circ B_{SES}) - (A \circ B_{SES+2})\} \tag{6.10}$$

where the '-' sign denotes pixelwise difference. *A* is the original image and *B* is a structuring element. Since *opening* removes objects smaller than a *SES,* the *pattern spectral value* indicates the proportion of grains of size *SES* in the original image. The entire *pattern spectrum* then reflects the grain size distribution, particularly when the image is a binary image of non-contacting particles.

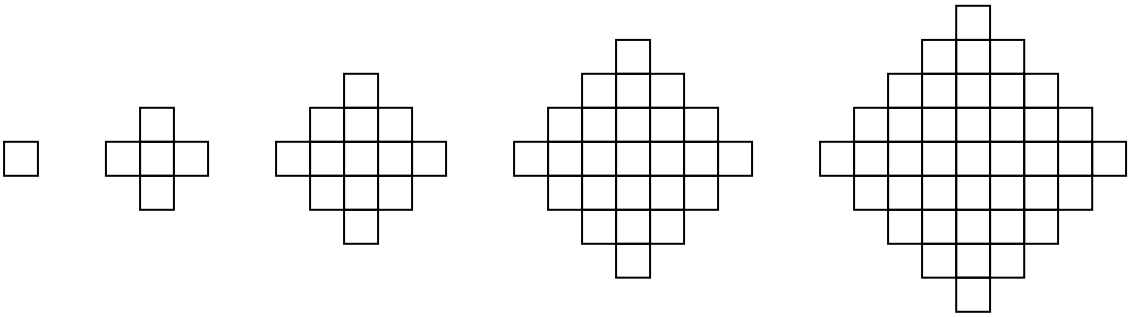

Figure 6.7 Various sizes of diamond shaped structuring element. The sizes of the structuring elements are 1, 3, 5, 7, 9 from left to right.

6.5 Determination of Uniform Soil Grain Size by Pattern Spectrum

When a binary image contains only detached objects all having exactly the same size and same shape, the pattern spectrum would display a single vertical spike at the corresponding *SES*. An example of determining the size of objects which have the same shape (square) and size is shown in Figure 6.8. In the example, a square structuring element is used to match the shape and size of the objects. Images produced by *opening* with *SES* of 7, 8, and 9 do not remove any objects because the size of the square objects in the original image is larger than the structuring elements. Opening with *SES* = 10 causes all of the squares to disappear because they are smaller than the *SES*. Nothing remains to be removed by *SES* = 11 and 12. Images used for computing *PSV* at *SES* of 8, 9, and 10 are shown in Figure 6.8 h) to j) which were obtained by having pixelwise difference between Figure 6.8 c) and d), between Figure 6.8 d) and e), and between Figure 6.8 e) and f), respectively. Only the image used for computing *PSV* at *SES* = 9 shows a response. Therefore, the size of squares in the original image is 9 pixel by 9 pixel.

Unlike such ideal binary images, an image of three dimensional soil assemblies of uniform grains would display some spread in the pattern spectrum, possibly with a peak at *SES* corresponding to the *PPD*. That is because real soils, even if they are "uniform", contain soil grains of various shapes and some size variations. Furthermore, real soil images are not binary, but gray scale. Depending on the mineral composition, the grains themselves can be similar in gray scale or exhibit vastly different gray scales. Lastly,

since the assemblies are three-dimensional, many grains will be hidden behind foreground grains and will thus appear to be smaller than they really are.

Figure 6.9 a) shows a very uniform soil consisting of grains passing the No.18 standard US sieve but retained on a No. 20 sieve. The average opening of these two sieves is 0.925 mm. The image was taken at a camera magnification of 12.8 pixel/mm. The *PPD* is thus computed to be 11.6 pixels. The image was *opened* using a diamond structuring element with *SES* ranging from 1 pixel to 59 pixel. The resulting pattern spectrum is shown in Figure 6.9 b). The *pattern spectral value* peaks at *SES* of 13 showing fairly good agreement with the *PPD*. This suggests that the *SES* corresponding to the peak of the pattern spectrum is an indicator of soil grain size provided that the particles are uniform in size.

Additional images were taken of the same soil at various magnifications corresponding to *PPD* values from 9.9 to 30.5. Figure 6.10 shows the corresponding pattern spectrum with one new twist. Plotted on the ordinate is a *normalized pattern spectral value* defined as the *pattern spectrum value* normalized by the sum of all pattern spectral values. For *PPD* below about 20, the *SES* values corresponding to the peak normalized spectral values match well with *PPD*. However, for *PPD* above about 20 there are noticeable differences between the *SES* at peak and *PPD*. This divergence with increasing *SES* is easily explainable. When magnification, *PPD*, and *SES* are all low, the difference between a diamond structuring element and the soil grains in terms of pixels is low. As the magnification, *PPD*, and *SES* increase, the difference in the number of pixels between a diamond structuring element and more rounded soil grains increases. The diamond structuring element is almost always smaller than a soil grain having the same

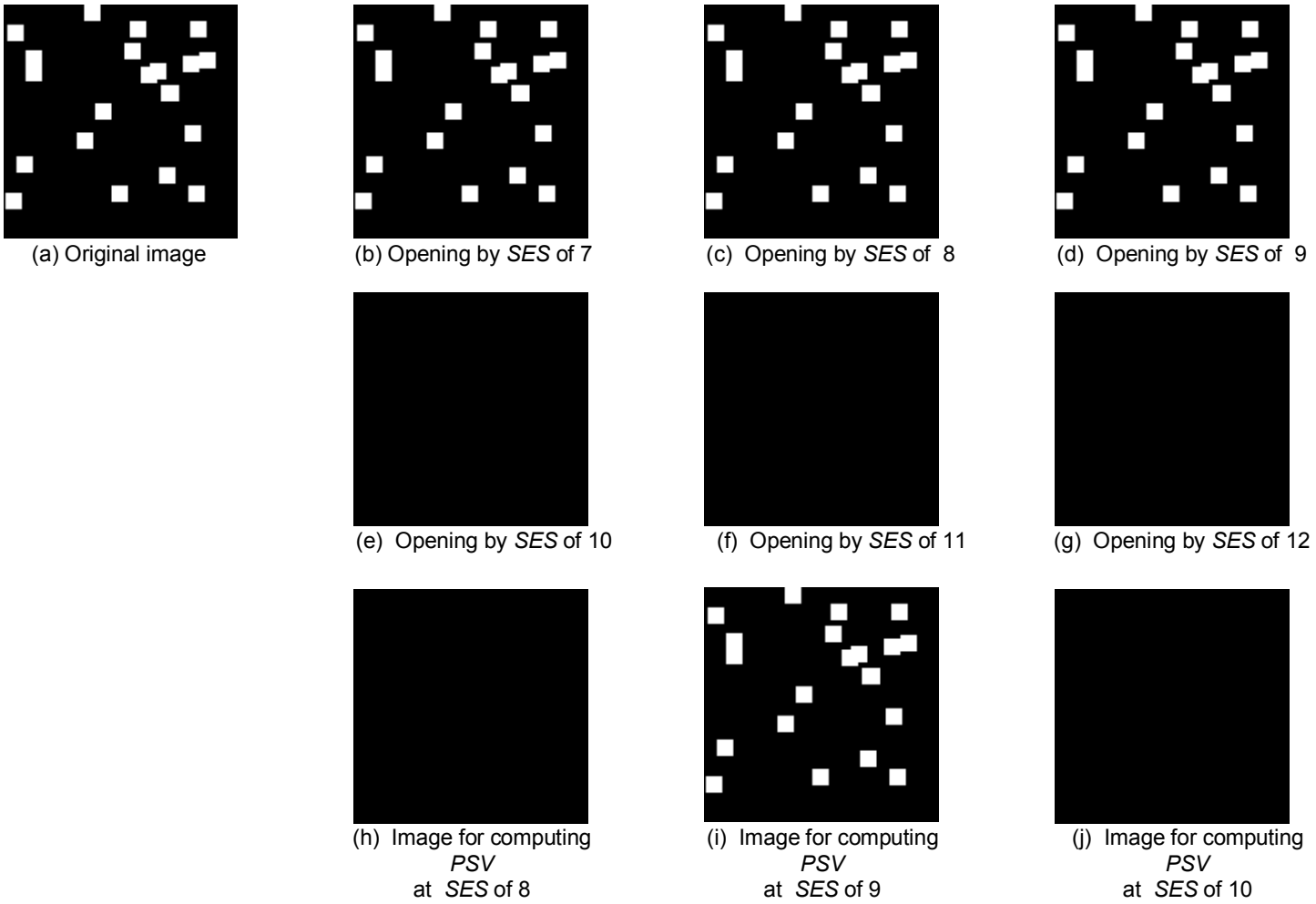

Figure 6.8 Determination of size of object having same shape and size by opening operation with sequentially increasing structuring elements.

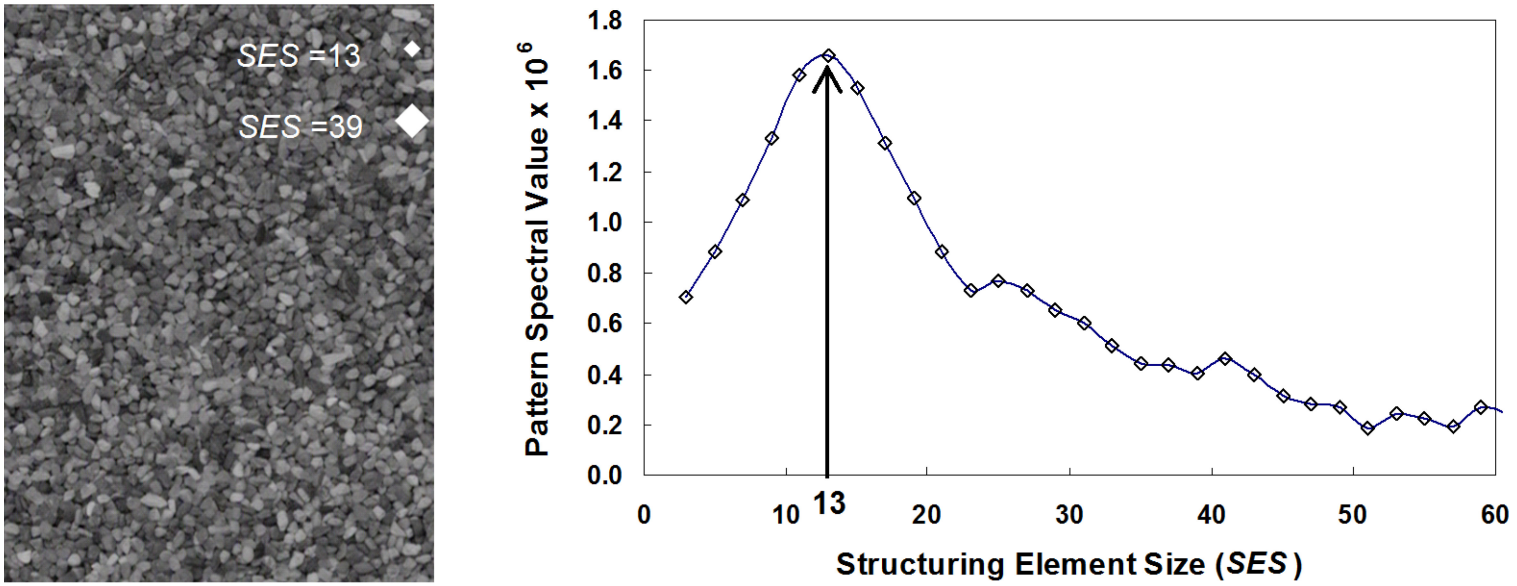

a) b)

Figure 6.9 a) Image of the No.18-No.20 sand, average sieve opening = 0.925 mm, magnification = 12.5 pixel/mm, *PPD* = 11.6
b) Corresponding pattern response spectra.

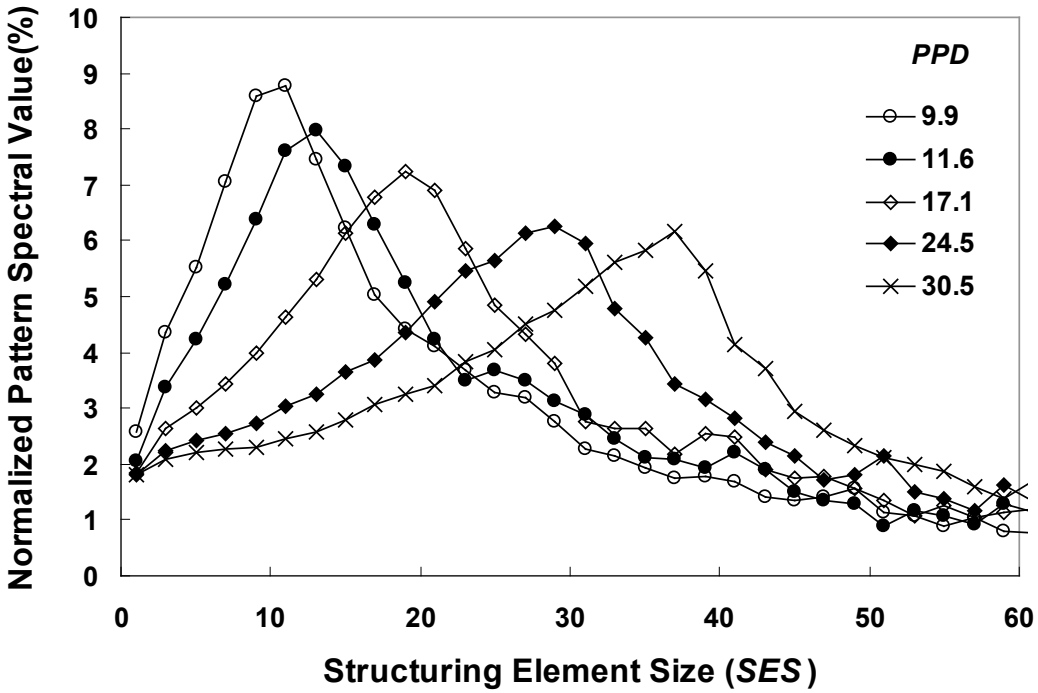

Figure 6.10 Normalized pattern spectrum for various *PPD*.

diameter. As such, the *SES* corresponding to the peak of the pattern spectrum will be larger than the *PPD*.

6.6 Soil Grain Size Calibration Chart by Pattern Spectrum

As just discussed, due to the inherent difference in shape between real soil grains and diamond structuring elements, the *SES* at peak of the *normalized pattern spectrum* can not be used as a direct indication of *PPD*. So, a relationship between the *SES* at peak

and *PPD* needs to be established so that the *SES* at peak can be converted into actual soil grain size and thus, can be implemented for *Sedimaging*.

Figure 6.11 shows the soil grain size calibration chart, *SES* at *Peak* (*SP*) versus *PPD* with a dot line representing when *SP* is equal to *PPD*. Only red image layer was used to obtain *SP*. Each data points in Figure 6.11 is the average of 10 *SP* of 10 images having same *PPD* and vertical bar represents one standard deviation in data spread. The size of each image is 480 pixel by 644 pixel.

The difference in size between the smallest and largest soil grains in a "uniform" soil becomes more pronounced as a magnification (*PPD*) increases. This is partly contributed to the large statistical spread at high *PPD*. However, a major reason for the large spread is that, with a fixed size of images, the number of soil grains in each image decreases with increasing *PPD*. Therefore, when bigger images are used for computing *PSV*, the statistical spread of *SES* at *Peak* will be reduced.

Finally by performing a linear regression analysis on all the data points in *SES* at the *Peak* (*SP*) versus *PPD* calibration chart, a unique relationship between *SP* and *PPD* was revealed as:

$$PPD = 0.916SP - 0.598 \tag{6.11}$$

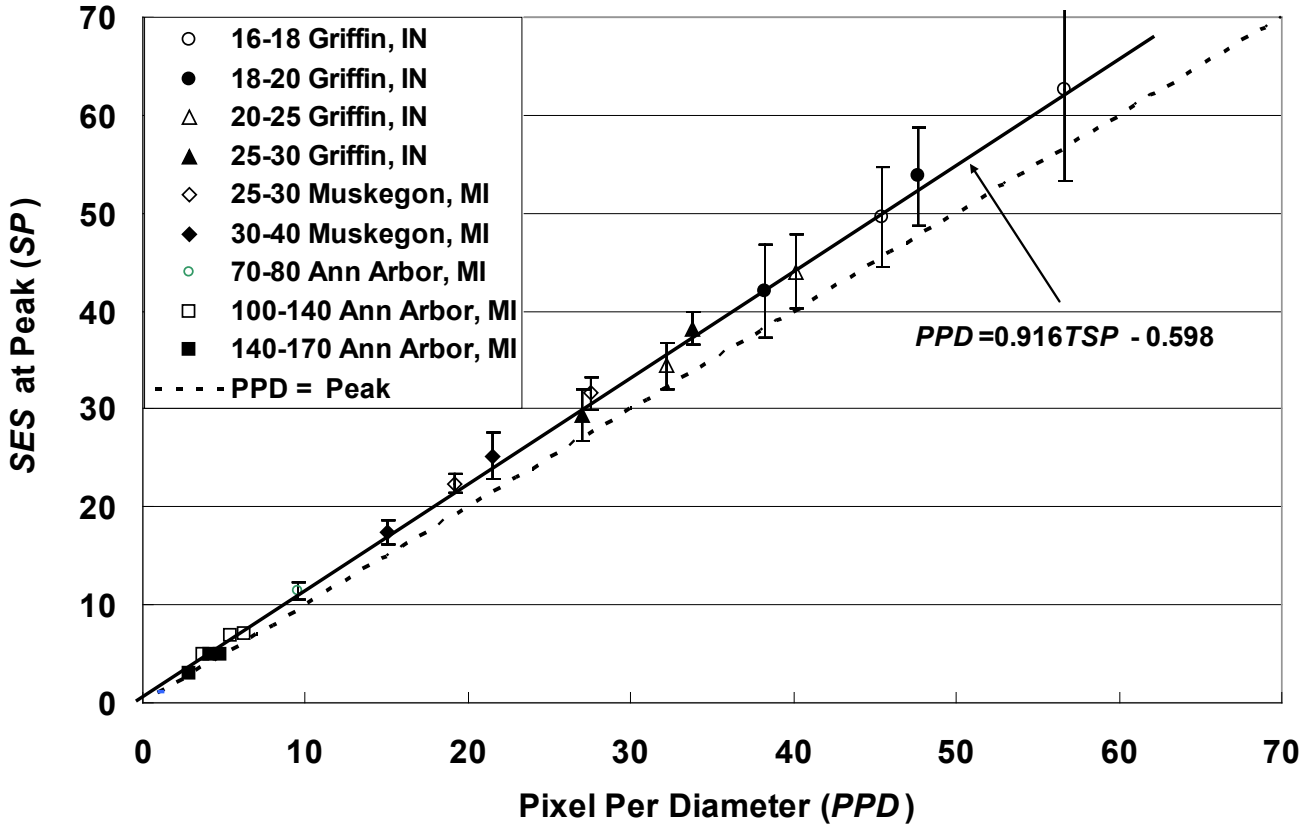

Figure 6.11 Soil grain size calibration, *SES* at Peak (*SP*) versus *PPD*.

6.7 Conclusions

An image processing method based on mathematical morphology was developed to determine the average size from images of three dimensional soil assemblies of uniform grains. The method takes a statistical approach by calculating the *pattern spectrum* of digital soil images as opposed to other image processing methods which seek geometric features of soil deterministically using mathematical morphology. The statistical aspect of the soil grain size determination method eliminates the necessity of preprocessing, such as image binarization and segmentation of individual soil grains whose result is greatly influenced by the operator skills.

Structuring element size (*SES*) corresponding to the peak of *pattern spectrum* of a soil image was expected to be soil grain size. However, due to the fact that the inherent difference in shape and size between real soil grains and diamond shaped structuring elements increases with *PPD*, noticeable differences between *SES* at peak and *PPD* were observed at high *PPD*. So, the soil grain size calibration chart, *SES* at Peak versus *PPD*, was established to determine the average size from images of three dimensional soil assemblies of uniform soil grains. *SES* at Peak obtained from *pattern spectrum* of a soil image is converted into *PPD* through the calibration chart. With known magnification level, actual soil grain size can be found.

CHAPTER VII

Image Edge Pixel Density Model for Soil Grain Size

7.1 Introduction

Soil grain size analyses methods such as Haralick's 14 textural indices, wavelet decomposition (Shin and Hryciw, 2004), and mathematical morphology that use image textures for assessing grain size generally do not recognize the significant effect of intragranular textures on test results. Such internal differences in gray scales arise from natural color variations and non uniform light reflections from rough surfaces. For image processing to provide a reliable index of grain size, the information must come from the particle boundaries and not from textural variations within the soil grains. The clarity of such internal texture in an image increases with the size of particles relative to the image pixel size. In other words, the higher the magnification or the larger the grains, the more likely the image is to reveal the internal surface features. With significant internal textures, a single relatively large grain will often be interpreted as several smaller grains. Thus, the overall particle sizes in the image are underpredicted. The results of wavelet decomposition and mathematical morphology, which were discussed in Chapter V and VI respectively, are naturally and undesirably affected by internal textures.

In this chapter, one of the most fundamental image processing techniques, *edge detection*, is utilized on images of contacting uniform-sized soil grains to delineate soil grain boundaries. Most importantly, undesirable internal edges are removed from soil edge maps using two methods, one based on the number of connecting pixels of each edge segments, the other based on elliptical fitting to edge segments. The result will be a more dependable and easily understandable index of soil grain size. A theoretical two-dimensional model, validated by images of perfectly uniform spheres is compared to results from images of real soil grain assemblies to rationalize the proposed index and its relation to grain size.

7.2 Selection of Edge Detector for Soils

An "edge" in a digital image could be thought of as a contour across which the brightness (gray scale value) changes abruptly in magnitude (first derivative) or in the rate of change of magnitude (second derivative). Edges are important features since they provide crucial clues to discriminate regions within or between objects.

The boundaries of non-contacting soil grains are easily delineated because of the generally large difference in gray scale pixel values between soil grains and the background. By contrast, in assemblies of contacting grains, the change in gray scale values around grain boundaries is less distinct and thus, the edges are not always as easily detectable. Some edge detectors are better suited than others for delineating boundaries of soil particles in assemblies. Therefore, selection of the best edge detector for soils is the first task. The clarity, or strength, of soil boundaries varies within an image. Some

boundaries are "*strong"*, others are "*weak"*. Strong and weak edges will be defined and explained shortly. The best edge detector would be one that detects both the strong and weak soil grain boundaries.

Many edge detectors have been developed for image processing but their functionalities and performances are not the same. Sharifi, et al. (2002) indicate that the four most commonly used detectors are: the Sobel (I. Sobel, unpublished but regularly cited in image processing literature); the Roberts (1965); the Zero Cross (Marr, 1982); and the Canny (1986). The first two are categorized as "gradient edge detectors" which search for maximums and minimums in the first derivative pixel grayscale in an image. Zero-cross and Canny are classified as Laplacian and Gaussian edge detectors, respectively. The former searches zero crossings in the second derivative of an image and the latter uses the derivative of a Gaussian to find edge strength by taking the gradient of an image. Figure 7.1 shows an image of a multi-sized grain assembly and the corresponding edge maps using the four detectors. The Sobel, Zero Cross and Roberts detectors are clearly less effective than the Canny at delineating soil grain boundaries. The reason why the three are less effective is that they do not detect weak soil grain boundaries. The edge map created by the Zero Cross method detects strong boundaries well but not the weak boundaries while the Sobel and Roberts edge maps miss not only weak boundaries but also many strong ones. By contrast, the Canny edge detector is superior at boundary identification because it finds all of the strong and some of the weak edges. Therefore, the present work will focus on and utilize only the Canny method, but

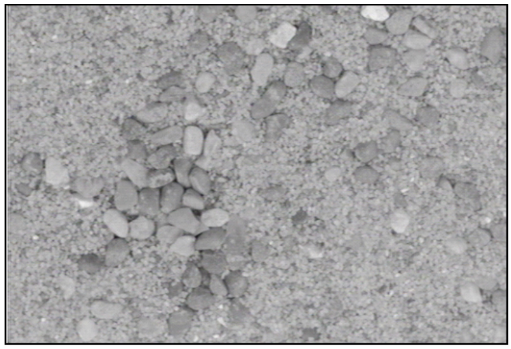

Original image

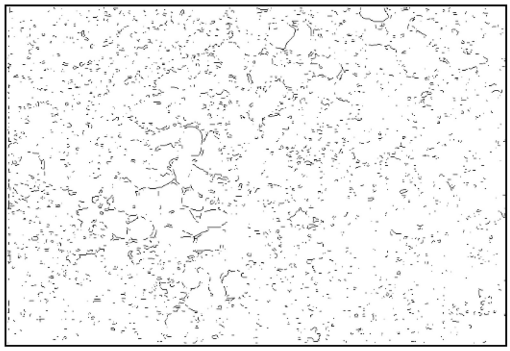

Sobel method

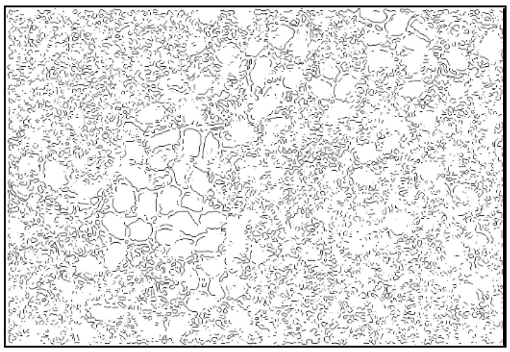

Zero-crossing method

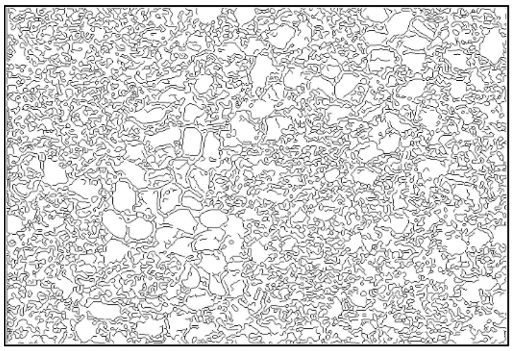

Canny method

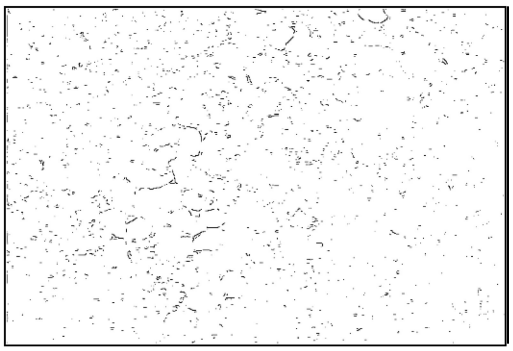

Roberts method

Figure 7.1 Edge maps using four different edge detectors.

with unique modifications that will prove to be particularly useful for the determination of size of three-dimensional assembly of uniform sized soil grains.

7.3 Canny Edge Detector

The first step in Canny edge detection is filtering to remove pixel-sized digital noise. Such noise typically arises from stray electricity, damaged imager pixels or during digitization of an analog camera signal. However, in this study, noise filtering was not used for two reasons. First, it was found that filtering blurs the images and removes parts of good soil edges especially when *PPD* is small. Secondly, an algorithm will later be employed on edge maps that removes likely "false" particle edges, including those created by pixel-sized noise.

The next step in Canny edge detection is computation of image gray scale gradients. This is done by convoluting the image using 9 by 9 Gaussian kernels in the pixel row (x) and pixel column (y) directions. The kernels shown in Figure 7.2 were found to be most effective for finding soil grain edges. The convolutions result in two gradient matrices, F_x and F_y. From F_x and F_y a single composite *edge strength matrix*, $F(x, y)$, is obtained as:

$$F(x,y) = \sqrt{F_x^{\,2} + F_y^{\,2}} \tag{7.1}$$

Also computed is the *maximum gradient direction* (normal to the edge) *matrix*, $\theta(x, y)$:

$$\theta(x, y) = \arctan\left(F_y / F_x\right) \tag{7.2}$$

Once $F(x, y)$ and $\theta(x, y)$ are computed, *nonmaxima suppression* is applied to $F(x, y)$. This procedure eliminates many pixel locations from consideration as edge pixels. The unique feature of the Canny edge detection algorithm is that the nonmaxima suppression is only performed in the maximum gradient direction as follows. At each edge strength matrix location, the maximum gradient direction is rounded to one of four image matrix directions (row-horizontal column-vertical or one of the two diagonals) and nonmaxima suppression is performed in this direction only. An example of nonmaxima suppression is shown in Figure 7.3. As indicated, a pixel retains its original pixel value in $F(x, y)$ only if it has the largest edge strength of the three successive pixels along the maximum gradient direction. Otherwise, its edge strength is set to zero. Performance of this operation over the entire edge strength matrix results in a thinning of the edges to only one pixel width. The new matrix is called the *nonmaxima suppressed edge strength matrix*.

The next step, also unique to Canny, is called *hysteresis*. Here, two edge strength thresholds, *high* and *low*, are applied to the nonmaxima-suppressed edge strength matrix. The two thresholds used in this study were 0.08 and 0.15 when the largest value in the edge strength matrix is scaled to 1.00. For example, if the largest edge strength is 100, edge strength of 5 is scaled to 0.05. If the value of an entry in the non-maxima suppressed edge strength matrix is larger than the high threshold, the pixels are considered *strong*

0	0	0	0	0	0	0	0	0
0	0	0.001	0.002	0	-0.002	-0.001	0	0
0	0.001	0.012	0.026	0	-0.026	-0.012	-0.001	0
0	0.006	0.052	0.117	0	-0.117	-0.052	-0.006	0
0	0.011	0.086	0.193	0	-0.193	-0.086	-0.011	0
0	0.006	0.052	0.117	0	-0.117	-0.052	0.006	0
0	0.001	0.012	0.026	0	-0.026	-0.012	-0.001	0
0	0	0.001	0.002	0	-0.002	-0.001	0	0
0	0	0	0	0	0	0	0	0

(a)

0	0	0	0	0	0	0	0	0
0	0	0.001	0.006	0.010	0.006	0.001	0	0
0	0.001	0.012	0.052	0.086	0.052	0.012	0.001	0
0	0.002	0.026	0.117	0.193	0.117	0.026	0.002	0
0	0	0	0	0	0	0	0	0
0	-0.002	-0.026	-0.117	-0.193	-0.117	-0.026	-0.002	0
0	-0.001	-0.012	-0.052	-0.086	-0.052	-0.012	-0.001	0
0	0	-0.001	-0.006	-0.010	-0.006	-0.001	0	0
0	0	0	0	0	0	0	0	0

(b)

Figure 7.2 Gaussian kernel used to compute the edge strength matrices: a) F_x in the horizontal direction; b) F_y in the vertical direction.

edges and automatically qualify as edge pixels. Entries below the low threshold are weak and are eliminated from further consideration. Entries between the two thresholds are also considered weak however, if such a weak pixel, or a chain of weak pixels, is attached to a pixel in a strong edge, the weak pixels become part of the strong edge. Weak edges not attached to strong edges are discarded. The recognition and attachment of weak edges to connected strong edges prevents many of the discontinuities in grain boundaries that are common in the Sobel, Roberts, and Zero-cross methods. At the same time, elimination of non-contacting weak edges discards many spurious edges attributed to noise of internal texture.

One final step will be added to the image processing to further eliminate additional spurious false edges and improve the resolution of the Edge Pixel Density technique for grain size assessment. The step is to remove all edges that are shorter than

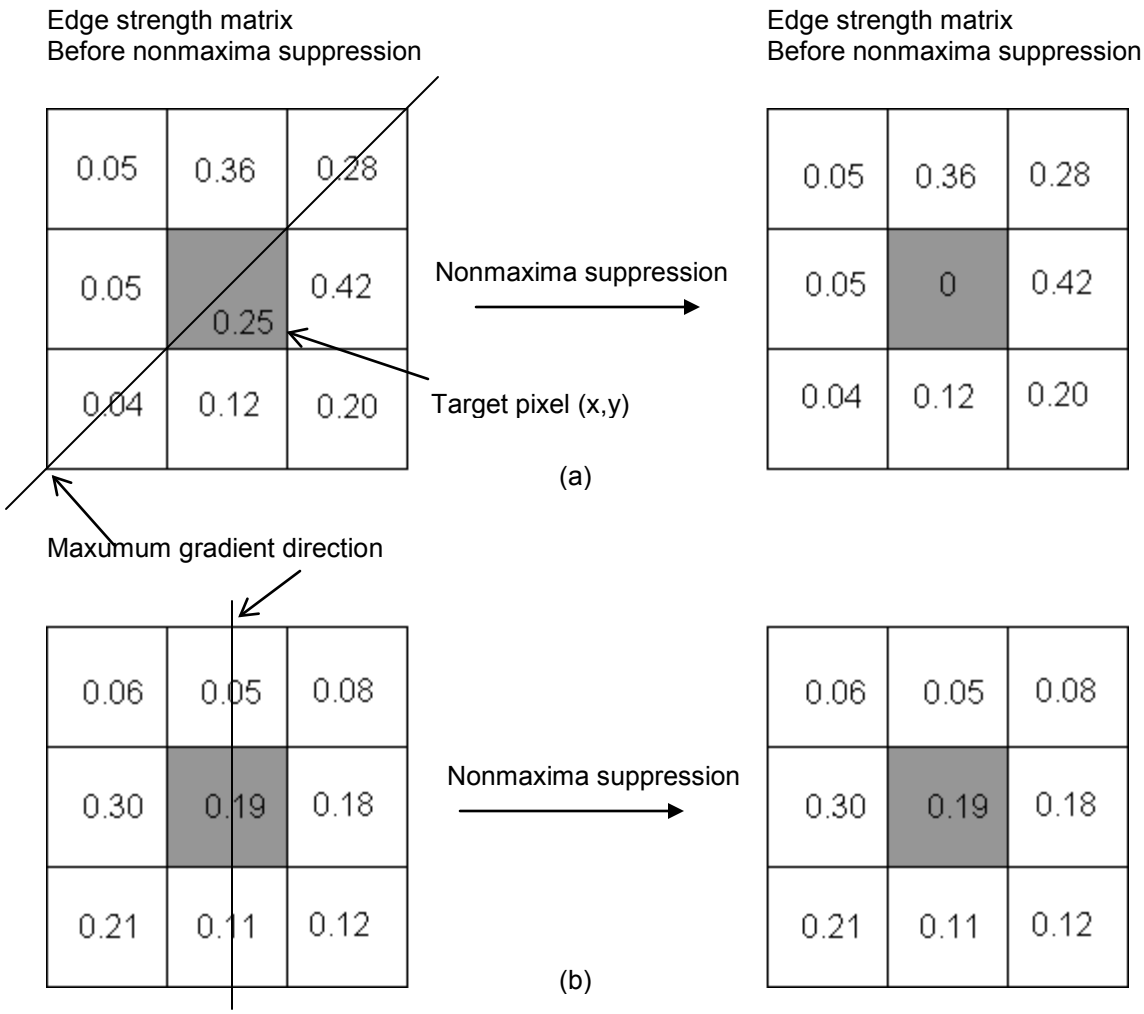

Figure 7.3 Description of nonmaxima suppression: a) suppressed target pixel; b) not suppressed target pixel.

the grain diameter and will be called *false edge removal*. Since false edge removal is a modification beyond the Canny algorithm; because it is uniquely suited to soil grain size determination; and because it requires a first estimate of grain size based on the unmodified Canny procedure, experimental and theoretical results will first be presented before implementation of the modification.

7.4 Edge Pixel Density (*EPD*)

Because most soil grains are roundish with few concave outward edges, the perimeter as measured by the number of edge pixels should be a good indicator of the nominal grain size diameter. It should be noted that consideration of the number of edge pixels as a soil grain size indicator comes from the premise that the thickness of an edge is always one pixel. This premise is achieved by one of the unique characteristics of the Canny edge detector, nonmaxima suppression.

In a three-dimensional assembly of uniform size soil grains, many edges will be hidden, yet it is expected that on a statistical basis, the number of edge pixels per unit area in an image should reflect the size of the grains in the assembly. Therefore, the *edge pixel density* (*EPD*), defined by Hryciw et al. (1998) as the ratio of edge pixels to total pixels in an image could be used as an index of *PPD*. Figure 7.4 shows images of uniform soil assemblies at three different *PPD*: 9.5, 21.5 and 45.0. Also shown are the corresponding edge maps by the Canny edge detector. A decrease in the number of edge pixels with increasing *PPD* is visually obvious, even before computing the *EPD*.

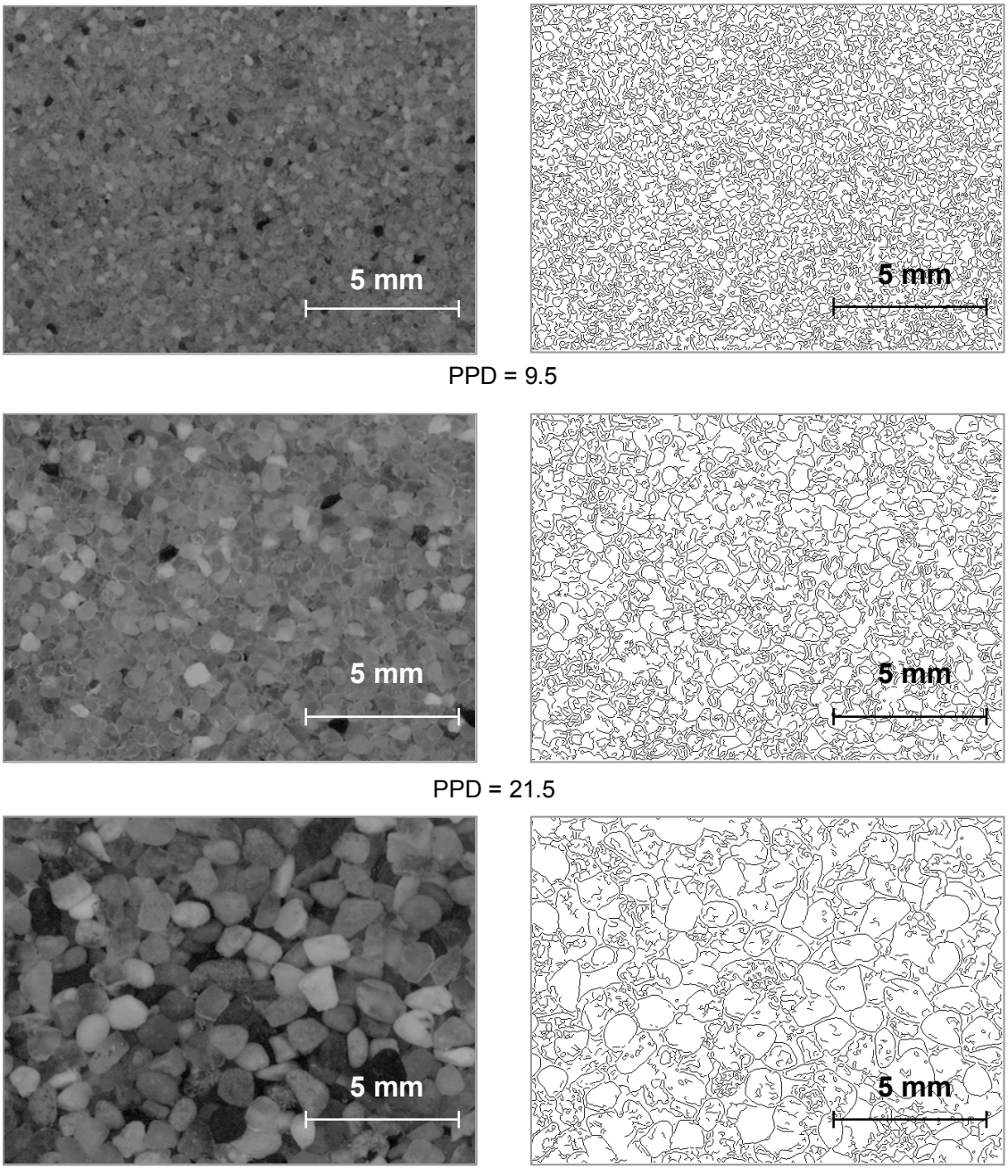

Figure 7.4 Soil images and corresponding Canny edge maps for several *PPD*.

To establish a universal correlation between *EPD* and *PPD*, common sands were collected from three sites: a sand quarry in Griffin, Indiana; Muskegon, MI dune sand; and a glacial deposit in Ann Arbor, MI. All three sands were sorted by size using standard US sieves. The soil grain size was defined as the average of the openings of the two successive sieves that had passed and retained the soil particles respectively. Using a CCD camera (Pulnix TM-7CN) with variable lens magnifications, images of each soil at *PPD* ranging from 3 to 57 were collected. All images were 558 pixel by 380 pixel in size. The *PPD* was then computed from the average grain size while the camera magnification was known from a high precision photo scale card. The images collected under various *PPD* were processed by the Canny edge detector and their *EPD* was computed.

The *EPD* versus *PPD* results are shown in Figure 7.5. Each data point represents the average *EPD* of 10 red layer images of the same soil at the same magnification. Standard deviation bars show the scatter of *EPD* values. However, it should be noted that the standard deviation is somewhat meaningless. It merely shows the statistical limitation of using 558 pixel by 380 pixel images. If all ten images had been fused into one, or a higher resolution camera was used, there would be no error bars and the mean values would be the same.

As expected, *EPD* decreases with increasing *PPD*. At high *PPD*, the correlation approaches a horizontal line and thus, the ability of the experimentally determined *EPD* to resolve the soil *PPD* (and therefore grain size) appears to decrease. However, it should be noted that the same change in *PPD* at high *PPD* values represents a smaller percentage change in grain size than the same change in *PPD* at low *PPD* values. Thus, the apparent decreasing resolution (slope of *EPD* versus *PPD* line) with increasing *PPD*

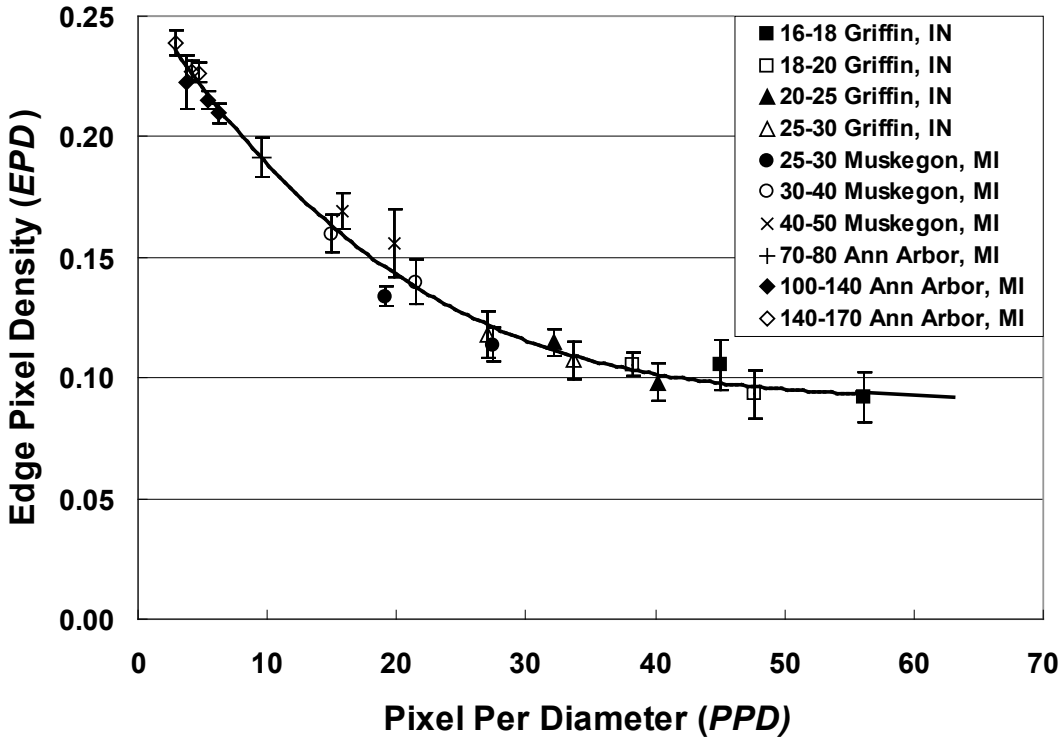

Figure 7.5 The relationship between EPD and PPD prior to false internal edge removal.

is logical and not problematic. It can also be shown that a logarithmic *PPD* scale would result in a nearly straight-line relationship. However, this trend is not shown since an even better model will be presented later.

7.5 Edge Pixel Density (*EPD*) Model

A rational explanation for the *EPD* versus *PPD* behavior, based on the abilities and nuances of the Canny Edge Detector was sought. The successful model would need to recognize that edge detection would fail at particle contacts. This would occur

particularly when the contacting particles have similar gray scale values. The model development consisted of a theoretical pixel level analysis of particle contacts at select *PPD* values and experimental imaging of perfect spheres at ideal packing geometry.

To develop the theoretical component of the *EPD* model, soil grains were simulated by perfect circles drawn on grid paper with the grid squares representing image pixels. The densest two-dimensional packing was assumed in which each circle had six contacts with six other circles at 60 degree intervals. *PPD* values of 8, 16, 32 and 64 were analyzed. Figure 7.6 shows some of the results. The dark grid squares represent the pixels that contain particle boundaries that are not in contact with other particles. In other words, these are the pixels that are expected to show the highest gray scale gradients and thus be identified as edges by the Canny edge detector. It should also be noted that because of non-maxima suppression, Canny edges will only be one pixel wide. Each edge pixel may only have one of its four sides bordering another edge pixel, the only exception being when edges intersect orthogonally. This necessitated some judgment in choosing which pixels to call "edge pixels" and which not. One can see in Figure 7.6 a) that in some cases alternate pixels could have been considered as the edge pixels. However, the overall number of edge pixels would not have changed significantly.

For an image repeat unit, identified by the rectangular boxes in Figure 7.6, the ratio of the number of black (edge) grid squares to the total number of grid squares was computed. This was the theoretical *EPD*. The theoretical *EPD* for *PPD* = 8, 16, 32 and 64 are shown by the solid points in Figure 7.7. Only four *PPD* were considered because it was difficult to compute the theoretical *EPD* for other *PPD* values. However, the four values bracketed the range of *PPD* values used for soil grain size determination. An

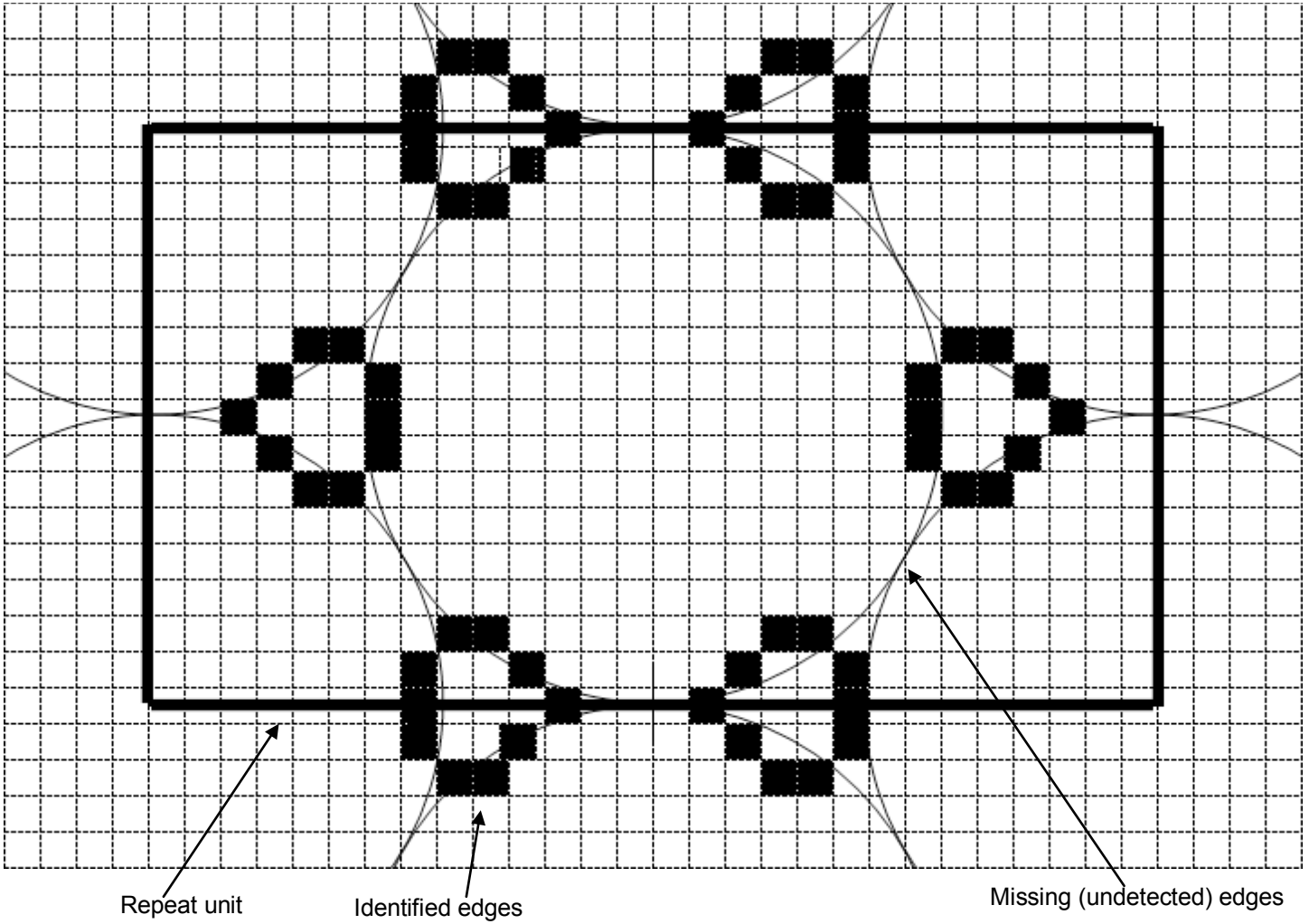

Figure 7.6.a) Theoretical *EPD* for *PPD* = 16.

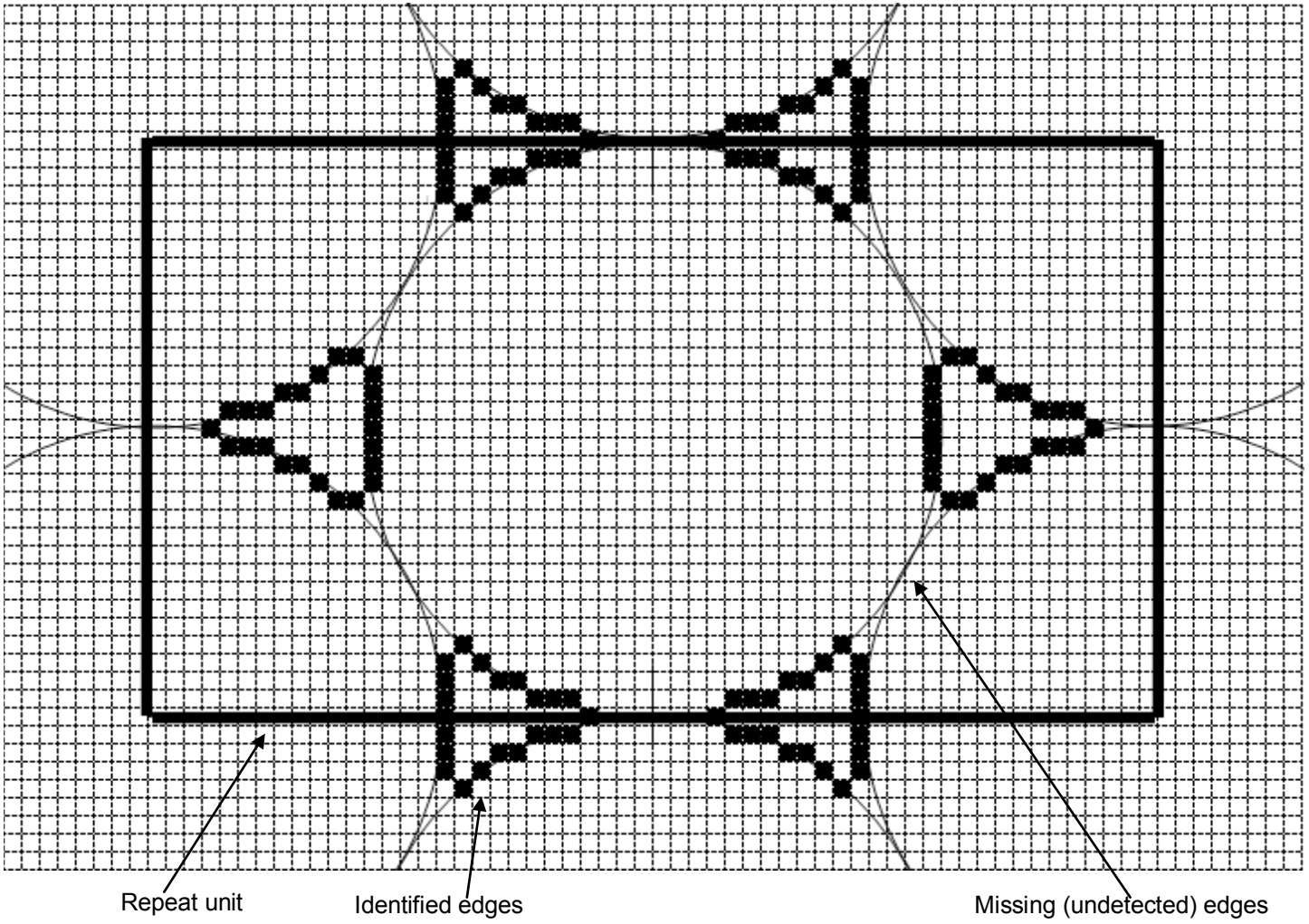

Figure 7.6.b) Theoretical *EPD* for *PPD* = 32.

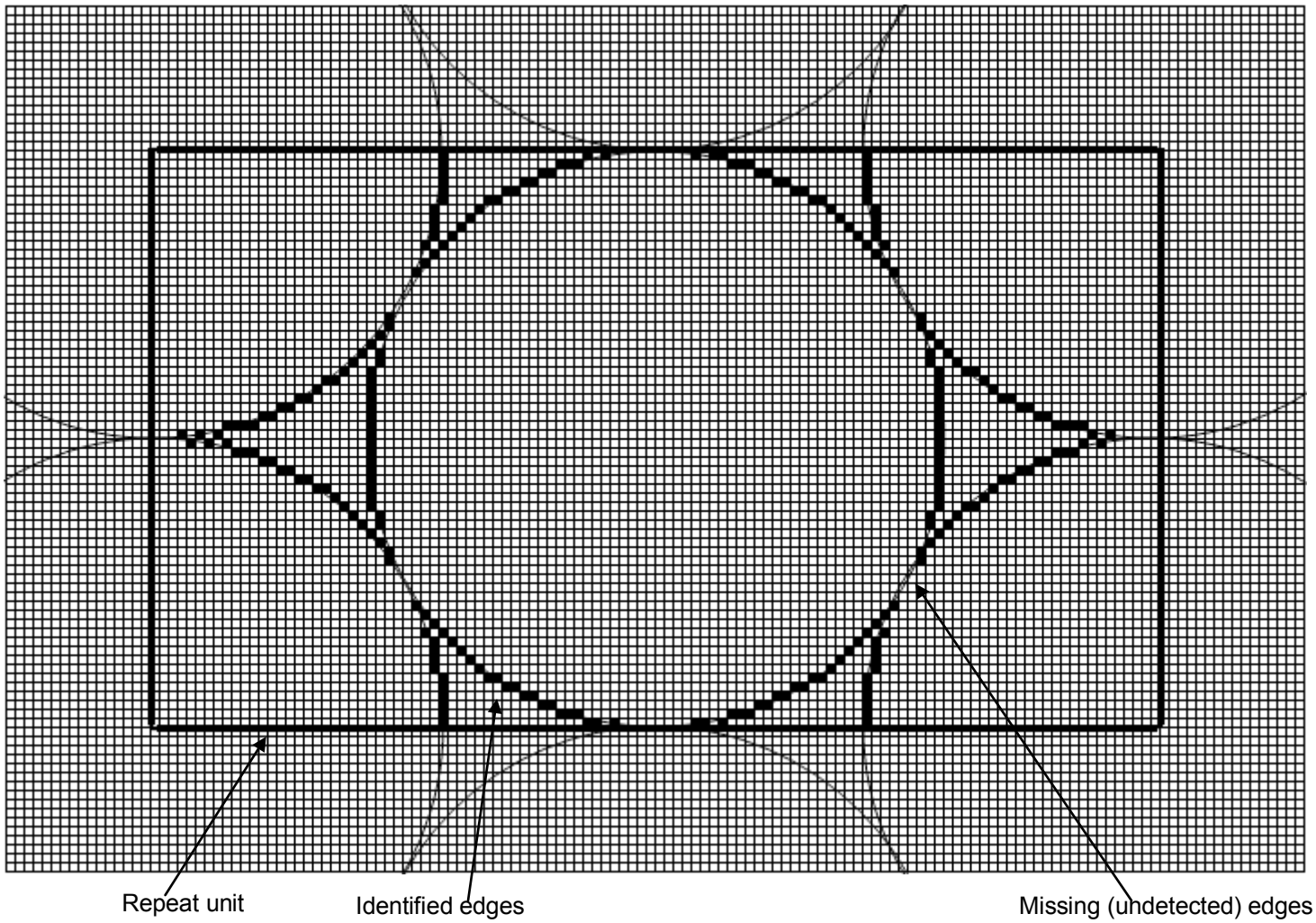

Figure 7.6.c) Theoretical *EPD* for *PPD* = 64.

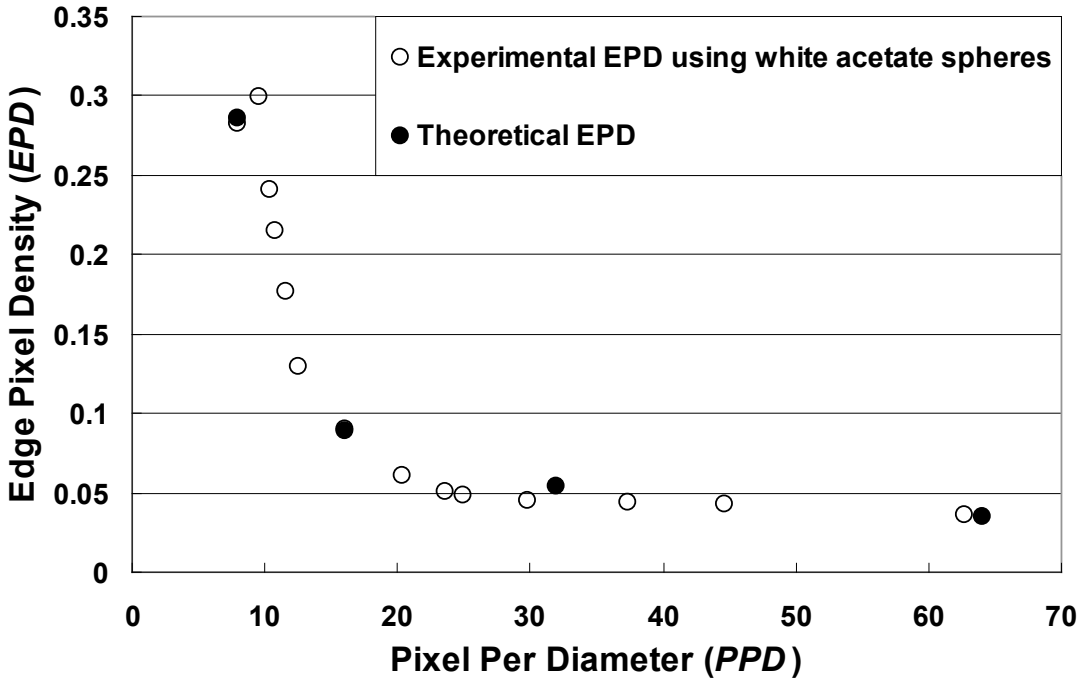

Figure 7.7 *EPD* versus *PPD* model for ideal 2-dimensional assembly of uniform circles.

analysis of *PPD* = 4 was attempted by the same approach but the exercise was too difficult and too subjective to be useful.

To verify the theoretical two-dimensional model just described, non-reflective opaque white acetate spheres of diameter 1.50 mm were arranged at their densest two-dimensional packing and photographed at various magnifications, i.e. at various *PPD*. Figure 7.8 shows the photos of the densely packed white acetate spheres at *PPD* = 29.8 and 62.7 along with their corresponding Canny edge maps. As expected, particle contacts resulted in missing edges, particularly at the lower *PPD*. It should be noted that although the particles were very uniform in size, no lateral confinement could be applied to the two-dimensional assembly, and thus some of the particles were not in contact. This

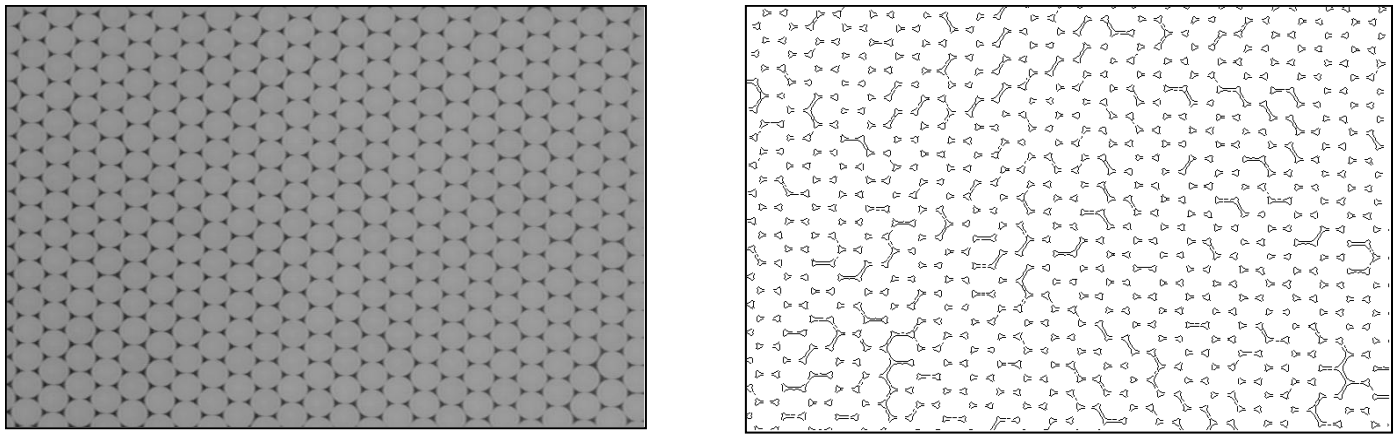

Figure 7.8 Image of white acetate spheres used for developing *EPD* model (left) with their edge maps (right).

resulted in separate completed edges for both particles at such points. The *EPD* values for the acetate spheres are shown by the open points in Figure 7.7 for comparison to the theoretical model. Excellent agreement was observed and thus, the experimental *EPD* data completes the model for *PPD* values other than 8, 16, 32 and 64.

A comparison of the two dimensional *EPD* model with the previously shown *EPD* for real three-dimensional soil assemblies is shown in Figure 7.9. When *PPD* is greater than about 12 the model under-predicts the *EPD* while for *PPD* below 12 the model over-predicts *EPD*. Both observed differences are explainable. At high *PPD*, meaning large soil grains and/or high magnification, the images capture significant gray scale variations (texture) within the particle as previously discussed. The texture produces false internal edges resulting in an increased *EPD*. By contrast, the uniform-colored, non-reflecting acetate spheres produce no false internal edges, and thus exhibit a lower *EPD*. At low *PPD*, meaning, small soil grains and/or low magnification, while the actual *EPD* of real soil is higher than at high *PPD*, it is lower than the two dimensional model predictions. In the two dimensional model, the theory assumed, and the acetate spheres confirmed, a measurable gray scale contrast between the particles and the background seen through the voids. In real three dimensional soil assemblies, no such large contrasting background exists because there are other particles in the background. These real background particles, as well as other neighboring particles, often exhibit similar grayscales to the foreground grains. Thus, at low *PPD*, many edges between similar gray-scaled particles go undetected because the contrasting "edge" is too thin relative to the pixel size to create a perceptible gray scale gradient. The result is that at low *PPD*, the *EPD* of real soils is smaller than the *EPD* of the model.

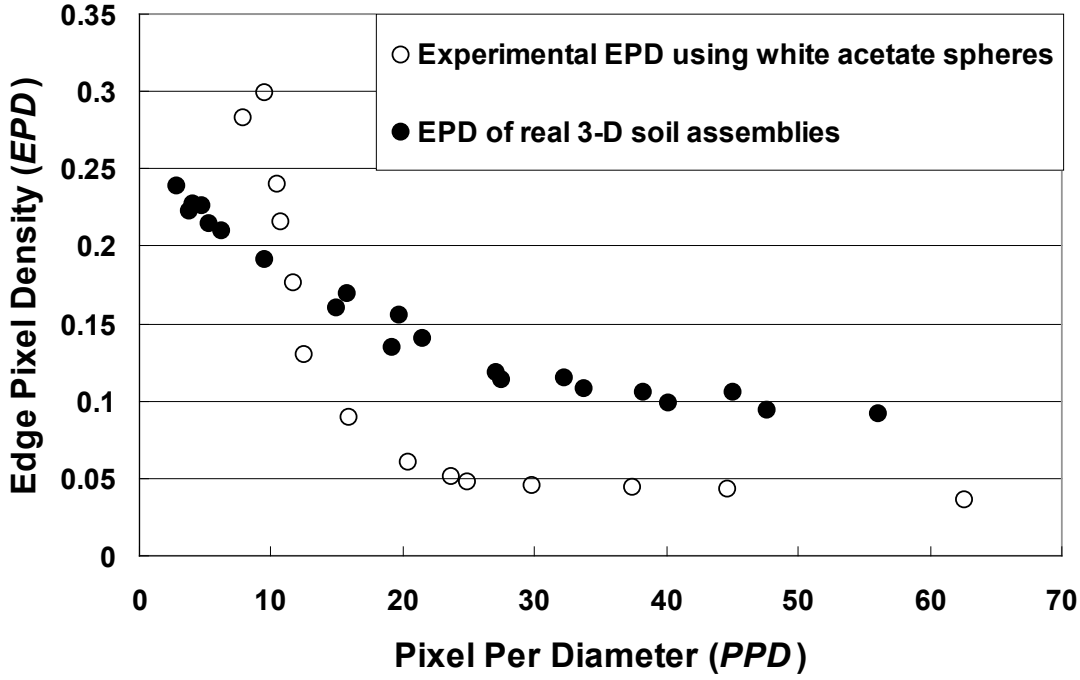

Figure 7.9 Comparison of *EPD* of real 3-dimensional soil assemblies with *EPD* of ideal two dimensional packing of acetate spheres.

7.6 False Edge Removal

Even though there are differences between *EPD* by the two dimensional model and real three dimensional soil assemblies, at low *PPD*, the slope of the real soil *EPD* vs. *PPD* curve shown in Figure 7.9, is large enough to make *EPD* a reliable predictor of grain size. However, at high *PPD*, the curve flattens and thus, the predicted *PPD* becomes undesirably more sensitive to changes in *EPD*. An attempt was therefore made to correct the *EPD* of real soils to better agree with the model prediction. Since false internal edges due to soil texture were believed to be the primary cause of the discrepancy, an algorithm was devised to remove the false internal edges. Two different false edge removal methods based on the length and geometry of edge segments are

presented in the following sections. Revised *EPD* versus *PPD* calibration charts that account for the edges removed by the methods are presented.

7.6.1 False Edge Removal Based on the Number of Connecting Pixels of Edge Segments

The guiding principles of the method are that false internal edges are shorter than those representing real particle boundaries and that the detected real particle boundaries are longer than the particle diameter. Both of these principles can be confirmed by observing the edge maps shown in the middle column of Figure 7.10. The author therefore established a first estimate of *PPD* as the minimum edge length that should be retained in an edge map. The first estimate of the *PPD* is made using the original Canny edge detector and the *EPD* versus *PPD* curve shown in Figure 7.5 or Table 7.1. All edges shorter than the first *PPD* estimate are then removed resulting in edge maps such as shown in the right column of Figure 7.10.

Table 7.1: The first estimate of the *PPD* from the original *EPD* versus *PPD* curve.

Initial *EPD*	Initial *PPD*	Initial *EPD*	Initial *PPD*
0.09	52	0.17	13
0.10	49	0.18	11
0.11	47	0.19	9
0.12	45	0.20	7
0.13	25	0.21	6
0.14	21	0.22	5
0.15	18	0.23	4
0.16	15	0.24	3

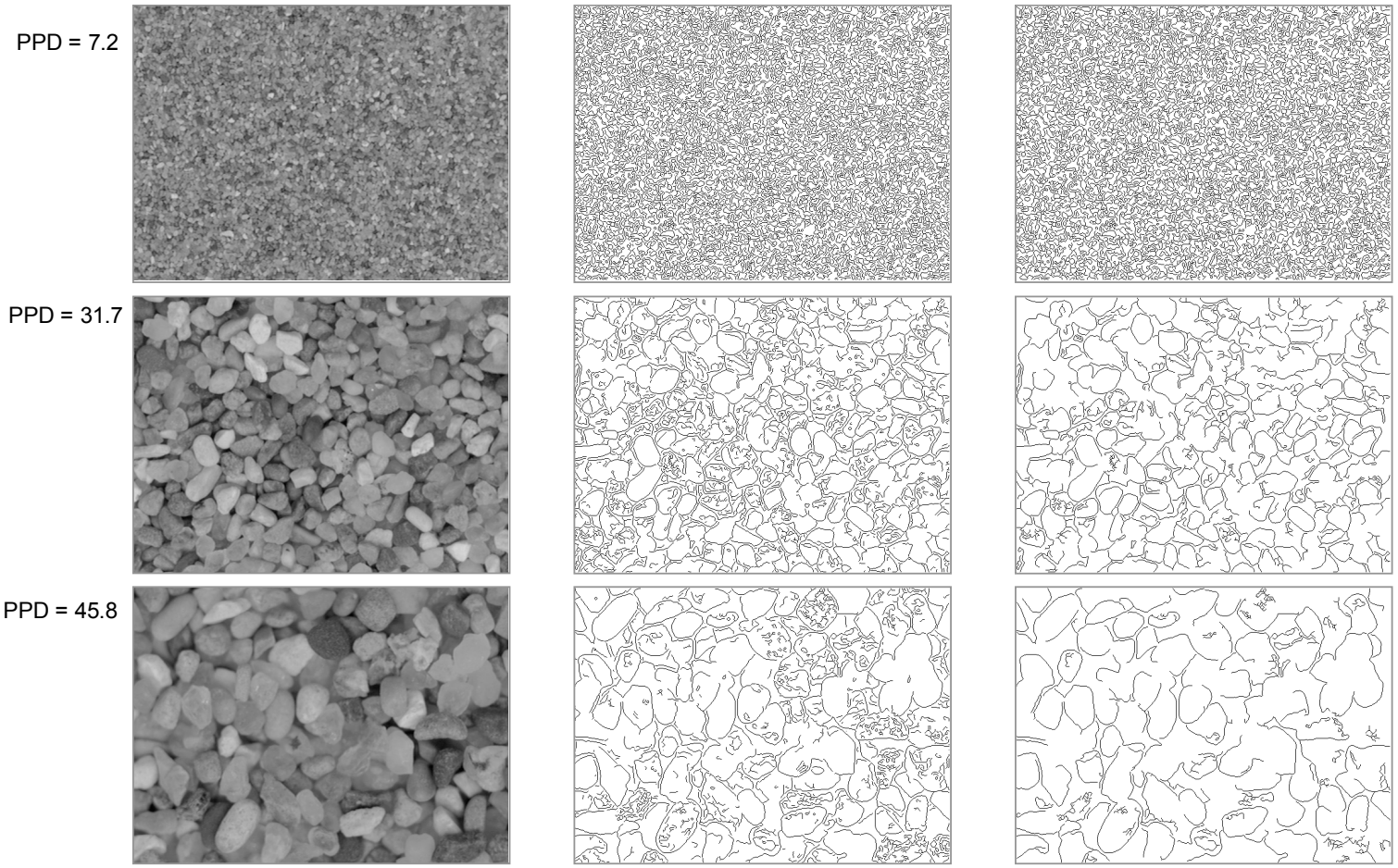

Figure 7.10 Edge maps before and after the removal of false internal edges for three different *PPD*.
The original images are in the left column. The central column shows edge maps prior to removal.
The right column shows edge maps after removal based on the number of connecting pixels of edge segments.

The new short-edge-removed *EPD* versus *PPD* calibration curve is shown in Figure 7.11. It better agrees with the theoretical model prediction (Figure 7.9) at high *PPD* values. More importantly, it provides a larger range of *EPD* values over the range of *PPD*s. As such, it affords superior resolution to the original pre-false edge removal calibration curve (Figure 7.5). In addition to removal of false short edges due to the inherent particle textures associated with cracks, mineral variations and other blemishes, the short edge removal reduces or eliminates edges created by light reflections. It is also observed that the statistical spreading (vertical error bars) in *EPD* values is smaller after removal of the short false edges (Figure 7.11) than it was in the original Canny Method (Figure 7.5). Finally, if short edges are removed, the effects of pixel-sized image noise are automatically filtered out thereby justifying the elimination of earlier pre-filtering. The benefit of not deploying a filter prior to Canny edge detection is that the images retain their crisp sharp edges for analysis.

A best-fitting mathematical expression for the *EPD* versus *PPD* curve is hyperbolic:

$$PPD = \frac{2.4}{EPD}\sqrt{1-17EPD^2} \tag{7.3}$$

It is best visualized by plotting the reciprocal of *EPD* versus *PPD* as shown in Figure 7.12. For *PPD* greater than about 20, the curve approaches the linear asymptote, *PPD* = 2.4/*EPD*. Extrapolation of the relationship 2.4/*EPD* beyond *PPD* = 60 would appear to be acceptable. However, at the 558 pixel by 380 pixel image used in this study, *PPD* =

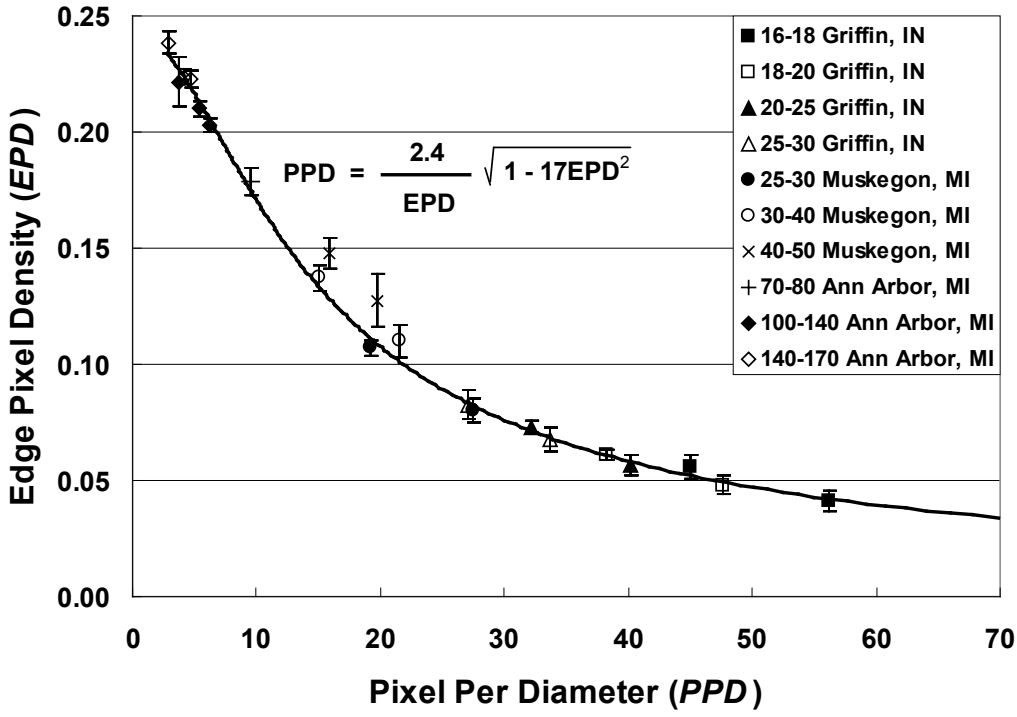

Figure 7.11 The relationship between *EPD* and *PPD* obtained after removing false internal edges based on the number of connecting pixels of edge segments.

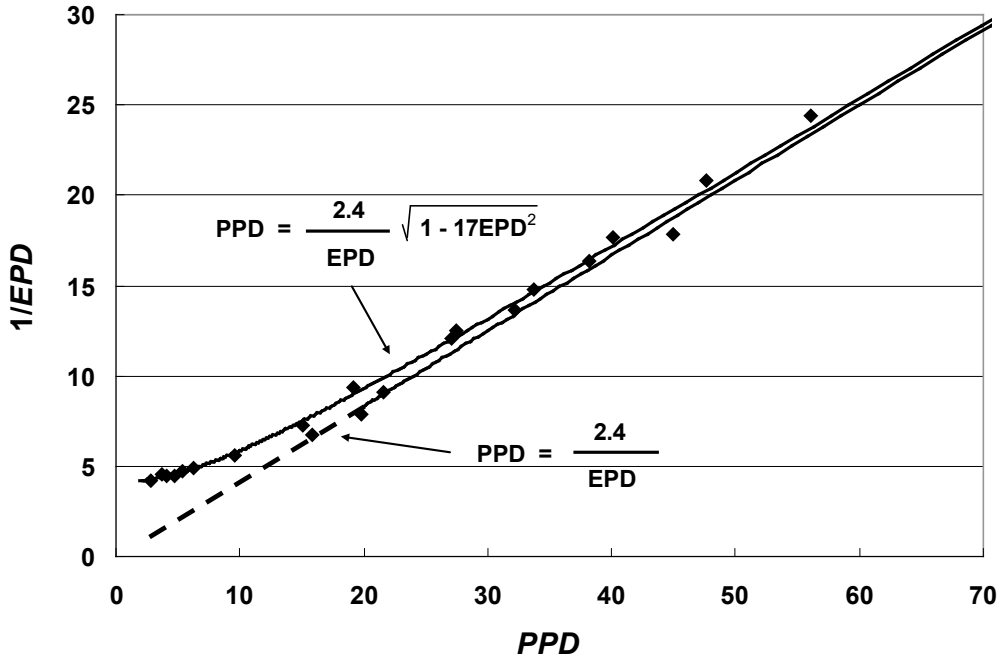

Figure 7.12 The relationship between reciprocal *EPD* and *PPD* with the removal of internal false edges based on the number of connecting pixels of edge segments.

60 represents only about 50 soil particles. Thus, larger image sizes are recommended to maintain statistical validity beyond *PPD* = 60.

7.6.2 False Edge Removal with Consideration of Geometry of Edge Segments

As seen in Figure 7.10, some false edges are not removed because the previously described false edge removal method uses the number of connecting pixels of individual edge segments as the indicator of edge length without considering their geometrical features (shape). Figure 7.13 shows an edge map of a single soil grain having *PPD* of 15 before and after the false edge removal based on the number of connecting pixels of edge segments. Within the soil grain, there are two false edge segments having the same length in their longest axes. However, only one of them is removed from the edge map after false edge removal since the other edge contains more than 15 pixels. This observation suggests that the method of false edge removal could be more effective if the geometry or shape of edge segments is taken into consideration.

Since even the longest dimension of an area bounding a false edge can not exceed the grain diameter, false edge removal should be performed by first measuring the longest dimension of such bounding areas. The simplest shape to bound an object is an ellipse and the procedure is known as elliptical fitting. The major axis of the ellipse defines the longest dimension of the object. Quantification of the longest and shortest dimensions and orientation by elliptical fitting is widely used for pattern recognition in image analysis and computer vision (Jain, 1989; Russ, 1995).

An area-based elliptical fitting method uses the *normalized second order central moments* of an object in finding the best-fit ellipse (Hu, 1962; Jain, 1989; Haralick and

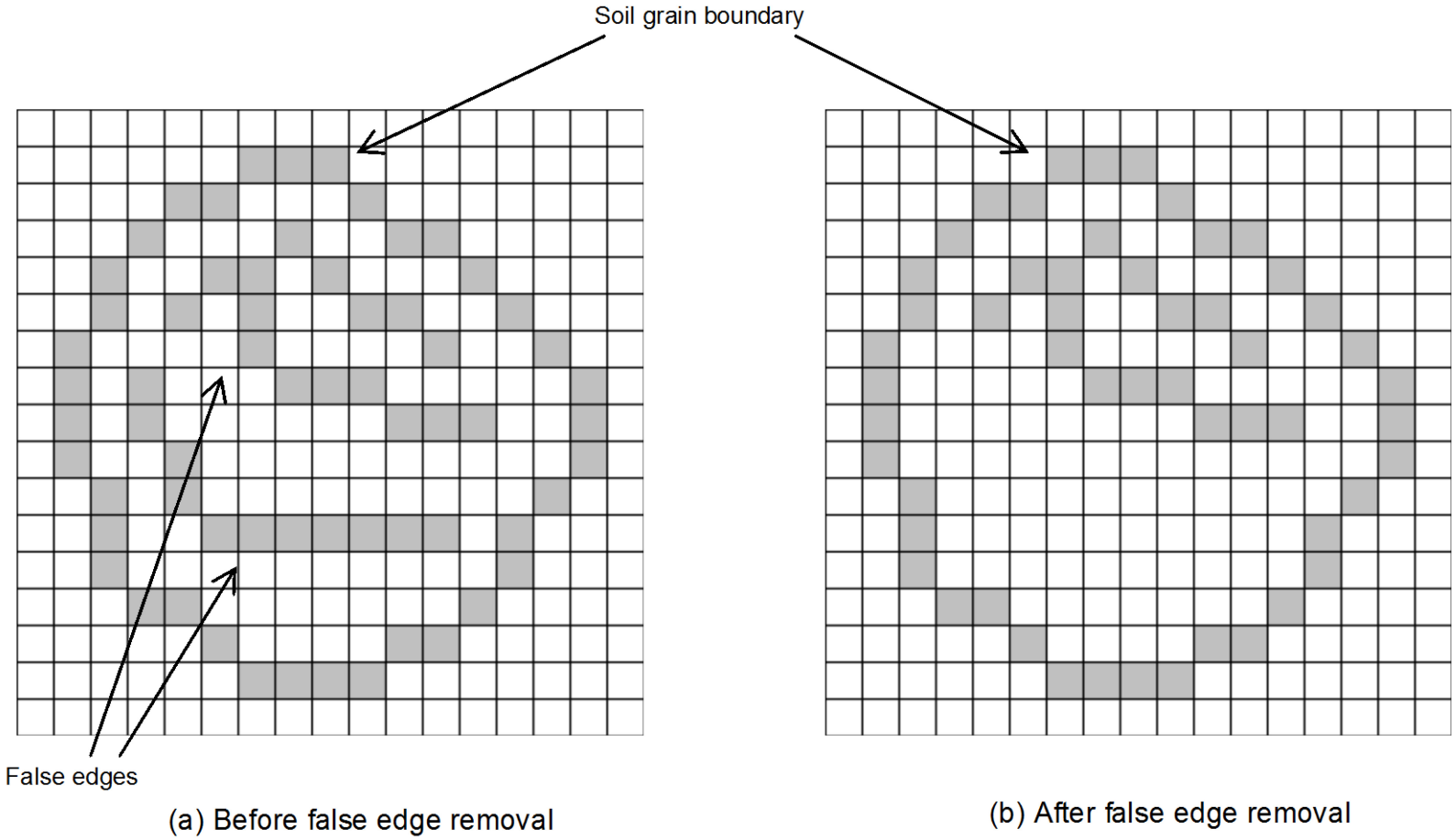

Figure 7.13 Disadvantage of false edge removal method based on the number of connecting pixels of edge segments a) before false edge removal; b) after false edge removal.

Shapiro, 1992) and equalizes the normalized second order central moments of the object with those of the best-fit ellipse. The normalized second order central moment of an object is defined as its second order central moments divided by its area.

Equations 7.4.1 and 7.4.2 show how the major and minor axis lengths of an ellipse are expressed in terms of their *normalized second order central moments*. The derivation of the equations can be found in Haralick and Shapiro, 1992.

$$Major \quad axis \quad length = \frac{2\sqrt{2}}{\sqrt{u_{xx} + u_{yy} - \sqrt{\left(u_{xx} - u_{yy}\right)^2 + 4u_{xy}{}^2}}} \tag{7.4.1}$$

$$Minor \quad axis \quad length = \frac{2\sqrt{2}}{\sqrt{u_{xx} + u_{yy} + \sqrt{\left(u_{xx} - u_{yy}\right)^2 + 4u_{xy}{}^2}}} \tag{7.4.2}$$

where u_{xx}, u_{yy}, and u_{xy} are normalized second order central moments of an object with respect to horizontal axis, vertical axis, and center of the ellipse, respectively.

For the purpose of area-based elliptical fitting of edge segments, one single pixel is considered as a square unit whose dimension is 1 by 1 and thus, has an area of 1. Its u_{xx}, u_{yy}, and u_{xy} are 1/12, 1/12, and 0, respectively. An example of area-based elliptical fitting of an edge segment is shown in Figure 7.14. The expressions for its u_{xx}, u_{yy}, and u_{xy} are:

$$u_{xx} = \frac{\sum_{i=1}^{n} \left\{A\left(y_i - y_c\right)^2 + M_{xx}\right\}}{A_{total}} \tag{7.5.1}$$

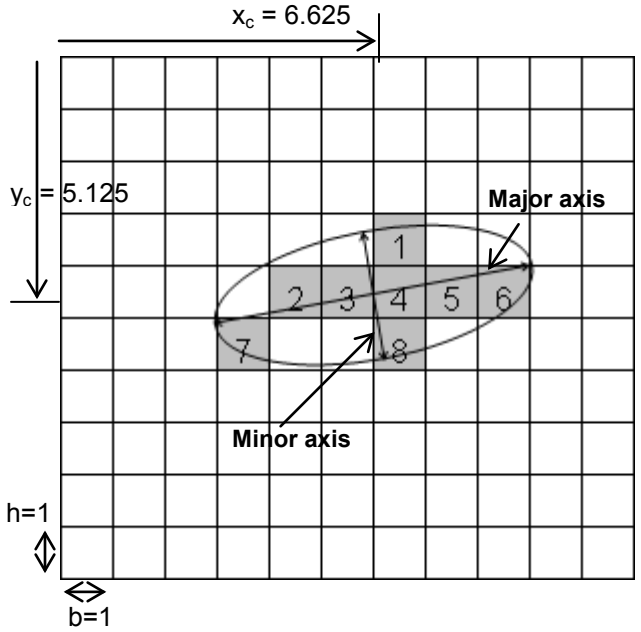

$$Major\ \ axis\ \ length = \frac{2\sqrt{2}}{\sqrt{2.32 + 0.44 - \sqrt{(2.32 - 0.44)^2 + 4x0.33^2}}} = 6.16$$

$$Minor\ \ axis\ \ length = \frac{2\sqrt{2}}{\sqrt{2.32 + 0.44 + \sqrt{(2.32 - 0.44)^2 + 4x0.33^2}}} = 2.45$$

$P_i = (x_i, y_i)$
$P_1 = (x_1, y_1) = (7,4)$
$P_2 = (x_2, y_2) = (5,5)$
$P_3 = (x_3, y_3) = (6,5)$
$P_4 = (x_4, y_4) = (7,5)$
$P_5 = (x_5, y_5) = (8,5)$
$P_6 = (x_6, y_6) = (9,5)$
$P_7 = (x_7, y_7) = (4,6)$
$P_8 = (x_8, y_8) = (7,6)$

Area of one pixel (A) = bh = 1
Total area of the edge (A_{total}) = 8bh = 8
The center of the edge, $P_c = (x_c, y_c)$
Second order central moment of a pixel
with regard to its x axis (M_{xx}) = $bh^3/12$ = 1/12
Second order central moment of a pixel
with regard to its y axis (M_{yy}) = $hb^3/12$ = 1/12
Product of inertia of a pixel
with regard to its center (M_{xy}) = 0

$$u_{xx} = \frac{\sum_{i=1}^{8}\{1(y_i - 5.125)^2 + 1/12\}}{8} = 2.32$$

$$u_{yy} = \frac{\sum_{i=1}^{8}\{A(x_i - 6.625)^2 + 1/12\}}{8} = 0.44$$

$$u_{xy} = \frac{\sum_{i=1}^{8}\{A(x_i - 6.625)(y_i - 5.125) + 0\}}{8} = 0.33$$

Figure 7.14 An example of area based elliptical fitting.

$$u_{yy} = \frac{\sum_{i=1}^{n} \left\{ A\left(x_i - x_c\right)^2 + M_{yy} \right\}}{A_{total}} \tag{7.5.2}$$

$$u_{xy} = \frac{\sum_{i=1}^{n} \left\{ A\left(x_i - x_c\right)\left(y_i - y_c\right) + M_{xy} \right\}}{A_{total}} \tag{7.5.3}$$

where A, A_{total}, x_c, y_c, M_{xx}, M_{yy}, and M_{xy} are defined in Figure 7.14.

After the longest dimension of an edge segment is measured by the elliptical fitting method, the edge is removed if its longest dimension is shorter than the first estimate of *PPD*. Figure 7.15 compares false edge removal based on the number of connecting pixels with the elliptical fitting method. It is clearly seen that the elliptical fitting method has a better ability to remove false edges.

The *EPD* versus *PPD* calibration curve utilizing the elliptical fitting method for false edge removal is shown in Figure 7.16. A best-fitting mathematical expression for calibration curve is:

$$PPD = \left(\frac{1.5}{EPD} + 9 \right)\left(1 + 16EPD^2\right)^{0.85} \tag{7.4}$$

It better agrees with theoretical *EPD* model prediction than the *EPD* versus *PPD* calibration curve shown in Figure 7.11. Also, it should be noted that the statistical spread in *EPD* values decreases. For better visualization, the reciprocal of *EPD* versus *PPD* is plotted as shown in Figure 7.17. For *PPD* greater than about 30, the *EPD* versus

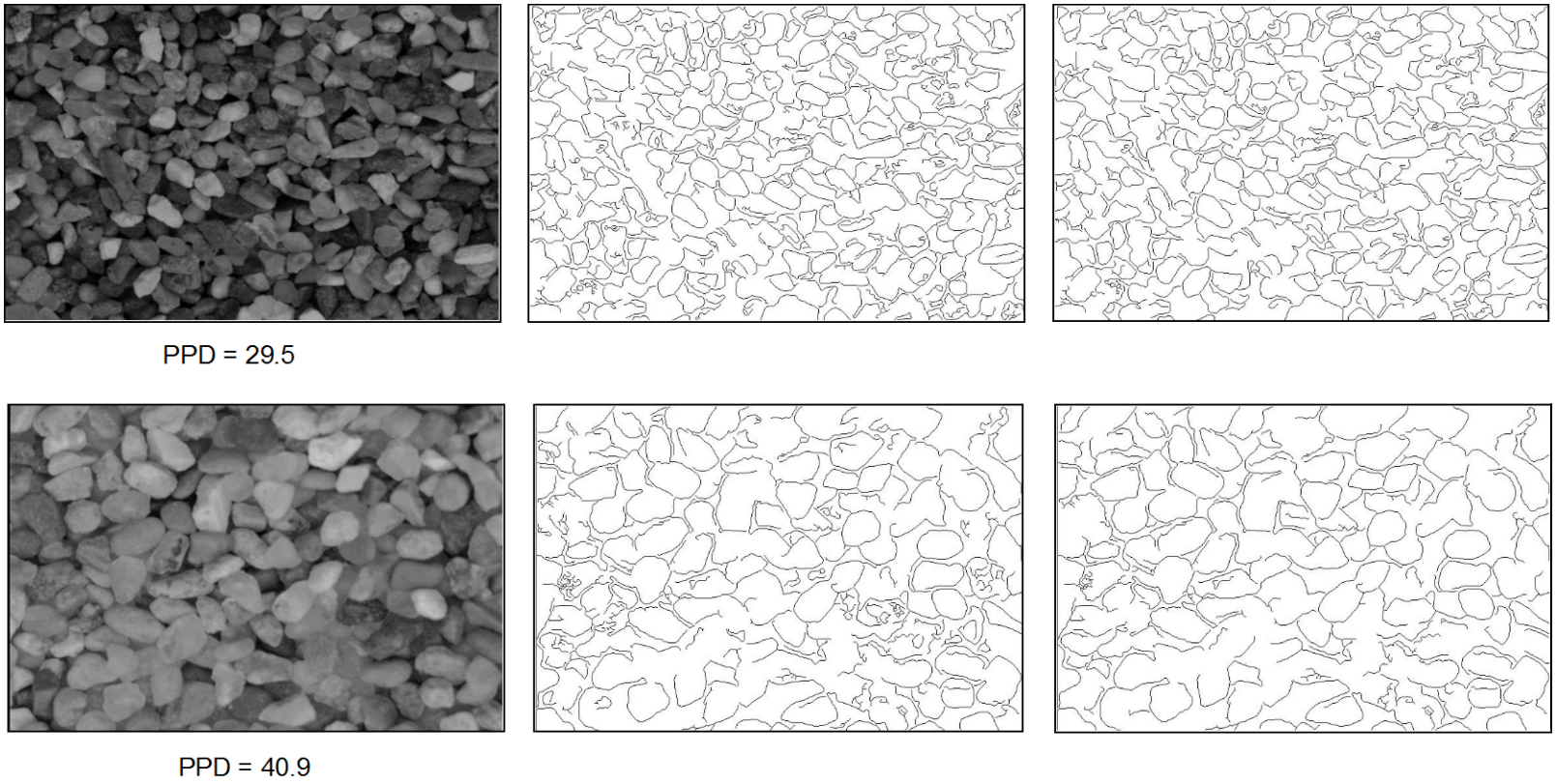

Figure 7.15 Comparison of the two false edge removal methods. The original images are in the left column. The central column shows edge maps after false edge removal based on the number of connecting pixels of edge segments. The right column shows edge maps after false edge removal by area-based elliptical fitting.

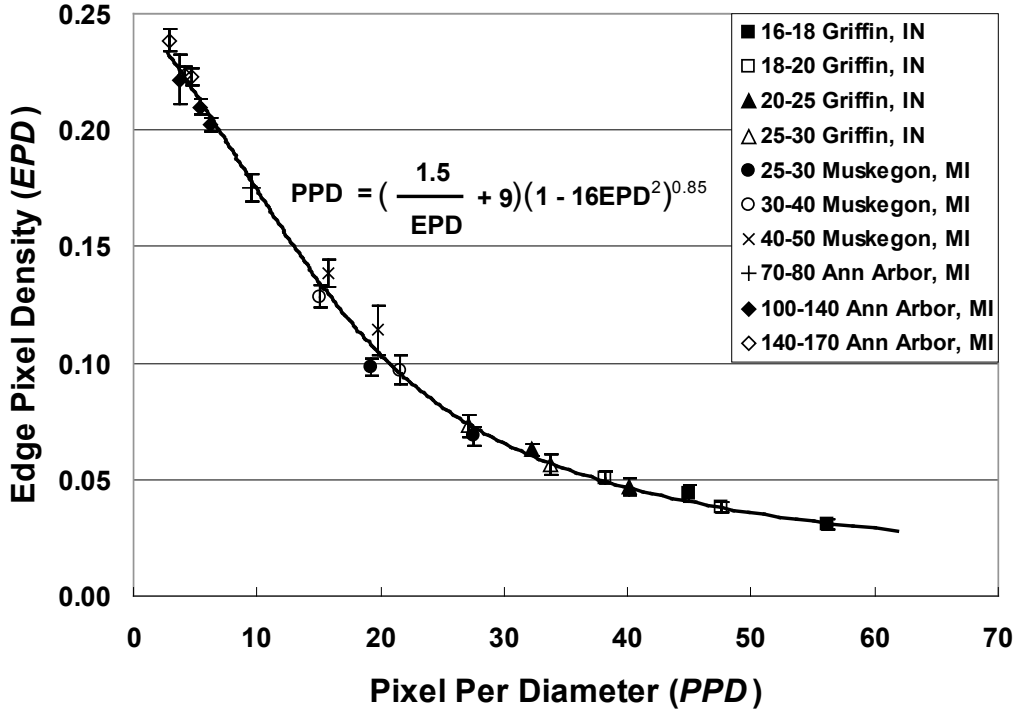

Figure 7.16 The relationship between *EPD* and *PPD* obtained after removing false internal edges by area-based elliptical fitting method.

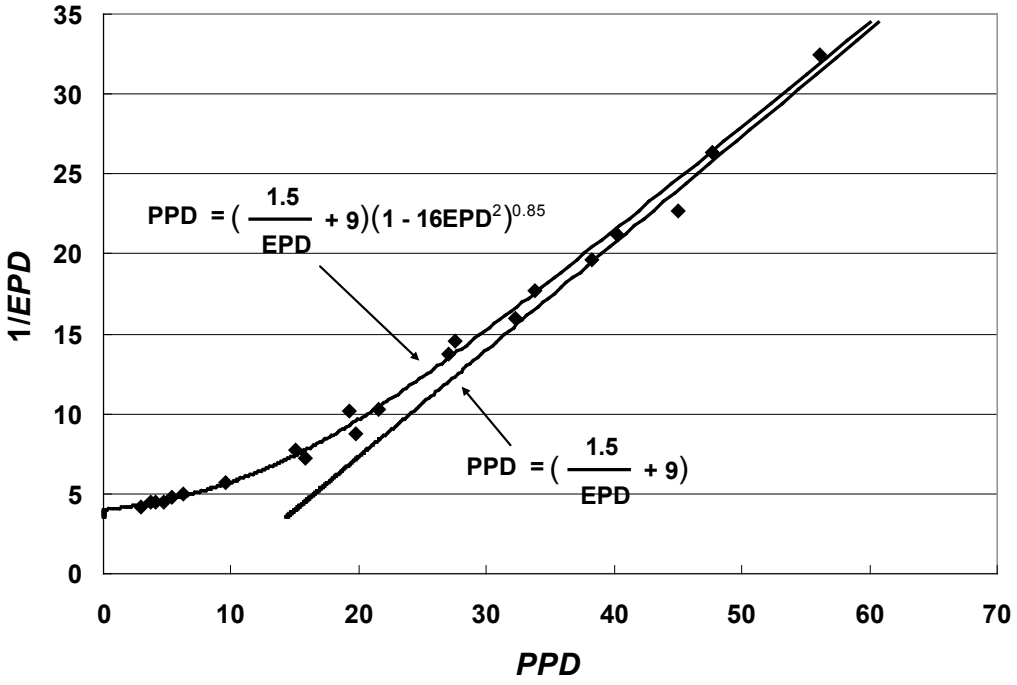

Figure 7.17 The relationship between the reciprocal of *EPD* and *PPD* with removal of false internal edges by area-based elliptical fitting method.

PPD curve approaches the linear asymptote. Therefore, when *PPD* is larger than 60 the extrapolation of the relationship, $1.5/EPD + 9$, would appear to be acceptable.

7.7 Conclusions

A procedure based on edge pixel density (*EPD*) has been developed for estimating the nominal grain size of soils from images of relatively uniform particles. The best edge detection for assemblies of uniform soil grains is based on a modified Canny algorithm. The modifications presented herein include elimination of noise filtering prior to edge detection and removal of short false edges after edge detection. Short edges are those that are less than the particle diameter in length. This requires a first estimate of the *PPD* from a preliminary pre-short-edge-removed *EPD* versus *PPD* curve.

Two different methods are used to remove false edges. In the first method, an edge is considered as a false edge and removed if it consists of a fewer number of pixels than the first estimate of *PPD*. In the second method, the longest dimension of an edge is measured by area-based elliptical fitting and edges are removed if their longest dimension is smaller than the first estimate of *PPD*. The second method is more effective in identifying false edges than the first method.

The results for real soils are compared to a theoretical model based on the assumption that contacting grains produce missing edges, particularly at low *PPD*. The theoretical model was verified by *EPD* analysis of images of uniform 1.50 mm acetate spheres arranged in perfect two-dimensional dense packing. Deviations between the two dimensional model and real three-dimensional soil grain assemblies are explained. The

final product of this study is a mathematical expression for *PPD* as a function of *EPD* given by Equation 7.4. For *PPD* above about 30, the model asymptotically approaches $PPD = 1.5/EPD + 9$.

CHAPTER VIII

Sedimaging Results and Analysis

8.1 Introduction

The three essential components of the *Sedimaging* method for soil grain size distribution determination were addressed in the previous chapters. Chapter III discussed the physical apparatus for segregation of soil grains by size, the imaging device, and the test procedure. Chapter IV evaluated void ratio variations in the sedimented soil column and showed that the variations are insignificant. As such, each increment of height in the soil column corresponds to a proportional percentage of the soil solids. In Chapter V, VI and VII, three different image processing techniques were presented for determining the size of approximately uniform soil grains at each increment of height in the soil column. This chapter integrates all the findings and procedures from the previous chapters to determine the soil grain size distribution by Sedimaging. The results are compared with sieve analysis throughout. Also, later in this chapter, a simplified test based on Sedimaging is suggested to classify soil according to the AASHTO system.

8.2 Sedimaging Results

8.2.1 Preparation of Soil Specimens

The soils used in the Sedimaging tests were collected from two different sites; a glacial deposit on the campus of the University of Michigan in Ann Arbor, MI; and a sand quarry in Griffin, IN. Each soil was initially air-dried and 200g of it was sieved for 20 minutes at a time using U.S. standard sieve No. 14, 16, 20, 30, 40, 50, 60, 70, 80, 100, 140, 170, and 200. Following shaking with mechanical shakers, the soil remaining on each sieve was washed to make sure that no soil aggregations remained and no fines were attached to larger sand grains. The washed soil was air-dried and sieved by hand until no soil grains smaller than the sieve opening remained on each sieve. The segregated soil particles were then combined in pre-determined percentages by weight for Sedimaging. Each of the 16 vertical chutes of the soil release box was filled with approximately the same weight fraction of the specimen. The distance between the water surface in the sedimentation column and the bottom of the soil release box was 7.6 cm (3 in.).

8.2.2 Results of Sedimaging and Comparison with Sieve Analysis

A Sedimaging test was performed on a 400g soil specimen of a relatively uniform, poorly graded sand collected from Ann Arbor, MI (AA-P). The sedimented soil column shown in Figure 8.1 was imaged by the CCD camera (Pulnix model TM-7CN) at a magnification level of 44.7 pixel/mm. Wavelet decomposition, pattern spectrum, and edge pixel density image processing methods were applied to each 256 pixel increment of height in the soil column to compute the *wavelet soil grain size index* (*CA*), the

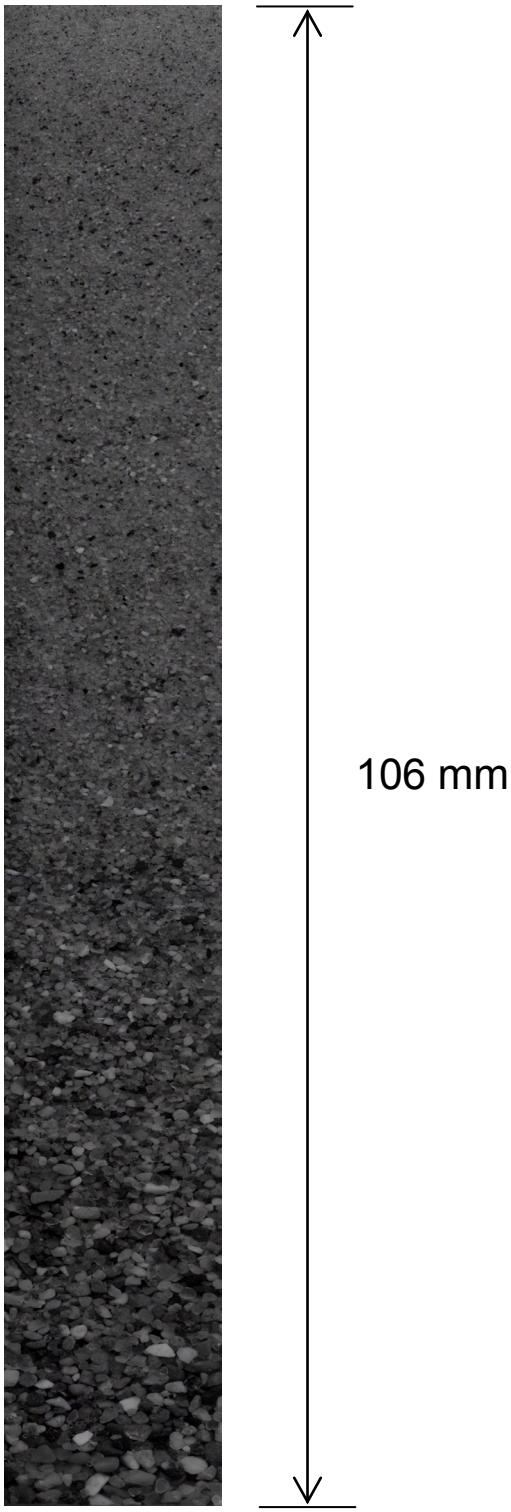

Figure 8.1 Sedimented soil column of 400g of soil collected from Ann Arbor, MI (AA-P soil).The soil column image was taken at a magnification of 44.7 pixel/mm.Coefficient of Uniformity (Cu) of the soil is 2.86.

structuring element size at *spectrum peak* (*SP*), and the *edge pixel density* (*EPD*). Elliptical fitting as described in Chapter VI was used to remove false edges when computing *EPD*. The *CA*, *SP*, and *EPD*, were used in Equations 5.15, 6.11, and 7.5 to compute the corresponding *PPD*s. The soil grain size distributions by Sedimaging are shown versus elevation in the soil column in Figure 8.2. The sieve analysis based soil grain size distribution is also shown in Figure 8.2 for comparison. For constructing the sieve analysis based curves, it was assumed that the grain sizes between any two successive sieves were linearly distributed by weight.

In the top half of the soil column where *PPD* is small, the computed soil grain size by the wavelet decomposition and pattern spectrum methods showed excellent agreement with the sieve based size. However, the computed soil grain size by the edge pixel density method showed some deviation from the sieve based distribution near the top of the soil column. This deviation may be due to the fact that, at small *PPD*, relatively large statistical spreads of *EPD* are observed in the *EPD* versus *PPD* calibration (Figure 7.16). The other two soil grain size calibrations, *CA* versus *PPD* (Figure 5.21) and *SP* versus *PPD* (Figure 6.11), have smaller statistical spreads in the small *PPD* range.

Figure 8.3 compares the traditional log-scale grain size distribution curves by Sedimaging with sieve analysis. Table 8.1 lists several soil grain size distribution parameters (D_{10}, D_{30}, D_{50}, and D_{60}) for comparison. The computed Coefficients of Uniformity (C_u) and Coefficients of Gradation (C_z) are also provided in the table. The parameters determined from the wavelet decomposition and pattern spectrum methods match very well with sieve results while those from the edge pixel density method do not match as well.

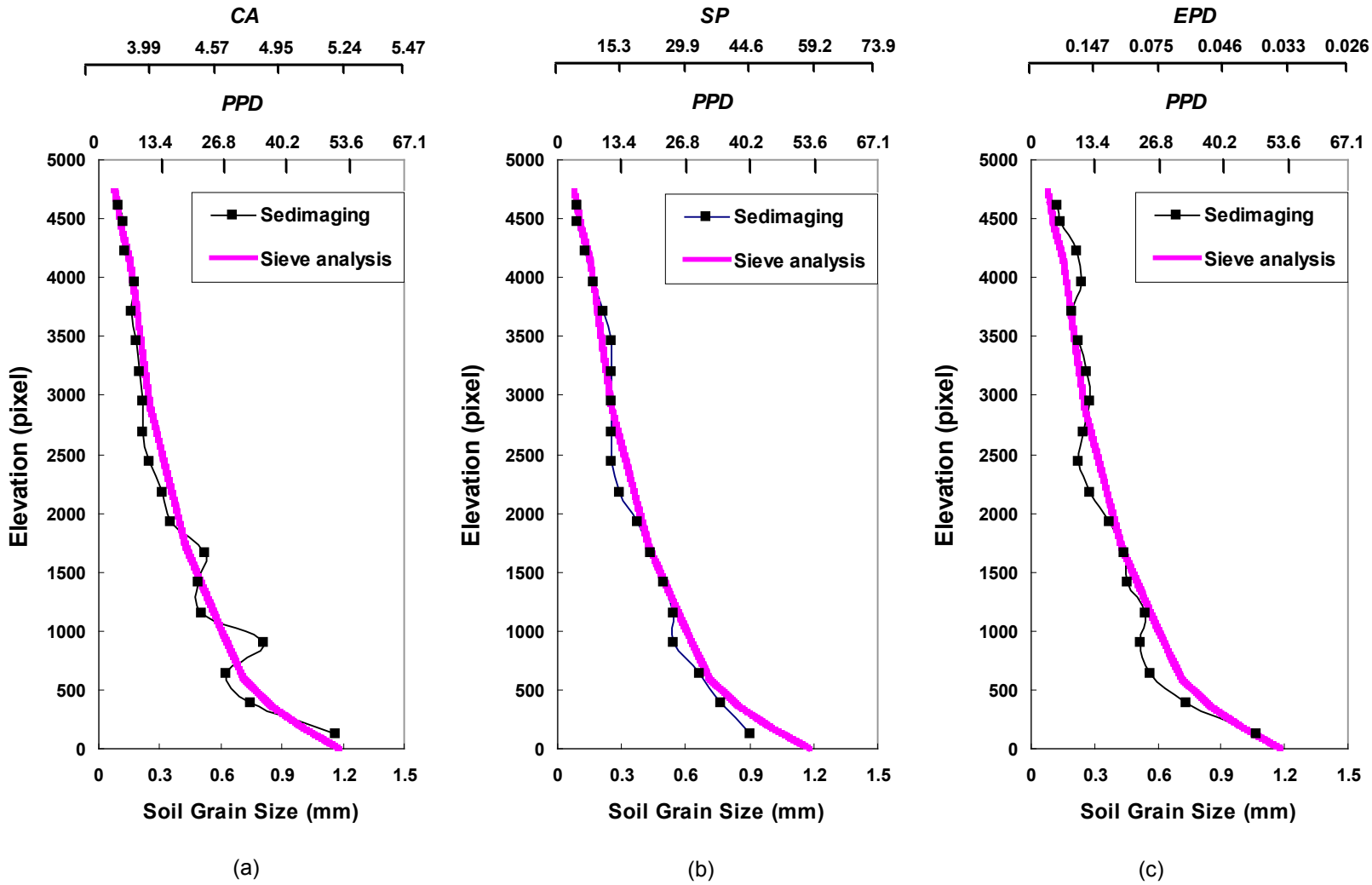

Figure 8.2 The computed soil grain size indices (*CA*, *SP*, and *EPD*), the corresponding *PPD*, and soil grain size are shown versus elevation of the soil column image of the AA-P soil.

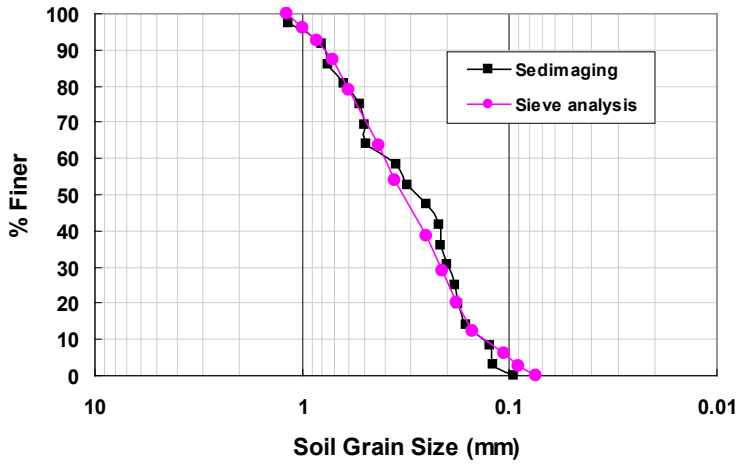

(a)

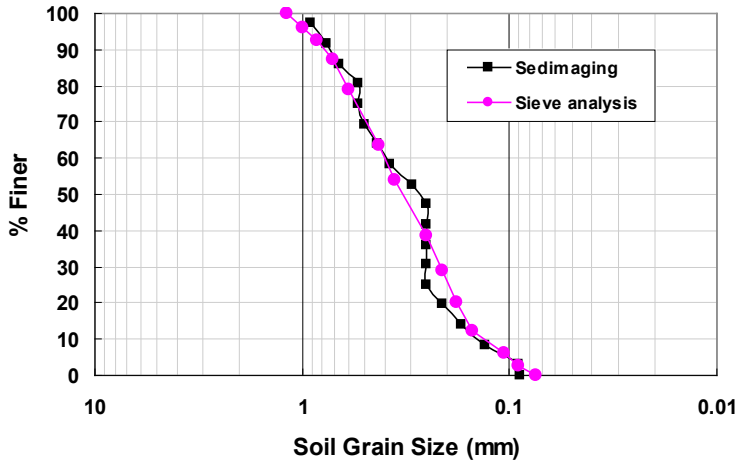

(b)

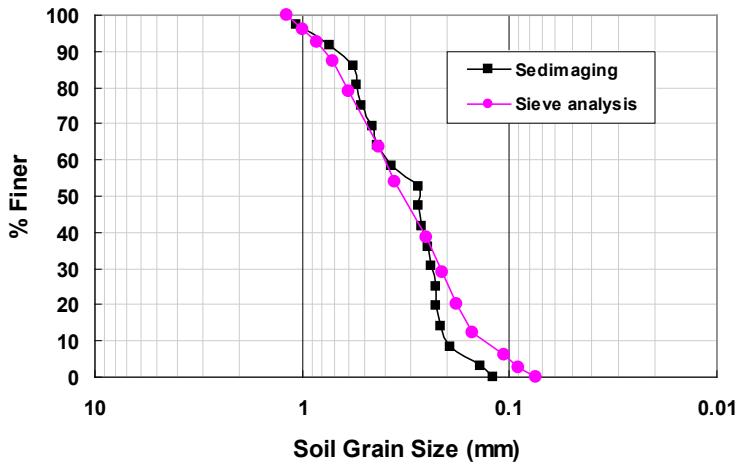

(c)

Figure 8.3 Traditional log-scale soil grain size distribution of the AA-P soil by Sedimaging using a) the wavelet decomposition method, b) the pattern spectrum method, and c) the edge pixel density method.

Table 8.1: Comparison of grain size distribution parameters for the AA-P soil.

	Sieve analysis	Wavelet decomposition	Pattern spectrum	Edge pixel density
D_{10} (mm)	0.14	0.13	0.14	0.20
D_{30} (mm)	0.22	0.20	0.25	0.23
D_{50} (mm)	0.32	0.28	0.28	0.28
D_{60} (mm)	0.40	0.38	0.40	0.39
$C_u = D_{60}/D_{10}$	2.86	2.92	2.58	1.95
$C_z = D^2_{30}/D_{60}D_{10}$	0.86	0.81	1.12	0.68

Two more Sedimaging tests were performed using 500g and 450g of soil collected from Griffin, IN and Ann Arbor, MI, respectively. The 500g Griffin soil (GR-P) was finer but also more poorly graded than the soil (AA-P) shown in Figure 8.1. The 450g Ann Arbor soil (AA-W) is coarser and better graded. The camera magnifications for the two tests are slightly different; 47.5 pixel/mm was used for the GR-P soil and 46.8 pixel/mm was used for the AA-W soil. The soil column images for the two soils are shown in Figures 8.4 and 8.7. Figures 8.5 and 8.8 show the *CA*, *SP*, *EPD*, and corresponding *PPD*s versus depth in the soil column. Figures 8.6 and 8.9 compare log-scale grain size distribution curves by Sedimaging with sieve analysis. The Sedimaging results are summarized in Tables 8.2 and Table 8.3.

The GR-P soil showed excellent agreement between wavelet decomposition, pattern spectrum and sieve based size distributions. However, soil grain size distribution by the edge pixel density method exhibited two spurious data points at approximately 1400 and 3700 pixels from the bottom of the soil column. It was observed in the soil column image shown in Figure 8.4 that the humps were not due to poor soil segregation. Instead, this deviation was due to an overly high first estimate of *PPD*, which was used as the minimum edge length that should be retained in an edge map. The overly high first

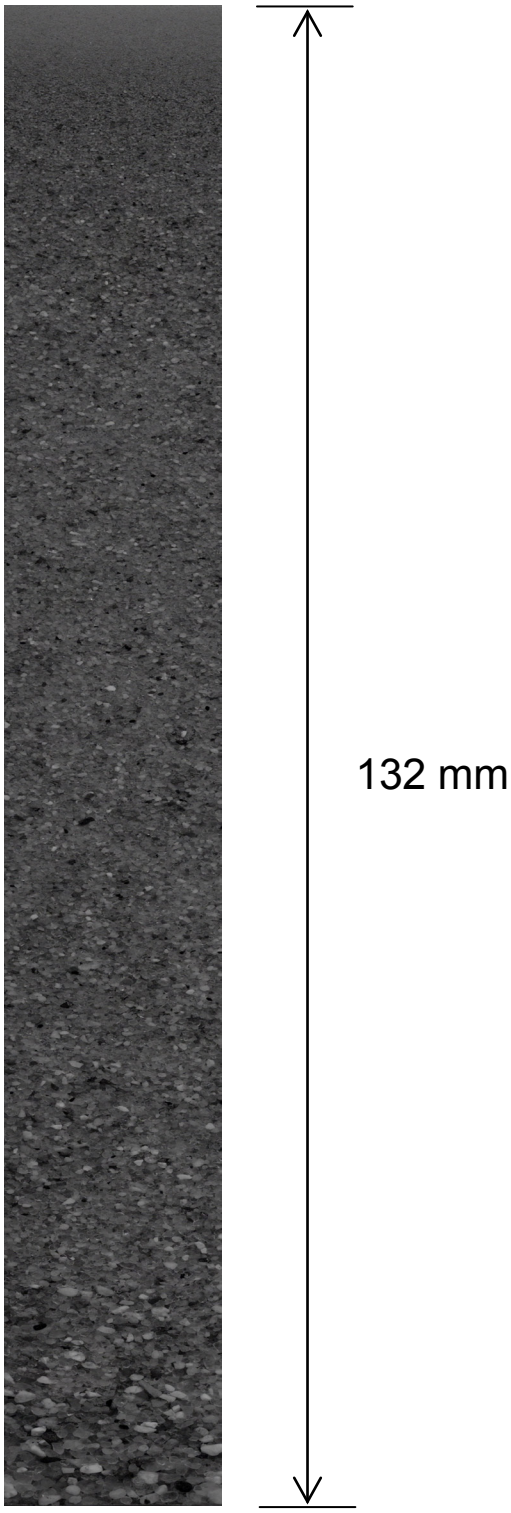

Figure 8.4 Sedimented soil column of 500g of soil collected from Griffin, IN (GR-P soil).The soil column image was taken at a magnification of 47.5 pixel/mm.Coefficient of Uniformity (Cu) of the soil is 2.20.

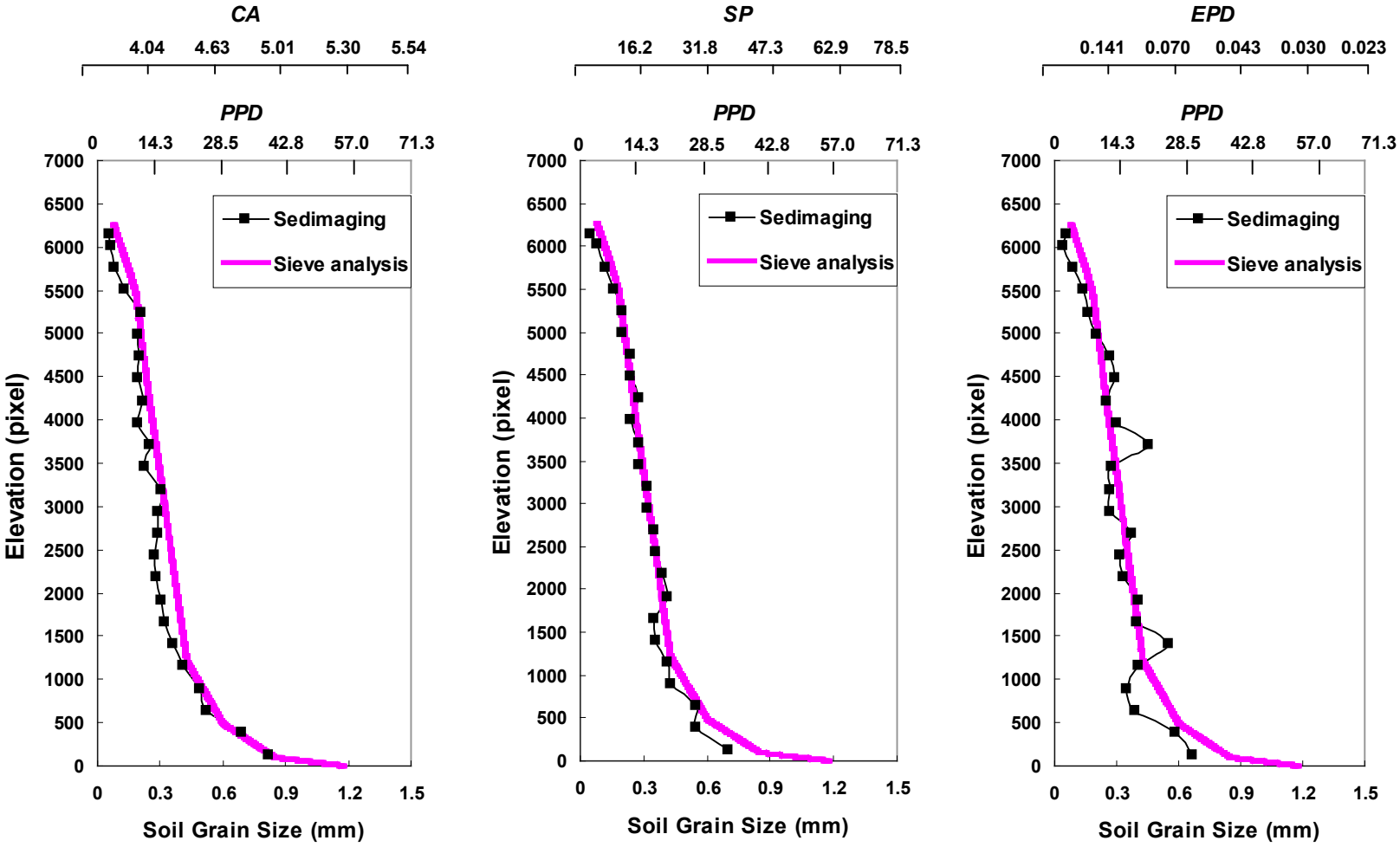

(a) (b) (c)

Figure 8.5 The computed soil grain size indices (*CA*, *SP*, and *EPD*), the corresponding *PPD*, and soil grain size are shown versus elevation of the soil column image of the GR-P soil.

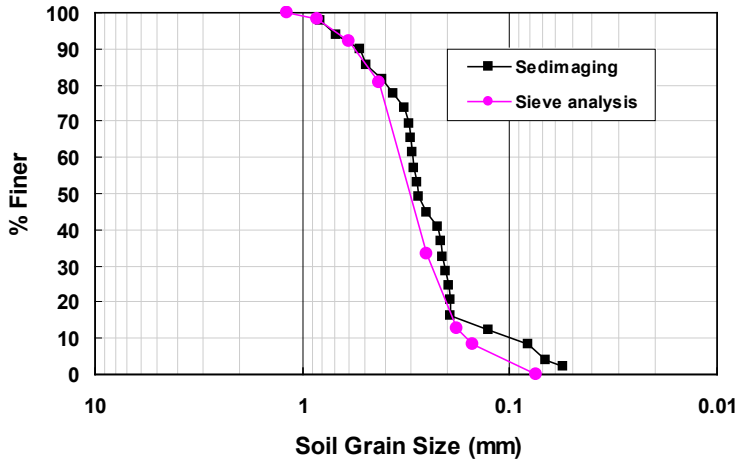

(a)

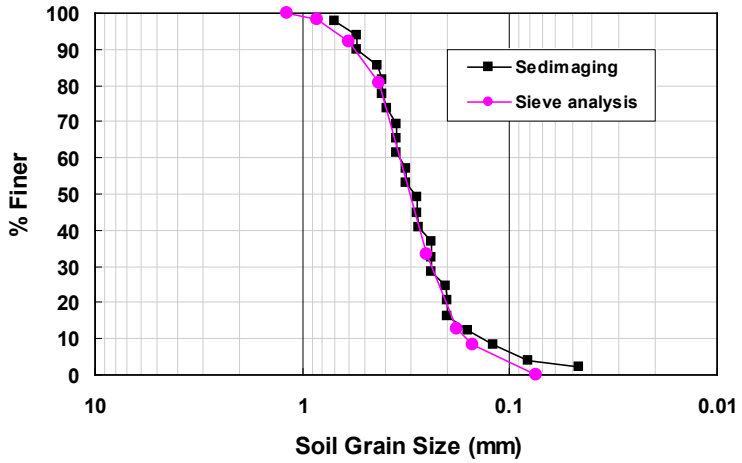

(b)

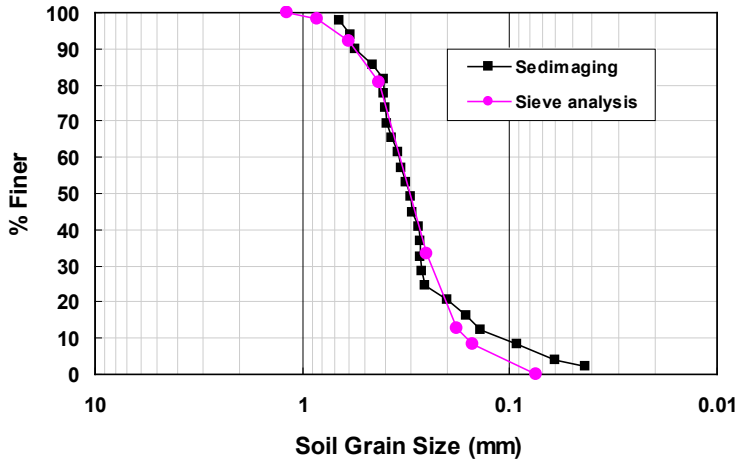

Figure 8.6 Traditional log-scale soil grain size distribution of the GR-P soil by Sedimaging using a) the wavelet decomposition method, b) the pattern spectrum mehtod, and c) the edge pixel density method.

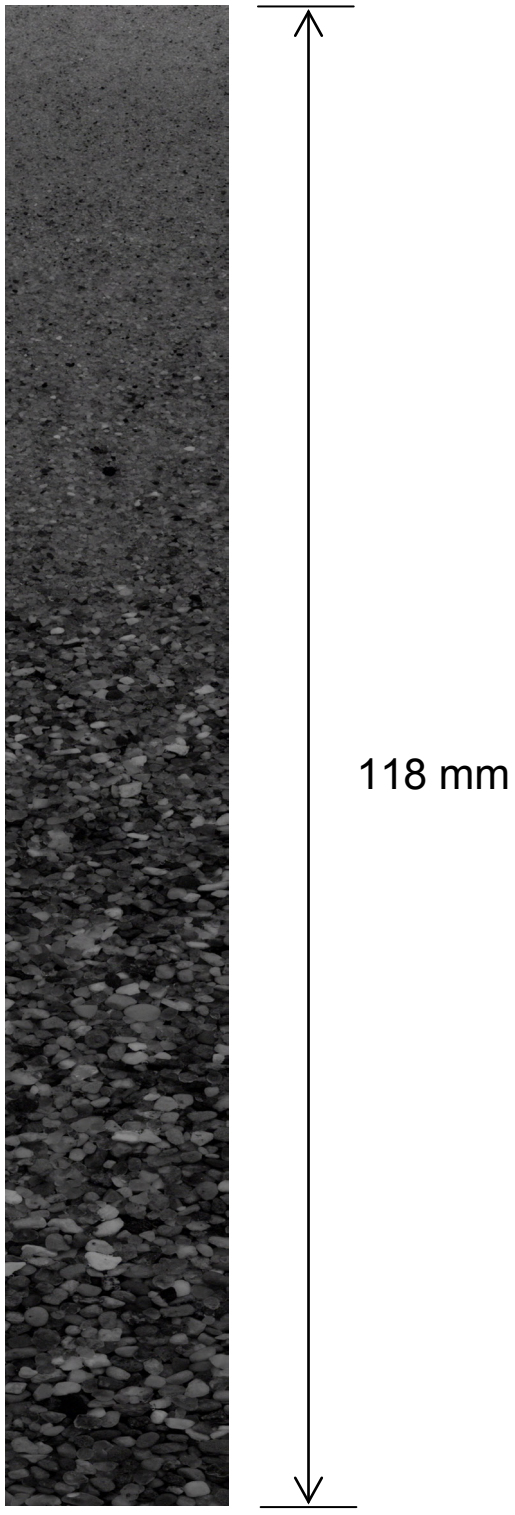

Figure 8.7 Sedimented soil column of 450g of soil collected from Ann Arbor, MI (AA-W soil).The soil column image was taken at a magnification of 46.8 pixel/mm.Coefficient of Uniformity (Cu) of the soil is 6.36.

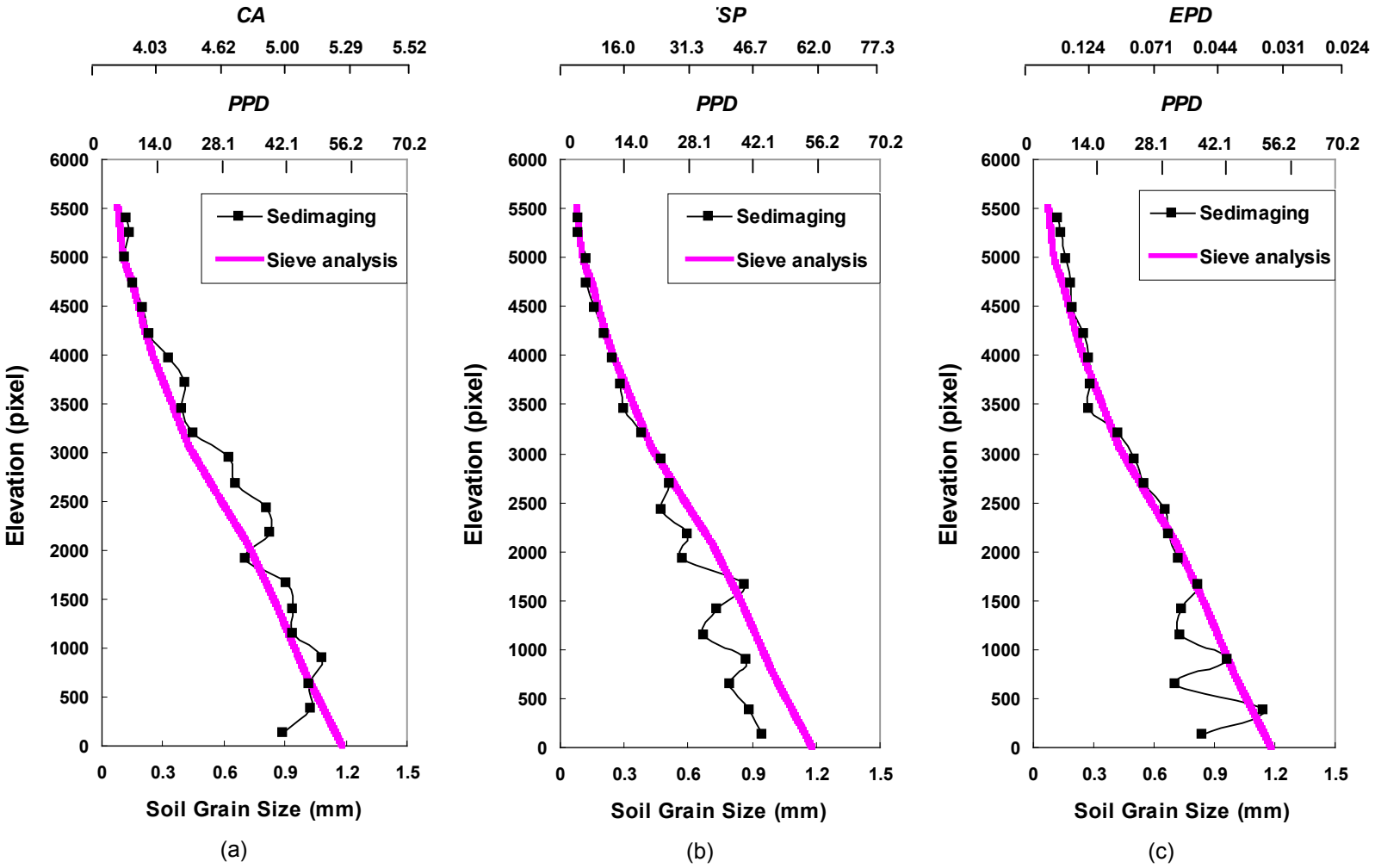

Figure 8.8 The computed soil grain size indices (*CA*, *SP*, and *EPD*), the corresponding *PPD*, and soil grain size are shown versus elevation of the soil column image of the AA-W soil.

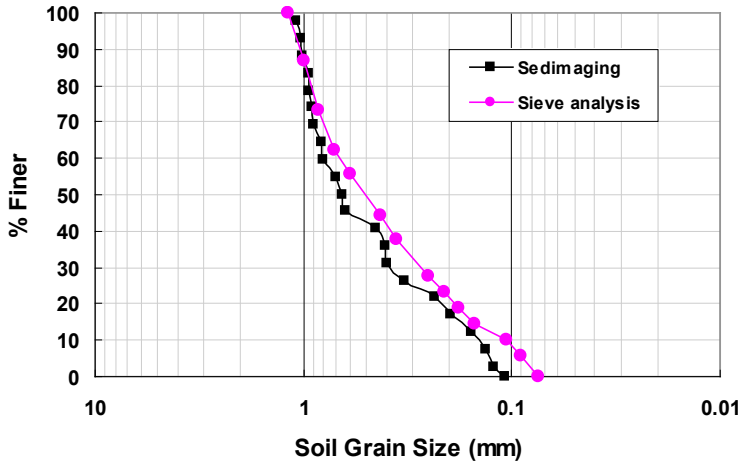

(a)

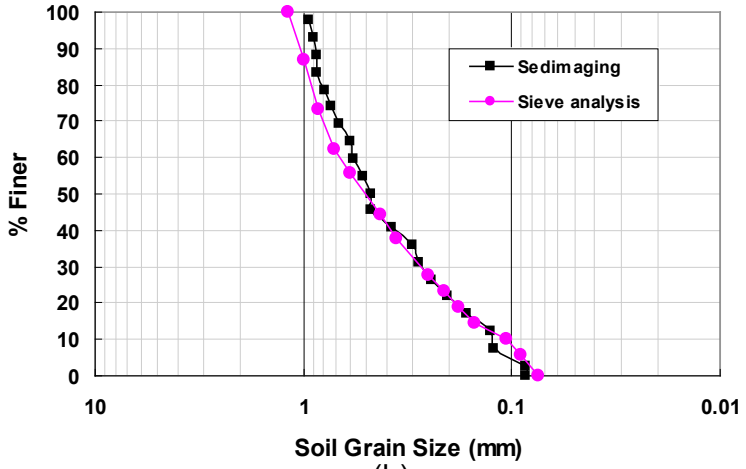

(b)

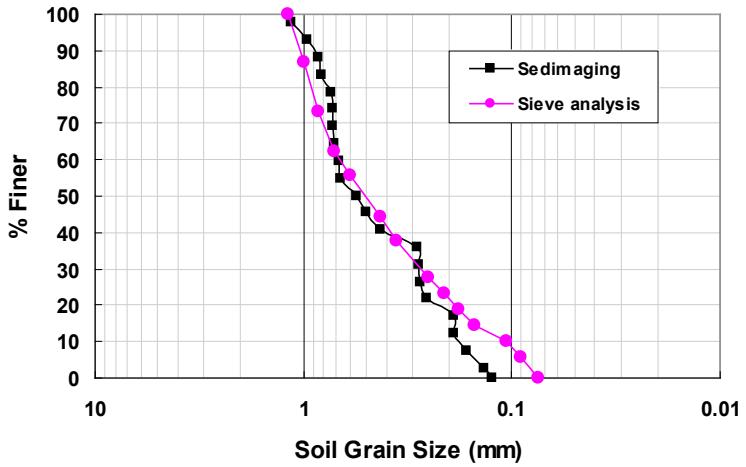

(c)

Figure 8.9 Traditional log-scale soil grain size distribution of the AA-W soil by Sedimaging using a) the wavelet decomposition method, b) the pattern spectrum mehtod, and c) the edge pixel density method.

Table 8.2: Comparison of grain size distribution parameters for the GR-P soil.

	Sieve analysis	Wavelet decomposition	Pattern spectrum	Edge pixel density
D_{10} (mm)	0.15	0.11	0.14	0.11
D_{30} (mm)	0.23	0.21	0.23	0.27
D_{50} (mm)	0.30	0.28	0.30	0.30
D_{60} (mm)	0.33	0.30	0.33	0.34
$C_u = D_{60}/D_{10}$	2.20	2.73	2.36	3.09
$C_z = D^2_{30}/D_{60}D_{10}$	1.07	1.34	1.15	1.95

Table 8.3: Comparison of grain size distribution parameters for the AA-W soil.

	Sieve analysis	Wavelet decomposition	Pattern spectrum	Edge pixel density
D_{10} (mm)	0.11	0.14	0.13	0.18
D_{30} (mm)	0.28	0.39	0.28	0.28
D_{50} (mm)	0.51	0.65	0.48	0.55
D_{60} (mm)	0.70	0.81	0.59	0.68
$C_u = D_{60}/D_{10}$	6.36	5.79	4.54	3.78
$C_z = D^2_{30}/D_{60}D_{10}$	1.02	1.34	1.02	0.64

estimate of *PPD* removed some true edges of soil grains and resulted in lower *EPD* and thus larger determined soil grain size than it should have been. The overly high first estimate of *PPD* was attributed to the Canny edge detector's misinterpretation of very weak but true soil grain boundaries as false edges.

The AA-W soil shown in Figure 8.7 exhibited larger deviations from sieve based size distributions than the other two other soils did. This is partly attributed to the increasing statistical spread of soil grain size indices with increasing *PPD* in the *CA* versus *PPD* and in the *SP* versus *PPD* calibration models as well as the decreasing *EPD* resolution with increasing *PPD* in the *EPD* versus *PPD* calibration model. Despite this,

the soil grain size differences between Sedimaging and sieve analysis are not significant on a percentage basis.

Overall, soil grain size distribution by Sedimaging fairly well mimics sieve based grain size distribution. In particular, the wavelet decomposition and pattern spectrum methods demonstrated their suitability to Sedimaging. However, the edge pixel density method's implementation into Sedimaging was not as successful as the other two methods for the following reasons: 1. Weak but true soil grain boundaries are often not interpreted as true edges by the Canny edge detector. So, if an image contains such soil grain boundaries the *EPD* will be underestimated. That could result in a significant difference between soil grain size estimated from *EPD* and the actual soil grain size. 2. Not all the first estimates of *PPD* used for false edge removal are accurate. In some cases, when a 256 pixel increment of height includes highly uniform sized soil grains like the images used to develop the *EPD* versus *PPD* model, the first estimate of *PPD* identifies false edges with high precision. In other cases when a 256 pixel increment contains less uniform sized soil grains, the first estimate of *PPD* is not accurate and thus, the removal of false edges is poor. A smaller pixel increment than 256 could be used to accommodate highly uniform sized soil grains. However, such a pixel increment contains less number of particles, which leads to poor statistical validity of *EPD*.

8.2.3 Identification of Problem Soils and Solutions

Problems may develop with some gap-graded soils. The sedimented soil column of a gap-graded soil will show abrupt change in soil grain size in the size distribution curve. The change can be characterized by a distinct boundary between finer and coarser

soil grain textures. Soil images that contain such boundaries are problematic to soil grain size analyses. Also, in Sedimaging the finer soil grains may infiltrate the skeleton of the coarser material below. The depth and amount of penetration of the finer grains into the coarser skeleton will increase with the size of the gap in the size distribution. Gap graded soils therefore were tested to assess the magnitude of the problems and, if necessary, to find a solution.

It is known that when an image includes two different sizes of soil grains, the computed *CA* represents a weighed average size based on the image area each soil grain size occupies. So, if a 256 pixel increment of height in a soil column image contains a boundary between two different particle sizes an imaginary intermediate grain size will be computed. Figure 8.10 shows the computed *CA* and the grain size distribution of a double gap-graded soil. The double gap-graded soil specimen was prepared by collecting three sizes of soil grains, which were retained between the No. 16 and 18, No. 40 and 50, and No. 140 and 170 sieves, respectively. A total of 400g of soil solids having 133.3g of each size was used for Sedimaging. The camera magnification was set at 43.8 pixel/mm.

As shown in Figure 8.10, at the interface of two dissimilar grain sizes the computed *CA* represents an average of the two sizes. This problem can be easily solved by keeping a 256 pixel increment of height from containing the boundary between finer and coarser soil grains.

If a soil is gap-graded and the grain size difference between finer and coarser soil grains is very large, the finer soil grains will sediment into the pores of the coarser soil below. Then, the finer soil showing through the glass column would not represent its actual volume. Rather, the volume of finer soil could be somewhat exaggerated because

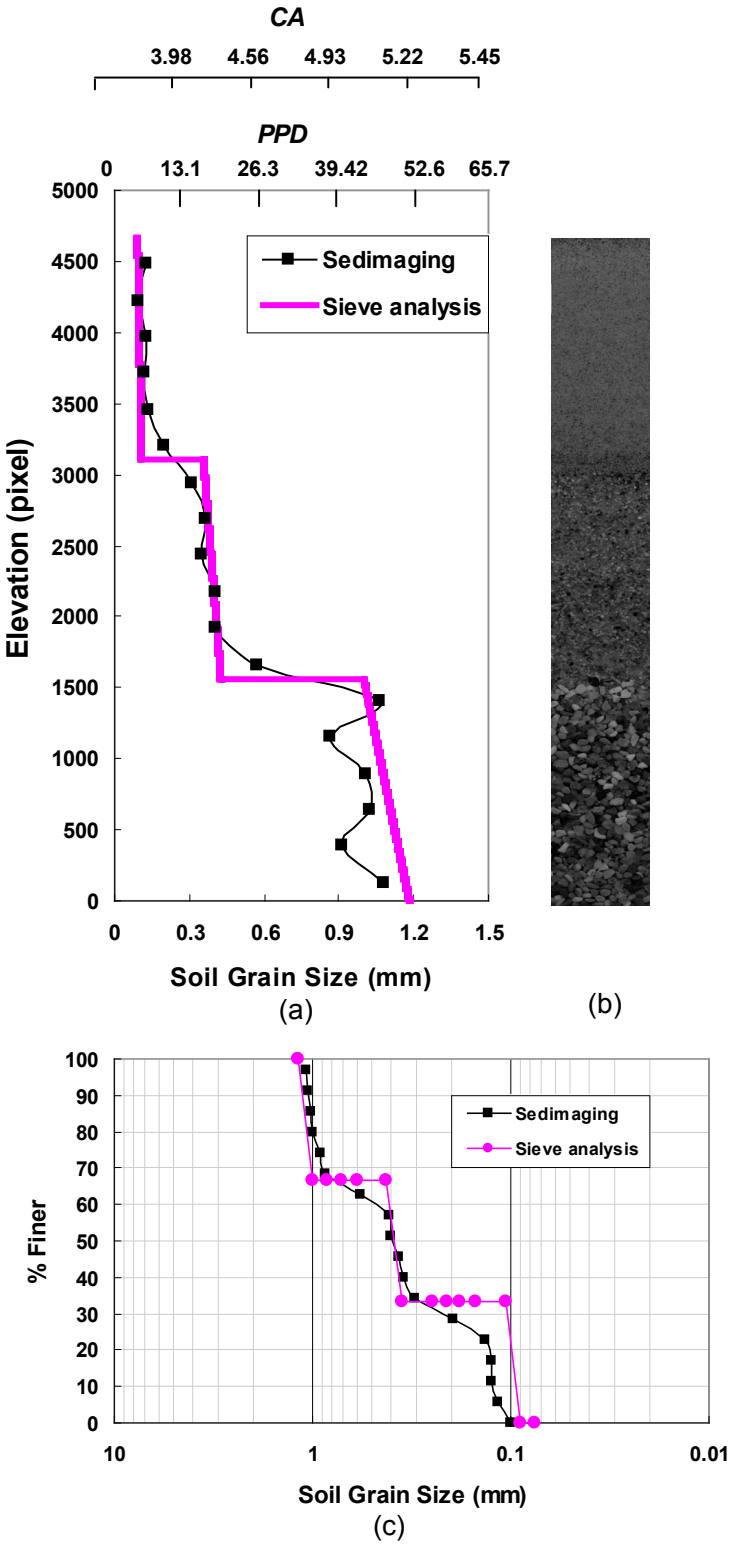

Figure 8.10 a) *CA*, *PPD*, and soil grain size versus elevation of the soil column of a 400g double gap-graded soil. b) soil column image taken at the magnification level of 43.8 pixel/mm. c) soil grain size distribution by Sedimaging and sieving.

pore spaces between the glass column and the uppermost coarser grains may be filled with the finer material and thus, some fraction of the uppermost coarser soil is hidden behind the finer particles.

A severely gap-graded soil was prepared and sedimented to observe the behavior of the fine soil in the boundary area and see its effect on the grain size distribution curve. The soil specimen consisted of two different sized soil grains, 200g of soil retained between the No. 16 and 18 and 200g of soil between the No. 140 and 170. Some of the finer soil grains infiltrated the pores of the coarse grains and thus the boundary between the finer and the coarser material is not as much distinct as in the double gap-graded soil, where the difference in particle size across both boundaries was smaller.

The lack of a distinctive boundary between the finer and the coarser grains made it too difficult to maintain a 256 pixel increment of height in the area where uniform soil particles are. As shown in Figure 8.11, the resulting *CA* value at the top of the coarser soil deposit is smaller than the expected due to the characteristic of *CA* representing a weighed average of the two sizes.

No noteworthy exaggeration of the finer soil volume is observed from the Sedimaging result shown in Figure 8.11. Instead, if the gap between the finer and the coarser is larger more of the finer soil grains would infiltrate the coarser soil below and thus, there would possibly be an exaggeration of the finer soil volume. In such a case, the amount of the finer soil infiltration should be also quantified for determining correct soil grain size distributions by Sedimaging. Fortunately, however, such severely gap-graded soils are not common in nature (they are most likely to be found in a research laboratory).

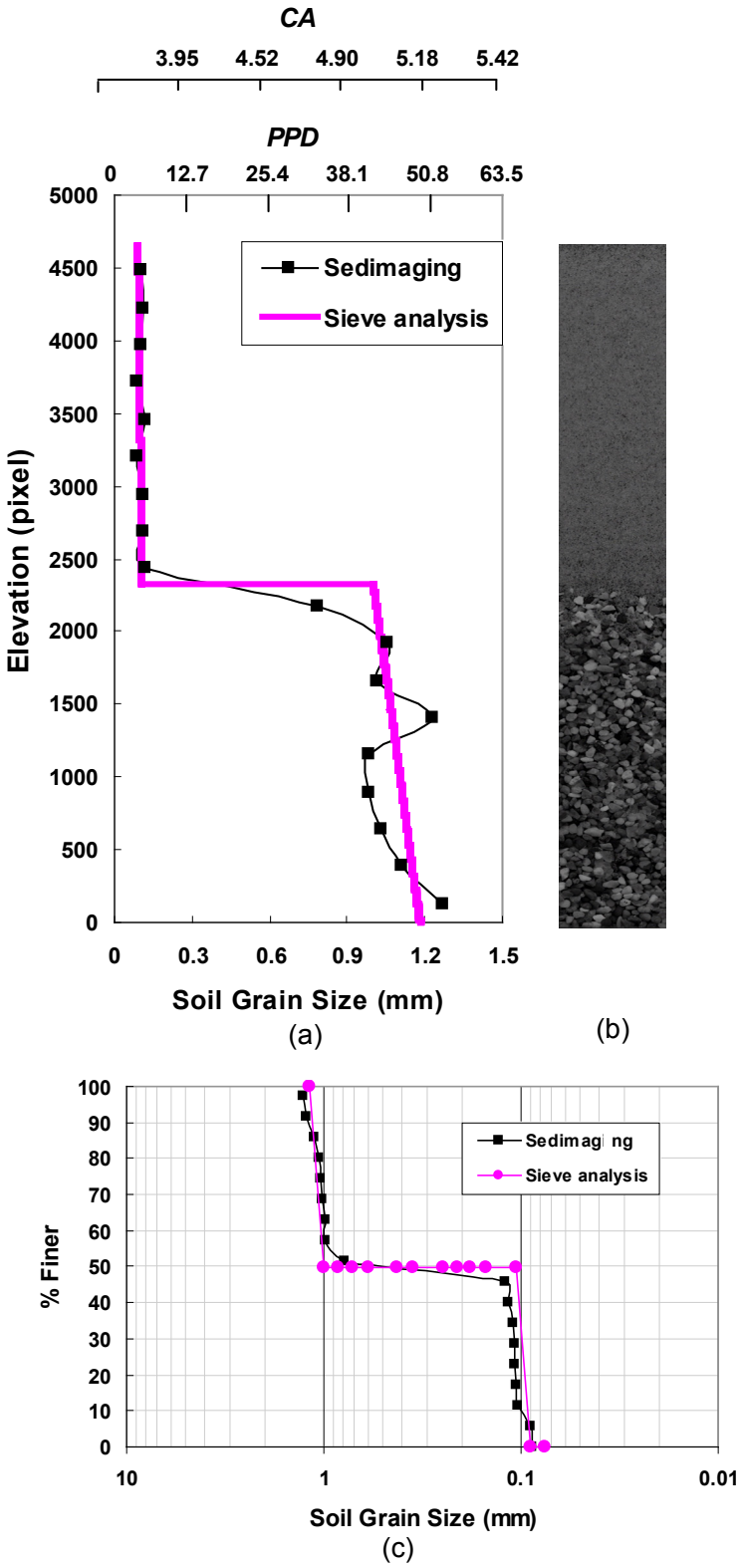

Figure 8.11 a) *CA*, *PPD*, and soil grain size versus elevation of the soil column of a 400g severely gap-graded soil. b) soil column image taken at the magnification level of 42.3 pixel/mm. c) soil grain size distribution by Sedimaging and sieving.

Furthermore, even “silty gravels” generally possess a sufficient fraction of intermediate sized material to form a natural filter between the gravel and silt during sedimentation.

8.3 Application of Sedimaging for ASSHTO Soil Classification

This section discusses a simple method based on Sedimaging to rapidly obtain the volume fractions of soils in the four grain size ranges needed to fully classify AASHTO soils in the A-1 and A-3 Groups, that is, soils with predominantly coarse-grained materials. Classification of soils in all other groups A-4 to A-7 also requires knowledge of the percentage passing the No. 200 sieve and separation of the minus No. 40 fraction for Atterberg limits testing. The method facilitates both tasks.

8.3.1 Soil Percentage for ASSHTO Classification

Digital soil grain size analysis by the three image processing techniques (wavelet decomposition, pattern spectrum, and edge pixel density) lends itself particularly well to the AASHTO soil classification system. This is because all of the images can be taken at a single fixed camera magnification of 32.5 pixels per image millimeter. At 32.5 pix/mm, the No.10 sieve opening of 2.00 mm corresponds to PPD_{10} = 65.0; the No. 40 sieve opening of 0.425 mm corresponds to PPD_{40} = 13.8; and the No. 200 sieve opening of 0.075 mm corresponds to PPD_{200} = 2.4. From the *CA* versus *PPD* calibration shown in Figure 5.21, the *CA* values corresponding to PPD_{10}, PPD_{40} and PPD_{200} are CA_{10} = 5.1, CA_{40} = 3.9 and CA_{200} = 2.9 respectively. From the *SP* vs. *PPD* and *EPD* vs. *PPD* calibration (Figure 6.11 and Figure 7.16, respectively), the *SP* and *EPD* values

corresponding to PPD_{10}, PPD_{40} and PPD_{200} are SP_{10} = 71.6 & EPD_{10} = 0.026, SP_{40} = 15.7 & EPD_{40} = 0.144, and SP_{200} = 3.3 & EPD_{200} = 0.235, respectively. These values are summarized in Table 8.4 for quick reference.

Table 8.4: *CA*, *SP*, *EPD*, and *PPD* at image magnification of 32.5 pixel/mm for the critical sieve openings based on Figure 5.21, Figure 6.11, and Figure 7.16.

Sieve No.	Opening size (mm)	*PPD*	*CA*	*SP*	*EPD*
10	2.000	65.0	5.1	71.6	0.026
40	0.425	13.8	3.9	15.7	0.144
200	0.075	2.4	2.9	3.3	0.235

8.3.2 Three Point Imaging (*TPI*) for ASSHTO Soil Classification

Unlike the Unified Soil Classification system which may require information of the grain size distribution curve above the No. 10 sieve and below the No. 200 sieve for computation of the coefficients of uniformity and gradation, the AASHTO system requires only the percentages of soil in the four zones shown in Figure 8.12. Therefore, the only task for image processing is to locate the height in the sedimented soil column at which the soil grain size index (*CA*, *SP*, and *EPD*) values corresponding to PPD_{10}, PPD_{40}, and PPD_{200} are found. The procedure can appropriately be called the *Three Point Imaging* (*TPI*) test for AASHTO Soil Classification.

8.3.3 Example Soil Classification by Three Point Imaging Test

A well graded sand with approximately 16% “fines” and 18% “coarse sand & gravel” was used to demonstrate the *TPI* test efficiency. The percentages of the soil in the

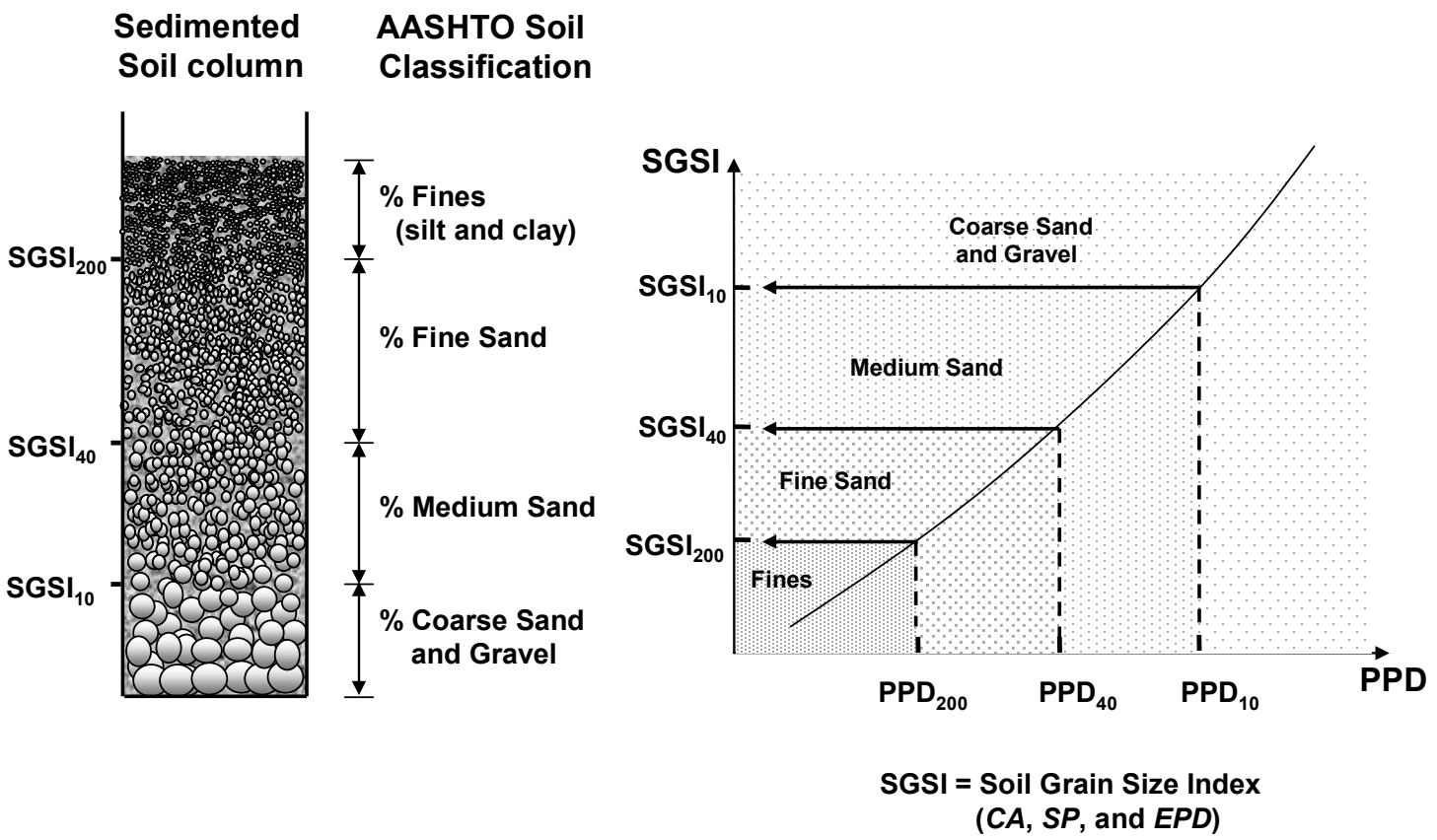

Figure 8.12 Soil regions by type, *PPD* and soil grain size index for a fixed magnification.

four zones ("fines", "fine sand", "medium sand", and "coarse sand & gravel") are provided in Figure 8.13. Also, the distributions from the sedimented soil column are shown in Figure 8.13. The soil column height can be expressed in image pixels or actual distances. While image pixels are used as the unit of measure they are easily converted to millimeters by dividing the pixels by the fixed image magnification of 32.5 pixel/mm. In Figure 8.13, CA_{10} was found at a height of 810 pixels (24.9 mm), CA_{40} was found at 2080 pixel height (64.0 mm) and CA_{200} was observed at 3490 pixel height (107.4 mm). SP_{10} was found at 570 pixel height (17.5 mm) while no "coarse sand & gravel" was not observed by the edge pixel density method. SP_{40} & EPD_{40} were found at a height of 2170 & 2120 pixels (66.8 & 65.2 mm) and SP_{200} & EPD_{200} were observed at 3450 & 3722 pixel height (106.2 & 114.5 mm). With an overall sedimented soil column height of 4096 pixels (126.0 mm), the percentages of the four soil sizes are easily computed. The image based results are compared with the sieve analysis, as shown in Figure 8.13. They are in very good agreement with those from sieving, except the result by the edge pixel density method which missed the "coarse sand & gravel" soil fraction. By the AASHTO system, the soil would be classified as A-1-b. ASTM D-3282 would describe it as "material consisting predominantly of coarse sand, either with or without a well-graded binder".

A second test was performed on a poorly graded sand. The results are presented in Figure 8.14. Once again, when the wavelet decomposition and pattern spectrum methods are used, the image-based results show very good agreement with the sieving result. The observed percentages of the various soil sizes by the three image processing methods are within approximately 2% of the sieving result. By the AASHTO system, the soil is

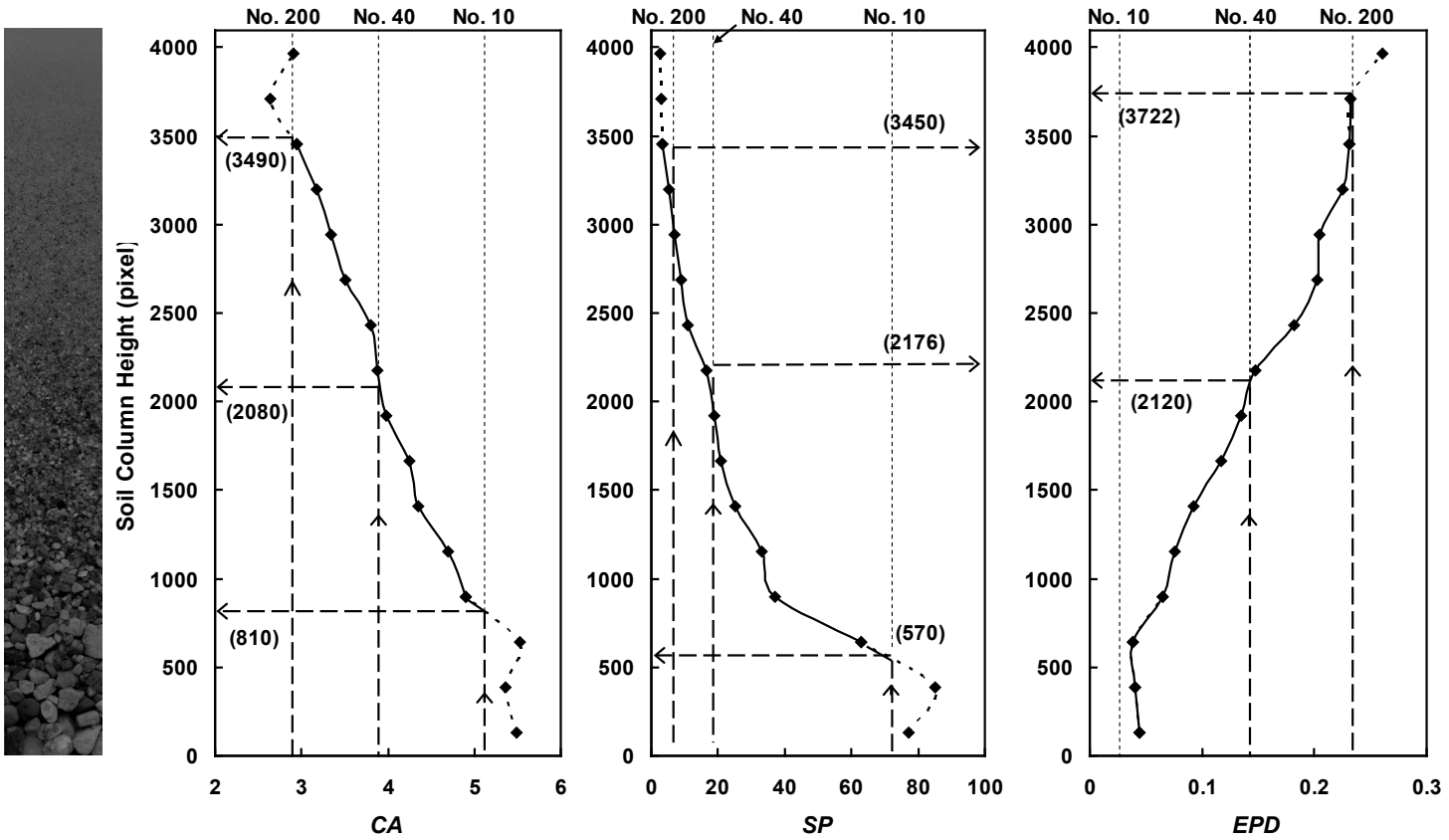

	Sieve analysis	Wavelet decomposition	Pattern spectrum	Edge pixel density
% fines (silt & clay)	15.8	14.8	15.8	9.2
% fine sand	34.2	34.4	31.1	39.1
% medium sand	31.9	31.0	39.2	51.7
% coarse sand & gravel	18.1	19.8	13.9	0

Figure 8.13 Three Point Imaging test results on a well graded sand and their comparisons with sieve analysis.

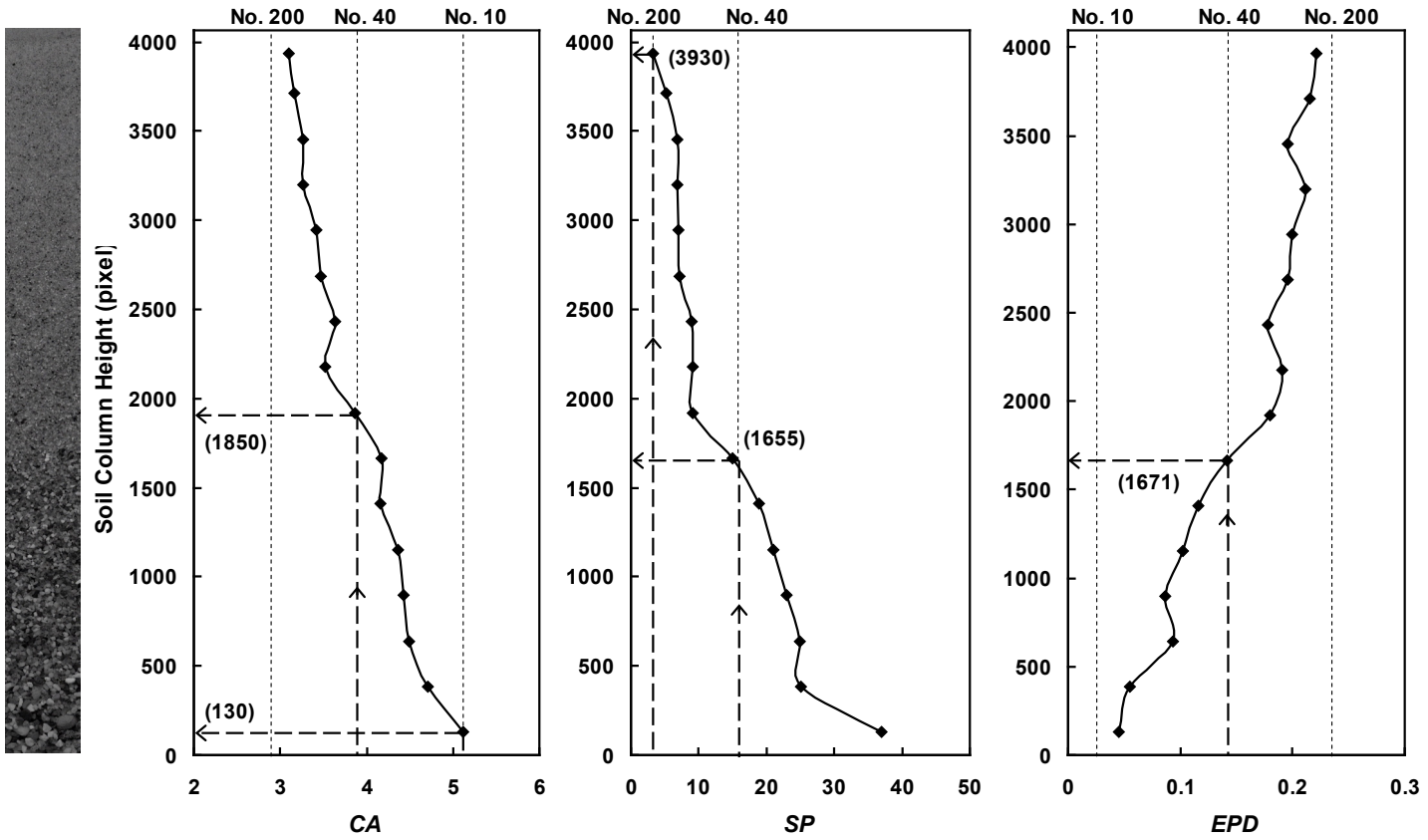

	Sieve analysis	Wavelet decomposition	Pattern spectrum	Edge pixel density
% fines (silt & clay)	2.1	0	3.3	0
% fine sand	56.2	54.5	56.0	58.9
% medium sand	39.6	42.3	40.7	41.1
% coarse sand & gravel	2.1	3.2	0	0

Figure 8.14 Three Point Imaging test results on a poorly graded sand and their comparisons with sieve analysis.

classified as A-3. This is typically a fine beach sand or fine desert blown sand without silty or clay fines, or with a very small amount of non-plastic silt.

8.3.4 One Point Imaging Test for Silty or Clayey Soils

The key value for classification of soils in AASHTO groups A-2, A-4, A-5, A-6, and A-7 is the percent passing the No. 200 sieve. If 35% or less of the material passes the No. 200 sieve the soil is in the broad A-2 grouping with further refinement into subgroups A-2-4, A-2-5, A-2-6, or A-2-7 based on Atterberg limits. If 36% or more of the material passes the No. 200 sieve the soil is A-4, A-5, A-6, or A-7 depending on the Atterberg limits. As such, to make the "35% determination" by imaging, only the depth at which the soil grain size index corresponding to PPD_{200} ($CA_{200} = 2.9$; $SP_{200} = 3.3$; $EPD_{200} = 0.235$) in the sedimentation column must be determined. If this depth is more than 35% of the way down from the surface the soil is a silt or clay. Depending on the Atterberg limits the soil would be A-4, A-5, A-6, or A-7.

If more than 10% of a soil passes the No. 200 sieve, AASHTO soil classification calls for Atterberg limits tests to be performed on the soil fraction passing No. 40 sieve. This requires splitting the original soil sample to perform both sedimentation imaging and the Atterberg tests. Alternatively, soil may be recovered from the sedimented column to the depth of the soil grain size index corresponding to PPD_{40} ($CA_{40} = 3.9$; $SP_{40} = 15.7$; $EPD_{40} = 0.144$). As a practical matter, it is recommended to remove a bit more soil and washing it over the No. 40 sieve to collect the soil for the Atterberg tests.

The results on a sandy silt are shown in Figure 8.15. The pixel heights corresponding to CA_{200}, SP_{200}, and EPD_{200} are 1408, 1400, and 1152, respectively. With a

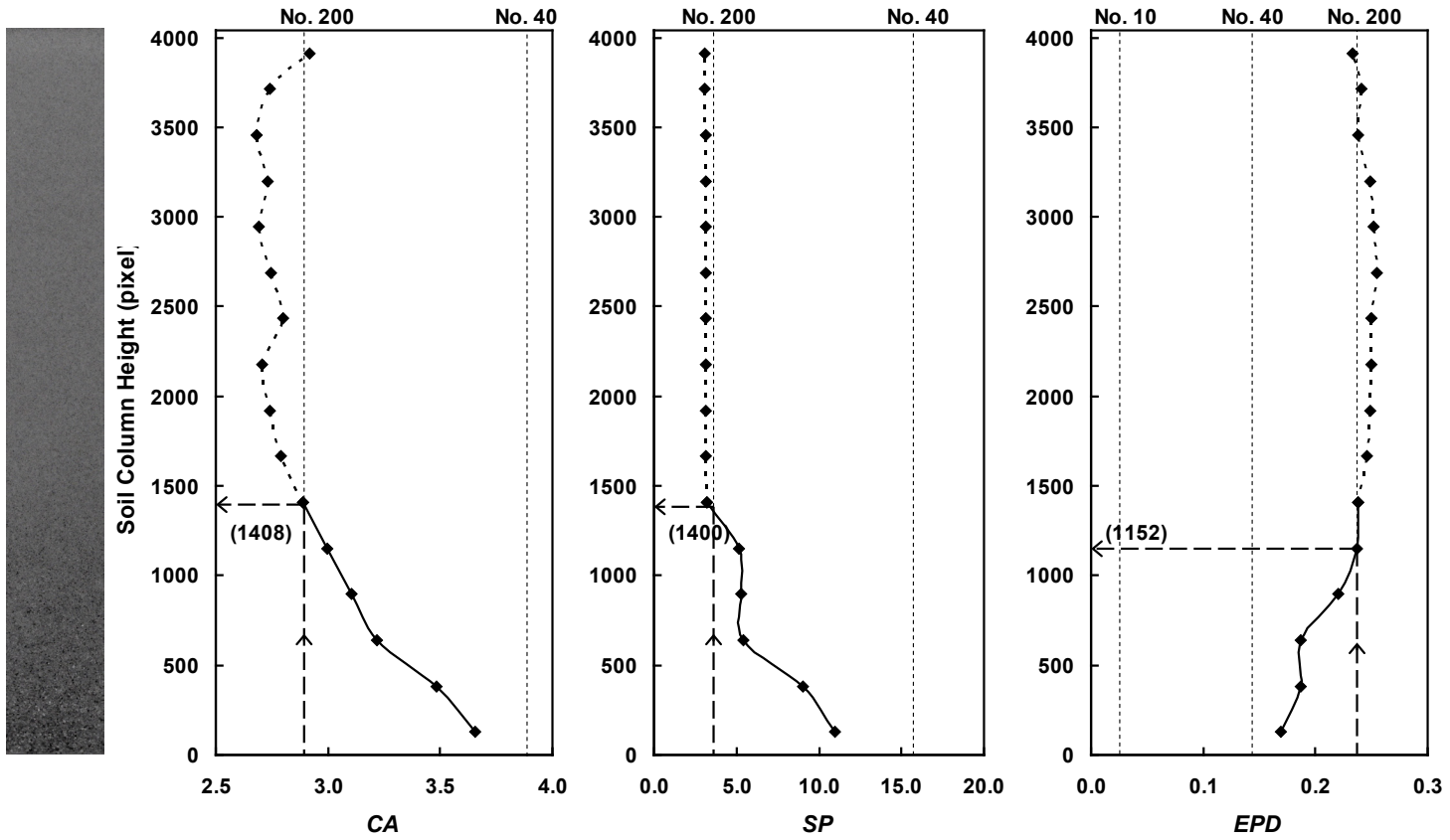

	Sieve analysis	Wavelet decomposition	Pattern spectrum	Edge pixel density
% fines (silt & clay)	63.6	65.1	65.4	71.5
% fine sand	36.4	34.9	34.6	28.5
% medium sand	0	0	0	0
% coarse sand & gravel	0	0	0	0

Figure 8.15 Three Point Imaging test results on a sandy silt and their comparisons with sieve analysis.

measured total specimen height of 4040 pixels, the computed fines content by the wavelet decomposition and pattern spectrum method is 65.1% and 65.4%, respectively, in very good agreement with 63.6% observed by sieving. The fine content determined by the edge pixel density method is 71.5%. The soil is A-4, A-5, A-6, or A-7 depending on the Atterberg Limits.

Overall, the *Three Point Imaging* (*TPI*) test is very well suited to AASHTO Soil Classification. However, the edge pixel density method's implementation into the *TPI* test was not as successful as the other two soil image processing methods. Although the same three soil classifications by the AASHTO system were drawn from sieving and the *TPI* test with the edge pixel density method, the percentages of the three soils in the four zones determined by the *TPI* test somewhat depart from those by sieve analysis.

Finally, in Figures 8.13 and 8.15, the *CA* value at the highest elevation (finest grain size) is uncharacteristically high. The apparent departure from the expected trend is due to laboratory fluorescent light illumination from above and can be fixed using a more uniform light source.

8.4 Conclusions

The information obtained from the previous chapters was combined together and implemented with *Sedimaging*. Sedimaging tests were performed on five soil specimens to determine their soil grain size distribution curves. Each soil specimen was sedimented through the water filled column to segregate it by grain size. Continuous gray scale images of the sedimented soil are taken at a magnification of around 45 pixel/mm. The

soil grain size determined by the wavelet decomposition, pattern spectrum, and edge pixel density methods were presented versus elevation in the column images for direct comparison with sieve based size distribution. The soil grain size distribution curves by sieve analysis and by Sedimaging with the wavelet decomposition and pattern spectrum methods were in good agreement.

As for the application of the edge pixel density method to Sedimaging, the image processing method often produces a less reliable soil grain size index than the wavelet decomposition and pattern spectrum methods, as shown in the soil grain size profiles from Figures 8.2, 8.5, and 8.8. The reliability issue comes from the high sensitivity of the false-edge-removed *EPD* to the soil grain size uniformity in a 256 pixel increment of height in a given soil column image. Even if soil grains in the 256 pixel increment are relatively uniform, the soil grains are still more likely to have a larger size distribution than those in images used for developing the *EPD* versus *PPD* calibration model. In such a case, the chances that the false edge removal step either removes true edges or retains unwanted false edges increase. The sensitivity of the false-edge-removed *EPD* combined with the poorly resolved *EPD* in the high *PPD* range and the larger statistical spreading in the small *PPD* range could result in an unacceptably high or low *EPD* at a given soil column elevation.

Potential problems of gap-graded soils were identified. The biggest problem of gap-graded soils is a lack of distinctive boundary between the finer and the coarser particles in the sedimented soil column. When such a boundary lies within a 256 pixel increment of height the wavelet decomposition method yields a weighted average size based on the fraction of the image area that each soil grain size occupies. The suggested

solution to such problem soils is simply to avoid having the boundary within the 256 pixel increment of height.

A *Three Point Imaging* (*TPI*) test based on Sedimaging was used to rapidly classify soils according to the AASHTO system. A sedimented soil column images is taken at a fixed camera magnification of 32.5 pixel/mm. At this camera magnification, the three critical grain sizes that separate coarse sands & gravels; medium sands; fine sands; and fines (i.e. sieves No. 10, 40, and 200), correspond to 65.0, 13.8, and 2.4 pixels per particle diameter (*PPD*). Each of the three critical values of *CA*, *SP*, and *EPD* corresponding to the three sieves of interest were provided in Table 8.4. AASHTO soil classification requires experimental determination of the three elevations in the sedimented soil column corresponding to the three critical soil grain size index values. Results of tests on a well graded sand with some silt and gravel, a poorly graded medium to fine sand, and a sandy silt demonstrated very good agreement between conventional sieve analysis and the *TPI* test when using the wavelet decomposition and pattern spectrum methods.

The edge pixel density method produced somewhat erroneous soil grain sizes in both the small and large *PPD* ranges by comparison to sieve based soil grain size distributions. Therefore, it is recommended that the wavelet decomposition and pattern spectrum methods be used for determining soil grain size distribution with Sedimaging. Further research with the *EPD* method may improve this method's capabilities.

CHAPTER IX

Conclusions and Recommendations for Future Research

9.1 Research Work Summary

Proper classification of the earth material is essential for anticipation of soil behavior. For classification by either the AASHTO or the Unified Soil Classification system the soil grain size distribution must be determined. The grain size distribution provides quantitative estimates of engineering behavior of soils. This research work focuses on the characterization of soil grain size and size distribution of soils using digital image processing techniques. A new method termed "Sedimaging", which combines rapid soil grain segregation by size through a water-filled sedimentation column with digital image processing, was developed to measure a grain size distribution. It should be noted that this volume-based distribution is fundamentally more appropriate for predicting the mechanical and hydrogeologic behavior of a soil than one based on mass. It is emphasized that Sedimaging does not redefine grain size or create a new classification system. The method requires calibrating image processing results against sieve based grain sizes in order to mimic traditional sieve analysis results. This is

important because soil classification and estimation of fundamental soil properties has a long tradition of being based on grain size distributions as determined by sieve analysis. However, Sedimaging has the potential to simplify, reduce cost and decrease the environmental impacts (noise, dust, energy consumption, and vibration) compared to sieve analysis by utilizing imaging technology to rapidly arrive at the same results.

Development of Sedimaging consisted of three tasks. The first was to develop a soil sedimentation system to rapidly segregate soil grains by size and a vision system to capture images of the sedimented soil column. The second task was to evaluate possible void ratio variations with height in the sedimented soil column and to gauge the significance of the void ratio variations on the soil grain size distribution determined by Sedimaging. The third task was to develop a soil image processing technique for obtaining grain sizes at successive increments of height in the soil column where soil grains are uniform in size.

This chapter presents the major findings from the three Sedimaging development tasks and draws conclusions from Sedimaging test results. Also, recommendations for further improvements to the Sedimaging testing method will be made.

9.2 Soil Sedimentation System

The segregation of soil grains by size during sedimentation is a critical step in Sedimaging. In the early stage of the study, a 48 inch long glass column with a 2 inch by 2 inch cross section was built. Unfortunately, the length of the water filled column was not long enough to adequately segregate the soil grains by size. To improve segregation,

a longer, 96 inch column with the same cross section was employed. The longer column combined with the "battle" between upward seepage and gravitational deposition of soil grains provides a sufficient depositional distance to insure good segregation.

In the early stage of the soil sedimentation system development, it was observed that uneven introduction of the soil into the column produced non-horizontal sediment surfaces. To avoid such non-horizontal layering, a soil release box was constructed. It contains 16 ½ inch by ½ inch vertical chutes with hinged trap doors at the bottom for instantaneous soil release.

An automated motor-driven X-Z camera positioning system, which can be controlled remotely from a personal computer, was adopted to take digital images of sedimented soil column at all elevations continuously.

9.3 Evaluation of Void Ratio in the Soil Column

The soil grain size distribution determined by Sedimaging is inherently volume based. Since a soil column includes both voids and solids, void ratio variations in the column were assessed to determine the volume of soil solids in each 256 pixel increment of the soil column image. Effective stress and soil grain size are two major factors that have influence on void ratio distribution in the soil column. The effect of effective stress on the distribution of void ratio was evaluated by staged soil deposition using uniform grained soils. The test result showed that uniform soils do not exhibit significant variation of void ratio with depth. The result was also supported by sedimenting different amounts of uniform soil into the column and observing that the heights of the sedimented soil

columns were almost perfectly and linearly correlated to the weights of the uniform soil specimens. However, the void ratios were observed to decrease somewhat with increasing grain size. While corrections can easily be applied to the image-based grain size distributions by Sedimaging to obtain better agreement with the actual grain size distribution, the corrections are very small and can be neglected for practical purposes.

9.4 Image Processing for Soil Grain Size

Deterministic pixel counting methods for sizing individual grains in images of three dimensional soil assemblies are too difficult since it is practically impossible to obtain an optimal image threshold value for edge detection and image segmentation to delineate all soil grain boundaries. To overcome the shortcoming of the deterministic methods, three statistical soil grain size analyses based on image texture were developed to compute soil grain size indices. The three soil grain size analysis methods are wavelet decomposition, pattern spectrum, and edge pixel density. Using each method, a unique relationship (calibration model) between an image index and the Pixels Per Diameter (*PPD*) was established. Once the index was computed from each 256 pixel increment of the segregated soil column image, the corresponding *PPD* was determined from the calibration model and with known camera magnification, the soil grain size at each elevation of the soil column was determined.

Wavelet decomposition method

Wavelet transformation is found to be effective in determining the particle size from images of three dimensional soil assemblies of uniform grains. This is because the mathematical transformation, which is a Multi Resolution Analysis method (MRA), is well suited to analyze soil images which have high (internal textures) and low frequency (soil grains) components for short and long durations, respectively.

Using wavelet transformation, Shin and Hryciw (2004) developed the soil grain size index (*CA*) to determine the particle size from images of three dimensional soil assemblies of uniform soil grains. The *CA* versus *PPD* calibration for dry soil conditions was developed. Initially, the calibration was available for a range of *PPD* from 2 to 50 from Shin and Hryciw (2004). In this study, the calibration was extended to a range from 0.2 to 110 *PPD*. It was shown that the *CA* for *PPD* less than 1 (*CA* corresponding to 1 *PPD* is 2.4) does not carry any useful soil grain size information.

For implementation of the wavelet decomposition method in Sedimaging, the effect of water on *CA* was studied by using the Vision Cone Penetrometer (VisCPT) and the double ring soil saturator (DRSS). It was shown that water blurs internal textures within individual soil grains and thus increases *CA*. The change in *CA* due to water was evaluated for various *PPD* and a new *CA* versus *PPD* calibration under saturated soil condition was presented.

It was also shown that *CA* is independent of the image capturing systems as long as the pixel aspect ratio is kept consistent by either digitally compressing digital images or by using camera systems that produce the same pixel aspect ratios.

Pattern spectrum method

A pattern spectrum method has been developed for statistical soil grain size analysis as opposed to other methods that take a deterministic approach using mathematical morphology. The statistical pattern spectrum method eliminates the need for image preprocessing, such as image binarization and segmentation of individual soil grains. Such preprocessing is greatly influenced by operator skill.

A *Structuring Element Size* (*SES*) at the peak of the *pattern spectrum* was initially considered to be a soil grain size index. However, due to the inherent difference in shape between real soil grains and diamond structuring element, the *SES* at peak of the pattern spectrum can not be used as direct indication of *PPD* or soil grain size. Therefore, the calibration, *SES* at the peak of the pattern spectrum (*SP*) versus *PPD*, was developed. The calibration showed a nice linear relationship between *SP* and *PPD* and was successfully applied to three dimensional soil assemblies of uniform grains.

In the calibration model, a wide statistical spreading was observed at high *PPD*. This spread can be simply diminished when larger images are used, which is not doable in the wavelet decomposition method which requires a fixed image size, 256 pixel by 256 pixel, to use the *CA* versus *PPD* calibration.

Edge pixel density method

An Edge pixel density (*EPD*) method based on a modified Canny edge detector was developed to determine the grain size of soils from images of three dimensional assemblies of uniform soil grains. A major modification made is the removal of false

edges (edges due to noise and internal textures) smaller than a soil grain diameter. This requires a first estimate of the *PPD* from a preliminary pre-short-edge-removed *EPD* versus *PPD* curve.

Two methods were suggested to remove false edges. The first method removes a false edge if it consists of fewer pixels than the first estimate of *PPD*. The second method performs false edge removal based on the longest dimension of an edge segment determined by area-based elliptical fitting. Edges were classified as false edges if their longest dimension was smaller than the first estimate of *PPD*. It was shown that the second method is more effective in identifying false edges than the first method although it is computationally more demanding.

9.5 Sedimaging

Sedimaging tests with the three developed image processing techniques were performed on three soil specimens having different size gradations. The soil grain size in each specimen ranged from 0.038 mm to 2 mm. The soil grain size distribution curves by sieve analysis and by Sedimaging with the wavelet decomposition and pattern spectrum methods were generally in good agreement even if slight differences in soil grain size was observed in the bottom area of the sedimentation column where *PPD* is high. The difference is largely attributed to the inherent statistical spreading of *CA* and *SP* at high *PPD*s in the *CA* vs. *PPD* and the *SP* vs. *PPD* calibration models.

The edge pixel density method produces a less accurate and reliable soil grain size distribution from a soil column image than the wavelet decomposition and pattern

spectrum methods. That would be because the false-edge-removed *EPD* is sensitive to soil grain size uniformity in a 256 pixel increment of height in the soil column image. Also, the sensitivity of the false-edge-removed *EPD* combined with the poorly resolved *EPD* in the high *PPD* range and the larger statistical spreading in the small *PPD* range may be the reason for an unacceptably high or low *EPD* values at a soil column elevation.

A *Three Point Imaging* (*TPI*) test based on Sedimaging was used to rapidly classify soils according to the AASHTO system. At a fixed magnification of 32.5 pixel/mm, the three critical soil grain size index values that separate coarse sands & gravels; medium sands; fine sands; and fines (i.e. sieves No. 10, 40, and 200) were found. AASHTO soil classification by *TPI* requires experimental determination of the three elevations in the sedimented soil column corresponding to the three critical soil grain size index values. Results of tests on three soil specimens having different gradations demonstrated very good agreement between conventional sieve analysis and the *TPI* test with the wavelet decomposition and pattern spectrum methods. However, *TPI* test with the edge pixel density method was not as successful as the other two methods.

Sedimaging grain size distributions by the edge pixel density method consistently showed larger deviations from sieve based results than the other two image processing methods did. Therefore, it is recommended that the wavelet decomposition and pattern spectrum methods be used for determining soil grain sizes until further improvement to the *EPD* method can be made.

9.6 Recommendations for Future Research

To date, Sedimaging has characterized soils with grain diameters up to 2.0 mm. The image processing methods developed are size and scale independent. Therefore, they can be used for sizing coarser aggregate. However, the Sedimaging hardware would have to be modified to accommodate particles at least up to 4.75 mm (No. 4 sieve) in size. A study needs to be performed to determine the required hardware modifications for such a task. It may involve design of a wider sedimentation column, although it may not need to be square in cross section. The sedimentation column length requirement may need to be reevaluated to accommodate segregation of larger grain sizes. Also, the soil release box needs to be modified for larger grain sizes. The air gap between the water surface in the sedimentation column and the bottom of the soil release box causes a large initial falling velocity. So, elimination of the undesirable air gap and saturation of soil specimen prior to release may provide better segregation of larger grain sizes.

When a series of Sedimaging tests are to be performed, the removal of water and the soil specimen out of the glass sedimentation column will take up the majority of Sedimaging testing time since the column has to be disassembled from the support tower. A modified system to reduce the pre- and post-test activity is needed to make Sedimaging user-friendly. This can be done by building a sedimentation system which consists of two parts, a sedimentation tube for segregation of soil grains and a cartridge having a glass window for soil deposition and imaging. The tube can be fixed to a sedimentation column support tower while the cartridge can be disassembled from the tube for easy disposal of

the used soil specimen. Also, permanently fixing the position of the tube can eliminate the need to adjust its verticality every test.

The number of soil grains that are actually used for the image processing techniques constitutes a small fraction of the overall number of grains in a typical soil specimen. Therefore, considerations should be given to find a way that maximizes the ratio of exposed surface area to volume while facilitating segregation by size.

Currently available camera magnifications do not extend Sedimaging into the clay sized grains range. However, considering the development rate of digital camera optics, off-the-shelf low-light digital camera optics will soon be available that will permit grain sizing into the micron range where 0.002 mm delineates silt-sized from clay-sized soil particles. Such a system will be able to extend soil classification to the upper clay-size particle limit. It should be noted that, when classifying the clay sized grains range, corrections for void ratio variations may have to be applied to the image-based grain size distribution since the difference in depositional void ratio for different sizes may be no longer insignificant in the soil grain size range.

Sedimaging tests have been performed mostly on alluvial and glaciofluvial soil. The soil grains are generally sub-rounded and multi-colored. Soil of other colors (including uniform and translucent) and angular particle shape have not been tested. So, it is desirable to perform tests on various soils to see if they pose any unusual problems for Sedimaging.

A digital image of the sedimented soil column can be obtained at higher resolution. After appropriate segmentation of non-occluded soil grains, an image could be used to determine particle shape and angularity.

It was shown that, in the high *PPD* range, soil grain sizes computed by the three image processing techniques are not in as good agreement with sieve based sizes as they are in the lower *PPD* range. That is attributed to the large statistical spreading in the calibration models. The statistical spreading is due to fewer soil grains included in a 256 pixel increment of height with increasing *PPD*. This problem can be overcome by using variable magnification so that all of the *PPD* values fall into the range where statistical spreading is a minimum, although this introduces complexity to the hardware requirement and data acquisition.

In this study, a fixed vertical image increment of 256 pixels was used to compute soil grain size indices. In some cases, the image increment could have some variation in size, which is not desirable. If the size of an image increment can be adjusted automatically depending on the uniformity of particle sizes so that each image increment only contains relatively uniform soil gains, more accurate Sedimaging results would be expected.

Since soil with some variation in size displays a wider distribution of the *Normalized Energy* and pattern spectrum across the decomposition levels and structuring element sizes, respectively, than observed for uniform grains, a numerical index of the spread in *Normalized Energy* and pattern spectrum could be useful for particle size uniformity assessment.

REFERENCES

Al-Rousan, T., Masad, E., Tutumluer, E., and Pan, T. (2007). "Evaluation of Image Analysis Techniques for Quantifying Aggregate Shape Characteristics". *Construction and Building Materials*, *21*, 978-990.

American Society for Testing and Materials (ASTM). (1995). "Standard Test Method for Flat Particles, Elongated Particles, or Flat and Elongated Particles in Coarse Aggregate". *ASTM Designation*, *4791-89*, Philadelphia.

Atherton, E. (1952). "Photoelectric Turbimeter for Particle Size Measurement". *Journal* of the *Textile Institute Trans*., *43*, T173-178.

Balagurunathan, Y. and Dougherty, E.R. (2003). "Morphological Quantification of Surface. Roughness". *Optical Engineering*, *42*(6), 1795-1804.

Barnard, P.L., Rubin, D.M., Harney, J., and Mustain, N. (2007). "Field Test Comparison of an Autocorrelation Technique for Determining Grain Size Using a Digital 'Beachball' Camera Versus Traditional Methods". *Sedimentary Geology*, *201*(1-2), 180-195.

Berg, S. (1940). *Ingen Vidensk*., Skr., B., No2.

Beuselinck, L., Govers, G., Poesen, J., Degraer, G., and Froyen, L. (1998). "Grain Size Analysis by Laser Diffractometry: Comparison with the Sieve Pipette Method". *Catena*, *32*, 193-208.

Brzezicki, J.M., Kasperkiewicz, J. (1999). "Automatic Image Analysis in Evaluation of Aggregate Shape". *Journal of Computing in Civil Engineering*, *13*(2), 123-128.

Buurman, P., Pape, T., and Muggler, C.C. (1997). "Laser Grain-Size Determination in Soil Genetic Studies 1.Practical Problems". *Soil Science*, *162*, 211-218.

Campbell, J.R. (2003). "Limitations in the Laser Particle Sizing of Soils". *Advances in Regolith: Proceedings of the CRC LEME Regional Regolith Symposia*, 38-42.

Canny, J. (1986). "A Computational Approach to Edge Detection". *IEEE Transactions on Pattern Analysis and Machine Intelligence*, *6*(6), 679-698.

Carrier III, W.D., Bromwell, L.G., and Somogyi, F. (1983). "Design Capacity of Slurried Mineral Waste Ponds". *Journal of Geotechnical Engineering, ASCE*, *109*(5), 699-716.

Dahl, C.K. and Esbensen, K.H. (2007). "Image Analytical Determination of Particle. Size Distribution for Natural and Industrial Bulk Solid Aggregates". *Chemometrics and Intelligent Laboratory Systems*, *89*(1), 9-25.

Darboux, F. and Huang, C. (2003). "An Instantaneous-Profile Laser Scanner to Measure Soil Surface Microtopography". *Soil Science Society of America Journal*, *67*(1), 92-97.

Devaux, M.F., Robert, P., Melcion, J.P., and Le Deschault de Monredon, F. (1997). "Particle Size Analysis of Bulk Powders Using Mathematical Morphology". *Powder Technol*ogy, *90*, 141-147.
Fernlund, J.M.R., Zimmerman, R.W., and Kragic, D. (2007). "Influence of Volume/Mass on Grain-Size Curves and Conversion of Image-Analysis Size to Sieve Size". *Engineering Geology*, *90*, 124-137.

Garboczi, E.J. (2002). "Three-dimensional Mathematical Analysis of Particle Shape Using X-ray Tomography and Spherical Harmonics: Application to Aggregates Used in Concrete". *Cement and Concrete Research*, *32*, 1621-1638.

Garboczi, E.J. and Bullard, J.W. (2004). "Shape Analysis of a Reference Cement". *Cement and Concrete Research*, *34*, 1933–1937.

Georges, M. (1975). "Random Sets and Integral Geometry". *John Wiley and Sons Inc*., *New York*, 510

Ghalib, A.M., Hryciw, R.D., and Shin, S. (1998). "Image Textural Analysis and Neural Networks for Characterization of Uniform Soils". *Proceedings Conference on Computing in Civil Engineering*, *ASCE*, *Reston*, *VA*., 671-682.

Ghalib, A.M. and Hryciw, R.D. (1999). "Soil Particle Size Distribution by Mosaic Imaging and Watershed Analysis". *Journal of Computing in Civil Engineering*, *13*(2), 80-87.

Ghalib, A.M., Hryciw, R.D., and Susila, E. (2000). "Soil Stratigraphy Delineation by VisCPT". *ASCE Geotechnical Special Publication No. 97 Innovations and Applications in Geotechnical Site Characterizations*, *Proceedings of GeoDenver* 2000, 65-79.

Graham, D.J., Reid, I., and Rice, S.P. (2005). "Automated Sizing of Coarse-grained Sediments: Image-processing Procedures". *Mathematical Geology*, *37*(1), 1-28.

Haar, A. (1910). "Zur Theorie der Orthogonalen Function en Systeme". *Math. Annal*., *69*, 331-371.

Han, Q.W., Wang, Y.C., and Xiang, X.L. (1981). "Initial Dry Density of Sediment Deposit". *Journal of Sediment Research*, *1* (in Chinese, as cited by Wu and Wang, 2006).

Haralick, R.M., Shanmugam, K., and Dinstein, I. (1973). "Textural Features for Image Classification". *IEEE Transactions on Systems*, *Man and Cybernetics*, *SMC-3*(6), 610-621.

Haralick, R.M. and Shapiro, L.G. (1992). *Computer and Robot Vision*, Addison-Wesley, Reading, MA.

Heisenberg, W. (1930). *The Physical Principles of Quantum Theory*, University of Chicago Press.

Horgan, G.W. (1998). "Mathematical Morphology for Analyzing Soil Structure from Images". *European Journal of Soil Science*, *49*, 161–173.

Hryciw, R.D., Ghalib, A.M., and Raschke, S.A. (1998). "Methods for Soil Characterization from Images of Grain Assemblies". *Proceedings of the Second International Conference on Imaging Technologies: Techniques and Civil Engineering Applications*, *ASCE*, 88-99.

Hryciw, R.D., Shin, S., and Jung, Y. (2006). "Soil Image Processing: Single Grains to Particle Assemblies". *Proceedings, GeoCongress 2006: Geotechnical Engineering in the Information Technology Age* (CD-ROM), *Atlanta*, *GA*., *Geo-Institute of the American Society of Civil Engineers*, *Reston*, *VA*.

Hu, M.K. (1962). "Visual Pattern Recognition Using Moment Invariants". *IRE Transactions on Information Theory*, *IT-8*, 179-187.

Isbell, R.F. (1996). *The Australian Soil Classification*, CSIRO Publishing, Melbourne, Australia.

Jain, A.K. (1989). *Fundamentals of Digital Image Processing*, Random House, New York.

Kass, M., Witkin, A., and Terzopoulos, D. (1987). "Snakes: Active Contour Models". *International Journal of Computer Vision*. *1*(4), 321-331.

Kim, H.K., Haas, C.T., Rauch, A.F., and Browne, C. (2002). "Wavelet-Based 3D Descriptors of Aggregate Particles". *Transportation Research Board*, *Washington*, *D.C.* (CD-ROM).

Konert, M. and Vandenburghe, J. (1997). "Comparison of Laser Grain Size Analysis with Pipette and Sieve Analysis: a Solution for the Underestimation of the Clay Fraction". *Sedimentology*, *44*, 523-535.

Krumbein, W.C. (1932). "The Mechanical Analysis of Fine Grained Sediments". *Journal of Sedimentary and Petrology*, *2*, 140-149.

Kuo, C-Y., Frost, J.D., Lai, J.S., and Wang, L.B. (1996). "Three-Dimensional Image Analysis of Aggregate Particles from Orthogonal Projections", *Transportation Research Record, National Research Council*, *Washington*, *D.C.*, *1526*, 98-103.

Kuo, C.Y. and Freeman, R.B. (2000). "Imaging Indices for Quantification of Shape, Angularity, and Surface Texture of Aggregates". *Transportation Research Board 79th Annual Meeting*, *Washington*, *D.C.*

Lanaro, F. and Tolppanen, P. (2002). "3D Characterization of Coarse Aggregates". *Engineering Geology*, *65*, 17–30.

Lassoued, N., Babin, P., Della Valle, G., Devaux, M.F., and Réguerre, A.L. (2007). "Granulometry of Bread Crumb Grain: Contribution of 2D and 3D Image Analysis at Different Scales". *Food Research International*, *40*, 1087-1097.

Lee, J.R.J., Smith, M.L., and Smith, L.N. (2007). "A New Approach to the Three-Dimensional Quantification of Angularity Using Image Analysis of the Size and Form of Coarse Aggregates". *Engineering Geology*, *91*, 254-264.

Li, L., Chan, P., Zollinger, D.G., and Lytton, R.L. (1993). "Quantitative Analysis of Aggregate Shape Based on Fractals". *ACI Materials Journal*, *90*(4), 357–365.

Lira, C., Saraiva, J., Pina, P., Bandeira, L., and Antunes, J. (2009). "A Mathematical Morphology Approach to the Analysis of Martian Soil Samples". *41st Lunar and Planetary Science Conference*, *Lisboa*, *Portugal*.

Loizeau, J.L., Arbouille, D., and Santiago, S. (1994). "Evaluation of a Wide Range Laser Diffraction Grain Size Analyser for Use with Sediments". *Sedimentology*, *41*, 353-361.

Maerz, N.H. and Zhou, W. (1998). "Optical digital fragmentation measuring systems – inherent sources of error". *FRAGBLAST*, *The International Journal for Blasting and Fragmentation*, *2*(4), 415-431.

Maerz, N.H. and Zhou, W. (1999). "Flat and Elongated: Advances Using Digital Image Analysis". *7th Annual ICAR Symposium*, *Aggregates*: *Concrete*, *Bases*, *and Fines*, *Austin*, *Texas*, B1-4-1–B1-4-12.

Maerz, N.H. and Lusher, M. (2000). "Measurement of Flat and Elongation of Coarse Aggregate Using Digital Image Processing". *Proceedings of Transportation Research Board, 80th Annual Meeting*, *Washington D.C.*, Paper No. 01-0177.

Maerz, N.H. (2004). "Technical and Computational Aspects of the Measurement of Aggregate Shape by Digital Image Analysis". *Journal of Computing in Civil Engineering*, *18*(1), 10-18.

Maragos, P., Sofou, A., Stamou, G.B., Tzouvaras, V., Papatheodorou, E., and Stamou, G.P. (2004). "Image Analysis of Soil Micromorphology: Feature Extraction, Segmentation, and Quality Inference". *EURASIP Journal on Applied Signal Processing*, *2004*(6), 902-912.

Marinoni, N., Pavesea, A., Foia, M., and Trombino, L. (2005). "Characterisation of Mortar Morphology in Thin Sections by Digital Image Processing". *Cement and Concrete Research*, 35, 1613-1619.

Marr, D. and Hildrcth, E. (1980). "Theory of Edge Detection". *Proc. R. Soc. London*, *Series B*, *207*, 187-217.

Masad, E. and Button, J.W. (2000). "Unified Imaging Approach for Measuring Aggregate Angularity and Texture". *The International Journal of Computer-Aided Civil and Infrastructure Engineering – Advanced Computer Technologies in Transportation Engineering*, *15*(4), 273-280.

Matheron, G. (1975). *Random Sets and Integral Geometry*. Wiley, New York.

Matsushima, T., Katagiri, J., Uesugi, K., Tsuchiyama, A., and Nakano, T. (2009). "3D Shape Characterization and Image-Based DEM Simulation of the Lunar Soil Simulant FJS-1". *Journal of Aerospace Engineering*, *22*(1), 15-23.

Mertens, G. and Elsen, J. (2006). "Use of Computer Assisted Image Analysis for the Determination of the Grain-Size Distribution of Sands Used in Mortars". *Cement and Concrete Research*, 36, 1453-1459.

Meyer, F. and Beucher, S. (1990). "Morphological Segmentation". *Journal of Visual Communication and Image Representation*, *1* (1), 21-46.
Mie, G. (1908). "Articles on the Optical Characteristics of Turbid Tubes, especially Colloidal Metal Solutions". *Annalen der Physik*, *25*(3), 377-445.

Mora, C.F., Kwan, A.K.H., and Chan, H.C. (1998). "Particle Size Distribution Analysis of Coarse Aggregate Using Digital Image Processing". *Cement and Concrete Research*, *28*, 921-932.

Pareschi, M.T., Pompilio, M., and Innocenti, F. (1990). "Automated Evaluation of Volumetric Grain-Size Distribution from Thin-Section Images". *Computers and Geosciences*, *16*(8), 1067-1084.

Park, J.S., Liu, Y., Kihm, K.D., and Taylor, L.A. (2008). "Characterization of Lunar Dust for Toxicological Studies. I: Particle Size Distribution". *Journal of Aerospace Engineering*, *21*(4), 266-271.

Pavlidis T. and Liow, Y.T. (1990). "Integrating Region Growing and Edge Detection". *IEEE Transaction Pattern Analysis Machine Intelligence*. *12*, 225-233.

Penumadu, D. and Wettimuny, R. (2002). "Characterization of Aggregate Shape Using Fourier Analysis and Digital Imaging Technique". *Transportation Research Board*, *Washington*, *D.C*. (CD-ROM).

Prodanov, D., Heeroma, J., and Marani, E. (2006). "Automatic Morphometry of Synaptic Boutons of Cultured Cells Using Granulometric Analysis of Digital Images". *Journal of Neuroscience Methods*, *151*, 168-177.

Rao, C., Tutumluer, E., and Stefanski, J.A. (2001). "Coarse Aggregate Shape and Size Properties Using a New Image Analyzer". *Journal of Testing and Evaluation*, *29*(5), 461-471.

Raschke, S.A. and Hryciw, R.D. (1997). "Soil Grain Size Distribution by Computer Vision". *ASTM Geotechnical Testing Journal*, *20*(4), 433-422.

Raschke, S.A. and Hryciw, R.D. (1997a). "Vision Cone Penetrometer (VisCPT) for Direct Subsurface Soil Observation". *ASCE Journal of Geotechnical and Geoenvironmental Engineering*, 123(11), 1074-1076.

Roberts, L. (1965). *Machine Perception of 3-D Solids*, *Optical and Electro-Optical Information Processing*, MIT Press.

Russ, J.C. (1995). *The Image Processing Handbook*, CRC Press, Inc.

Serra, J. (1982). "Image Analysis and Mathematical Morphology". *Academic Press*, *London*.

Sharifi, M., Fathy, M., and Mahmoudi, M.T. (2002). "A Classified and Comparative Study of Edge Detection Algorithms". *Proceedings International Conference on Information Technology: Coding and Computing*, 117-120.

Shin, S. and Hryciw R.D. (2004). "Wavelet Analysis of Soil Mass Images for Particle Size Determination". *ASCE Journal of Computing in Civil Engineering*, *18*(1), 19-27.

Simmons, G. (1959). "The Photo Extinction Method for the Measurement of Silt Sized Particles". *Journal of Sedimentary and Petrology*, *29*(2), 233-245.

Sofou, A., Evangelopoulos, G., and Maragos, P. (2005). "Soil Image Segmentation and Texture Analysis: A Computer Vision Approach". *IEEE Geoscience and Remote Sensing Letters*, *2*(4), 394-398.

Somogyi, F. (1979). "Analysis and Prediction of Phosphatic Clay Consolidation". *Implementation Package*, *Technical Report*, *Florida Phosphatic Clay Research Project*, *Lakeland*, *FL*.

Stratton, A. (1941). *Electromagnetic Theory*, McGraw-Hill, New York.

Tolppanen, P., Illerstrom, A., and Stephansson, O. (1999). "3-D Laser Analysis of Size, Shape and Roughness of Railway Ballast - Research in Progress". *7th Annual ICAR Symposium*, *Aggregates*: *Concrete*, *Bases*, *and Fines*, *Austin*, *Texas*, F2-3-1 - F2-3-8.

Van den Berg, E. H., Meesters, A.G.C.A., Kenter, J.A.M., and Schlager, W. (2002). "Automated Separation of Touching Grains in Digital Images of Thin Sections". *Computers and Geosciences*, *28*(2), 179-190.

Wang, L.B. and Lai, J.S. (1998). "Quantifying Surface Area of Aggregates Using an Imaging Technique." *Transportation Research Board 77th Annual Meeting*, *Washington*, *D.C*.

Wang, L.B., Frost, J.D., and Mohammad, L. (2002). "Three-dimensional Aggregate Evaluation Using X-ray Tomography Imaging". *Transportation Research Board*, *Washington*, *D.C*. (CD-ROM).

Wang, L., Wang, X., Mohammad, L., and Abadie, C. (2005). "Unified Method to Quantify Aggregate Shape Angularity and Texture Using Fourier Analysis". *Journal of Materials in Civil Engineering, 17*(5), 498-504.

Wettimuny, R. and Penumadu, D. (2004). "Application of Fourier Analysis to Digital Imaging for Particle Shape Analysis". *Journal of Computing in Civil Engineering*, *18*(1) 2-9.

Wilson, J.D. and Klotz, L.D. (1996). "Quantitative Analysis of Aggregate Based on Hough Transform". *Transportation Research Record*, *Washington*, *D.C*., *1530*, 111-115.

Wu, W. and Wang, S.S.Y. (2006). "Formulas for Sediment Porosity and Settling Velocity". *ASCE Journal of Hydraulic Engineering*, *132*(8), 858-862.

Wu, Y.S., van Vliet, L.J., Frijlink, H.W., and van der Voort Maarschalk, K. (2007). "Pore Size Distribution in Tablets Measured with a Morphological Sieve". *International Journal of Pharmaceutics*, *342*, 176-183.

Yen, Y.K., Lin, C.L., and Miller, J.D. (1998). "Particle Overlap and Segregation Problems in On-line Coarse Particle Size Measurement". *Powder technology*, *98*(1), 1-12.

Yudhbir, J. and Abedinzadeh, R. (1991). "Quantification of Particle Shape and Angularity Using the Image Analyzer". *ASTM Geotech Test Journal*, *14* (3), 296- 308.

Zhou, Y., Starkey, J., and Mansinha, L. (2004). "Segmentation of Petrographic Images by Integrating Edge Detection and Region Growing". *Computers and Geosciences*, *30*(8), 817-831.